The development and breakaway of a compressible air jet with streamline curvature and its application to the coanda flare

Andrew Robert Gilchrist

THE DEVELOPMENT AND BREAKAWAY OF A COMPRESSIBLE AIR JET WITH STREAMLINE CURVATURE AND ITS APPLICATION TO THE COANDA FLARE

by

ANDREW ROBERT GILCHRIST B.Sc. (Dunelm)

Department of Engineering
University of Durham

A thesis submitted for the degree of Doctor of Philosophy
of the University of Durham

NOVEMBER 1985

Dedicated to my parents

ABSTRACT

This study concerns an underexpanded jet, issuing from a convergent slot into quiescent air, as it is deflected by a convex surface of constant radius. Emphasis is placed on the mechanism of breakaway, a phenomenon whereby the jet leaves the surface tangentially.

An optical system based on the standard Z-type Schlieren configuration and capable of interferometric, Schlieren and shadowgraph techniques has been designed. The techniques are interchanged simply, a laser source being employed for interferometry and a Xenon spark source for Schlieren and shadowgraph. Vibrations limit the interferometry and improvements are discussed. Shadowgraph and both spark and continuous Schlieren techniques gave good results.

Total pressure traverses and surface oil flow visualization show that the influence of secondary flows on breakaway is small. Measurements of the coefficient of discharge show an increase both as the stagnation pressure is increased and as the slot width is reduced. The existence of a separation bubble has been established from surface static pressure measurements and shadowgraph and Schlieren photographs. Surface oil flow visualization shows a region of reversed flow within the bubble. The bubble grows as the stagnation pressure is increased and eventually causes breakaway.

A potential flow calculation method using the method of characteristics has been developed. Calculation of a fully attached jet is inaccurate because the separation bubble is ignored. A calculation using the measured surface static pressures accurately predicts the main features of the first shock cell. Reattachment occurs further downstream of the jet and its breakaway should involve a coupling of the solutions of the outer shear layer, potential core and separated boundary layer, the latter including reversed flow.

ACKNOWLEDGEMENTS

I would like to express my gratitude to the people and organisations that have contributed to the work presented in this thesis. In particular to my supervisor Dr. David Gregory-Smith, not only for setting up the project, but also for his guidance throughout the study and the preparation of this thesis. To the Science and Engineering Research Council and British Petroleum Research Centre at Sunbury-on-Thames for their financial support. To Dr. John Boden and Dave Chesters of the B.P. Research Centre and Dave Etheridge and Garry Oskam of Kaldair Ltd. for their help and advice. To Bill, Terry, Ray, Mike, Frank and Brian for their technical help. To Chris for her efficient speedy typing. To Joe, who at last proved more of a help than a hinderance when acting as a solid ultra-violet lamp holder during the flow visualization photography. And to Alastair, whose light-fingeredness on the flow control valve enabled photographs such as those in Plate 23 to be taken.

C O N T E N T S

LIST OF FIGURES

LIST OF PLATES

PRINCIPAL NOTATION

A	area of slot
a	Coanda radius, speed of sound (Section 3.1, Appendix A)
b	slot width
c	settling tube width, speed of light (Chapter 4)
c_D	discharge coefficient
c_p	surface static pressure coefficient
$c_{p'}$	surface static pressure coefficient with curvature, $= - c_p(a/b)$
d	height of light source image above knife edge
e	breadth of light source image
f	focal length
I	light intensity
K	Gladstone–Dale constant
k	coefficient of heat viscosity
M	Mach number
m	mass flow rate
n	refractive index
p	static pressure
p_0	stagnation pressure
Q	coefficient in finite difference equations
R	universal gas constant, coefficient in finite difference equations (Section 3.1, Appendix A)
r	radius of curvature
Re	slot Reynolds number $= [(p_0-p_a)ab/\rho\nu^2]^{1/2}$
S	physical path length
T	static temperature, coefficient in finite difference equations (Section 3.1, Appendix A)
T_0	stagnation temperature

t	time
u	x-component of velocity
u_τ	wall shear velocity = $\sqrt{\tau_w/\rho}$
V	total velocity = $\sqrt{u^2 + v^2}$
v	y-component of velocity
x	streamwise coordinate along or parallel to surface
y	coordinate perpendicular to x-direction
$y_{1/2}$	value of y where $u = u_{m/2}$
z	coordinate along optical beam

Greek Symbols

α	Mach angle
γ	ratio of specific heats
ϵ	angle of light ray to z-direction
θ	angle of streamline to x-direction
λ_+	gradient of positive characteristic
λ_-	gradient of negative characteristic
λ_s	gradient of streamline
μ	viscosity
ν	dynamic viscosity = μ/ρ
ρ	static density
ρ_o	stagnation density
τ	shear stress
τ_w	wall shear stress
ϕ	angle round Coanda from slot exit
ϕ_o	angle round Coanda from hypothetical slot of zero width
ϕ_{SEP}	separation angle round Coanda from hypothetical slot of zero width

DECLARATION

The work contained in this thesis has not been submitted elsewhere for any other degree or qualification and that unless otherwise referenced it is my own work.

STATEMENT OF COPYRIGHT

CHAPTER 1

INTRODUCTION

1.1 THE COANDA EFFECT

The behaviour of fluids in the vicinity of curved solid surfaces is of prime importance in fluid mechanics. Smeaton (1759), after various experiments on windmills, was one of the first people to state that a curved surface gave more lift than a plane one. The deflection of a jet of air due to contact with a cylinder, and the resulting force on the cylinder, was first documented by Young (1800). This phenomenon has become known as the Coanda Effect, named after the Rumanian aeronautical engineer Henri Coanda (1885-1972) who patented several devices employing the effect, but contributed very little to the understanding of it. It can be readily observed by holding a finger against a steady vertical jet of water running from a tap. The jet will adhere to some extent to the finger and thus be deflected, producing a horizontal force on the finger.

The term Coanda Effect is used as a blanket term for the deflection of jets by solid surfaces and covers a number of important features of the flow. Wille and Fernholz (1965) identify two features that explain the effect:-

a) An inviscid effect, known as the "teapot" effect, where the curvature is explained as a simple consequence of the inviscid flow equations.

b) A viscid effect where the entrainment of ambient fluid causes a low pressure region on the side of a jet adjacent to a solid surface (i.e. the jet sucks itself onto the wall). This has also been called the "Chilowsky Effect" by Metral and Zerner (1948).

Walker (1984) has investigated the 'teapot' effect and showed that fluid poured sufficiently slowly from a teapot does not leave in an arc, but flows down the outside of the spout. He also showed that coating the spout with margarine did not alter the effect.

Bradshaw (1973) identifies a third feature of jets attached to convex surfaces, that of the increased growth rate compared to a plane wall jet, and suggests the term 'Coanda Effect' should be reserved for this phenomenon. Rayleigh (1917) determined, by balancing centripetal accelerations and pressure forces on an element, that a curved flow will be unstable if the angular momentum decreases with radial distance (the special case of irrotational flow with concentric streamlines implies constant angular momentum with radial distance). In such a flow radial displacement of an element of fluid away from the centre of curvature places it in a region of lower angular momentum. The smaller local pressure gradient in this region is insufficient to contain the element and so it moves further away from the centre of curvature. The tangential velocity in a convex jet, outside the small inner boundary layer, decreases with an increase in radial distance, as does the angular momentum and so it is unstable by Rayleigh's criterion. This instability increases the turbulence and thus causes the increased growth rate of the jet.

1.2 COANDA FLARES

The design of flares for the burning off of light, non-commercial hydrocarbon fuels, which are released at oil production platforms and at oil refineries, is becoming increasingly specialised. Flares must not only provide a stable smokeless flame, but also be able to cope with a wide range of flow rates, from low purge through continuous flaring to emergency

disposal, while operating in hostile environments such as the North Sea. To meet this challenge a group under Professor D.H. Desty, working at B.P. Research Centre, Sunbury-on-Thames, developed two flares based on the Coanda Effect during the early 1970s; the Indair and the Mardair flares. These proved so successful that British Petroleum set up a wholly owned subsidiary, Kaldair Ltd., in March 1978 to market these flares. Their flares, including the new Stedair, can now be found on many of the North Sea oil production platforms and in locations such as Alaska, Brazil, India and Kuwait. In 1982 the company won the MacRobert Award Gold Medal and in 1984 the Queens's Award to Industry for technology.

The basic principles of the Coanda flares are illustrated in Figure 1.1. A high pressure gas exits from a narrow slot at the base of the flare as a supersonic jet and follows a curved surface. The gas entrains up to twenty times its own volume of atmospheric air which ensures the gas is thoroughly pre-mixed before combustion to ensure a smokeless flame. The jet is ignited on its outer edge at the maximum diameter of the flare and burns inwards so that there is a protective layer of unburned gas which insulates the lip of the flare against flame impingement. Thus the flare tip can be made of conventional steel alloys and be manufactured by normal welding methods. Another major advantage of the flares is that the radiation levels are much lower and the flame lengths shorter than the traditional pipe flare. The boom or tower that holds the flare can thus be made shorter and a considerable reduction in the cost of the flare plus its installation is achieved.

The Indair (Induced-Air) flare is an axisymmetric flare whose cross-section has the same shape as that of Figure 1.1. The entrainment properties of the jet are so good that gas at near atmospheric pressure can

be added into the jet at the top of the Coanda surface, via an axial duct, without producing any smoke. The Mardair (Marine-Induced-Air) flare is the involute of the Indair flare (i.e. the jet issues into the flare and travels round a convex surface (Figure 1.2)). It is normally used in a matrix of small individual flares (to achieve shorter less radiative flames) although recently a large single flare has been developed. It has even shorter flame lengths and emits lower radiation levels than the Indair which makes it particularly suited to small-field off-shore platforms. The Stedair (Steam-Induced-Air) flare has a similar shape to the Indair flare without the conical section after the convex surface. Steam is ejected from the slot, entrains air while following the convex surface and then mixes with the gas which issues from an axial duct. This flare is particularly suitable for very low-pressure gases. The design and development of both the Indair and Mardair flares are outlined by Wilkins et al (1977).

Research into the performance of these flares has been undertaken at British Petroleum's Research Centre at Sunbury-on-Thames and at both Durham and Exeter universities. At Exeter the research has concentrated on the noise production of the flares, Carpenter and Green (1983), which has not been considered in the present research. The research at Sunbury-on-Thames and Durham has concentrated mainly on the performance of various flare geometries, concentrating in particular on an undesirable phenomenon known as breakaway. Under normal operating conditions the issuing gas follows the convex curvature of the Indair flare (Figure 1.1), but as the pressure behind the slot is increased a critical pressure is reached at which the jet suddenly separates from the surface and travels out horizontally. The upstream stagnation pressure at which this occurs is defined as the

breakaway stagnation pressure. At stagnation pressures below this the jet can separate from the surface, but it always reattaches, thus following the general outline of the surface. At the critical pressure and above it, the mixing properties of the flare are lost.

Two definitions are used throughout this work. Firstly, the stagnation pressure ratio is defined as the ratio of the downstream static pressure (in this case atmospheric pressure, p_a) to the upstream stagnation pressure, p_0. This ratio is always less than unity. Secondly the Coanda surface is defined as the surface downstream of the slot exit and which deflects the jet. This is usually a surface of constant radius followed by a flat section,although sometimes a short flat exists before the circular arc.

Breakaway tests on Indair flares have been conducted by British Petroleum (1979, 1980, 1982) and indicate that as the slot width to downstream radius ratio is reduced the breakaway stagnation pressure ratio (p_a/p_0) decreases. There is also a hysteresis effect between the breakaway stagnation pressure ratio and the ratio at which the jet reattaches to the Coanda surface. The inclusion of a step between the slot and the Coanda surface was also found to decrease the breakaway stagnation pressure ratio at a set slot width. The ratio progressively decreases as the step height is increased up to an optimum height, beyond which the ratio increases. In addition to these axisymmetric tests at Sunbury-on-Thames, Sadler (1983) investigated the effect of altering the angle through which the Coanda surface turned the flow on a plane two-dimensional rig. The breakaway stagnation pressure ratio at a set slot width progressively increased as the Coanda surface was reduced below a turning angle of 150^0,

although the change of turning angle had little effect on the reattachment stagnation pressure ratio.

At Durham, Gregory-Smith and Robinson (1982) investigated the discharge coefficients and the downstream surface static pressure distributions on a plane two-dimensional model. The latter investigation was restricted to incompressible flow. An investigation of the breakaway and reattachment stagnation pressure ratios was also carried out. However, due to restrictions on the air supply to the rig, the radius of the Coanda surface was reduced to one only just bigger than the slot thickness. This resulted in the flow attaching itself to the nozzle rather than the Coanda, thus issuing horizontally, at large slot widths. In two unpublished works, Gilchrist (1981) and Savin (1982) extended these experiments, investigating the effect of altering the shape of the nozzle and including a step between the slot and the Coanda surface. The breakaway stagnation pressure ratio at a set slot width was unaffected by a change in the shape of the nozzle and, as in the axisymmetric flare, was decreased by the inclusion of a step. A few Schlieren photographs were also taken to visualize the structure of the jet, although problems were encountered with oil coming over from the compressor and obscuring the final picture. In addition to these investigations , Morrison (1982) has investigated the mean properties and the turbulence structure of a low speed jet flowing over a half-model of the axisymmetric Indair flare. This investigation is discussed in section 2.5.

1.3 OBJECTIVES

The stagnation pressure ratio required to achieve the phenomenon of breakaway at a set slot width to downstream radius has been investigated on both plane and axisymmetric flare models (Section 1.2). However, the

mechanism of this phenomenon has not been studied and in particular the dependence of the phenomenon on the slot configuration and/or the shape of the downstream surface is unknown. An understanding of the mechanism of breakaway would enable the flare designers to alter their designs in order to delay breakaway.

The main aim of this project was to investigate the jet structure from a plane model of the axisymmetric I8-H-AS flare marketed by Kaldair. A range of slot widths to downstream radius ratios were to be studied. At each ratio the resultant jet was to be studied over a range of stagnation pressure ratios down to that required for breakaway. The experiments were to include oil surface flow visualization and static pressure measurements round the Coanda surface. In addition, the density changes within the jet would enable shadowgraph, Schlieren and interferometric techniques to be used. It was aimed to design and develop an optical system that would allow all three techniques to be used and that required only simple changes to switch from one technique to another. The jet was to be photographed over a range of stagnation pressure ratios down to that required for breakaway at several slot widths to downstream radius ratios. This would enable the structure of the jet to be determined.

The theoretical work was to include two prediction techniques. Firstly the whole jet was to be modelled assuming potential flow, thus ignoring the effects on the jet structure of both the inner boundary layer and the outer shear layer. The properties of the predicted jet would be compared to those obtained experimentally to test how far downstream of the slot the calculation method accurately predicted the jet. This technique cannot predict separation of the jet from the surface, so the second aspect of the theoretical work was to model the boundary layer. It was hoped a

boundary layer calculation method could be found, or adapted, to model the layer from the static pressure distributions obtained from either experimental measurements or the potential flow model. This would enable a prediction of the separation, or possibly the breakaway, to be made. The method could then be applied to different geometries in order to improve the flare design such as to avoid breakaway of the jet.

CHAPTER 2

THEORETICAL BACKGROUND

2.1 BASIC RELATIONSHIPS

The static temperature is related by the Mach number to the stagnation temperature for steady adiabatic flow on which no work is done and on which gravitational effects are negligible.

$$\frac{T_o}{T} = 1 + \left(\frac{\gamma-1}{2}\right)M^2 \qquad \ldots(2.1)$$

For a perfect gas

$$p = \rho RT \qquad \ldots(2.2)$$

and if the flow is isentropic

$$\frac{p}{\rho^{\gamma}} = \text{const} \qquad \ldots(2.3)$$

Equations 2.1, 2.2 and 2.3 can be combined to relate the static pressure and density to their stagnation values.

$$\frac{p_o}{p} = \left[1 + \left(\frac{\gamma-1}{2}\right)M^2\right]^{\gamma/\gamma-1} \qquad \ldots(2.4)$$

$$\frac{\rho_o}{\rho} = \left[1 + \left(\frac{\gamma-1}{2}\right)M^2\right]^{1/\gamma-1} \qquad \ldots(2.5)$$

2.2 CALCULATION METHODS

The Navier-Stokes equations for two-dimensional steady flow in which body forces and heat sources can be neglected can be written as

$$\frac{\partial F}{\partial x} + \frac{\partial G}{\partial y} = 0 \qquad \ldots(2.6)$$

where

$$F = \begin{bmatrix} \rho u \\ \rho u^2 + \sigma_x \\ \rho uv + \tau_{xy} \\ (e+\sigma_x)u + \tau_{yx}v - k\,(\partial T/\partial x) \end{bmatrix}$$

$$G = \begin{bmatrix} \rho v \\ \rho uv + \tau_{yx} \\ \rho v^2 + \sigma_y \\ (e+\sigma_y)\,v + \tau_{xy}u - k\,(\partial T/\partial y) \end{bmatrix}$$

and where

$$\sigma_x = p - \lambda\left(\frac{\partial u}{\partial x} + \frac{\partial v}{\partial y}\right) - 2\mu\frac{\partial u}{\partial x}$$

$$\tau_{xy} = \tau_{yx} = -\mu\left(\frac{\partial u}{\partial y} + \frac{\partial v}{\partial x}\right)$$

$$\sigma_y = p - \lambda\left(\frac{\partial u}{\partial x} + \frac{\partial v}{\partial y}\right) - 2\mu\frac{\partial v}{\partial y}$$

and where λ and μ are viscosity coefficients, e is the total energy per unit volume and k is the coefficient of heat conductivity.

The Navier-Stokes equations are non-linear second-order partial differential equations. Such equations have the general form

$$A\frac{\partial^2 f}{\partial x} + B\frac{\partial^2 f}{\partial x \partial y} + C\frac{\partial^2 f}{\partial y^2} = D \qquad \ldots(2.7)$$

where A, B, C and D may be functions of x, y, f, $\partial f/\partial x$ and $\partial f/\partial y$. A characteristic is a line in the flow where the second-order derivatives of f are indeterminate, their gradients being given by Chow (1979) as the solution of

$$A\left(\frac{dy}{dx}\right)^2 - B\left(\frac{dy}{dx}\right) + C = 0 \qquad \ldots(2.8)$$

There are three possible types of solution to equation 2.8 and these form the classifications of equation 2.7:-

$B^2 - AC > 0$ — There exist two real values of dy/dx and equation 2.7 is hyperbolic.

$B^2 - AC = 0$ — There exists a single repeated value of dy/dx and equation 2.7 is parabolic.

$B^2 - AC < 0$ — There exist two imaginary values of dy/dx and thus the characteristic lines do not exist and equation 2.7 is elliptic.

The physical significance of the three types of classification can be understood by considering the regions of influence of a point in a flow field. Disturbances from this point are propagated at the speed of sound. If the flow is supersonic disturbances cannot be propagated upstream and the region of influence of a point is confined to an area downstream of the Mach lines from that point. The equations of motion are hyperbolic, the characteristics being the Mach lines, and the whole flow field can be

solved in a single sweep downstream. If the flow is subsonic the region of influence of a point is unbounded and the characteristics do not exist. The equations of motion are elliptic and the solution must be obtained by matrix methods or by making an initial guess of the solution and then iterating the whole flowfield until convergence to the solution is achieved.

Under certain conditions, such as the classical boundary layer assumptions, the elliptical equations can be approximated to become parabolic equations. The region of influence of a point is limited to a region downstream of the characteristic, the characteristic running normal to the surface. The equations of motion can be solved directly by a single sweep downstream through the flowfield.

An additional complication in the set of equations 2.6 is that they do not form a closed set of equations if the flow is turbulent. The methods of closure are discussed by Schlichting (1979), Cebeci and Smith (1974) and by Bradshaw et al (1981). There are two main approaches to the solution of the differential form of equation 2.6 for boundary layer type flows, the approaches being identified by their closure assumptions. The first approach combines the mean flow equations with a closure assumption that models the Reynolds stresses. These include the mixing-length approach of Patankar and Spalding and the eddy viscosity approach of Cebeci and Smith (1974). In both these methods the governing equations are approximated to become parabolic equations for boundary layer type flows. The Patankar and Spalding method transforms the y ordinate into a non-dimensional stream function and uses an upwind difference scheme for the simultaneous solution of all points at a given x. The method of Cebeci and Smith transforms the equations into a rectangular grid. The governing

equations are written in the form of a first order system and then solved by Kellers Box method (Keller (1978)). The resulting equations are implicit and the scheme is unconditionally stable.

The second approach combines the mean governing equations with an equation for the transport of the Reynolds stress. The method of Bradshaw, originally described for incompressible flow by Bradshaw et al (1967) and extended to compressible flow by Bradshaw and Ferriss (1971), uses the turbulent energy equation. Three non-dimensional empèrical relationships are defined in this equation. An important feature of this set of equations is that they are hyperbolic for boundary layer flows and can thus be solved by the method of characteristics. This allows large streamwise steps and is a fast, efficient method. Three characteristics exist, one normal to the shear layer and two that spread downstream from each point of the flow field. These latter two characteristics are related to the spread of turbulence downstream from a point..

One feature of these methods for solving boundary layer flows is that influences are passed upstream only through an imposed streamwise pressure gradient, the calculation method marching spatially downstream. Thus any regions of reversed flow, where information is passed upstream through the mean momentum cannot be calculated. The set of equations 2.6 are now elliptic.* An alternative approach in the calculation of the elliptic equations of a shear layer is by re-introducing the unsteady terms into the Navier-Stokes equations. A solution is guessed and the flow is then artificially marched forward in time until a steady solution is reached. These methods require all the grid points to be stored and often require a large number of iterations (McNally and Sockol (1985)). However these methods do allow the computation of a flowfield that contains regions of

* The full set of equations 2.6 are always elliptic, the boundary layer assumptions giving a parabolic approximation to the elliptic equations

reversed flow. MacCormack (1982) has accurately computed a shock/boundary-layer interaction that includes a region of separation.

The usual method of coupling the potential flow solution that provides the streamwise pressure gradient and the shear layer calculation is through a displacement thickness approach. The potential solution is found initially ignoring the presence of the shear layer and the resultant pressure imposed upon the solution of the shear layer. The latter calculation usually ignores the y momentum equation. The potential solution is then recalculated with any boundaries displaced by an amount equal to the displacement thickness of the shear layer. The new pressure gradients can then be used to recalculate the shear layer and the process iterated until convergence. Dash et al (1979) have used this method to calculate the flow field in the region just downstream of a nozzle exhausting into an external stream.

However the use of a displacement thickness does not accurately model the effect of the shear layer on the potential flow if there is a strong interaction between the shear layer and the potential flow. A strong interaction can occur in the presence of pressure gradients normal to the shear layer or can result in the reflection of wave processes in supersonic flow. These waves will be attenuated and curved in the shear layer. One alternative method of coupling is that of pressure-split coupling, one of the first developments being by Mahgoub and Bradshaw (1979). The potential flow solution is initially found ignoring the presence of the shear layer. The resulting streamwise pressure gradient is imposed at the edge of a shear layer calculation, this calculation including the y momentum equation. An initial guess of the normal pressure gradient must be made and the fluid properties along the normal calculated. The resultant

properties can be used to correct the normal pressure gradient and the fluid properties recalculated. Once the total shear layer has been calculated, the potential flow can be recalculated with the known entrainment velocities at the known outer edge of the shear layer as a boundary condition. The potential flow and the shear layer are solved alternately until a converged matched solution is found.

Dash et al (1983) reviews the progress made in the calculation of curved wall jets with or without an external stream. The pressure-split method was applied to the solution of subsonic turbulent wall jets and results are presented. The extension of this methodology to the solution of underexpanded jets is proposed and results from a program that models an inviscid jet presented.

2.3 TURBULENT WALL JETS ON FLAT SURFACES

The mean velocity profile of a fully developed turbulent wall jet flowing over a flat surface can be considered to consist of two layers. The outer layer is analogous to that of a half free jet and the inner layer analogous to a typical wall layer. Glauert (1956) obtained a near similar solution using this model. A solution was sought where

$$U_m \propto x^a, \qquad y_{m/2} \propto x^b \qquad \ldots(2.9)$$

The eddy viscosity in the outer layer was assumed to be constant and the velocity profile in the inner layer was assumed to vary as $y^{1/7}$ (Blasius' pipe flow formula) and that the eddy viscosity varied as u^6. The two layers were patched at the velocity maximum, with the assumption that the shear stress was zero at this point, and the effect of the viscous sublayer was ignored. The values of the constants were found to be a =-0.5 to -0.6 and b = 1.0. Experimental values of these constants were determined by Schwarz and Cosart (1960), who quote a value for a of -0.555

(this value was an average of results ranging from - 0.5 to - 0.6) and $b = 1.0$.

Launder and Rodi (1981) critically review all the available experimental data. Where sufficient data was available the results were checked for two-dimensionality using the momentum integral equation and if the flow was found to depart significantly from two-dimensionality the results were disregarded. They found that the growth rate of the jet agrees with the theory of Glauert and was given by

$$\frac{dy_{1/2}}{dx} = 0.073 \pm 0.002 \qquad \ldots(2.10)$$

This growth rate is about 30% below that of a free jet. Launder and Rodi (1983) suggested that the reason for this is that the normal fluctuations near the wall are damped. The mean velocity profile is also accurately predicted by Glauert. Launder and Rodi (1981) showing that the similarity of experimental profiles is very satisfactory when plotted as U/U_m against $y/y_{1/2}$. Wilson and Goldstein (1976) show that the normal velocity profiles are also similar when plotted as V/U_m against $y/y_{1/2}$.

Bradshaw and Gee (1960) note two discrepancies between the real flow and the theory of Glauert. Firstly, the theory underestimates the wall shear stress by 25%. Launder and Rodi (1981) show there is a wide variation in the measurement of the wall shear stress, but suggest the data of Bradshaw and Gee, measured with a Preston tube, is one of the most accurate. They found that

$$\frac{\tau_\omega}{1/2\ \rho\ U^2_m} = 0.0315 \left(\frac{U_m y_m}{\nu} \right)^{-0.182} \qquad \ldots(2.11)$$

Launder and Rodi (1981) suggest that this is valid in the range $3 \times 10^3 < U_m y_m/\nu < 4 \times 10^4$. The errors in the measurement of the wall shear stress have also led to difficulties in applying the log law of the wall to the inner layer. Launder and Rodi (1983) also suggest that authors have also attempted to apply the formula to too large a portion of the inner layer. However, the inner layer can be described by

$$\frac{U}{U_\tau} = A \log\left(\frac{y\, U_\tau}{\nu}\right) + B \qquad \ldots(2.12)$$

where the results proposed by Patel (1965) of A = 5.5 and B = 5.45 appear to be the most accurate.

The second discrepancy, noted by Bradshaw and Gee, is that the shear stress is not zero at the velocity maximum. Thus any theory that models the shear stress on the first derivative of velocity is inadequate. Launder and Rodi (1981) note that large scale eddies from the outer layer, bearing a shear stress of the opposite sign to that from the wall encroach into the inner layer. This not only reduces the range of validity of equation 2.12, but is also the reason for the shear stress zero occurring within the inner layer and before the velocity maximum. They note that, while the velocity maximum occurs approximately at $y/y_{1/2} = 0.2$, the zero shear stress occurs at approximately $y/y_{1/2} = 0.1$ and the value of the shear stress at the velocity maximum is of the same order, although of opposite sign, as the wall shear stress.

2.4 CURVED WALL JETS

During the 1960s there was a surge of interest in the flow of a turbulent jet over a convex surface, motivated mainly by the aeronautical industry. The work consisted mainly of the flow of an incompressible jet

flowing over a convex surface of constant radius, with interest being focused on the increased growth rate of the jet, the surface static pressure distributions around the surface and the separation of the jet from the surface. Wille and Fernholz (1965) and Fernholz (1971), in a translation of an earlier work, review the progress made during this period and only the works directly relevant to the present investigation will be mentioned here.

Newman (1961) describes the flow of an incompressible jet over a surface of constant radius (Figure 2.1). If the fluid were inviscid and non-turbulent, the flow would become independent of ϕ just downstream of the slot and thus the jet width, velocity distribution and the static pressure at the surface would be invariant. In addition the flow would never separate from the surface. The radial momentum equation can be integrated across the jet to give a non-dimensional surface pressure

$$C_p = \frac{p_s - p_a}{p_o - p_a} = -\left[2\,\frac{b}{a} + \left(\frac{b}{a}\right)^2 \right] \qquad \ldots(2.13)$$

Fernholz (1964) has integrated the radial momentum equation, together with energy and perfect gas equations (equations 2.1 and 2.2) to give the non-dimensional surface pressure for compressible flow

$$C_p = \frac{1}{1-(p_o/p_a)} + \frac{1}{1-(p_a/p_o)} \left[\left\{ \left(\frac{p_a}{p_o}\right)^{(\gamma-1)/\gamma} - 1 \right\} \left(1 + \frac{b}{a}\right)^2 + 1 \right]^{\gamma/(\gamma-1)} \qquad \ldots(2.14)$$

Gregory-Smith and Robinson (1982) integrate the radial momentum equation to show the Mach number distribution through the jet is given by

$$\frac{r}{r^*} = \left[\frac{1 + \left(\frac{\gamma-1}{2}\right) M^2}{\left(\frac{\gamma+1}{2}\right)} \right]^{1/2} \cdot \frac{1}{M} \qquad \ldots(2.15)$$

where r^* is the radius at which the Mach number is unity.

The real fluid continuously entrains air from the surroundings. (Figure 2.1), increasing the jet width and decreasing the jet velocities as the angle round the surface increases. If the fluid is incompressible this causes a gradual increase in the static pressure at the surface which finally leads to the separation of the jet from the surface. Newman (1961) suggested that at some distance from the slot, where the flow is fully developed, the flow becomes independent of the slot conditions $(p_o - p_a)$ and b, but depends on their product, the jet momentum. A similar velocity profile at an angle ϕ could have been formed by a larger slot situated downstream or a smaller slot situated upstream of the original slot, provided the exit momentum was the same. He showed the non-dimensional surface static pressure was related by

$$C_{p'} = \frac{p_a - p_s}{p_o - p_a}\left(\frac{a}{b}\right) = f\left[\phi_o, \left(\frac{(p_o - p_a)ab}{\rho\, \nu^2} \right)^{1/2} \right] \qquad \ldots(2.16)$$

where ϕ_o is measured from the position of a hypothetical slot of zero height but whose exit momentum is the same as the original slot (Figure 2.1). In addition, at high Reynolds number the flow becomes independent of

viscosity and the non-dimensional surface static pressure becomes a function of angle only.

A similar analysis for the angular position of the separation of a fully developed incompressible jet gives

$$\phi_{sep} = f\left[\left(\frac{(p_o - p_a)\,ab}{\rho\,\nu^2}\right)^{1/2}\right] \qquad \ldots(2.17)$$

which suggests that it tends to become constant at high Reynolds number provided a suitable origin is chosen.

The experimental surface static pressure distributions of Newman (1961) and the more accurate ones of Fekete (1963) confirm the results of equation 2.16, the critical Reynolds number being about 4×10^4. Fekete noted that the ideal jet momentum, $(p_o - p_a)b$, in the non-dimensional surface pressure should be replaced by the actual jet momentum, the latter being smaller due to the boundary layers at the slot exit. Newman (1969) gives the range of validity of these results as $0.01 < b/a < 0.05$, viscosity being important at smaller slot widths. At larger slot widths the flow does not become fully developed until very large angles.

The universal angle of separation given by equation 2.17 is $226^0 \pm 3^0$ (Newman (1969)) and is valid at Reynolds numbers greater than 4×10^4. Wilson and Goldstein (1976) confirm the separation angle is constant at Reynolds numbers greater than this. Keshavan (1975) extends the theory to a jet issuing from a tangential slot on a cylinder that is in a uniform external stream. He found the separation angle at high Reynolds numbers depended only on the angle of the slot to the direction of the external flow and on the ratio of the jet momentum to the external dynamic head.

Roderick (1961) investigated the deflection of a compressible jet, covering a stagnation pressure ratio range of 0.625 to 0.355. The jet

issued over a deflection surface that consisted of a short flat section set tangentially to a circular arc that deflected the flow through 90^0. The deflection surface could be set such that the flat was at an angle α to the initial jet axis, the range of α that was tested being $0^0 < \alpha < 25^0$. A slot width to downstream radius ratio range of 0.0156 to 0.0625 was studied, but variations in the slot width of up to 50% were found across the breadth at the smallest slot width. These variations, caused by warping during welding of the nozzle section, cast doubt on the two-dimensionality of the flow. An extensive investigation was made of the surface static pressure distribution round the surface. These were found to exhibit a wave-like structure about a constant mean negative value at small angles round the surface, the waves damping out as the angle increased. The angular distance between the wave peaks and the amplitude of waves increased as the stagnation pressure ratio was decreased. The mean value at a set stagnation pressure ratio decreased as the slot width was increased.

Korbacher (1962) investigated the surface static distributions over a similar deflection surface to that of Roderick (1961), though the leading edge of the flat was displaced away from the nozzle edge, both along the jet axis and vertically to it. A compressible jet was studied at stagnation pressure ratios mainly above the critical ratio (i.e. unchoked). The non-dimensional surface static pressure distributions were found to consist of an initial 'adjustment' region followed by a constant region as predicted by equation 2.14.

Bradbury and Wood (1965) investigated the deflection of a thick jet ($b/a = 0.5$) over a deflection surface that consisted of a circular drum with a straight flap attached tangentially to it. The drum could be

rotated to vary the angle of the flap to the initial jet axis, although there was some doubt about the position of the zero. The drum and the flap contained a limited number of static pressure tappings which indicated the flow at the surface became supersonic even at stagnation pressure ratios above the critical ratio. The breakaway of the jet from the flap was also studied, the angle of the flap to the jet being increased until breakaway at a set stagnation pressure ratio. Only small deflections, of the order of 10^0, were achieved before breakaway at stagnation pressure ratios less than 0.5. The presence of an auxilliary jet issuing tangentially from the drum, was found to increase the possible deflection angle before breakaway at stagnation pressure ratios near unity. However, at ratios of less than 0.5 it had no effect. Recent experiments into the breakaway of a jet are reviewed in Section 1.2.

Launder and Rodi (1981, 1983) review recent progress of experimental work on curved wall jets. Two detailed studies on the turbulence structure of an incompressible jet flowing over a constant radius convex surface are by Wilson and Goldstein (1976) and by Alcaraz et al (1977). Wilson and Goldstein measured the structure of the flow over a flat plate and over a convex surface, the slot width to downstream radius being 0.0605. Alcaraz et al measured the flow from an 18 mm slot flowing over a surface of radius 5800 mm (b/a = 0.0031). Wilson and Goldstein reported a growth of

$$\frac{y_{1/2}}{b} = 0.0787 \left(\frac{x + 6}{b} \right) \left[1 + 2.956 \left(\frac{y_{1/2}}{a} \right) - 0.1559 \left(\frac{y_{1/2}}{a} \right)^2 \right] \quad \ldots (2.18)$$

where $y_{1/2}$ was well represented by a simple linear fit until 180^0 round the cylinder, where the quadratic term was required. Launder and Rodi (1981)

suggest that for the apparatus used, the flow ceases to be two dimensional by the 180° position. Newman (1961) gives the growth as *

$$\frac{y_{1/2}}{} = 0.11 \left(1 + 1.5 \frac{y_{1/2}}{a}\right) \quad \ldots(2.19)$$

and Newman (1969) gives a correlation of the results of Fekete (1963) and Guitton, who measured flow over a concave surface, as

$$\frac{y_{1/2}}{x} = 0.069 + 0.3\left(\frac{y_{1/2}}{a}\right) - 0.08\left(\frac{y_{1/2}}{a}\right)^2 \quad \ldots(2.20)$$

Wilson and Goldstein (1976) found that the mean velocity profiles appeared to be similar when plotted as U/U_m against $y/y_{1/2}$. The maximum velocity occurred at approximately the same position as a wall jet flowing over a flat plate. However the non-similarity of the flow was evident in the non-dimensional plots of the mean normal velocity, the ratio of V/U_m increasing at a given $y/y_{1/2}$ as the angle round the surface increased.

Both Wilson and Goldstein (1976) and Alcaraz et al (1977) showed that the zero value of shear stress occurred in the inner layer. The maximum shear stress in the outer layer and the two fluctuating velocities were found to increase as the angle round the surface increased. Wilson and Goldstein found the normal fluctuating component increased more rapidly than the streamwise fluctuation, but Alcaraz et al found the increase was similar in both cases. The increases in these components were mainly confined to the region $y < y_{1/2}$. The discrepancy between the two results is given by Launder and Rodi (1981) as probably due to the difference in $y_{1/2}/a$. In the experiment of Alcaraz et al this was approximately 0.01 whereas in that of Wilson and Goldstein it was approximately 0.4 at the 130° station. Thus the wall can be expected to damp the normal fluctuations to a greater degree in the experiments of Alcaraz et al.

* Equations 2.18, 2.19 and 2.20 are plotted in this form to show the influence of the curvature

Wilson and Goldstein recorded turbulence intensities of up to 25% over the convex surface compared with about 18% over the flat plate, the maximum intensities occurring in the outer layer where dU/dy, and thus the production of turbulence, was a maximum.

The flow of a wall jet over a logarithmic spiral has been shown by Guitton and Newman (1977) to be self-preserving. They took great care to establish two-dimensional flow and were to a large extent successful. The streamwise and normal mean velocity profiles were similar at all downstream stations and the position of the zero stress point was again found to be inside the inner layer.

There have been two studies of concave jets flowing round the inside of a circular arc, which are reviewed by Launder and Rodi (1981). The Rayleigh criterion (Section 1.1) shows that these are stably curved shear layers and they are not strictly relevant to the present study.

2.5 AXISYMMETRIC WALL JETS

An early investigation into an axisymmetric jet is that of Bakke (1957) who investigated a turbulent low speed jet of air spreading out radially over a flat plate. A series of pitot traverses were made perpendicular to the plate and velocity profiles deduced assuming the static pressure to be atmospheric everywhere. The resultant velocity profiles were found to be similar and found to agree with the theory of Glauert (1956). The two similarity constants a and b (equation 2.9) were found be to -1.12 and 0.94 respectively.

Sharma (1981) investigated a conical wall jet whose apex angle, α, varied from 0^0 to 90^0 and compared his results with several previous investigations. The two limits of the investigation, 0^0 and 90^0, represent a cylindrical wall jet and a radial wall jet respectively. The results

showed that the growth rate was independent of α and of the initial slot width and could be expressed as

$$y_{1/2}/b = 0.120\ (x/b)^{0.91} \qquad \ldots(2.21)$$

where b was the height of the slot. The velocity profiles were similar both in the inner and outer layers for a set value of α, and proved to be independent of the slot width. There was also a close resemblance of the shape of the similar profiles at varying values of α. An earlier investigation by Starr and Sparrow (1967) on a cylindrical wall jet found that whilst the outer layer velocity profiles were similar the inner layer were not. Sharma suggests that this is a result of curvature effects, the ratio of the slot height to the diameter of the rod used by Starr and Sparrow being over four times greater than that of Sharma. All the inner layers measured by Sharma could be described by the log law of the wall (equation 2.12) with the constants A = 4.17 and B = 7.6 for distances $y\ U_\tau/\nu < 200$. However there is some doubt as to the accuracy of these results because the outer diameter of the pitot tube was large in comparison with the jet width.

Morrison (1982) investigated the flow over a half model of an Indair flare (Section 1.2). Two slot width to downstream radius ratios of 0.167 and 0.066 were investigated at stagnation pressure ratios of 0.98 and 0.94 respectively. Surface static pressure measurements showed that the pressure gradually increases round the Coanda to atmospheric after an initial drop caused by the curvature of the jet. The mean properties were measured at various stations round the Coanda by both a three-hole probe and hot wires. The measurements show that the streamwise velocity profiles appear to be similar, as found by Wilson and Goldstein (1976) in their experiments on a plane convex downstream surface, until an angle of 75^0

round the Coanda had been reached, when the similarity broke down in the outer layer. This breakdown in the apparent similarity was caused by the influence of the flat section further downstream. The non-similarity of the flow is shown, as with Wilson and Goldstein, by the normal velocity profiles, the non-dimensional normal velocity increasing at a set $y/y_{1/2}$ as the flow proceeded downstream.

The growth rate of the jet from the smaller slot is similar to that found by Wilson and Goldstein (1976) in their experiments on a plane convex wall jet (equation 2.18). As the growth rate of a plane and a radial jet are similar, this result was expected. However the growth rate of the jet from the larger slot was below that found by Wilson and Goldstein, the reason being that the potential flow region was larger and thus the jet was not fully developed.

Detailed hot wire analysis at the larger slot width showed normal turbulence intensities of up to 45% on the curved part of the Coanda. The maximum intensities were recorded at $y/y_{1/2} = 0.6$, which coincided with the maximum negative gradient of the streamwise velocity. The shear stress profiles show that the zero shear stress is inside the inner layer, as found on plane and curved wall jets.

Tests were also made on a full scale 8" Indair flare with a three-hole probe. The mean velocity profiles were found to be similar and the growth rate similar to that measured by Wilson and Goldstein.

2.6 SUPERSONIC JETS

The classification of supersonic jets exiting from a convergent-divergent nozzle is given by Shapiro (1953) together with Schlieren photographs of the three types. The structure of the jet differs depending

on the ratio of the free air downstream to that of the static pressure at the nozzle exit. A jet is termed underexpanded if this ratio is less than unity and a Prandtl-Meyer expansion at the nozzle lip decreases the static pressure of the jet to that of the free air. A jet is fully expanded if the ratio is unity and termed overexpanded if the ratio is greater than unity. The latter jet requires a compression at the nozzle lip to raise the static pressure to that of the free air. This compression can take on two forms depending on the pressure ratio. An oblique shock forms at the nozzle lip that either undergoes a regular reflection at the jet axis or, if the shock is strong, leads to the formation of a Mach disk (Chow and Chang (1972)). The nozzle configuration of the present study is of a purely convergent type and thus only underexpanded jets are considered.

The structure of a typical underexpanded axisymmetric jet is shown in Figure 2.2. A Prandtl-Meyer expansion centred on the nozzle lip reduces the static pressure to that of the still air. These expansion waves are reflected at the jet axis and then, as compression waves, from the free jet edge. These compression waves coalesce to form an oblique shock which, if the stagnation pressure ratio is close to the choking value, undergoes a regular reflection at the jet axis. However if the stagnation pressure ratio is low the oblique shocks lead to a normal shock that bridges the oblique shocks. This normal shock is commonly known as the Mach disk, or sometimes as a Riemann wave. The central core of the jet is decelerated through this shock to subsonic speeds. The initial incident oblique shock is reflected at the edge of the Mach disk and the flow in the outer annulus of the jet remains supersonic. The oblique shock is reflected again at the free edge of the jet as a Prandtl-Meyer expansion. A slip line divides the outer supersonic and inner subsonic regions. The area of the inner region

decreases further downstream and the flow is accelerated up to supersonic speeds.

Love et al (1959) describe a detailed study of axisymmetric underexpanded jets. Nozzles whose exit divergence angles ranged from 0^0 to 20^0 and whose exit Mach numbers ranged from 1.5 to 3.00 were tested over a range of stagnation pressure ratios. In addition a simple convergent nozzle whose exit angle was 0^0 was tested. Schlieren photographs were taken and compared with a potential flow model using the method of characteristics (Chapter 3). Investigations were made of the existence and location of the Mach disk, of the length of the first shock cell and of the inclination of the jet boundary to the jet axis at the nozzle exit. The divergence angle of the nozzle was found to have little effect on the length of the first shock cell, the length increasing as the stagnation pressure ratio was reduced. As the stagnation pressure ratio was decreased below the value at which the Mach disk appeared, the disk moved further downstream and increased in diameter. The method of characteristics was found to predict accurately the jet boundary in the initial part of the jet and to predict accurately the location of the incident oblique shock.

Theoretical predictions of the size and position of the Mach disk and of the wavelength of the first shock cell have been made by Abbett (1971), Fox (1974) and Chang and Chow (1974). The method of characteristics is used to solve the supersonic flow together with the standard shock equations. The subsonic flow downstream of the Mach disk is treated as one-dimensional flow, the pressures and velocity directions being continuous across the slip line. The position of the Mach disk is initially guessed and the flow field calculated. An improved prediction can then be made because, if the disk has been introduced too early the

flow downstream of the Mach disk is still subsonic by the point at which a minimum area of the central core has been reached. If it has been introduced too late the flow in the central core becomes supersonic before the minimum area has been reached. Chang and Chow show that the rotationality of the flow after the oblique shocks has a strong influence on the final solution, the effect being to bring the Mach disk closer to the nozzle. This inviscid method agrees closely with the data of Love et al (1959) for exit Mach numbers less than 2.5. The one-dimensional stream tube approach for the subsonic region has also been used by Dash and Thorpe (1981).

Several studies, motivated by the space industry and VTOL aircraft, have been made on the impingement of axisymmetric jets upon downstream surfaces. The shock structure of the jet is further complicated by the presence of the solid surface. Hunt and Lamont (1976, 1980) have studied the shock structure and surface static pressure distributions of axisymmetric jets that impinge on wedges and flat plates, both perpendicular and inclined to the jet respectively. Jennions and Hunt (1982) studied the impingement of jets on cones of various angles and recorded static pressure distributions showing regions of compression and expansion as the jet flowed down the outside of the cone.

An early study of plane two-dimensional underexpanded jets was made by Ladenburg et al (1949). Interferometric pictures of two jets confined by side walls were made, the stagnation pressure ratios being 0.164 and 0.103. The aspect ratio of the slot was 5.0. They found a strong normal shock at the lower stagnation pressure ratio, although there was no evidence of an oblique shock leading to it. The measured pressure rise across the normal shock was much less than that predicted by normal shock

theory. Ladenburg et al suggest that the side wall boundary layer separates due to the large pressure gradient across the shock, thus implying that the flow is no longer two-dimensional. Thus the normal shock does not extend across the entire breadth of the flow field, which led to large errors due to the small aspect ratio.

Benson and Poole (1965a) investigated the structure of a plane two-dimensional jet by taking Schlieren photographs over a stagnation pressure ratio range from 0.7085 down to 0.075. The method of charcteristics was used to provide a theoretical prediction of the structure of the first shock cell at stagnation pressure ratios below the critical ratio. Three types of shock systems (Figure 2.3) were identified, similar to those found in axisymmetric jets. At stagnation pressure ratios just below the critical ratio the shock pattern is as Figure 2.3a. The Mach waves from the initial Prandtl-Meyer expansion at A are reflected at the jet axis (B) as expansion waves to satisfy the condition that the flow follows the jet axis. These waves are reflected off the free surface (C) as compression waves and again at D. The compression waves then coalesce to form a weak oblique shock at point F.

As the stagnation pressure ratio was reduced the cell length increased and the oblique shock moved physically downstream, although the coalescing of the waves occurred at an earlier point within the shock cell. A second shock system appeared by a stagnation pressure ratio of 0.1234, where the coalescing of the compression waves occurred at E before they reached the jet axis (Figure 2.3b). The weak oblique shock underwent a regular shock reflection at the jet axis, the flow being rotational after this shock. Benson and Poole made no attempt to investigate the rotational

part of the flow, although the method of characteristics accurately predicted the occurrence of these two shock systems.

As the stagnation pressure ratio was further reduced a third shock system appeared on the Schlieren photographs equivalent to the appearance of the Mach disk in axisymmetric flows (Figure 2.3c). Thus the incident oblique shock became highly curved and led to the formation of a normal shock. The method of characteristics however, still predicted that a shock system of Figure 2.3b was possible (i.e. that a strong reflection of the incident oblique shock was still theoretically possible). No explanation of this early transition to the Mach disk shock system is given.

Interferometric pictures were taken at two stagnation pressure ratios, 0.7085 and 0.4250. The latter was compared with lines of constant Mach number predicted by the method of characteristics and a good agreement was found. Benson and Poole concluded that numerical solutions based on the compressible potential flow theory accurately predicted the structure of the first shock cell and that the influence of the mixing region did not appear to influence the jet in this region.

The author is not aware of the existence of any previous published work on an underexpanded plane wall jet. The structure of a plane wall jet is expected to be similar to a plane free jet, the free jet axis being replaced by the wall. A Schlieren photograph of Gilchrist (1981) confirms this. An additional complication is introduced by the boundary layer at the wall. The strong adverse pressure gradient in region D (Figure 2.3) could cause the boundary layer to separate which could have a marked effect on the shock cell structure because supersonic flow is very sensitive to the flow angle, especially at Mach numbers close to unity. The boundary

layer also transmits information upstream which can affect the shock structure and jet shape.

The shock cell pattern of a plane underexpanded jet flowing over a convex curved downstream section is further complicated by expansion waves emanating from the surface. The effects of the curvature can be expected to depend on the ratio of the curvature to the initial jet width and on the stagnation pressure ratio. The surface static pressure measurements of Roderick (1961) and Korbacher (1962) are discussed in Section 2.4, as is the investigation of Bradbury and Wood (1965) into the deflection of thick jets. Under certain conditions the jet ceases to follow a curved convex downstream surface, a phenomenon known as breakaway. Previous investigations into this phenomenon are discussed in Section 1.2

2.7 DISCHARGE COEFFICIENT

The discharge coefficient, C_D , at a given stagnation pressure ratio across a nozzle or slot is defined as

$$C_D = \frac{\text{Actual mass flowrate}}{\text{Ideal mass flowrate}} \qquad \ldots(2.22)$$

The mass flow through a nozzle or slot is given by

$$\dot{m} = \int_A \rho U \, dA \qquad \ldots(2.23)$$

where U is the velocity component normal to the plane of the slot exit. If the flow is one dimensional and isentropic, the mass flow rate can be related to the upstream stagnation conditions and to the exit Mach number (Section 2.1). Thus the ideal mass flow rate through a nozzle or slot becomes

$$\dot{m} = A\, p_a\, M \sqrt{\frac{\gamma}{RT_0}} \left[1 + \left(\frac{\gamma - 1}{2} \right) M^2 \right]^{1/2} \qquad \ldots(2.24)$$

At a stagnation pressure ratio below the critical ratio, an ideal slot becomes choked and equation 2.24 reduces to

$$\dot{m} = A\left[\rho_0 p_0 \gamma \left(\frac{2}{\gamma+1}\right)^{\left(\frac{\gamma+1}{\gamma-1}\right)}\right]^{1/2} \quad \ldots(2.25)$$

Thus the ideal mass flow rate becomes independent of the downstream conditions and depends only upon the slot area, the stagnation conditions and the ratio of the specific heats. The critical pressure ratio for air, and thus the ratio for transition from equation 2.24 to 2.25 is 0.528.

The behaviour of two-dimensional flow through a slot at various stagnation pressure ratios is described by Guderley (1962). At stagnation pressure ratios close to unity (Figure 2.4a) the entire flow field is subsonic. The flow at points A and D is stationary, the flow accelerating along AB such that the static pressure at B has dropped to the downstream value. The flow is then turned along BE such that the static pressure remains constant, the streamlines becoming parallel at point E. As the stagnation pressure ratio is reduced the critical pressure ratio is reached and a sonic line appears (Figure 2.4b). A Prandtl-Meyer expansion is centred at B to further reduce the static pressure from the sonic pressure to the downstream value. The last of these expansion waves is shown intersecting the sonic line at point F, from where the downstream conditions are transmitted further upstream. Thus the slot is not choked because downstream information can be transmitted upstream. However, information from some point C on the jet edge does not reach the sonic line and so cannot be transmitted upstream. As the stagnation pressure ratio is further reduced, the point C moves closer to B until they coincide

(Figure 2.4c). A further reduction in the downstream pressure cannot be transmitted upstream, and the slot is choked.

A review of both theoretical methods and experimental results of flow through plane and axisymmetric nozzles is given by Alder (1976) and only plane supercritical nozzles will be discussed here. The difficulty in the theoretical solution of this flow is that the governing equations change from the elliptic to the hyperbolic form as the sonic line is crossed (Section 2.2). Norwood (1962) investigated the flow of air from a sharp-edged slit supplied from a chamber having a wall perpendicular to the plane of symmetry of the slot (Figure 2.5a). The flow was transformed into the hodograph plane which simplifies the boundary conditions of the free jet edge. A stream function distribution was assumed along the sonic line and the supersonic and subsonic regions solved separately. The assumed stream function distribution along the sonic line was then altered and the flow recalculated until the solution was continuous across the sonic line. After this solution was found, it was transformed into the physical plane. The effect of the upstream wall was included by specifying an input Mach number, M_1, which corresponded to an area ratio, b/c, after the solution was transformed back into the physical plane. A set input Mach number corresponded to a decrease in the area ratio, b/c, as the stagnation pressure ratio was decreased to the choking ratio, because the slot discharge coefficient increased. The position of the sonic line was also investigated and found to intersect with the axis of symmetry at a distance of 0.43 b units downstream of the exit plane of a choked slot when the input Mach, M_1, number was zero.

Benson and Poole (1965a) used Norwood's method to predict the discharge coefficient from a two-dimensional slot (Figure 2.5b) over the

entire range of stagnation pressure ratios. They also continued the downstream solution to predict the structure of first shock cell (Section 2.6). Benson and Poole (1965 a, b) also carried out experimental studies on the jet. The discharge coefficients were found to be accurately predicted by the theory down to a stagnation pressure ratio of 0.4. Below this the measured values of the coefficient of discharge deviated from the theoretical ones and by a stagnation pressure ratio of 0.1 the measured value was 2.5% higher than the predicted value. This discrepancy was put down to experimental error.

Alder (1976, 1979) extended this work to convergent nozzles, the angle of convergence being constant (Figure 2.5c). The entire stagnation pressure ratio range was calculated over a range of convergence angles, β, of 15^0 to 90^0. The coefficient of discharge was found to increase at a set stagnation pressure ratio as the angle of convergence was decreased and the ratio at which the slot choked increased with a decrease in the angle of convergence. Experimental tests on a nozzle whose convergence angle was 30^0 gave discharge coefficients about 2% below the predicted values over the entire stagnation pressure ratio range. This discrepency was assumed to be a result of side wall boundary layers. The theoretical results were also compared with experimental results that Alder (1976) quotes from Brown (1968), who tested two nozzles whose convergence angles were 20^0 and 40^0. The theoretical results were below those measured by Brown, but there is some doubt about the accuracy of the measured results because some of the coefficients were greater than unity.

Gregory-Smith and Robinson (1982) investigated the discharge of a plane two-dimensional jet from a nozzle over both flat and convex downstream surfaces. The coefficients from a sharp nozzle over a flat

plate were 3% higher than those obtained by Benson and Poole (1965 b) at stagnation pressure ratios below the critical ratio. Two further series of discharge coefficient tests were carried out; firstly from a circular nozzle over a flat plate and secondly from a circular nozzle over a convex downstream curvature of constant radius (Figure 2.5d). The streamwise length to slot width ratio varied from 1.75 to 7.0 and it was thus a thick orifice. Below the critical stagnation pressure ratio, the discharge coefficient increased at a set pressure ratio as the slot width was decreased. A rise in the coefficient was also found from the slot with a downstream curvature (Figure 2.5d) as the stagnation pressure ratio was increased from the critical value. This rise was more rapid as the slot width was increased. However the rise could not be reproduced by Gilchrist (1981) in tests on the same apparatus. In both the above investigations coefficients of discharge greater than unity were recorded at small slot widths which was attributed to errors in the measurement of the slot width and possibly to distortion of the slot at high upstream stagnation pressures.

An investigation into the discharge coefficient from thick axisymmetric orifices was undertaken by Deckker and Chang (1965-6). The streamwise length to diameter ratio was varied from 2.0 to zero (or a sharp-edged orifice). At subsonic and critical stagnation pressure ratios the coefficient of discharge increased as the thickness of the orifice was increased. However at low stagnation pressure ratios the sharp-edge orifice had a slightly higher discharge coefficient.

CHAPTER 3

THEORETICAL ANALYSIS

3.1 THEORY OF THE METHOD OF CHARACTERISTICS

3.1.1 Equations of Motion for Isentropic Flow

The Navier-Stokes equations (Section 2.2) are simplified for steady plane two-dimensional adiabatic inviscid compressible flow. They become

$$(\rho u)u_x + (\rho v)u_y + p_x = 0 \qquad \ldots(3.1)$$

$$(\rho u)v_x + (\rho v)v_y + p_y = 0 \qquad \ldots(3.2)$$

The continuity equation becomes

$$\rho u_x + \rho v_y + u\rho_x + v\rho_y = 0 \qquad \ldots(3.3)$$

The energy equation can be replaced by the speed of sound equation if the flow is isentropic. This has the advantage of eliminating the enthalpy derivatives from the governing equations. The speed of sound is given by

$$a^2 = \left(\frac{\partial p}{\partial \rho}\right) \text{ is} \qquad \ldots(3.4)$$

If the flow is isentropic, the partial derivatives can be written as total derivatives. Thus along a streamline in two-dimensional steady flow, equation (3.4) becomes

$$up_x + vp_y - a^2u\rho_x - a^2v\rho_y = 0 \qquad \ldots(3.5)$$

Equations (3.1), (3.2), (3.3) and (3.5) form a closed set of hyperbolic equations for a supersonic flow which can be solved by the method of characteristics. An additional simplification can be made if the flow is irrotational. This implies there are no gradients of entropy or stagnation properties normal to the streamlines and thus equation (3.4) is valid throughout the flow field. The condition of irrotationality in two-dimensional flow is

$$\frac{\partial u}{\partial y} - \frac{\partial v}{\partial x} = 0 \qquad \ldots(3.6)$$

The continuity, momentum and speed of sound equations, together with equation (3.6), can be combined to give the gas dynamic equation

$$(u^2 - a^2)u_x + (v^2 - a^2)v_y + 2uvu_y = 0 \qquad \ldots(3.7)$$

The local speed of sound is related to the stagnation speed of sound of the flow, the stagnation conditions being constant throughout the flow field

$$a^2 = a_o^2 - \frac{(\gamma-1)(u^2 + v^2)}{2} \qquad \ldots(3.8)$$

Equations (3.6), (3.7) and (3.8) form a closed set of hyperbolic equations. The use of the speed of sound equation has also enabled the density derivatives to be eliminated. The other flow properties are related to the stagnation conditions of the flow and the local Mach number (Section 2.1).

3.1.2 Method of Characteristics For Supersonic Flow

The two different sets of equations in section 3.1.1 both form a set of hyperbolic equations and thus there exist in the flow characteristics along which the governing equations become ordinary differential equations. The advantage of the method of characteristics over other finite difference methods for solving hyperbolic equations is that much larger steps can be used without a significant loss of accuracy. The method of characteristics is thus quicker and more efficient. This method has been used successfully by, among others, Love et al (1959) in their study of axisymmetric free jets, by Benson and Poole (1965a) in their study of plane free jets and by Mesli et al (1981) in their study of a plane plasma jet exhausting into a vacuum.

The theoretical derivation of the characteristic lines of hyperbolic

equations and the total differential equations along these lines, the compatibility equations, is given by Shapiro (1953) and Zucrow and Hoffman (1977) and by Smith (1978). Only the results will be quoted here.

3.1.2.1 Irrotational Flow

The governing equations for steady, irrotational, isentropic, planar flow are the gas dynamic equation (3.7), the condition of irrotationality (3.6), and the equation for the local speed of sound (3.8). These equations yield two characteristics given by

$$(dy/dx)_{\pm} = \lambda_{\pm} = \tan(\theta \pm \alpha) \qquad \ldots(3.9)$$

where θ is the angle of the flow to the x axis and α, the Mach angle, is defined by

$$\alpha = \sin^{-1}(1/M) \qquad \ldots(3.10)$$

The two characteristics, defined in Figure 3.1, are the Mach lines of the flow. The point A can only influence flow contained in the region between the right and left running characteristics originating from that point. Similarly, the point can only be influenced by upstream points contained within the region of the two characteristics that intersect at point A. An important feature of the flow is that the two characteristics do not exist if the flow becomes subsonic ($M < 1.0$) and thus the method of characteristics for supersonic flow can only be used provided the flow remains supersonic.

Along each Mach line there is a compatibility equation given by

$$(u^2-a^2)\, du_{\pm} + [2uv - (u^2-a^2)\lambda_{\pm}]\, dv_{\pm} = 0 \qquad \ldots(3.11)$$

There are several alternative forms of the compatibility equation that are theoretically equivalent, although one might lead to greater accuracy than another. Two such forms are

$$du_{\pm} + \lambda_{\mp}\, dv_{\pm} = 0 \qquad \ldots(3.12)$$

and

$$\frac{\sqrt{M^2 - 1}}{V} dV_{\pm} \mp d\theta_{\pm} = 0 \qquad \ldots(3.13)$$

3.1.2.2 Rotational Flow

The governing equations for steady, isentropic, rotational planar flow are the continuity equation (3.3), the two momentum equations (3.1, 3.2) and the speed of sound equation (3.5). These equations yield three characteristics, the two Mach lines (equation (3.9)) and the streamline,

$$(dy/dx)_s = \lambda_s = v/u = \tan \theta \qquad \ldots(3.14)$$

Two equivalent forms of the compatibility equation along the Mach lines are given by

$$(\rho v)du_{\pm} - (\rho u)dv_{\pm} + [\lambda_{\pm} - u(u\lambda_{\pm} - v)/a^2]dp_{\pm} = 0 \qquad \ldots(3.15)$$

and

$$\frac{\sqrt{M^2 - 1}}{\rho V^2} dp_{\pm} \pm d\theta_{\pm} = 0 \qquad \ldots(3.16)$$

There are two different compatibility equations along the streamline, given by

$$\rho V dV + dp = 0 \qquad \ldots(3.17)$$

and

$$dp - a^2 d\rho = 0 \qquad \ldots(3.18)$$

Equation 3.17 is Bernoulli's equation and equation 3.18 is the equation for the speed of sound, valid for an isentropic process.

3.1.3 General Method of Solution

The general method for the solution of the characteristic and compatibility equations is to form finite difference equations and then solve them by the Euler predictor-corrector method. The finite difference

equations for irrotational flow are given in detail in Appendix A and by Zucrow and Hoffman (1977) and thus only the principles will be presented here.

In irrotational flow the position and properties of point 3 (Figure 3.2) can be found if the position and properties of points 1 and 2 are known. A prediction of the position of point 3 can be made by substituting the values of the properties at point 1 into the right running characteristic equation passing through point 1, together with the properties of point 2 into the left running characteristic equation passing through point 2, and solving the two resulting equations simultaneously. A similar prediction of the velocities at point 3 can be made by the simultaneous solution of the compatibility equations valid along either characteristic. There are two methods of improving the estimation of the position and properties at point 3 (Appendix A): the average property method and the average coefficient method. The average property method involves replacing the flow properties in the finite difference equations, initially assumed to be those of points 1 or 2 for the right and left running characteristic respectively, by the average of the flow properties at 1 and 3 or 2 and 3. The average coefficient method involves replacing the coefficients of the terms in the finite difference equations, initially calculated from points 1 or 2, by the average of the two coefficients calculated from points 1 and 3 for the right running characteristic, or from points 2 and 3 for the left running characteristic. In either case the two improved characteristic equations are solved simultaneously to give a corrected estimate of the position of point 3 and the two compatibility equations are solved simultaneously to give a corrected estimate of the velocities at that point. The corrector is then reapplied until the

required convergence at point 3 is achieved. Hoffman (1973), who drew some general guidelines from a series of accuracy studies, suggests that in general the average property method of correction produces more accurate results.

These are two methods of applying the solution method outlined above: the direct marching method and the inverse marching method (Figure 3.3). In the direct marching method the left and right running characteristics are followed throughout the flow field, the solutions being obtained at their intersections. Thus any solution at a predetermined point on the flow must be interpolated from the grid generated by the characteristics. In the inverse marching method the solution is obtained at predetermined grid points. This involves running characteristics back to the previous grid line (column P) and interpolating for the property values at points 1 and 2 from known points on the grid (points A, B, C). To ensure stability for the interpolation, points must be known outside the intersection of the rearward characteristics from point 3 with the previous grid line. Zucrow and Hoffman (1977) suggest that, in general, the direct marching method is the more accurate of the two methods because errors are introduced in the interpolation of points 1 and 2 in the inverse marching method. The inverse marching method is also difficult to employ where the boundary of the solution is unknown, such as the free surface of a jet.

There are several procedures for solving the equations for rotational flow, which are discussed by Zucrow and Hoffman (1977). All the procedures involve interpolating for at least one point on the known grid. One method using the direct marching method is shown in Figure 3.4. The two characteristic equations can be solved to initially predict the solution point (point 4). The intersection of an estimated streamline running

through this point with a line joining points 1 and 2 can then be found. The conditions at point 3 can then be interpolated from the known values at points 1 and 2. The compatibility equations along the two characteristics can be solved simultaneously to give p_4 and θ_4 and the two compatibility equations along the streamline can be solved to give V_4 and ρ_4. The prediction can then be improved by either the average coefficient or average property method described above.

3.1.4 Boundary Conditions and Shocks in Irrotational Flows

3.1.4.1 Free Surface

At a free surface boundary only one characteristic and one compatibility equation are available (Figure 3.5). Thus two extra equations are required to solve for point 3. The first equation is obtained from the fact that the jet edge is a streamline

$$(dy/dx) = \lambda_s = v/u \qquad \ldots (3.19)$$

This can be solved simultaneously with the relevant characteristic equation to give the position of the solution point. The second equation is obtained from the fact that the total velocity is known because there exists a unique relationship between the static pressure and the total velocity

$$V_3^2 = (u^2_3 + v^2_3) = f(p_3) = f(p_o) \qquad \ldots (3.20)$$

The compatibility equation can be written in finite difference form

$$Q_{\pm}\, u_3 + R_{\pm} v_3 = T_{\pm} \qquad \ldots (3.21)$$

where Q, R and T are defined in Appendix A

Equation (3.20) and (3.21) can be solved simultaneously to give

$$u_3 = Q_{\pm}\, T_{\pm} \mp \sqrt{R^2_{\pm}\,[\,V_3^2\,(Q^2_{\pm} + R^2_{\pm}) - T^2_{\pm}\,]} \;\Big/\; (Q^2_{\pm} + R^2_{\pm}) \qquad \ldots (3.22)$$

$$v_3 = \sqrt{(V^2_3 - u^2_3)} \qquad \ldots(3.23)$$

The negative root of equation (3.22) is valid if the left running characteristic is used (an upper boundary point) and the positive root valid if the right running characteristic is used. (a lower boundary point).

3.1.4.2 Solid Boundary

As in section 3.1.4.1, only one characteristic and one compatibility equation are available (Figure 3.6). However the location of the wall is known and the wall itself is a streamline. Thus

$$y = y(x) \qquad \ldots(3.24)$$

$$\frac{dy}{dx} = \frac{v}{u} \qquad \ldots(3.25)$$

Equation (3.24) can be solved simultaneously with the characteristic equation to give the location of the solution point and equation (3.25) can be solved simultaneously with the compatibility equation to give the properties at the solution point.

3.1.4.3 Shocks

There are two methods of including shocks in the method of characteristics: the method of foldback and the method which includes the standard oblique shock equations. The former method effectively ignores the shock and the characteristics are allowed to fold back on top of one another. Eventually the solution again marches downstream, the flow being assumed to be irrotational throughout if the initial flow is irrotational. Zucrow and Hoffman (1977) suggest that in general this method yields reasonable results downstream of the "shock" provided the static pressure ratio (downstream pressure/upstream pressure) across the real shock is less than 1.25.

The second method involves combining the method of characteristics with the standard oblique shock equations. The flow must be supersonic after the shock. The conditions just behind the shock can be found and then the standard shock equations used to find the conditions after the shock. An initial guess of the angle of the shock must be made and an iterative procedure employed to correct this guess. The flow downstream of the shock will be rotational if the shock is curved.

3.2 PROGRAM DESCRIPTION

A computer program has been developed to calculate an inviscid irrotational supersonic jet, flowing either over a flat or convex wall. The method of characteristics is used as outlined in section 3.1 and uses some subroutines developed by Zucrow and Hoffman (1977). The coordinate system is the Cartesian system, Figure 3.7, and the Euler predictor-corrector method based on average properties was used throughout. The program establishes an initial profile and marches downstream by the direct marching process and uses the foldback method in the treatment of shocks. A flow chart is shown in Figure 3.8.

The program, which is written in FORTRAN IV, initially reads in the jet parameters such as the stagnation pressure ratio and the slot width to downstream radius. The subroutine INITIAL then calculates the properties on the initial starting column and the Prandtl-Meyer expansion (Figure 3.9). The Mach number along the first column at x = 0.0 can be specified either to be constant or to increase linearly to a specified value at the nozzle lip. The method of characteristics breaks down if the Mach number is equal to unity because the tangent of the characteristics becomes infinite, and so as an approximation to a unity exit Mach number, a minimum

Mach number of 1.02 was chosen. The Prandtl-Meyer expansion is modelled by propagating several expansion waves from the nozzle lip. The number of grid points is increased during this expansion (Figure 3.9). The first grid point of each column is held at the point (0.0, 1.0), the nozzle exit. The properties, specified by subroutine INITIAL, are such that there is an equal static pressure ratio drop across adjacent expansion waves.

The calculation marches downstream from the initial line. After the initial Prandtl-Meyer expansion the number of each solution points in each column is kept constant, the solution column alternating between a wall column and a free pressure column (Figure 3.10. Each point in a set column is shown with a constant value of x for clarity. This will not be the case in the calculated jet). Subroutine MOVE picks out points from previous columns which are then used to solve for a downstream point, subroutine INTER being used to solve an interior point in the flow, subroutine JET being used to solve a free pressure point and subroutine WALL being used to solve a solid boundary point. The latter subroutine calls a further subroutine BOUNDY which generates a specified wall contour. The flow properties at the solution point are calculated by subroutine THERMO from the isentropic stagnation and static relationships (Section 2.1). The calculation is continued for a specified number of columns and the results then outputted.

Two additional subroutines, CHECK and ROTATE, are required to calculate flow over the convex surface to avoid any of the gradients of the characteristics becoming infinite. After each calculation of a new column, the tangent of the right running characteristic is examined by subroutine CHECK and if any of the tangents are less than a specified value, subroutine ROTATE is called to rotate the entire column back by an angle ϕ_1

(a decrease in ϕ, where $\phi^1 < \phi$ (Figure 3.7)). The calculation is then renewed downstream and the resultant positions and velocities rotated forward by the angle ϕ^1 at the end of the program.

The program was run on an IBM 4341/1 mainframe computer operating under MTS. The running time of the program depends on the number of columns calculated downstream, but is typically 60 seconds of C.P.U. time.

3.3 TESTS AND RESULTS

3.3.1 Flat Plate Tests

Tests were carried out on an underexpanded jet flowing over a flat plate downstream of the nozzle exit. This is equivalent to the plane underexpanded jet investigated by Benson and Poole (1965a) and provided a check on the program.

The absolute accuracy of the method of characteristics cannot be determined because the true result is not known and there are no theoretical methods available to calculate the accuracy of the Euler predictor-corrector method. However as the number of rows in the mesh is increased the step size is reduced and the accuracy is increased. Three mesh sizes were tested:-

a) 10 rows with 5 initial Prandtl-Meyer expansion waves

b) 20 " " 11 " " " " "

c) 40 " " 21 " " " " "

The meshes were run at two different stagnation pressure ratios, 0.357 and 0.167, the exit Mach number being 1.02 across the nozzle as an approximation to an exit Mach number of unity (Section 3.2). The compatibility equation used was equation 3.11, although tests were also carried out using equation 3.12 and also equation 3.13.

Tests were also made at several other stagnation pressure ratios to

examine the effect of the stagnation pressure ratio on the jet structure. The initial tests were of underexpanded jets exhausting with a uniform Mach number of 1.02. An investigation of the effect of a linear variation of exit Mach number was also made. The Mach number varied from 1.02 at the flat plate downstream surface to a specified higher Mach number at the nozzle lip.

3.3.2 Flat Plate Results

The tests involving meshes of different size produced no change in the structure or length of the first shock cell of a jet and are not shown here. The only slight change between the meshes was in the location of the start of the shock at the end of the cells, the change between meshes (b) and (c) being very small. This change was due to the increased sensitivity created by the increase in the initial number of Prandtl-Meyer expansion waves. Similarly, there was no change produced in the jet by a change of the compatibility equation. The results presented below use compatibility equation 3.11 and were produced by a grid of 20 rows with 11 initial Prandtl-Meyer expansion waves.

Figures 3.11 to 3.13 show the effect of decreasing the stagnation pressure ratio on the structure of an initially uniform jet. It should be noted that the scales on the three graphs are different. Figure 3.11 shows the jet predicted for a stagnation pressure ratio of 0.286. The figure shows the jet edge and the initial Mach lines produced by the Prandtl-Meyer expansion at the nozzle lip and their continuation downstream. The initial Prandtl-Meyer waves are straight lines, each successively propagating a lower pressure until they reach the point where they meet the reflection of the first wave from the wall. These reflections further expand the flow to

satisfy the boundary condition that the flow does not separate from the wall. In the region where the initial expansion waves interact with their reflections the Mach lines are curved. After they have interacted with the last initial expansion wave, the reflected Mach waves again become straight lines, each propagating a unique static pressure until they interact with the reflections from the free surface. These reflections are compression waves to satisfy the free-stream boundary condition of constant pressure. These compression waves are then reflected from the wall as further compression waves. They then coalesce and form a shock, indicated by the characteristics folding back upon themselves. The initial shock occurs close to the wall near the intersection of the last two characteristics. The intersection shows that two distinct pressures exist at the same point which is a physical impossibility. This shock is a weak oblique shock and of the first type described by Benson and Poole (1965a) (Figure 2.3a).

As the stagnation pressure ratio is reduced the shock moves downstream and the maximum width of the jet increases due to the increased expansion at the nozzle (Figure 3.12). The oblique shock at the end of the first shock cell is now formed earlier in the shock cell by the coalescing of compression waves resulting from reflections of the first few original Prandtl-Meyer expansion waves. As the stagnation pressure ratio is further reduced (Figure 3.13), the shock appears before the reflected compression waves from the free surface reach the wall and is of the second type described by Benson and Poole (Figure 2.3b). However at the stagnation pressure ratio of Figure 3.13, Benson and Poole found experimentally that the third type of system existed, although this was not predicted by the method of characteristics. Thus the oblique shock, formed by the coalescing of the compression waves, leads to a normal shock that

decelerates the flow near the wall to subsonic speeds. At the junction of the oblique and normal shocks, a third shock propagates into the upper part of the jet. This is a reflection of the incident oblique shock.

The effect of decreasing the stagnation pressure ratio on the surface static pressure can be seen in Figure 3.14, where atmospheric pressure is 1 bar. The pressure remains constant until the Prandtl-Meyer expansion waves reach the surface. A pressure drop then takes place until the expansion is complete, the size of the drop being dependent on the stagnation pressure ratio. The pressure then remains constant until the compression waves, caused by the reflection of the Prandtl-Meyer expansion off the free surface, reach the surface. The pressure rise caused by the compression waves raises the pressure to that at the nozzle. The increase in the length of the first cell as the stagnation pressure ratio is reduced is clearly visible, the lowest stagnation pressure ratio calculation being terminated before the pressure rise at the end of the cell has begun.

The structure of the jets in Figures 3.11 to 3.13 are similar to those calculated by Benson and Poole (1965a). A direct comparison is difficult because the conditions at their slot are difficult to determine and a vena contracta also exists after their nozzle exit. Also they only present the jet structure and so measurements of shock positions and maximum jet diameters taken from the jet structure pictures would be only estimates. However, the jet structures produced by the present program are similar to those of Benson and Poole and give confidence that the program was functioning correctly.

The effect of a linear variation of exit Mach number of 1.4 at the nozzle lip to 1.02 at the surface is shown in Figure 3.15. The stagnation pressure ratio is 0.123 and the structure can be compared with Figure 3.12.

Only the Mach lines originating from the Prandtl-Meyer expansion are shown, although expansion and compression now also occur elsewhere in the jet. The cell structure is very similar to that of a uniform exit Mach number, although the maximum diameter and the cell length are reduced. The first coalescing of the compression waves also occurs slightly earlier and is at the wall. The effect on the linear variation of Mach number at the nozzle exit on the surface static pressure is shown in Figure 3.16. The initial part of the first expansion occurs earlier due to the initial expansion waves reaching the surface earlier. The main difference however occurs at the end of the shock cell, the compression coming earlier as the nozzle Mach number variation is increased.

3.3.3 Fully Attached Curved Jet Tests

Tests were carried out on an underexpanded jet flowing round a circular cylinder, the jet being assumed to be always fully attached to the cylinder. Three different slot width/downstream radius ratios were investigated, the ratios being equivalent to 2 mm, 4 mm and 8 mm slot widths on the experimental model (Section 5.1.2). A range of stagnation pressure ratios were tested at each slot, down to the ratio at which breakaway was observed (Section 6.4). The exit Mach number was assumed to be a constant value of 1.02.

A method for calculating the exit Mach number profile at the nozzle exit of the axisymmetric Indair flare (Section 1.2) has been developed by Green (1982). This combines the continuity equation with the centripetal momentum equation as the flow approaches the nozzle exit. Variations of exit Mach number from 0.8 at the solid wall surface to 1.3 at the nozzle lip have been recorded. However there is some doubt about the validty of the method because the centripetal force disappears at the exit of the

nozzle, resulting in a discontinuity in the flow as it "jumps" to a uniform Mach number profile. A series of tests were run with the present program to find the effect of a linear variation of Mach number across the nozzle exit. The Mach number ranged from 1.02 at the solid surface (a subsonic Mach number not being possible in the method of characteristics) to a specified Mach number at the nozzle lip.

3.3.4 Fully Attached Curved Jet Results

The results of selected tests are shown in Figures 3.17 to 3.25. Figure 3.17 shows the effect of a decrease in stagnation pressure ratio on the structure of the jet exiting at a uniform Mach number of 1.02 from a 4 mm slot over the 30 mm downstream radius. Figure 3.17a shows a stagnation pressure ratio of 0.394. The free pressure surface is shown together with the Prandtl-Meyer expansion waves from the nozzle lip and their subsequent reflections. These expansion waves and their reflections interact with additional expansion waves originating from the solid surface, which in turn are reflected as compression waves from the free surface. These additional expansion waves are not shown. However their effects can be seen by examining the path of the Prandtl-Meyer expansion waves from the nozzle lip. These initially travel in straight lines, each wave propagating a unique constant pressure. When the jet flowed over a flat plate these expansion waves continued as straight lines until they interacted with their own reflections from the solid surface (Section 3.3.2). However, those of Figure 3.17a can be seen to bend before the interaction with their own reflections from the surface. This is caused by the surface expansion waves turning the flow round the surface. After the interaction with the surface expansion waves, the Prandtl-Meyer expansion

waves no longer propagate constant pressures. The initial Prandtl-Meyer expansion waves are reflected from the solid surface and then reach the free surface where they are reflected as compression waves which in turn are reflected off the solid surface. Some of these latter reflections then coalesce near the outer edge of the jet to form a very weak oblique shock. It was found impossible to continue the calculation further downstream because the flow is further compressed by reflections from the free surface of surface expansion waves. This results in the flow becoming subsonic in the middle of the jet.

As the stagnation pressure ratio is reduced the cell length increases (Figures 3.17 b to d, note the scale changes in the latter two) and the initial coalescing of the compression waves occurs earlier in the cell. The calculation had to be terminated earlier as the stagnation pressure ratio was reduced because the point at which the flow became subsonic appeared earlier in the cell. At the stagnation pressure ratio of 0.238 (Figure 3.17d) the compression waves coalesce before they reach the solid surface, suggesting a regular shock reflection occurs. The characteristics that foldback can also be seen to fold into the surface and this calculation was terminated before the flow became subsonic.

The surface static pressure distributions of the four stagnation pressure ratios presented in Figure 3.17 are shown in Figure 3.18. There is an initial drop caused by the surface expansion waves turning the flow round the surface. This is followed by a more rapid drop as the Prandtl-Meyer expansion waves arrive at the surface. The pressure continues to drop after the last Prandtl-Meyer expansion wave has been reflected due to more surface expansion waves, but the rate of this drop is slowed before the reflections from the free surface of the Prandtl-Meyer waves arrive at

the surface. There are two reasons for this, firstly as the Mach number increases the pressure drop to turn the flow through a given angle decreases and secondly the surface expansion waves originating from near the slot arrive at the surface again, having been reflected off the free surface as compression waves. These latter waves help turn the flow further round the surface. The pressure then rises sharply as the reflections off the free surface of the original Prandtl-Meyer waves reach the surface. After the last of these waves have left the surface the pressure continues to rise, indicating that reflections from the free surface of earlier surface expansion waves are of sufficient strength to turn the flow round the surface. Figure 3.18 also shows the increase of the cell length as the stagnation pressure ratio is reduced. The foldback of the characteristics at the start of the compression at a stagnation pressure ratio of 0.238 is also shown.

Figure 3.19 shows the structure of a jet from an 8 mm slot and Figure 3.20 shows the surface static pressure distributions. The increase in the initial jet width lengthens the angular distance covered by the first shock cell. The curvature of the initial Prandtl-Meyer expansion waves before they interact with their own reflections from the solid surface can clearly be seen. The compressive reflections of the Prandtl-Meyer expansion waves from the surface do not coalesce until they are close to the jet edge. Figure 3.19b shows the structure of the jet at the breakaway stagnation pressure ratio and shows that the compression waves at the end of the cell do not coalesce until they are close to the jet edge.

Figure 3.21 shows the structure of jets from a 2 mm slot width and Figure 3.22 shows the surface static pressure distributions at these stagnation pressure ratios. The length of the cell at a given stagnation

pressure ratio is reduced compared to the two previous slots, although the structure is similar. However the appearance of a shock before the compressive reflections of the Prandtl-Meyer waves reach the solid surface does not occur until a much lower stagnation pressure ratio compared with the 4 mm slot. Figure 3.17d shows this has occurred by a stagnation pressure ratio of 0.238 at the 4 mm slot whereas it has not occurred by a ratio of 0.192 at the 2 mm slot (Figure 3.21c). Figure 3.21d shows it has occurred by a stagnation pressure ratio of 0.161, the breakaway ratio, and also shows foldback into the solid surface. The surface static pressure at this pressure ratio reaches a minimum of 1000 Pa (Figure 3.22). This calculation was terminated just before the compression initiated by the reflections of the initial Prandtl-Meyer expansion waves to avoid the foldback.

The effect of a linear variation of the nozzle exit Mach number on the static pressure profiles of jets, at their breakaway stagnation pressure ratio can be seen in Figures 3.23 to 3.25, the slot widths being 4, 8 and 2 mm respectively. The graphs all show a similar trend. As the linear variation is increased the initial expansion at the surface occurs earlier, although this effect vanishes as the Prandtl-Meyer expansion waves reach the surface. The static pressure is then unaffected by the linear variation of nozzle exit Mach number until the end of the cell when very large variations cause the pressure rise to occur earlier. When the exit Mach number varies from 1.40 to 1.02 this rise occurs 5^0 earlier than that from a jet whose exit Mach number is constant (Figure 3.23). The rise occurs even earlier when the exit Mach number varies from 1.57 (a full expansion) to 1.02.

3.4 MODIFICATION OF PREDICTION PROGRAM

The method of charateristics program described in Section 3.2 calculates the properties of an inviscid jet flowing fully attached over a radius of constant curvature. The characteristic running into the wall was solved such that the flow remained tangent to the wall. It is shown in Chapters 6 and 7 that the real jet does not remain fully attached to the wall, but a separation bubble is formed. This leads to gross inaccuracies in the prediction of the jet which are discussed in Section 8.5.1. Thus, to improve this prediction, a modification was made to the program that replaced the condition that the flow remained tangent to the wall by one that calculated the inner edge to a known static pressure. These static pressures were interpolated from the measured values obtained in the mechanical experiments (Section 6.5.4).

The modified program initially calculates the jet such that it remains tangent to the wall, because the first measured static pressures were at 5^0 or 10^0 round the surface. At a specified angle the program switches to calculating the inner edge of the jet to a known static pressure. The pressure is interpolated from the input data by a parabolic interpolation using known values at one angle directly downstream of the calculated point and two data points directly upstream (Appendix B). An assumption is made that the static pressure remains constant along an extended radius from the Coanda to the inner surface of the jet. The calculation proceeds downstream for a specified number of columns. In most cases the calculation of the jet was not limited by the subsonic region found in the fully attached jet and thus the calculation could proceed further downstream than the fully attached jets.

The program outputs the jet shape, the interpolated surface static

pressure distribution and the known surface pressures. In some cases the interpolated static pressure distribution departed from a reasonable fit through the known values, in particular near the region of initial separation. The actual static pressure between the measured angles is not known, but in regions where the interpolation seemed unreasonable, extra (hand interpolated) data points were inputted and the program rerun. It should be emphasised that these extra points are the author's personal interpretation of the static pressure profiles. The results of this program are presented and discussed in Section 8.5.2.

CHAPTER 4

OPTICAL THEORY AND REVIEW

4.1 INTRODUCTION

Methods involving optical techniques have found widespread use in the measurement of flow fields and have the advantage that they do not generally disturb the flow. Some of the most useful of these techniques are based on the fact that the refractive index of a gas changes with density. The connection between the two properties derives from classical electromagnetic theory which models light as an electromagnetic wave and assumes that a gas consists of independent neutral molecules which have no natural electric dipole moment. An additional assumption is that the natural frequencies of these molecules are appreciably different from the frequency of the visualizing light. The resonant wavelengths of electronic transitions in air are well into the ultra-violet unless the internal states of the molecules are excited and so this assumption is valid for most flow studies. The relationship between the density and the refractive index of a gas is given by the Gladstone-Dale formula.

$$n - 1 = K\rho \qquad \ldots(4.1)$$

An additional assumption, valid for gases, is that the refractive index is close to unity. If the gas consists of a mixture of several components, the Gladstone-Dale constant, K, of the mixture becomes

$$K = \sum_i K_i \frac{\rho_i}{\rho} \qquad \ldots(4.2)$$

where ρ is the total mixture density and the subscript i refers to a partial density of a gas whose Gladstone-Dale constant is K_i. The Gladstone-Dale constant is a function of the nature of the gas and a weak

function of the wavelength of the visualizing light, but is to a large extent independent of the pressure and temperature of the gas. The index of refraction of dry air for various wavelengths is tabulated in standard books of physical constants, for example the CRC Handbook of Chemistry and Physics (1984-5) or the Physics Handbook (1980), and from this the Gladstone-Dale constant can be calculated.

Mach number	0.2	0.5	1.0	2.0
$\Delta\rho/\rho_0$	0.02	0.12	0.37	0.77

Table 1: Variation of density with Mach number

There are two main forms of variable density flow; those of a high Mach number and those where heat is added or removed. Table 1 shows the variation of density from stagnation conditions at various Mach numbers, and shows that even at a Mach number of 0.2, there is a 2% change in density. The change in density of a fluid by the addition of heat is given by the perfect gas law (equation 2.2) with the assumption that the static pressure is constant.

$$\frac{\Delta\rho}{\rho} = \frac{-\Delta T}{T} \qquad \ldots(4.4)$$

Thus a few degrees change in temperature can result in a measurable density change.

In flows of a high Mach number the static density is related to the stagnation density by the Mach number (Section 2.1). Thus if the upstream stagnation conditions are known and the flow is reversible and isentropic (or in the case of a shock wave where the change in stagnation conditions can be calculated) a knowledge of the density at a point defines the Mach number and hence all the other properties of the flow.

The first part of this chapter covers the deflection of light in an inhomogeneous refractive field. The remaining sections discuss the shadowgraph, Schlieren and interferometric techniques respectively, the latter section containing a discussion of the two main types of interference and the various systems developed.

4.2 LIGHT DEFLECTION IN AN INHOMOGENEOUS REFRACTIVE FIELD

The behaviour of light when passing through an inhomogeneous refractive field is covered in many text books, especially Merzkirch (1974) and Hauf and Grigull (1970) and that edited by Ladenburg (1955), and thus only a brief summary of the results is given here.

In a steady compressible two-dimensional flow-field the refractive index, n, is a function of the two spatial coordinates, $n = n(x,y)$, (Section 4.1). A light ray will be deflected from its original direction and arrives at a screen at point Q* instead of Q (Figure 4.1). The optical path length covered by a light ray is defined by the integral

$$\int_{S_1}^{S_2} n\,ds \qquad \ldots(4.4)$$

where s is the geometrical path length along the light path. Thus the optical path lengths of the undisturbed and disturbed rays are different and it is possible to measure three different quantities of the disturbed ray:-

a) The displacement, QQ*

b) The angular deflection of the disturbed ray with respect to the undisturbed ray, ε^*

c) The phase shift between both rays, owing to their different optical path lengths, $\omega-\omega^*$

The three basic optical visualization methods of shadowgraph, Schlieren and interferometry measure the quantities of a, b and c respectively.

A beam of light can be considered to consist of a series of surfaces, or eikonals, made up of rays that have travelled the same optical distance from the source. If these eikonals are initially plane and perpendicular to the beam axis, they will remain so on reflection from a spherical mirror. However they will be distorted if the beam travels through an inhomogeneous optical disturbance. If the field of the optical disturbance has no discontinuous changes of refractive index, Fermat's principle applies.

$$\delta \int n\,(x, y, z)\, ds = 0 \qquad \ldots(4.5)$$

This states that the variation of optical path length along a light ray must vanish, or that if an initially plane eikonal passes through an optical disturbance, the resulting eikonal will be distorted such that each ray has travelled the same, and shortest possible, optical distance.

The solution to equation 4.5 is given by Merzkirch (1974) for rays of light initially parallel to the z axis and which pass through a two-dimensional flow field. An assumption is made that each ray undergoes only an infinitessimal deviation (i.e. a ray enters and leaves the field with the same x and y coordinates), but has a non-negligible curvature.

The observable quantities discussed above take the following form.

$$(QQ)^*_x = L \int_S^{S_1} \frac{1}{n} \frac{dn}{dx} dz$$

$$(QQ)^*_y = L \int_S^{S_1} \frac{1}{n} \frac{dn}{dy} dz \qquad \ldots(4.6)$$

$$\tan \epsilon_x = \int_S^{S_1} \frac{1}{n} \frac{dn}{dx} dz$$

$$\tan \epsilon_y = \int_S^{S_1} \frac{1}{n} \frac{dn}{dy} dz \qquad \ldots(4.7)$$

$$\Delta t = t^* - t = \frac{1}{c} \int_S^{S_1} [n(x,y,z) - n_0] dz \qquad \ldots(4.8)$$

where the S and S_1 are the z coordinates at the beginning and end of the disturbance respectively.

In both the Schlieren and interferometric systems a lens is introduced before the final screen to focus the working section onto the screen and thus eliminate the displacement QQ*. A focusing error is introduced because the individual rays, which travel in straight lines after the disturbance, are deflected by differing angles. The ray shown will have a virtual origin at plane f (Figure 4.1) if correctly focused, the position along the z-axis of this plane varying with the final angle of deflection of each ray. Thus if the system was focused on plane g, the ray shown would appear to originate from an undeflected position Q1. In

general, this error, which depends on the placement of the plane of focus in the working section, is negligible.

4.3 SHADOWGRAPH

The shadowgraph technique is the simplest of all optical visualizing procedures. The original arrangement is attributed to Dvorak and consists of a single lens that collimates light from a source, the beam then passing through the optical disturbance and striking a screen. Many shadowgraphs are observable naturally such as those produced by sunlight passing through convection currents in the air. The principle can be seen in Figure 4.2. The rays that pass through a region of zero refractive index gradient perpendicular to the ray are undeflected (rays 1). Those that pass through a region of constant change of refractive index (rays 3) and are deflected by a uniform angle, produce an unchanged uniform intensity at the screen. However in regions of a change in the gradient of refractive index, the rays are deflected by differing amounts (rays 2 and 4) and a change in intensity is seen at the screen.

This is shown mathematically, Ladenburg (1955), by assuming that the initial state of illumination of the screen is $I(x,y)$. The intensity, function I^* of (x^*,y^*) in the disturbed case results from the sum of all the intensities I of all the points x,y mapped onto x^*,y^*. Since x^* and y^* are functions of x and y, each intensity I_i must be divided by the Jacobian of the transformation of (x,y) to (x^*,y^*).

$$I^*(x^*,y^*) = \sum_i \frac{I_i(x,y)}{\partial(x^*,y^*)/\partial(x,y)} \qquad \ldots(4.9)$$

If the assumption that the deflections are infinitesimal holds, the two systems are connected by a small quantity, Δ, which is a function of x and y.

$$x^* = x + \Delta_x (x,y),$$

$$y^* = y + \Delta_y (x,y) \qquad \ldots(4.10)$$

A linearisation of the Jacobian can be introduced by assuming the products and higher powers of Δ_x and Δ_y can be neglected and the derivatives of equation 4.10 then substituted into equation 4.9. The result combined with those of equation 4.6, which give the deflections in terms of the density gradient, give the change in intensity at the screen due to the optical disturbance.

$$\frac{I-I^*}{I^*} = \frac{\Delta I}{I^*} \approx L \int_{S_2}^{S_1} \left(\frac{d^2}{dx^2} + \frac{d^2}{dy^2} \right) (\ln n)\, dz \qquad \ldots(4.11)$$

Thus the shadowgraph is sensitive to the second derivative of density, if the refractive index is close to unity, and a double integral of the intensity distribution would be required to obtain quantitative data. This integration is prone to large errors for three reasons; firstly only a few data points are obtained because the method is only sensitive to the second derivative. Secondly, the one to one mapping from (x,y) to (x^*,y^*) is violated and it is impossible to conclude how many values of I_i reach a given $I^*(x^*,y^*)$. Thirdly, the linearisation of the mapping function is invalid if the displacements become large such as through a shock wave. However, because it is so simple, the shadowgraph technique is often used to obtain qualitative data of a flow field.

4.4 SCHLIEREN

The Schlieren method is a term usually used to describe optical

methods that show the first derivative of the density without using the interference properties of light. It is often used for qualitative measurements, although quantitative results are more easily obtained than from the shadowgraph method. The method was developed over a century ago, one of the earliest people who recognised its importance being Toepler. His system consisted of two lenses and a knife edge (Figure 4.3). A light source, S, of finite length is placed at the focus of lens L1, and so any point P in the flow receives light from all points of the source. A second lens, L2, focuses the light at A, so for each point of the flow field, P, there corresponds an image of the source at A. Provided there are no optical disturbances in the test region all these images will coincide and a lens, L3, focuses an image of the working section onto a screen or photographic plate. If a knife edge is introduced at A to cut off some of the image of the light source, the screen will be uniformly darkened. Let d be the reduced height of the image passing the knife edge and e be the width perpendicular to it (Figure 4.4). The light intensity, I(x,y), arriving at any point of the screen will be constant and ignoring any loss of light or aberrations in the system, an approximation is given by

$$I(x,y) \approx I_0 \left(\frac{de}{f_3^2} \right) = \text{const} \qquad \ldots(4.12)$$

where I_0 is the original intensity of the source and f_3 is the focal length of lens L3. If a disturbance is now introduced into the flow at point P, the corresponding image at A will be laterally translated (Figure 4.4). This will result in a change in the intensity of the light arriving at the image of point P on the screen. If ϵ_y is the y component of the total angle of deflection, ϵ, due to the disturbance, the shift of the source image at A is given by

$$\Delta d \approx f_2 \tan \varepsilon_y \simeq \varepsilon_y f_2 \qquad \ldots(4.13)$$

where f_2 is the focal length of lens L2. Thus the relative increase in the light intensity arriving at the screen at the image of point P is given by

$$\frac{\Delta I}{I} = \frac{\Delta d}{d} \approx \frac{\varepsilon_y f_2}{d} \qquad \ldots(4.14)$$

Substitution for ε_y from equation 4.7 reveals that, if the refractive index is close to unity, the change in intensity is proportional to the density gradient at point P,

$$\frac{\Delta I}{I} = \frac{f_2}{d} \int_{S_2}^{S_1} \frac{dn}{dy}\, dz \qquad \ldots(4.15)$$

Thus the y-component of the density gradient can be recorded and if both the source and the knife edge are rotated by 90^0 the x-component can also be recorded.

The placement of the knife edge relative to the image of the light source at A controls both the sensitivity and the "range" of the system. The system can be made very sensitive by cutting off almost all the image at A (d becomes small in equation 4.12). However this results in no light passing the knife edge even for a small density gradient, and so no distinction at the screen will be apparent for a small or large density gradient. The usual combination between the sensitivity and "range " of a system is achieved by placing the knife edge so as to cut off half the source image when there are no disturbances in the working section.

There are numerous variations of the basic configuration cited in the literature, often systems being designed for a specific experiment. There are many review papers of these systems, in particular those of Holder et al (1956), Weinberg (1963), Hauf and Grigull (1970) and

Merzkirch (1981). One specific development was that of a colour Schlieren system by Holder and North (1952). A prism is placed between the white light source and the first lens, which ensures that the image of the source at A (Figure 4.3) appears as a series of coloured bands. A slot is placed at this image, cutting off both sides and thus ensuring only yellow light arrives at the screen (yellow light being in the middle of the visible spectrum). If the image moves due to a disturbance the colour arriving at the screen changes, one example being compressions appear red and expansions green. An alternative form of colour Schlieren is achieved by replacing the knife edge of a Toepler system with a coloured filter that consists of two or more bands. Reviews of these colour systems are given by Settles (1980, 1985). The advantage of these systems is that the eye is more sensitive to a change of colour than a change of light intensity, but this is offset by the increased complexity and cost of the colour photography.

In systems where the change of density is small, a double traverse system similar to the Mickelson Interferometer (Section 4.5.2) is used. However in systems where sensitivity is not the overriding concern, the standard configuration has become that shown in Figure 4.5. There are several advantages of this system, Weinberg (1963); firstly mirrors of large diameters are easier to make and are thus cheaper than a lens of equivalent optical tolerances, secondly, the folding of the optical axis reduces the length of the system and thirdly, chromatic aberrations, caused by a variation with wave-length of ray refraction in a lens, are absent in reflections from the surface of a mirror. The sensitivity and range, together with a discussion of the individual optical components and a set-up procedure, are given by Holder et al (1956).

There are two optical aberrations introduced into an off-axis system if, as in most systems, spherical and not parabolic mirrors are used. These are coma and astigmatism. Coma is due to the same cause as spherical aberration, which is that different zones of a lens or mirror do not form images at the same point, Houston (1957). One of its consequences is to make the magnification of an image vary with distance from the axis, the image of a point having the appearance of a comet. This aberration can be eliminated in the Z-type Schlieren system provided both mirrors have the same focal length, thus ensuring the aberration is of equal and opposite sign, or by the use of parabolic mirrors. Astigmatism arises when a spherical wave front is reflected from an off-axis spherical mirror because the wave front becomes ellipsoidal and has different curvatures in and perpendicular to the plane containing the axis and the direction of the source. This results in the image of the source consisting not of a point, but of two perpendicular lines separated by a short distance along the optical axis. This aberration can be corrected by the addition of a suitably shaped lens, Holder et al (1956, ref. 46), or by the use of a parabolic mirror. Under most practical conditions neither coma or astigmatism are serious if the angular offset of the source and the optical axis of the spherical mirror is less than 5^0 and both can be reduced if the ratio of the focal length to the diameter of the mirrors is increased.

The problems encountered when a laser is used as the light source are discussed by Oppenheim et al (1966). The laser is effectively a point source, so by geometrical optics (where each ray is treated individually and does not interact with others) the light should focus at a point after the second mirror, thus resulting in the knife edge acting as an on-off switch. However this does not happen due to the wave properties of

coherent light, so physically the knife edge interacts with fringes of a diffraction pattern rather than a geometric point of light. The knife edge amplifies the diffraction pattern so the final picture becomes a series of diffraction lines, rather than a variation of intensity, when there is an optical disturbance in the working section. This strengthening of the diffraction effect was reduced, although not eliminated, by replacing the knife edge by a neutral wedge with a sufficiently gradual gradient of light transmission with position across the beam. This neutral wedge proved insufficiently robust when the high intensities of a ruby flash laser were used and so it was replaced by a prism of quartz. This rotates the plane of polarization by an amount proportional to the distance traversed through the prism, and when used in conjunction with a sheet of polaroid effectively eliminates the diffraction lines.

The use of a laser in a Schlieren system is advantageous if the system is also designed for interferometric measurement (Section 4.5). It is also of use if Schlieren measurements are to be made of combustion processes, where normally the luminosity of the process interferes with the final patterns. If a laser is used whose wave-length is well away from the expected peak of the luminosity, a filter can be used to block out all the frequencies except that of the laser. Such a system has been developed by Andrews and Netzer (1976). A laser Schlieren system, based on the original Toepler configuration, has been developed by Whiffen and Ahuja (1983) for their study of accoustically excited jets. This system incorporates a Bragg cell after the laser, which deflects light away from the system until it is excited at its centre frequency. This allows very accurate control of the time between the excitation of the jet and the Schlieren picture.

4.5 INTERFEROMETRY

4.5.1 Principles of Interference

The distortion of a wave front that has passed through a region of variable density can be made visible when it is made to interfere with another beam. The phase relationship between the two beams must be constant for this interference to occur, which implies they must be coherent. This is achieved by splitting the beam before the optical disturbance and recombining afterwards, because separate physical light sources with the same frequency and phase are difficult to attain even with lasers. If non-coherent light sources are used, the optical path length of both beams must be made almost identical. There are two main forms of interferometry, normal and differential, which correspond to two different types of interferometer, namely the Mach-Zehnder type and the Schlieren or wave-shearing type. In the former interferometer the measuring beam is re-combined with an undistorted beam and in the latter it is recombined with a beam that has also passed through the optical disturbance, but displaced by a small lateral distance.

The difference between the two methods can be seen in Figure 4.6 after Hauf and Grigull (1970). The peaks of a wave front are represented by solid lines and the troughs by dashed lines. Figure 4.6a shows normal interference, with the reference beam travelling along the z-axis. A single peak of the measuring beam is shown, other fronts being omitted for clarity. Constructive interference occurs when this front coincides with a peak front of the measuring beam and destructive interference occurs when it coincides with a trough. Thus a series of dark and bright lines appear at the focusing plane, from which the optical path difference at any point between the measuring and reference beam can be determined provided the

sign of the gradient of the deformed wave front is known. Hence the density in the disturbance can be found using the Gladstone-Dale formula (Section 4.1). This method is known as infinite fringe interferometry because if there is no disturbance in the measuring beam, the screen would be uniformly illuminated. Any resulting fringe due to an optical disturbance in the measuring beam represents a line of constant refractive index and thus density. An alternative form of normal interferometry is finite fringe interferometry. This is achieved by tilting one wave front, either that of the measuring beam or that of the reference beam by a small angle. If there is no disturbance in the working section and thus the measuring beam remains as plane wave fronts, an interference pattern of straight parallel fringes will be seen on the screen. Any disturbance in the measuring beam results in shifts of these fringes, the direction of the shift depending on whether the optical path length in the disturbance has increased or decreased. A line where the fringe shift is constant represents a line of constant refractive index in the working section. A finite fringe form of normal interferogram has the advantage that a shift of a fringe can be measured much more accurately than the position of the fringes in an infinite fringe interferogram, although both pictures allow the refractive index to be measured directly.

The second form of interference, the differential, is shown in Figure 4.6b. Both beams pass through the optical disturbance, laterally translated by a small known distance Δy. It is assumed that both wave fronts are identical and it can be seen that the resulting interference pattern occurs in regions of refractive index gradient, hence the name of Schlieren interferometry. An increase in the displacement of Δy increases

the sensitivity of the system, but the assumption that both wave fronts are identical becomes dubious and a position on the screen ceases to correspond to a physical point in the flow field (even at very small displacements, a 'double' image of the working section is produced). This method enables the gradient of refractive index to be accurately obtained, and a single integration gives the refractive index in the flow field.

4.5.2 Review of Interferometers Employing a Non-Coherent Light Source

Before the advent of lasers, interferometers had to be designed with incoherent light sources. These sources, which were usually monochromatic such as a mercury-vapour lamp, introduced severe restrictions into the design of an interferometer. Firstly, their very short coherence length of approximately 5×10^{-6} m requires that both the reference and measuring beams travel almost exactly the same optical path lengths, and secondly they cannot be considered as point sources and so the beams cannot be made exactly parallel. The latter restriction means the fringe contrast at the interference is often poor unless great care is taken.

One of the earliest designs of normal interferometers is that of Jamin, which consisted of two inclined parallel glass plates of the same refractive index (Figure 4.7). The displacement of the reference beam from the measuring beam is controlled by the thickness of the mirrors and is generally very small, thus restricting the area of the working section. Another early design was that of Michelson, shown in Figure 4.8. The measuring beam travels through the test section twice, along different paths which makes it only suitable for measuring the refractive index of gases, or alternatively for the measurement of surface defects if the mirror M2 is replaced with the surface to be investigated.

The Mach-Zehnder interferometer was the first interferometer that was suitable for the measurement of transparent objects and it is still used as a standard interferometer (Figure 4.9). A beam is expanded to the diameter of the working section and then split into the measuring and reference beams at the beam splitter B1. The measuring beam is reflected at the mirror M1 before passing through the working section, the reference beam being reflected at the mirror M2 before being re-combined with the measuring beam at B2. The incoherence of the light source usually requires a pair of compensating windows, identical to those of the working section, to be placed in the reference beam to ensure that the optical path lengths of both beams are almost identical. The interferometer can be placed in two anti-vibration boxes, such as shown by the dotted lines in Figure 4.9. The interferometer is complex to set up and operate, the procedure and guidelines for their design being given by Holder et al (1956) and Tanner (1957). The expense of the interferometer also increases drastically with an increase in the diameter of the working beam because both mirrors, both beam splitters and all four windows (the compensating and working section pairs) must be of the same diameter. Tanner (1957) reviews various methods of treating the reference beam including passing it through the tunnel well ahead of the model where the flow is uniform. This makes the system very insensitive to vibration and also further reduces the optical path length difference between the reference and measuring beams, so improving fringe contrast.

Weinberg and Wood (1959) replaced the mirrors and beam splitters by diffraction gratings which reduced the cost of a system and made it easier to operate (Figure 4.10a). However as only two diffraction orders were used at each grating, the system was very wasteful of light, a problem that

was avoided in a system developed by Kraushaar (1950). The system was based on the Schlieren configuration using two lenses (Figure 4.10b), the diffraction gratings being placed at the focii of the lenses. All but two diffraction orders were lost at each grating, but the lessening of light loss was been achieved at the expense of the lateral separation of the beams, and so only small test objects could be viewed.

The most common method of shearing the light beam for use in a differential interferometer is by use of a birefringent device such as a Wollaston prism. A birefringent device has two mutually perpendicular axes, each with a different refractive index, so that light whose plane of polarization is at 45^0 to both axes will be split into two beams of equal intensity. A Wollaston prism consists of two such prisms laminated together so that the axis of higher refractive index in one prism is aligned with the axis of lower refractive index in the other (Figure 4.11). Thus if a ray passes through the centre, or median plane, of the Wollaston prism, both planes of polarization have the same optical path length but will diverge by an angle ϵ after leaving the prism. Chevalerias et al (1957) developed two systems using monochromatic light one based on the standard lens, the other on the standard Z-configuration Schlieren system. The light was polarized and split before the working section and then recombined by a second prism afterwards, two prisms being necessary to achieve good fringe contrast from the light source of finite width. Kamutzki and Griffiths (1970) developed a similar system that used a white light source so that any optical path difference appeared as a change in colour.

The above is a brief outline of the main developments of early interferometers in fluid dynamics. Ladenburg (1955) and Holder et al

(1956) review several systems for the measurement of high speed flow, concentrating mainly on the Mach-Zehnder interferometer and various modifications. Born and Wolf (1959) give a comprehensive review of interferometers and their many different fields of application and Weinberg (1963) reviews interferometers suitable for measuring combustion processes, many of which are suitable for use in high speed flows.

4.5.3 Review of Interferometers Employing a Coherent Light Source

The advent of inexpensive lasers, which produce monochromatic coherent light, in the early 1960's revolutionised interferometry. Three of the main advantages of the coherence property of laser light, discussed by Tanner (1966), are:

1. The necessity of having closely equal path lengths in the two beams is removed.
2. The difficulty of obtaining good fringe contrast in the presence of dispersion in the optics is reduced, i.e. no compensating windows are required.
3. The difficulty of obtaining good fringe contrast despite the finite aperture of the light source disappears because a laser behaves as an ideal point source.

The coherence, however, introduces two main problems; firstly that stray reflections must be avoided to prevent unwanted interference, and secondly that light will diffract at any out-of-focus particle, such as dust or fingerprints. The former can be overcome by the use of suitable anti-reflection coatings on lenses and the latter by a good standard of cleanliness.

Grigull and Rottenkolber (1967) developed modifications of both the standard Mach-Zehnder (Figure 4.9) and Michelson (Figure 4.8)

interferometers, using these special properties of laser light to treat the reference and measuring beams independently. The reference beam of their Mach-Zehnder was not expanded to the diameter of the working section and compensating windows were not used. The only optical components whose diameter was of the working section were two lenses that collimate the measuring beam, the other components being of small diameter whose required optical accuracy of a flatness of $\lambda/10$ was easily achieved. Thus this Mach-Zehnder variant was much cheaper than that of Section 4.5.2. Similarly, the reference beam in their Michelson interferometer was reflected back directly after being split, thus reducing the diameter of the mirror and the cost of the system. However the fundamental disadvantage of this interferometer's application to fluid dynamics still remained, the measuring beam travelling twice through the working section. (Section 4.5.2).

The coherence and monochromatic properties of laser light give much more freedom to the designer of a system. During the 1960's several interferometers were based on standard Schlieren configurations and have the obvious advantage that, with small alterations they can be used for more than one type of flow visualization. Goldstein (1965) developed a system based on the standard Z-configuration, although both the laser and the camera were on the same side of the main beam, the reference beam passing directly to the recombination unenlarged. This configuration introduced rather large aberrations but despite this, and the fact that the individual quality of his optical components was poor, he obtained fairly straight interference fringes of good contrast in the no-flow finite fringe picture. All the optical components were individually mounted which meant

the system was very prone to vibrations, a problem that was overcome by the use of very short time exposures for the photography.

Tanner (1965) and (1966) reviews several interferometers based on the Schlieren configuration and the various possibilities of splitting and then recombining the beams. Various simplifications can be made to early differential interferometers, for instance the system of Chevalerias et al (1957) no longer needs the first polarizer or birefringent device because the light is initially polarized and coherent. Merzkirch (1964) has developed a system using this principle.

Oppenheim et al (1966) developed a system based on the standard Z-type Schlieren configuration that combined several flow-visualization techniques and discussed the problems involved when using a laser in a Schlieren system (Section 4.4). In the interferometer the knife-edge was replaced by a concave lens placed just before the focus, and the resulting parallel beam was then sheared at a glass slab, similar to the shear produced in a Jamin interferometer (Figure 4.7). The thickness of this slab determines the amount of shear, a very thin slab resulting in a small shear and hence differential interferometry. A very thick slab results in the bottom half of the beam being folded onto the top and hence, if only half the beam has passed through the working section, giving normal interferometry. To obtain shadowgraphs the system is set as for Schlieren, the knife-edge removed and the final picture made slightly out of focus.

A major review of interferometers is given by Schwar and Weinberg (1969). They discuss the attributes of laser light, the criteria for the choice of laser and the several methods of splitting and recombining beams. Over sixty laser interferometers developed for use in combustion research are cited, many of which can be applied to supersonic flow problems. Hauf

and Grigull (1970) review interferometers for use in heat transfer experiments and more recent developments are given by Merzkirch (1974) and Murty and Shukla (1976). The latter paper gives modifications to the Jamin and Mach-Zehnder interferometers to reduce the problems of vibrations. Ways of increasing the beam separation in the Jamin interferometer are shown by replacing the front and back faces of the glass slabs (Figure 4.7) by a beam splitter and a plane mirror respectively, the two being mechanically connected. Also wedge shaped plates are introduced to enable finite fringe interferograms to be made.

Pollock (1980) has developed an interferometer based on the standard Z-type Schlieren configuration (Figure 4.5) and known as an aperture reducing type of interferometer, in which the reference beam passes through the working section. A lens is introduced, between the light source and the first mirror, that focuses half the beam to a point at the mid-plane of the working section, the other half being the parallel measuring beam. The reference beam is focused after the second mirror and folded onto the measuring beam by a plane mirror placed at the focus of the second mirror. Thus this system produces normal interferometry and is virtually insensitive to vibrations because both measuring and reference beams travel virtually the same geometrical path. It is also optically robust (i.e. there are no problems when high powered lasers are used) but has the disadvantage that the cross-sectional area of the measuring beam is only about a third of that of the Schlieren mirrors.

A polarization interferometer that produces a large lateral shear, and thus normal interferometry, has been developed by Lee and Woolsey (1981). This consists of six matching calcite-glass prisms, which are cheaper than the Wollaston prism but produce only half the shear, arranged

in a regular hexagon formation. The two 'halves' of the hexagon are independent, thus ensuring the possibility of long beam lengths and large shear. This interferometer proved relatively easy to set up and adjust and was fairly insensitive to vibrations.

Merzkirch (1981) reviews various optical systems and points out the increasing popularity of holographic over conventional interferometry. The principles of its operation are given by Heflinger et al (1966) and involves a double exposure of the film, a no-flow and a flow interference pattern with a reference beam that arrives at a different angle to the film, superimposed. The negative, when illuminated from the same angle as the original reference beam, will act as a diffraction grating and produce in its first order an interference pattern between the no-flow and flow test beams. Thus the main difference between holographic and conventional interferometry is that in the former the reference beam is temporally separated from the test beam but follows the same spatial path, and in the latter the separation is spatial. Thus in holography, optical imperfections are eliminated and so components of poorer quality can be used. Holography, which also contains information about three-dimensional properties, Merzkirch (1981), is not considered further.

4.5.4 Measurement of Fringes

There are two main methods used to measure the location of fringes on an interferogram, and thus for evaluating the fringe shifts in the finite fringe method. The first method is where the light intensity is measured by eye, either through a travelling microscope or on a digitiser, and the second method is where it is measured by a densitometer or a photo-electric cell.

The former method is widely used, for example by Kuehn and Goldstein (1976) who use a tool-makers microscope to view the negative. The cross-wires of the microscope are placed at the centre of the fringe by eye and the position manually recorded. The best accuracy of this method is generally accepted to be about 1/10 to 1/20 of a fringe width, the limitation being of the eye. Ben-Dor et al (1979) propose the use of a digitiser together with computer programs to evaluate fringe shifts and hence flow properties. A digitising table consists of a fine rectangular mesh of wires and a travelling cursor with a pair of cross-wires. When a 'log' button on the cursor is depressed, the position of the cross-wires relative to the origin of the rectangular mesh is recorded digitally in terms of x and y coordinates. These digitised results can be used as data for computer programs, which can be written to eliminate fringe shifts due to optical imperfections (by analysis of no-flow interferograms) and also to remove uniform changes in the flow field due to the fluid motion by the analysis of a reference point. This method eliminates a lot of the pain-staking drudgery in the use of microscopes and is, as a result, not only faster but less prone to human error. However the accuracy of this method is not improved over the use of a microscope, because the light intensity is still measured by eye.

Arzoan and Ben-Dor (1985) have developed a fully computerised extension of this method. The interferogram is transfered to the computer memory using a television camera. The recorded interferogram is then 'touched up' by the manual input of dark and light spots and then evaluated by a fully computerised method. Thus this method eliminates the time-consuming and tiresome process of the manual digitisation of the

interferogram, and a big reduction in the time taken to evaluate an interferogram is achieved.

A more accurate method of obtaining fringe positions is by use of photocells which produce a voltage proportional to the intensity of light reaching the cell. Dew (1964) describes a system where the negative is held in a plate whose movement is controlled by micrometers. Light is shone at the plate and passes through onto two 'matched' photocells, placed approximately half a fringe width apart. When both photocells give the same reading, the centre of a fringe is exactly between them, and because the intensity distribution of the interference pattern is of a sine squared type and the photocells were monitoring the steep gradient, an accuracy of 1/100th fringe was achieved on 1 cm width fringes. The accuracy depends on the micrometers and the sensitivity of the photocells, although problems were also encountered due to 'drift' of the photocells. The main disadvantage of this technique is that, though the fringes need not be straight, the fringe spacing must be nearly constant throughout the interferogram. Thus this method is of use in the evaluation of interferograms of surface defects or optical defects (i.e. a no-flow picture), but it is of little use in the evaluation of flow interferograms. An earlier method, developed by Werner and Leadon (1953), uses one photocell together with reference and test pictures. The two photographs are developed in several high-contrast processes, one finishing as a negative, the other as a positive. The reference picture is then solidly mounted and the test picture is placed on top so that it can move relative to the reference picture, the movement being controlled by micrometers. The pictures are moved relative to one another until light passing through produces a minimum voltage from the photocell. At this moment the positive

and negative versions of the fringe exactly coincide and the coordinates can be recorded. Although accuracies of 1/500th fringe shift were obtained, this method has the same limitations as the previous one, both also being very tedious because each point must be recorded by hand.

These draw-backs are overcome in a machine devised by McKeen and Tarasuk (1981). A densitometer traverses across the photograph in small steps, its analogue output being converted to an Intensity Digital Number. These numbers are stored as the densitometer traverses the light part of a fringe and when the intensity falls below a reference value both the mode (the location of the brightest part of the fringe) and the median (the location of the average intensity) are calculated and then stored for output. The mode is taken as the centre of a fringe if the flow is changing rapidly across a fringe (i.e. the sine squared intensity distribution is distorted) and the median used if the photograph is of poor quality (for instance there might be several 'peaks' of intensity within a single fringe). The entire flow field can be covered in several traverses, each fringe appearing once in a traverse. A fringe can then be followed through the traverses, great care being taken to match the same fringe through the traverses in rapidly changing flows. The machine is capable of locating fringes that are at least two steps apart (i.e. 0.5 mm in width), its accuracy being primarily dependent on the accuracy of the densitometer.

CHAPTER 5

EXPERIMENTAL APPARATUS

5.1 MECHANICAL APPARATUS

5.1.1 Air Supply

The compressed air was supplied by a Reavell CSA9 two-stage water cooled compressor, operating at 720 rev/min, rated at 450 p.s.i.g. at a rate of 434.5 m^3/h F.A.D. This was stored in a 200 ft^3 welded air receiver and as no drier was installed with the compressor, a valve at its base was cracked open to drain off some of the water. The receiver fed a high pressure line 1.5" diameter B.S.P. which had several drop valves situated along its length. The compressor was commissioned and the high pressure line extensively purged to remove the graphite left from the drawing process on the inside of the pipes. A diagram of the inlet line to the rig from one of the drop valves is shown in Figure 5.1.

An Auld double control high pressure regulator, which was fitted with a spring that enabled the downstream pressure to be varied from 110 to 55 p.s.i.g., controlled the pressure in the inlet line. The regulator also incorporated a safety blow-off valve to prevent the downstream pressure exceeding 140 p.s.i.g.

As it was important to prevent the problems, experienced by Gilchrist (1981), of oil carry-over from the compressor to the windows of the rig, a high degree of filtration was required. The presence in the air of the water and graphite, picked up off the walls of the high pressure line, together with the cost of the disposable high-grade filter element meant a two stage filtration process was required. A Norgren 30CG-10 filter, with a 25 micron sintered bronze element and an automatic drain, provided the first stage of filtration that removed the water, graphite and some oil.

The element could be removed and cleaned in an ultra-sonic bath with ethanol when Budenberg pressure gauges showed an excessive pressure drop across the filter. The second stage of the filtration process was a Balston A15 filter, fitted with a differential pressure gauge and an automatic drain, whose microfibre disposable element gave a 99.99% efficiency for 0.1 micron particles and droplets.

The air mass flow rate was measured by an orifice plate with D and D/2 tappings, designed according to B.S. 1042. The size of the orifice plate could be changed and the static pressure altered by the regulator, to give a reasonable pressure drop across the plate, thus reducing errors at all operating conditions of the mechanical rig.

A 2" bore flexible reinforced rubber pipe connected the air line to a valve which controlled the mass flow into the rig.

5.1.2 Mechanical Rig

The aim of the mechanical rig was to produce a plane jet which could be viewed through two windows as it followed the Coanda surface. The basis for the design was to be the axisymmetric I8-H-AS flare, marketed by Kaldair Ltd., whose Coanda surface consists of a small flat section downstream of the slot, followed by a curve of constant radius through 100^0 and ending in long flat section at a tangent to the end of this curve. At the largest estimated flow rates through the rig, the rig was to be run for up to two minutes on the blow-down principle. The final design consisted of two sections, a settling tube supported by adjustable feet and a top section that contained the nozzle and the Coanda surface (Figure 5.2).

The diameter of the glass windows determined the radius of the Coanda surface as the jet had to be visible from behind the slot to the flat

portion of the Coanda surface over a range of slot widths up to one-third that of the Coanda radius. After considering several different radii, it was decided that 30 mm was the largest feasible radius that allowed not only a view of the attached jet, but also one of a jet after breakaway from the Coanda surface. The radius of curvature on the nozzle and the width of the settling tube were in the same ratios to the Coanda radius as found on the 18-H-AS flare. To satisfy the two minute running time criterion, a 60 mm breadth slot was designed, which gave an aspect ratio of 6 at the largest slot widths envisaged.

Of the two ways of altering the slot width, movement of the Coanda or movement of the nozzle, the former was more simple. Figure 5.3 shows that the motion was achieved by a screw-thread assembly mounted above the surface and the direction controlled by five feet which slid in grooves milled into the back plate. The Coanda was then clamped into position by screws attached to these feet. The slot width was measured by two micrometers mounted above the Coanda. Its uniformity across the breadth was checked by slip gauges and found to vary by 0.01 mm in the worst case, an inaccuracy of 0.5% at a 2 mm slot width.

The Coanda surface contained 0.75 mm diameter surface pressure tappings, which were staggered across its breadth, at every 5^0 over the first 40^0 of curvature and every 10^0 thereafter. More tappings were not included for two reasons: firstly that they might start interfering with the flow, and secondly that there was little space behind the Coanda where the tappings emerged. Plastic tubing, which exited through a hole in the back plate, was fitted to the nipples recessed into the back of the Coanda.

Two different nozzles were made, one designed so that the slot configuration was as on the I8-H-AS flare, with a small flat on the Coanda after the slot exit, the other designed with a larger radius so that the slot exit coincided with the start of the curvature of the Coanda (Figure 5.3). The window frames bolted onto the back plate and near the nozzle and could easily be removed to enable the glass and perspex windows to be interchanged. The windows rested in the frames and were restrained by a rim on the outer side. Rubber 'O'-rings minimised leaks at the joins between the Coanda, back plate, window frames and the nozzle.

The settling tube was designed to be twenty maximum slot widths in length, ensuring the flow was two-dimensional at the slot and at three static pressure tappings which were fitted upstream of the slot. These tappings gave, after a correction dependent on the local Mach number, the stagnation pressure in the tube.

A flange connected the top Coanda section to the settling tube, which in turn was supported on a tripod bolted to the floor, and an arm bolted to the wall. The height of two of the feet of the tripod could be adjusted to ensure that the rig was vertical to the ground, essential in the setting up of the interferometer (section 5.2.2).

5.1.3 Instrumentation

The static pressure upstream of the slot was measured on a Budenberg gauge. Three different ranges were used, the low pressure range gauge being calibrated against a mercury manometer, the intermediate and high pressure range gauges against a dead-weight tester. After a change in the valve setting at the base of the rig, the drift in the static pressure was less than 0.02 bar over a long time period.

The surface pressure tappings were connected to a mercury or water filled inclined multimanometer, depending on the magnitude of the pressures being measured. The height difference between a surface static pressure and atmospheric pressure could be read to the nearest millimetre and the angle of inclination of the manometer to the nearest degree. When surface static pressure measurements were not being taken, the manometer was removed and the plastic tubing clamped.

Two Druck pressure transducers, which could be read to 0.01 volts on a 100mvolt full scale deflection, were used to measure the pressures at the orifice plate. A 1.0 bar differential transducer, calibrated against a mercury manometer, measured the pressure difference across the plate and a 35 bar differential transducer, calibrated against a Budenberg gauge, measured the upstream static pressure. A mercury thermometer, which could be read to 0.1^0, was placed in an oil pocket downstream of the plate to measure the static temperature. This temperature rose by as much as 8^0 over a long run, due to increased heating of the air as the compressor warmed up.

5.2 OPTICAL APPARATUS

5.2.1 Design Considerations and System Development

A system was required to measure optically the properties of an air jet flowing either round the Coanda surface onto its flat section, or away from the surface after breakaway. The system was to be capable of interferometric, Schlieren and shadowgraph techniques, the former being normal interferometry rather than differential interferometry (section 4.5.1). This enables quantitative measurements of the density to be made from the interferometry and qualitative measurements of its first and

second derivatives from the Schlieren and shadowgraph respectively (Chapter 4). The three techniques were to be readily interchangeable using the minimum re-arrangement of the optical components.

The advantages of using a laser in an interferometric system are discussed in section 4.5.3, and allow an interferometer to take a Schlieren-type configuration. The coherent light also means the system is easier to adjust than a conventional Mach-Zehnder and improves the fringe contrast. The aberrations in the system of Goldstein (1965) can be eliminated by using the standard Z-configuration Schlieren system, and if parabolic mirrors designed to deflect light through the desired angle are used, coma is eliminated and an exactly parallel beam is produced to pass through the working section. Two configurations of optical components were considered (Figure 5.4 amd 5.5) and tested, both of which allow the total area of the Schlieren mirrors to be used for the measuring beam. Both the systems of Pollock (1980) and Oppenheim et al (1966) require the area of the mirrors to be at least twice that of the measuring beam. In the present configurations only the two mirrors and the glass in the working section are of the working section diameter and their total area is used, thus reducing the cost of the system. There are many warnings in the literature on the problems of vibrations when the measuring and reference beams follow totally different paths. Goldstein's optical components were all individually mounted, the vibration problem being overcome by use of very short time exposures for the photography. In the present rig it was proposed to overcome the problem of vibration by mounting the optical components on connected optical benches. These benches were to be mounted on anti-vibration feet, thus isolating the system from any disturbances transmitted through the floors.

Although both the configurations considered lose half the light at the second beam splitter, it was calculated that a laser source of 2 mW would provide enough power to darken the negative even if short time exposures were used. The beam from a standard Helium-Neon laser, which produces red light, is very narrow in diameter and the resulting high intensities make it dangerous to view with the naked eye. It was proposed to expand this beam, which would become the reference beam, so that it could be viewed comfortably, thus making the process of setting up the interferometer easier. This was initially achieved using a beam expander which consists of a diverging lens and a collimating lens (Figure 5.6) and is thus simple to operate, cheap, and results in little power loss in the beam. However the final pictures at the camera were found to contain numerous interference rings even when only one beam was viewed. The origin of this interference was traced to the laser and beam expander. An examination of the laser output revealed a single dark line across the beam, presumably caused by a mark on the output mirror, and one of the beam expander revealed that the diverging lens produced several interference rings despite several efforts to clean it. Thus it was decided to replace the beam expander by a spatial filter, which consists of a focusing lens, a pin-hole and a collimating lens, (Figure 5.6). Any light that is not parallel at the input lens (Ray A), or that is diffracted by dust on, or imperfections in the input lens, does not pass through the pin-hole and provided the collimating lens is optically perfect a clean beam is produced. The pin-hole produced a very faint diffraction pattern itself, consisting of concentric circles, which was not obtrusive at the camera but did enable the centre of the beam to be accurately placed. This proved an

invaluable aid in the setting up and alignment of the system (Section 5.2.2).

The beam splitter holders were modified, by cutting away the sides, to avoid impingement of the reference beam as it passed through the splitter. The measuring beam was reflected off the front surface and expanded at lens L1 (Figures 5.4 and 5.5). The beam was overexpanded at the mirror M1 and thus only the central area was reflected through the working section, the outer edge being lost. This overexpansion is desirable because a laser beam has a Gausian intensity distribution across its diameter which causes problems when the interference pattern is photographed. The fringe clarity is unaffected by this variation of intensity because the interference is formed by two rays of equal intensity, as they originated from the same part of the beam. By overexpanding the beam, the intensity distribution is almost constant over its useful area, and thus it darkens a photographic plate uniformly.

The system was set up in both configurations (Figures 5.4 and 5.5) and shadowgraph, Schlieren and interferometric pictures of a candle flame viewed. All the optical components were locked onto connected optical benches supported on anti-vibration feet. These feet were effective from ten to several thousand hertz, and sat on rubber pads. These measures were designed to eliminate external vibrations. Near infinite fringe photographs were obtained (Plate 1) even though the parabolic mirrors were deflecting the beam through a greater angle than their design angle of 2.7^{0}. The required deflection, to avoid contact of the reflected beam from mirror M1 with the lens holder of L1, was greater in system B (Figure 5.5) than system A (Figure 5.4) and thus the extra aberrations caused an additional fringe in the 'infinite' fringe picture. A finite fringe

picture, achieved by rotation of mirror M2, is also shown in Plate 1 for comparison. There seemed to be no difference between the two configurations in their sensitivity to external vibrations caused by movement of people in the room or machinery in adjacent rooms.

Photographs of Schlieren and shadowgraph pictures caused by the candle are shown in Plates 2 and 3 respectively. The cut off for the Schlieren was a razor blade and the resulting diffraction pattern, shown by Oppenheim et al (1966), is clearly visible. It was decided to overcome this problem by using an alternative light source rather than using a prism and a sheet of polaroid, as used by Oppenheim et al (Section 4.4). A Xenon spark source emits incoherent light at a range of frequencies thus avoiding the problem of diffraction at the knife edge and is also a source of finite width, which allows greater control of the amount of light cut off at the knife edge. The intensity of the spark could be varied, its duration varying from 2.5 μ sec at low intensities to 6.5 μ sec at high ones. The frequency of the pulse could also be varied, from 1 to 100 Hz at low intensities and from 1 to 9 Hz at high ones. The advantage of using this source is that it enables both spark and continuous Schlieren pictures to be taken, the former by a single pulse of high intensity and the latter by the superposition of several low intensity pulses upon the same photographic plate. This source replaced lens L1 of the interferometer (Figure 5.4) and a razor blade was used to cut off the light at the focus of mirror M2.

Experiments with the mechanical rig (Chapter 7) produced very satisfactory results with both Schlieren and shadowgraph techniques. However the interferometer was prone to vibrations and no final picture could be viewed by eye. Pictures taken 1/1000th second revealed

satisfactory finite fringe pictures over a range of pressure ratios down to p_a/p_o = 0.55. Wooden covers were placed over the beam paths to prevent re-circulation of the air from the mechanical rig through them, but this resulted in no improvement in the fringe stability. This vibration problem might partly be due to vibration of the mechanical rig itself and is discussed in Section 5.4.

The photographs were taken with a Cannon AE1 camera mounted on a tripod with a standard 50 mm lens. The camera was fitted with bellows to give the desired magnification and the photographs taken by means of a cable release. A range of speeds of conventional black and white films were tested to obtain the best results for both the laser and white light sources. A red-sensitive HIE 2481 Kodak film at 80 ASA was also tested with the former source to try to improve the contrast, but it was found to give inferior results to conventional films.

The most satisfactory results for the interferometer were obtained using a 400 ASA film at 1/1000th second exposure, this being the shortest exposure possible and thus minimised the vibration problems. The continuous Schlieren photographs were taken on a 125 ASA film at a speed of 1/60th second which was long enough to ensure a time-averaged picture was obtained. The same film speed was used for the spark Schlieren, the source being at a higher intensity setting (Section 7.3.1), and also for shadowgraph photographs.

5.2.2 Initial Set Up Of Optical System

It was important to avoid any aberrations in the final picture by ensuring that the light travelled through the various optical components undistorted and undeflected. Great care was taken to ensure this and it involved repeating several stages in the setting up process many times.

The first stage in the setting up process was to replace the perspex windows with the high quality optical windows in the mechanical rig and to ensure the rig was exactly vertical to the floor. The latter was achieved by adjusting the height of two of the feet of the tripod stand whilst monitoring the angle of the settling tube with a large spirit level. The optical benches were joined together, the right angles being checked by a large set square, and levelled using a spirit level by adjusting the height of the anti-vibration feet.

The spatial filter was attached to the laser and adjusted until the beam emerged undeflected from it. The pin hole caused a set of faint diffraction rings to be observed in the beam which consisted of concentric circles reducing to a point at the centre of the beam. This point enabled the centre of the beam to be accurately located and was used in the alignment of the beam through the optical system. The light source was mounted in a Vee-block and the direction of the beam altered by tilting the laser using paper pads until the beam travelled directly down the middle of and parallel to the central optical benches (Figure 5.4). The beam splitter, B1, was roughly set in position such that the reflected beam was reflected off its front surface, the modifications to the holder ensuring that the reference beam travelled through unimpeded. The beam splitter was then rotated until the centre of the reflected beam fell upon the centre of mirror M1. This centre was made visible by placing a piece of paper in front of the mirror upon which there was a circle of the same radius as the mirror and a cross at its centre. The position of the beam splitter was adjusted along the central optical table, together with the angle of deflection and the height of lens L1, until the centre of the beam remained on the cross, whether or not lens L1 was present, or where it was placed

along the optical table holding mirror M1. The beam was now aligned up to the mirror, although the position of the lens L1 still had to be determined such that the reflected beam from the mirror was a parallel beam.

At this stage it had to be ensured that the light reflected from the mirror M1 would pass perpendicular through the plane containing the mechanical rig. The angle of deflection at the mirror was adjusted so that a nominally parallel reflected beam did not impinge upon the lens holder of L1. It was found that if the unexpanded beam (i.e. lens L1 removed) was shone onto the glass windows, a reflection was visible at the mirror, M1. The beam was correctly aligned when this reflection coincided with the beam falling on the mirror from the beam splitter. This required rotation of the optical benches and some fine adjustment of the mechanical rig itself. The height of the optical benches were also adjusted until the centre of the beam at the optical windows coincided with the centre of the windows, again made visible by placing a circle of paper, whose centre was marked and whose radius was the same as that of the window, in front of the window. The height was altered by screw threads on the anti-vibration feet, the process being checked by use of the spirit level. The process of aligning the optical system with the mechanical rig was lengthy, involving several 'restarts'.

Once this alignment had been achieved, the position of lens L1 was determined such that the beam passing through the working section was exactly parallel. The lens was moved along the optical table until the diameter of the beam at the working section was exactly the same as that of the mirror. The mirror M2 was then placed such that the centre of the measuring beam coincided with the centre of the mirror in the xz plane, the alignment being automatically right in the yz plane provided that all the

previous alignments were accurate (Figure 5.4). A check was then made to ensure that the focus of the mirror M2 and its collimation occurred before the beam splitter B2. The whole optical table holding mirror M2 was moved along the central one until this was achieved whilst the centre of the beam from mirror M1 was aligned with the centre of mirror M2. The direction of the reflected beam from M2 was adjusted until it travelled down the mid-plane of the optical table and so that its height at B2 was the same as that of the original reference beam. Lens L2 was then placed after the focus of mirror M2, such that the beam was approximately parallel, its height being adjusted until the beam was undeflected from its position after the beam splitter when no lens was present.

The lens L3 could then be inserted after the second beam splitter and moved until the working section became in focus at a screen. The system was now ready for fine adjustment and although this coarse set up was tedious and lengthy, once it had been done the system needed no further coarse adjustment during the tests, a period of several months.

5.2.3 Components

The configuration of the optical components in the optical system is shown in Figure 5.4. The components were held in carriers whose dovetail fittings with the optical benches eased alignment of the components and allowed the carriers to be accurately positioned longitudinally along the tables. Four high stability optical benches were used, two 4 ft in length joined longitudinally to form the central "body" and two 8 ft benches which held the mirrors. These benches, which were rigidly connected together, were supported by four pairs of anti-vibration feet which had screw adjustments so that the height of the benches could be altered.

The laser light source was an Oriel Helium-Neon Research Laser (wavelength of 6328 Å) with a rated minimum output power of 2.0 mW. The laser operated in the TEM_{00} mode, the Gausian beam being 0.8 mm in diameter and having a divergence of 1.2 mr. An Ealing spatial filter which screwed onto the front of the laser consisted of a 4 mm focal length lens which focused the beam onto a 5 micron diameter pin hole. The beam was then collimated by a lens resulting in an output beam of 9.6 mm in diameter. The pin hole could be moved laterally across the beam and the focusing lens rotated about axis perpendicular to the beam to ensure the correct alignment of all the components. The laser and spatial filter were held in a Vee-block and could be tilted, using padding, to ensure the beam travelled in the desired direction.

The Schlieren light source was an Oriel pulsed Xenon light source emitting light at a band of wavelengths from 200 to 900 nm. The power output and the pulse frequency could be varied from 1 to 100 Hz on a low energy pulse of 0.125 μJ, from 1 to 80 Hz on an 1.25 μJ pulse and from 1 to 9 Hz on a 12.5 μJ pulse. An ultra violet grade fused silica condensing lens was placed next to the source and the resulting virtual image of the spark was placed at the focus of mirror M1. The light source could be mounted so that the spark was either parallel or vertical to the top of the bench in a plane perpendicular to the length of the bench. Whilst this source was on order a conventional light source which consisted of a single helical filament supplied by a 12 volt car battery, a focusing lens and a rectangular slit was used. The lens focused an image of the filament onto the rectangular slit which was then placed at the focus of mirror M1. The knife edge of the Schlieren system consisted of a razor blade that could be freely moved and locked in a holder mounted on a standard carrier.

The beam splitters were an inch in diameter and made from fused silicon and had a front coating that gave a 50% reflectivity and 50% transmission when the plane of polarization of the input beam was at 45° to both the z and y axis (Figure 5.4). The other surface was coated with an anti-reflection coating to prevent higher order reflections. The two lenses L1 and L2, were also an inch in diameter and had a focal length of 100 mm.

The two mirrors M1 and M2, were 4" diameter off-axis paraboloid mirrors, made from a 9" diameter on-axis parabola and designed to deflect the beam 2.7°. They had a surface coating of Aluminium oxide, the front surface reflection eliminating extra reflections, and were supported in holders that allowed rotations about the x and y axis. Their long focal length of 1334 mm ensured the beam was clear of the lens holder of L1 and the focal length to diameter ratio of 12 minimised any aberrations (Holder and North (1956)).

The two windows in the working section were also 4" diameter and 1" thick, their surfaces being parallel to 1/20th wavelength of the laser light. These were also coated with an anti-reflection coating.

The focusing lens L3 was 1" diameter and of 80 mm focal length. This focused the image onto a screen, made from tracing paper, or onto the Canon AE1 camera which was fitted with bellows to magnify the image to any desired size.

The total cost of the system was £6500 at 1982 prices. The major expenses were the laser and spatial filter (£1000), Xenon source (£1300), the working section windows (£1000) and the optical benches and the holders for the optical components (£2600). The cost of increasing the diameter of

the measuring beam is dependent only on the increased cost of the working section windows, the parabolic mirrors being cheap in comparison.

5.3 OPTICAL SYSTEM CONVERSION AND ADJUSTMENT

5.3.1 Interferometry

After the system had been set up as in section 5.2.2, it was ready for fine adjustments for interferometry. Control over the fringe pattern was by three adjustments, the number of horizontal or vertical fringes being controlled by rotations of mirror M2 and their curvature by movement of lens L2 along the optical bench (Figure 5.4). The no-flow interference fringes appeared as straight lines only if the focus of lens L2 coincided exactly with the focus of mirror M2, concentric rings appearing if they did not coincide. Once this lens had been accurately placed, the number and direction of the final fringes was controlled by the fine rotations of mirror M2 about the x and y axis (Figure 5.4).

The position of the holder of lens L1 was carefully marked, this being the only component disturbed on conversion to a Schlieren system. To convert the system back to an interferometer this lens was simply placed back in position, the conversion being done several times throughout the series of tests without any loss of quality in the final picture.

5.3.2 Schlieren

To convert the interferometer to use for Schlieren techniques, the lens L1 was replaced by the spark light source and a knife edge was inserted at the focus of mirror M2 (Figure 5.4). The spark source consisted of the lamp and a collimating lens which was placed as close as possible to the spark in order to focus as much of the power of the source as possible. This resulted in a virtual image which, when placed at the

focal point of mirror M1 produced a parallel beam through the working section. The position of the spark source along the optical bench, and its height above it were correct when the reflected parallel beam from mirror M1 exactly filled mirror M2. The spark source could be mounted such that the spark was horizontal or vertical, the knife edge being horizontal or vertical respectively. The knife edge itself consisted of a razor blade mounted in a holder, the entire assembly being moved away from the mirror M2 until the focal point was reached. The position of the razor blade in the holder was then adjusted so as to cut off approximately half the image of the light source.

The setting up process was carried out when the spark source was set to a rapid low intensity spark which gave a continuous image of the working section. After setting up, reflections from the Coanda surface were sometimes observed which was an indication that either the light was not exactly parallel through the working section or that the light beam was not exactly perpendicular to the plane of the working section. The setting up process was therefore repeated until these reflections were absent and the intensity of the light source and its frequency then changed for the particular experiment (Section 7.2 and 7.3).

5.3.3 Shadowgraph

Shadowgraph pictures could be made from either light source, the change from the interferometer being to block out the reference beam using a piece of card and to defocus the final picture by moving lens L3. The change from the Schlieren system was to remove the knife edge and defocus the system. The sensitivity of the system depended on the amount that the final picture was made out of focus. This was restricted when the laser source was used because the coherence of the light meant that it was

severely diffracted at the Coanda surface and at shock waves causing a series of diffraction lines at the final picture which made the position of the surface or shock wave difficult to place accurately. This was not a problem when the incoherent, multi-frequency spark source was used and the system could be made out of focus until the solid surfaces became slightly blurred.

5.4 PERFORMANCE OF THE OPTICAL SYSTEM

The development of an optical system combining shadowgraph, Schlieren and interferometric techniques is described in Section 5.2 and experiments employing this system in Chapter 7. Three light sources were employed, a laser, a spark source and a continuous source. The latter source was used as a temporary source while the spark source was on order.

The shadowgraph photographs were taken employing either the continuous light source or the laser. Those obtained employing the laser showed severe diffraction not only at solid surfaces but also at shocks and thus the laser source is not recommended for shadowgraphy. The continuous light source produced photographs of a good quality and it is expected similar photographs can be obtained by use of the spark source.

Schlieren photographs were taken employing either the continuous light source or the spark source. Continuous Schlieren photographs were obtained using either source, the latter being the superposition of several sparks, and spark photographs were obtained using a single pulse from the spark source. The photographs obtained were of a good quality.

Interferometric photographs were taken employing the laser source and were satisfactory at stagnation pressure ratios above 0.55. However the extensive vibration that made the interferograms impossible to view by eye

prevented interferograms being obtained at lower stagnation pressure ratios. Three reasons for these vibrations were examined: firstly recirculation of the air exiting from the rig, secondly vibration caused by noise emissions from the rig and thirdly vibrations either of the rig itself or transmitted through the floor into the optical system.

Wooden covers were designed to enclose the beam paths of the optical system to reduce any effect caused by recirculating air. However this resulted in no improvement in the stability of the final picture. Thus it is thought unlikely that the recirculation is the cause of the problem. Similarly the vibration is unlikely to be caused by sound vibration, even though sound levels of up to 140 dB were recorded near the nozzle. The sound intensity is proportional to the square of the pressure amplitude (Whelan and Hodgson, (1977)), and is proportional to the inverse square of the distance from an isolated noise source. The density changes caused by the pressure changes are insufficient to produce a detectable fringe shift.

The third possible cause examined was vibration either of the mechanical rig or the optical rig. Two series of tests were devised to try to trace the source of any vibrations. In the first series the mechanical rig was unbolted from the floor and allowed to stand free. Interferograms were then taken over a range of stagnation pressure ratios. In the second series of tests, the mechanical rig was moved away from the paths of the laser beams and allowed to stand free. Interferograms were again taken over a range of stagnation pressure ratios. The results show that clear fringes in the still air can be distinguished down to stagnation pressure ratios of 0.25. Fringes can also be distinguished within some regions of the jet itself. However at a stagnation pressure ratio of 0.25 the diffraction of the light at the Coanda is very noticeable. These results

suggest that the cause of the original vibrations are vibrations from the mechanical rig that are transmitted by the feet of the rig through the floor and into the optical rig. These results also show that recirculation of the air from the mechanical rig is not a problem.

Thus further work on the prevention of the transmission of vibration from the mechanical rig to the optical rig is required. This can either be done by altering the supports of the mechanical rig or by altering the support system of the optical system. The former should be designed to prevent vibrations being transmitted into the floor and the latter to prevent vibrations being transmitted from the floor into the optical system. There is some doubt that the anti-vibration feet, that sit on rubber pads and support the optical system at present, perform up to the manufacturer's specification. Apart from this problem, the optical system performed well and required very little adjustment after the initial set up procedure.

CHAPTER 6

MECHANICAL EXPERIMENTS AND RESULTS

6.1 TOTAL PRESSURE TRAVERSES

6.1.1 Experimental Method

Several traverses were made across the jet to check the two-dimensionality of the flow as it flowed round the Coanda surface. The traverses were made with a total pressure tube that consisted of a long aluminium tube, whose external diameter was 4 mm, which decreased to a 0.8 mm external diameter hyperdermic tip. This probe was mounted on traversing gear set away from the rig. The angle of the probe could be adjusted such that it lay tangentially to the Coanda surface and the tip then moved until it lay on the surface. Movement of the probe was then possible in the plane normal to this tangent. The stagnation pressures were measured by a mercury manometer.

Tests were conducted at angles of 0^0, 20^0 and 40^0 round the Coanda surface, traverses across the jet being carried out at several distances from the Coanda surface at each stagnation pressure ratio. Slot widths of 2 mm and 4 mm were tested. At low stagnation pressure ratios the force of the jet on the end of the probe caused severe deflections as the probe was moved into the jet. This prevented readings being taken near the surface at low stagnation pressure ratios.

6.1.2 Results

All the traverses across the slot exit showed that the stagnation pressure was constant over the whole slot area. The influence of the side wall on the main jet is shown in Figures 6.1 and 6.2, which show respectively traverses at 20^0 and 40^0 round the Coanda surface of flow from a 4 mm slot at a stagnation pressure ratio of 0.662. The distance of

the centre-line of the probe from the Coanda surface is marked for each traverse and as the total pressure traverses were virtually symmetrical about the centre-line of the slot breadth, only half the slot breadth is plotted. At 20^0 (Figure 6.1), the flow near the surface is virtually unaffected by the side wall, though near the edge of the jet 40% of the breadth showed a variation of total pressure. At 40^0 (Figure 6.2), 10% of the breadth has been affected near the Coanda surface and the variations in total pressure of the flow near the wall and further from the Coanda surface have increased. Only 40% of the breadth is affected by the variations.

The effect of decreasing the stagnation pressure ratio on a traverse 6.4 mm from the surface at an angle of 40^0 round the surface is shown in Figure 6.3. At the two higher stagnation pressure ratios the traverse is near the edge of the jet, and approximately 40% of the breadth is affected by the side wall. At the lowest stagnation pressure ratio the jet grows more quickly due to the greater initial turning angle of the flow at the nozzle and the traverse is inside the jet. The effect of the side wall influences up to 50% of the breadth of the jet.

The result of decreasing the slot width on the effect of the side wall can be seen in a comparison of Figures 6.2 and 6.4. The encroachment of the effect of the side wall has been reduced from 40% to approximately 25% of the slot breadth by the halving of the slot width.

6.2 FLOW VISUALIZATION

6.2.1 Experimental Method

A surface oil flow technique was used to visualize the flow on the Coanda surface and on the side walls to check the two dimensionality of the

flow and for any separation bubbles on the Coanda surface. The side windows were covered with adhesive cellophane to protect the perspex and frames, but it proved impossible to protect the surface pressure tappings on the Coanda surface in the same way because the cellophane lifted off as soon as the flow control valve was opened. A discussion of the oil surface flow visualization technique is given by Maltby (1962). In the present work a silicone fluid, MS 200/1000 cs, was mixed in a ratio of 3:1 by weight with a pink "Dayglo" pigment and painted directly onto the Coanda surface and onto the cellophane on the window frames. This mixture allowed the oil pattern to develop, set and leave a clear picture at all slot widths and stagnation pressure ratios tested.

Initial observations revealed bands of fluid accumulating on the curved portion of the Coanda surface and regions of reverse flow between them. These bands collapsed as the rig was shut down which obliterated the pattern. Thus observations or photographs of the curved section of the Coanda surface had to be made while the rig was running. The pattern on the flat of the Coanda surface and on the side walls were unaffected by shut down. Two series of experiments were devised:-

Build 1: Written Observations

A record was made of the position of the bands and the direction of flows on the Coanda surface. Three slot widths of 2, 4 and 8 mm were tested at nominally the same stagnation pressure ratios as those of the surface pressure measurement tests (Section 6.5). The surface was painted and the rig was quickly set at the desired pressure ratio. Once the pattern had set, the position of the bands were recorded in relation to the surface pressure tappings, whose angle round the surface was known. At low stagnation pressure ratios regions of reverse flow between bands were

clearly visible, because oil was being continuously 'flicked' from one band to the next one downstream and then running back along the surface to the original band.

Build 2: Photographic Record

Three representative stagnation pressure ratios, the lowest being near breakaway (Section 6.4), were photographed at each slot width of 2, 4 and 8 mm. Four views were taken at each stagnation pressure ratio:-

a) Curved section of the Coanda surface,

b) Corner of Coanda flat with the side wall,

c) Flat section of the Coanda surface, and

d) Side wall.

The oil was painted on, the rig set to the desired pressure and the first view taken as soon as the pattern had set. The rig was then shut down, one window frame removed and the second view taken. The second frame was then removed and the third and fourth views taken, the camera being normal to the surface being photographed. The oil was illuminated with an ultra-violet lamp to enhance the pattern, the lamp being held as close as possible to the surface being photographed. A range of shutter speeds was used for each view and the best negative selected for printing. A Canon AE1 camera with a standard 50 mm lens was used to take the photographs together with a black and white film whose speed was 125 ASA.

6.2.2 Results of Build 1

The angles round the Coanda surface at which beads of oil accumulated are plotted against the stagnation pressure ratio in Figures 6.5, 6.6 and 6.7 for the three slot widths of 2, 4 and 8 mm respectively. The accuracy of the measured angles is estimated to be 1^0 at surface angles of less than 40^0 (where the static pressure tappings were at 5^0 intervals) and to be 2^0

at surface angles greater than 40^0 (where they were at 10^0 intervals). Occasionally a very faint band appeared, these positions being marked by a cross. Except at stagnation pressure ratios near unity reverse flow on the surface was detected between the second and first bands. However it was never detected between other bands.

Five bands were detected at stagnation pressure ratios near unity at the 2 mm slot width. As the pressure ratio was reduced, the leading edge of the first band moved slightly further downstream and the band increased in width. All the other bands moved appreciably downstream and disappeared once they reached an angle of approximately 70^0 round the Coanda surface. As the breakaway stagnation pressure ratio was approached only the first and second bands remained, the leading edge of the first band settling at about 10^0 round the surface. A similar progression of the bands occurred at the 4 mm slot width (Figure 6.6). A maximum of three bands were clearly visible, the angle at which these bands appeared being greater than the 2 mm slot due to the increased width of the jet. A slight difference occurred at the 8 mm slot width, where the first band moved upstream as the separation stagnation pressure ratio was approached. A maximum of two bands were visible at this slot width.

6.2.3 Results of Build 2

The photographs taken all show similar features, four representative ones being shown in Plates 4 to 7. Plates 4, 6 and 7 show the flow from a nominally 4 mm slot at a stagnation pressure ratio of 0.333 over the curved section of the Coanda, at the intersection of the Coanda with the side wall and along the side wall respectively. Plate 5 shows flow over the curved section of the Coanda from an 8 mm slot at a stagnation pressure ratio of 0.667.

The flow in Plate 4 emerges from the slot at the bottom of the photograph and flows up the picture. Three bands are visible, the first main one, together with smaller ones just below and above the 'glare'. An additional line, which can be seen above the third, is situated at the start of the flat part of the Coanda. Six accumulations of oil can be seen in the first band, one situated at each corner and one centred along the lines of surface pressure tappings. Small trailing vortices were visible behind each tapping which resulted in the accumulation of oil in a separated region along the lines of tappings. It is not thought that these vortices affected the main flow. These accumulations of oil continually lost oil which was then deposited by the main jet onto the second band. The oil then flowed along the surface rapidly back to the trailing edge of the first band.

The first two bands stretch uniformily across the surface suggesting the flow, at least at the surface, is two-dimensional. However by the third band a vortex from either side has encroached into the surface flow. This vortex is possibly initiated from the first band and others are initiated at the third band and at the start of the flat of the Coanda. This first vortex is however still present in Plate 5, where the stagnation pressure ratio was not low enough to cause any separation. A second vortex can be seen initiated at the start of the flat.

The growth of these vortices round the Coanda and their interaction with side wall can be seen in Plates 6 and 7. At the Coanda surface the vortices, which sweep flow away from the side wall, grow rapidly until the flat of the Coanda is reached where the growth is reduced. The size of these vortices and their encroachment onto the Coanda surface increases with an increase in the slot width. Only the middle third of the jet from

an 8 mm slot width is unaffected at the start of the flat (Plate 5). The inner part of the jet on the side wall is swept down onto the surface by those vortices, while the outer part is swept away as it loses momentum in the mixing layer. The outer edge of the jet is sharply defined, the oil outside the jet being undisturbed.

6.3 DISCHARGE COEFFICIENT

6.3.1 Experimental Method

Before the mass flow rates through the slot could be measured the leakage rates of both the inlet line and the settling tube had to be determined. This required two series of experiments because, at a set slot stagnation pressure ratio, the two sections were at different static pressures due to the pressure drop across the flow control valve. The two series were:-

Build 1:- Inlet line

Build 2:- Settling tube

The flow control valve (Figure 5.1) was kept closed for the experiments of Build 1 and open for Build 2, the Coanda surface being forced down onto a sheet of rubber placed on the nozzle to prevent flow through the slot.

In each experiment the line was pressurised to the test pressure and the drop valve on the ring main closed. The time taken for a small pressure drop of the line was measured on a stop watch, the pressure being monitored at the orifice plate using the 35 bar differential pressure transducer. The temperature of the air in the line was measured at the orifice plate. A range of initial static pressures were tested in each Build, the highest pressure in Build 1 being 10 bar gauge which was the design limit of the inlet line. The highest pressure of Build 2 was

limited to 3 bar gauge for two reasons: firstly the time taken for a small pressure drop became small and secondly leaks round the rubber blocking the slot occurred and the pad itself was blown out. The volume of the inlet line and the settling tube were also estimated from an approximate measurement.

Mass flow rate measurements through slot configuration A (Figure 5.3) were taken over a range of stagnation pressure ratios down to breakaway. Three nominal slot widths of 2, 4 and 8 mm were tested. The static pressure upstream of the orifice plate and the pressure drop across it were measured by pressure transducers and the temperature of the air flowing through the orifice was also recorded. A 26.5 mm diameter orifice plate was used (orifice diameter to pipe diameter ratio of 0.52) and the pressure of the inlet line controlled by the regulator to ensure the maximum pressure drop across the plate for a set mass flow rate.

6.3.2 Leakage Results

The leakage rate was calculated from the calculated air density in the pipe before and after a test, the volume of the pipe and the time taken for the mass loss. This leakage rate was plotted against the median pressure of the test. The results of the Build 1 tests showed that the maximum mass loss rate of the inlet line was less than 0.1 g/s. This leak, that occurred at the join between the inlet line and the reinforced rubber tube, represented less than 0.1% of the measured mass flow rate through the 2 mm slot width and so was ignored.

The results of the Build 2 tests are shown in Figure 6.8, the line extrapolated to a gauge pressure of 4 bar on the assumption that the increase in leakage rate follows the same trend. This extrapolation is required to obtained estimates of the leakage rates for low stagnation

pressure ratio measurements of the 2 mm slot width. The leaks occurred mainly at the corner where the window frame, back plate and settling tube join. The rate of increase of leakage flow rate with stagnation pressure in the tube is faster than a directly proportional relationship, which is an indication that the area through which the leaks occur also increases with the stagnation pressure.

The errors in the measurement of the mass leakage rates are difficult to assess but increase as the stagnation pressure is increased. However the leaks represent approximately 1% of the flow rate measured through the smallest slot width of 2 mm. Thus an error of 10% in the leakage measurement would represent an error of 0.1% in the mass flow through a 2 mm slot. This error decreases as the slot width is increased if it is assumed the leakage flow depends only on the stagnation pressure inside the settling tube.

6.3.3 Discharge Coefficient Results

The actual mass flow rate through the nozzle at a set slot width and settling tube static pressure was calculated according to BS1042. The British Standard also lays down a procedure for determining the uncertainty of the flow rate, the two main contributions to the uncertainty of the present flow rates being an error in the measurement of the pressure drop across the orifice plate and an error in the measurement of the pipe diameter. The pressure difference across the orifice plate fluctuated rapidly about a mean by up to 1.0% and the internal diameter of the inlet pipe, although nominally 2 inches, was 51.4 ± 0.3 mm. The total error in the measured mass flow was calculated to be 0.8%.

The known mass flow rate can be used to provide a Mach number correction to convert the static pressure in the settling tube into the stagnation pressure. The variation of Mach number in the settling tube with stagnation pressure ratio is plotted in Figure 6.9. The Mach number increases with a decrease in stagnation pressure ratio up to a limiting value which signifies that the slot has become choked. The Mach number at a set stagnation pressure ratio increases with an increase in the slot width due to the decreased area ratio.

There are two errors in the readings taken for the theoretical calculation of the ideal mass flow rate, namely in the measurement of the slot width and of the settling tube static pressure. The errors in the measurement of the slot width were determined using slip gauges and are estimated to vary from 0.5% for a 2 mm slot width to 0.1% for an 8 mm slot width. The error in the measurement of the static pressure in the settling tube was 0.2% at one bar gauge and decreased as the pressure was raised. The theoretical mass flow rate was calculated from equation 2.24 at stagnation pressure ratios of greater than 0.528 and from equation 2.25 for those less than 0.528. The uncertainty in the discharge coefficient thus varies from a maximum of 1.6% for a 2 mm slot and from 1.1% for an 8 mm slot.

The variation of the discharge coefficient for the three tested slot widths is plotted in Figure 6.10. At a set stagnation pressure ratio the coefficient increases with a decrease in slot width, the slot approaching a one-dimensional nozzle. The coefficient increases as the stagnation pressure is reduced. However the coefficient becomes greater than unity at stagnation pressure ratios of less than 0.26 when the slot width is 2 mm, and reaches a maximum of 1.018 which lies outside the estimated error

range. There are two possible explanations for these high readings, firstly that the slot becomes distorted at the high settling tube stagnation pressures, thereby increasing the area of the slot, and secondly that the estimation of the leakage rate at the high pressures was inaccurate, the limit of the leakage measurements being at a stagnation pressure ratio of 0.28.

6.4 JET BREAKAWAY AND REATTACHMENT

6.4.1 Experimental Method

The breakaway stagnation pressure ratio was defined as the ratio at which the jet 'flipped' from the Coanda surface to a horizontal quasi-free jet. The breakaway occurred at a definite ratio as the stagnation pressure in the settling tube was increased. As the stagnation pressure was reduced after breakaway, the jet was progressively deflected towards the Coanda surface. This deflection did not result in a deflection from the horizontal of more than ten degrees before the jet 'flipped' back onto the Coanda surface. The stagnation pressure ratio at which this occurred was defined as the reattachment stagnation pressure ratio.

The static pressures in the settling tube at which breakaway and reattachment occurred were recorded over a range of slot widths for both nozzle configurations (Figure 5.3). The slot width ranged from the maximum possible to the minimum width that breakaway could be achieved. At a set nozzle configuration the flow control value was slowly opened until breakaway was achieved and then slowly but smoothly closed until reattachment occurred. The static pressures were measured on a Budenberg pressure gauge. Up to eight readings were taken at each slot width and an average for the breakaway and reattachment calculated. These were then corrected to include the effect of the air velocity at the static pressure

tapping in the settling tube (Figure 6.9). Occasionally the reattachment pressure was noticeably different from similar tests and if this occurred the result was not included in the averaging process.

6.4.2 Results

The stagnation pressure ratios at which jet breakaway and reattachment occurred are plotted against the variation of slot width in Figure 6.11 for nozzle configuration A (no flat) and in Figure 6.12 for configuration B (a flat before the constant radius curvature). The jet was always attached to the Coanda at all pressure ratios down to breakaway. As the slot width was reduced the pressure ratios at which breakaway and reattachment occurred decreased, although the hysteresis between the two increased. The scatter of the points that contribute to the average points plotted was ± 0.5% for the breakaway and ± 2% for the reattachment.

A discontinuity in the breakaway stagnation pressure ratio was noticed at a slot width/downstream radius (b/a) ratio of 0.14 in Figure 6.11 and a second series of tests were carried out. These are also plotted in Figure 6.11 and outside the range $0.12 < b/a < 0.15$ the breakaway occurred at the same stagnation pressure ratios. However within this range the plotted points differ by up to 7%, even though each point represents an average of points whose scatter was less than ± 0.5%. A variation of up to 8% in the reattachment stagnation pressure ratio was also noticed at small slot widths. Neither effect occurred during the re-tests of the ratios for nozzle B.

6.5 SURFACE STATIC PRESSURES

6.5.1 Experimental Method

Three series of tests were conducted at various slot widths over different stagnation pressure ratio ranges. The slot width was set for each test and the static pressure tappings connected to a mercury or water multimanometer, whose angle could be varied depending on the range of pressures required. The stagnation pressure ratio was then set and the surface pressures relative to atmospheric pressure recorded, the stagnation pressure ratio being continually monitored to ensure there was no drift. In all the tests nozzle configuration A was used (Figure 5.3). The three series of the tests are described below:-

a) Build 1 - Low Speed Flow

Tests were carried out over several stagnation pressure ratios near unity at nominal slot widths of 1, 1.5, 2, 4, 6 and 8 mm. The majority of the tests were at stagnation pressure ratios higher than 0.95, where the flow was effectively incompressible, although pressure ratios down to 0.83 were also tested. The tappings were connected to the water multimanometer which was inclined at an angle of 30^0. The settling tube static tapping was either connected to the same multimanometer or to the mercury multimanometer, depending on the settling tube stagnation pressure.

b) Build 2 - Compressible Flow

Tests were carried out at nominally the same stagnation pressure ratios as the interferometric experiments (Section 7.4) at nominal slot widths of 2, 4 and 8 mm. The tappings were connected to the mercury multimanometer which was inclined at 30^0 and the settling tube static pressure was measured on a Budenberg gauge.

c) Build 3 - Choked Flow

Tests were carried out over several stagnation pressure ratios down to breakaway at slot widths of 2, 4, 6 and 8 mm. The pressure tappings were connected to the mercury multimanometer, either placed vertically or at 30^0 depending upon the pressure range required, and the upstream static pressure was measured on a Budenberg gauge. The settling tube static pressure was raised in steps of 0.5 bar for the 4 and 6 mm slot widths. The static pressure was found to drop rapidly initially, but then recover as the jet flowed round the Coanda and so the test stagnation pressure ratios for the 2 and 8 mm slots were chosen such that the peak of this recovery coincided with a pressure tapping on the surface. An additional series of tests were carried out at a 2 mm slot width using nozzle B (Figure 5.3).

6.5.2 Results of Build 1

The results of the low speed, mainly incompressible flow tests are plotted in Figures 6.13 to 6.18, the graphs progressively showing the effect of increasing the slot width. The surface pressures are plotted as the non-dimensional parameter $(p_s-p_a)/(p_o-p_a)$ for various stagnation pressure ratios against the angle round the Coanda surface.

The uncertainties of the results varied both with the slot width and the stagnation pressure ratio. The pressure difference between atmospheric pressure and either the surface static or the upstream static pressure could be measured to the nearest millimetre. Thus the reading errors in (p_s-p_a) for the 1 mm slot width, varied from 11% at $p_a/p_o = 0.990$, through 4% at $p_a/p_o = 0.971$ to less than 1% at $p_a/p_o = 0.907$. The reading error of the upstream static pressure was less than 1% and so the total error of $(p_s-p_a)/(p_o-p_a)$ varied from 12% to less than 1% as the stagnation pressure

was increased. The errors reduced at a set stagnation pressure ratio as the slot width was increased because the surface static pressures decreased. The error at the maximum stagnation pressure ratio of 0.990 in the non-dimensional parameter was estimated to be 9% at a slot width of 1.5 mm, 6% at 2 mm and 3% at a 4 mm slot width. All these errors were reduced in a similar manner to those of the 1 mm slot width as the stagnation pressure ratio was reduced.

The graphs in Figure 6.15 to 6.18 all follow a similar trend. The surface pressure decreases to a minimum about two slot widths downstream of the slot. It then either remains constant or rises slightly until the jet approaches the flat part of the Coanda surface, where the pressure rises rapidly. A line can be drawn through the mean points of each graph and, although the absolute scatter of the pressures from this line increases as the slot width increases, the percentage scatter of the points is ± 3% in all the graphs until the influence of the flat part of the Coanda becomes apparent. A similar trend can be seen in Figures 6.13 and 6.14, although the initial scatter is greatly increased and even in the central section of 40^0 to 70^0 the scatter has increased to ± 8%. The results at the highest stagnation pressure ratio of 0.990 show a marked deviation from the others and were not included in the above scatter. A retest at this stagnation pressure ratio is shown in Figure 6.14, displaced slightly for clarity. This shows a marked deviation from the original test which was not apparent in similar retests at other stagnation pressure ratios. A possible reason for these variations is that the flow rate was difficult to control at the stagnation pressure ratios near unity.

6.5.3 Results of Build 2

The results of the compressible flow tests are plotted in Figures 6.19 to 6.21. The surface static pressures could be read to the nearest millimetre and the upstream static pressure to the nearest 0.05 bar. These resulted in reading errors of 3.5% at the low stagnation pressures at the 2 mm slot width reducing to 2.5% at the 8 mm slot width. These reduced to 1.5% at a 2 mm slot width and to 0.5% at a 8 mm slot width as the stagnation pressure was increased.

A decrease in the stagnation pressure ratio resulted in a reduction of the surface pressure coefficient over the first 10^0 of the surface, when a 2 mm slot width was tested (Figure 6.19). This was followed by a surface pressure coefficient rise at angles further round the Coanda as the stagnation pressure ratio was decreased. This rise was observed until an angle of 60^0. At all the stagnation pressure ratios tested the surface pressure exhibited a wave-like variation for the first 40^0, before settling to a constant value.

A similar wave-like variation near the nozzle can also be seen in the static pressure coefficient profiles from the 4 mm slot (Figure 6.20). The coefficient then becomes almost constant as the stagnation pressure ratio is reduced, though an increase can be seen at a ratio of 0.492. The wave-like variation near the nozzle is less noticeable at the 8 mm slot (Figure 8.21) until the stagnation pressure ratio has been reduced to 0.536.

6.5.4 Results of Build 3

The results of the choked flow tests are shown in Figures 6.22 to 6.26, where the actual surface pressure is plotted against the angle round the Coanda surface for several stagnation pressure ratios. The pressures

have been joined by lines, although these lines are only approximations of the pressure because it is not known where a tapping lies relative to a peak or trough of the static pressure. The errors in the measurement of the surface pressures are ± 0.002 bar.

The surface pressure distributions from a nominally 4 mm slot at six stagnation pressure ratios are shown in Figure 6.22. As the stagnation pressure ratio was reduced the first minimum of the surface static pressure decreased and moved further round the surface and there was a rise in the absolute static pressure after the first recovery. The shock cell structure could also be seen more clearly downstream, the cells increasing in length and in their pressure ranges. However, as the stagnation pressure ratio was further reduced (Figure 6.22b), the static pressure remained constant for an increasing angle at its first minimum. Also the first peak in pressure began to decrease in amplitude, although it still moved further downstream. At a stagnation pressure ratio just above that which caused breakaway of the jet, the constant pressure region after the initial expansion extended from approximately 15^0 to 45^0 round the surface and the peak of the first pressure recovery occurred at 80^0.

A similar process preceded the breakaway of jets from 2, 6 and 8 mm slots (Figures 6.23, 6.24 and 6.25 respectively). As the slot width was increased the length of the first shock cell increased and the pressure recovery at the end was smaller. A notable feature in all cases was that at a stagnation pressure ratio just higher than that required to breakaway the jet, the position of the first peak in the surface pressure after the constant pressure region was at approximately 80^0. Also, although the angle of the start of the constant pressure region increased with slot width, the start of the first pressure rise was at approximately 45^0.

The surface pressure distributions from a 2 mm slot of nozzle B is shown in Figure 6.26. At a stagnation pressure ratio close to breakaway the peak of the first pressure recovery was also at an angle of 80^0 and the end of the constant pressure region after the initial expansion at approximately 50^0. There seemed to be no major differences between the two nozzles in the pressure distributions from a 2 mm slot.

CHAPTER 7

OPTICAL EXPERIMENTS AND RESULTS

7.1 SHADOWGRAPH

7.1.1 Experimental Method

The optical apparatus was set up for the shadowgraph technique as described in Section 5.3.3. Shadowgraphs were taken using both a laser and the conventional light bulb source. During tests made with the former, lens L1 (Figure 5.4) remained in place and the reference beam was blocked by a piece of card. For the light bulb source, lens L1 was removed and the source assembly placed such that the focus of the bulb's filament was at the focus of mirror M1. The position of lens L3 and the length of the bellows extension were altered until the image at the photographic plate was in focus and of the required magnification. The focusing of the rig was achieved by setting the mechanical rig at a given stagnation pressure ratio and moving the lens L3 along the optical bench until the shadowgraph produced gave the weakest image that could be seen.

A series of shadowgraphs were taken over a range of stagnation pressure ratios at three slot widths, 2 mm, 4 mm and 8 mm. In each test, lens L3 was moved sufficiently to obtain a visible shadowgraph. A 125 ASA black and white film, together with a shutter speed of 1/500th second, was used throughout these tests.

7.1.2 Results

Severe diffraction at shocks and the Coanda surface, similar to that shown in Plate 3, occurred when the laser light source was used and thus the results presented here were obtained using the conventional light bulb source. Plates 8 to 11 show shadowgraphs of the 4 mm slot at four

different stagnation pressure ratios, the lowest being just before breakaway. Plates 12 and 13 show representative shadowgraphs taken of the 8 mm and 2 mm slots respectively.

Plate 8 shows the jet from a 4 mm slot at a stagnation pressure ratio of 0.370. A line representing the edge of the jet can be clearly seen for the first half of the first shock cell. There are several disturbances in the flow as it approaches the nozzle exit, the majority emanating from the nozzle surface. These culminate in an oblique line at the nozzle lip that reaches the Coanda surface at 7^0. These disturbances indicate the acceleration round the nozzle is not smooth and that a weak oblique shock exists at the nozzle exit.

The reflections from the Coanda surface of some of the waves emanating from the nozzle lip can just be seen. Further round the Coanda surface at about 15^0 a weak line is just visible propagating into the flow. This indicates the presence of a very weak shock. A stronger line is visible emanating from a position about 27^0 round the Coanda surface. This propagates into the flow and near the edge of the jet is bent slightly. At this discontinuity another line propagates down onto the surface where its initial reflecton can be seen. Further round the surface at approximately 60^0 and 85^0 two slight disturbances can also be seen.

As the stagnation pressure ratio is reduced to 0.323 (Plate 9) the pattern is similar, but individual features move further round the Coanda surface. The line representing the initial jet edge indicates the maximum extent of the jet increases. The disturbances at the edge of the nozzle are similar to the higher stagnation pressure ratio, although the oblique shock emanating from the nozzle lip reaches the surface further round at approximately 8^0. Again occasional reflections from the Coanda surface of

disturbances at the nozzle lip can be seen. The weak shock emanating from the surface, only just visible in Plate 8, can clearly be seen and emanates from a position slightly further round the Coanda at about 17^0. A further line closely following the surface can also be seen starting from the same point on the Coanda as the weak shock. This is a line representing the separation of the jet from the Coanda surface, the separation being too small for this line to appear at the higher stagnation pressure ratio. A stronger oblique shock can be seen at about 35^0 round the surface. At this point the separation line is turned almost parallel to the surface and can be seen continuing beyond the shock. The oblique shock is again bent near the jet edge, a second shock starting at this point and reaching the surface at about 43^0. A reflection of the shock is just visible. An additional disturbance can just be seen at about 75^0 round the surface.

A further decrease in the stagnation pressure ratio to 0.267 is shown in Plate 10. The divergence from the surface of the line representing the initial jet edge has again increased and the disturbances upstream of the nozzle exit have increased. The angle at which the oblique shock from the nozzle lip reaches the surface has increased to about 14^0. However, the angle at which the weak shock at the beginning of the separated region emanates is similar to Plate 9. A slight disturbance can be seen at the intersection of this shock with the jet edge. The line representing the separated region has become stronger and moved further away from the surface. Initially it is almost tangent to the surface, but it is then bent back towards the surface. A faint line which can be traced back to the nozzle lip via reflections from the jet edge and the Coanda surface can just be seen at this point. At an angle of about 45^0 round the surface the separation line is again turned away from the surface and a shock is

propagated into the flow. The flow reattaches at a point about 67^0 from the nozzle lip.

Plate 11 shows the pattern of the flow at a stagnation pressure ratio of 0.241, which is just above breakaway. The jet width has again increased and the angle at which the oblique shock from the nozzle lip reaches the surface has increased to 17^0, although it cannot be seen extending right to the surface. The point at which separation occurs and the oblique shock with it have remained similar to the two previous higher stagnation pressure ratios. The separation line again leaves almost tangentially from the surface and is turned back towards the surface at a distance further away than shown in Plate 10. The line is again turned away from the surface at about 55^0, although the shock seen at this point in Plate 10 is not visible in Plate 11. It is hard to determine any features, including the reattachment angle, beyond this point.

Plate 12 shows the structure of the jet from an 8 mm slot at a stagnation pressure ratio just above breakaway. The structure is similar to that of the 4 mm slot with lines showing the jet edge and the oblique nozzle shock clearly visible. The separation point denoted by the oblique shock and the separation line can be seen extending through a large angle and has a similar shape to that of the 4 mm slot shadowgraph. Plate 13 shows the structure of the jet from a 2 mm slot at a stagnation pressure ratio just above breakaway. The rapid changes in this flow obscure some of the detail, but the structure is again similar to the previous slots. The outer edge of the jet can be seen further downstream extending beyond the first shock cell. The oblique shock from the nozzle is obscured, but a line possibly resulting from a diffraction of this shock can be seen just downstream of the nozzle. The oblique shock at the point of separation is

clearly visible and the shape of the separation line is similar to the larger slot widths. However the structure cannot be seen after about 60^0 round the surface and thus the reattachment point is not known from this photograph.

7.2 CONTINUOUS SCHLIEREN

7.2.1 Experimental Method

The optical system was converted to a Schlieren system as described in Section 5.3.2. The majority of the continuous Schlieren photographs were taken using the conventional light bulb source. The helical filament was focused onto the rectangular slit and the slit was then placed at the focus of mirror M1 (Figure 5.4). It could be placed such that the slit was either horizontal or vertical to the optical bench. The knife edge was carefully placed at the focus of mirror M2 and placed to cut off approximately half the light. The position of lens L3 and the length of the bellows extension were altered until the required image magnification was achieved at the photographic plate. To ensure the working section was focused onto the photographic plate the knife edge was removed and the mechanical rig set at a given stagnation pressure ratio. The resultant shadowgraph at the photographic plate was minimised by fine movement of lens L3. Lens L3 was then locked onto the optical bench and the knife edge replaced for the Schlieren tests.

A series of Schlieren photographs were taken over a range of stagnation pressure ratios at three slot widths, 2 mm, 4 mm and 8 mm. The photographs were taken on a 125 ASA film at a shutter speed of 1/60th second. When the spark source was used, the low power spark of 0.125 μJ and the maximum spark rate of 100 Hz were selected. A shutter speed of 1/2 second then gave the best results. At each stagnation pressure ratio four

photographs were taken; two with the knife edge vertical and two with the knife edge horizontal to the optical bench. The two photographs taken with the knife edge vertical were such that the knife edge cut off firstly from one side of the image of the slit and secondly from the other. A similar procedure was adopted for the horizontal cut off.

7.2.2 Results

Plates 14 to 19 show the jet from a 4 mm slot at five different stagnation pressure ratios, the last one showing the jet just after breakaway. Each plate consists of two photographs, photograph A being taken with a horizontal knife edge and thus showing vertical density gradients, and photograph B being taken with a vertical knife edge and thus showing horizontal density gradients. Each photograph has a pair, the same photograph taken with the knife edge cutting off the other side of the image of the slit. This has the effect of inverting the light intensity changes (i.e. white becomes black and visa versa). This is illustrated by Plates 15 and 16, and can be used firstly to help clarify certain features of a photograph and secondly to eliminate any shadowgraph effects. The features of the jets issuing from the 2 mm and 8 mm slots are analogous to those of the 4 mm slot and the photographs are not presented here.

Plate 14a shows the jet from a 4 mm slot at a stagnation pressure ratio of 0.370. The photograph shows vertical density gradients, a black region denoting an increase in density from top to bottom of the photograph, a white region denoting a decrease in density. Plate 14b shows the same jet taken with a vertical knife edge, a white region denoting a decrease in density from left to right of the photograph, a black region denoting an increase. The region upstream of the nozzle exit in Plate 14b

is white, showing the flow is accelerating towards the nozzle exit. However Plate 14a shows the conditions at the nozzle exit are not uniform, the black region near the nozzle lip denoting that the density initially increases towards the Coanda surface. The region on the Coanda surface at the exit of the nozzle is white, denoting a decrease in density near the Coanda. Thus the density must reach a maximum at approximately one third of the slot width from the Coanda surface.

The initial shear layer of the jet is clearly visible in Plate 14a, a black region showing the increase in density from the quiescent air to the core of the jet. (As the stagnation temperature of the jet is near atmospheric temperature, the static temperature is lower than atmospheric temperature which results in an increase in the density.) This layer thickens as the jet flows round the Coanda. The white region between the shear layer and the Coanda shows the density decreases towards the surface. Two dark lines can be seen in this white region, the first one originating at 15^0 and the second, thicker one, at 27^0 round the Coanda. These show the density increases across them and they are thus oblique shock waves. The second of these two shocks has a complicated reflection from the free surface, part of which consists of a second shock that is just visible at its intersection with the Coanda at 35^0.

The continuing expansion of the flow after it has passed through the slot is visible in Plate 14b. There are two faint black lines near the nozzle lip, showing the density increases. These are shocks resulting from a slight overexpansion of the flow at the nozzle lip. The jet starts to darken about 10^0 round the Coanda and is dark by 15^0, indicating a gradual change from the expansion at the nozzle to compression, a result of the reflected nozzle expansion waves from the free surface. A white band,

starting at the outer edge of the jet, can be seen near the end of this compression. The start of this expansion coincides with the arrival of the first oblique shock from the surface at the jet edge. The shock itself is obscured in the compression of the jet. The second of the oblique shocks from the surface can be seen crossing the expansion region resulting from the reflection of the first from the free surface.

As the jet flows further round the surface Plate 14a shows density changes along the jet axis and alternating regions of expansion and compression can be seen. Plate 14b shows density changes across the jet axis at large angles round the Coanda, a light band just visible at the outer edge of the jet indicating an increase of density into the jet. A dark band is visible at the Coanda surface showing a decrease in density from the centre of the jet to the Coanda surface.

Plate 15 shows the pictures obtained from horizontal and vertical knife edge of the jet at a stagnation pressure ratio of 0.323. The features are similar to those of the previous Plate discussed above. The non-uniformity of the flow at the nozzle exit is clearly visible in Plate 15a, and the jet can be seen to expand to a larger radius than the previous stagnation pressure ratio. The two oblique shocks, visible in Plate 15a, emanate from further round the surface at 17^0 and 35^0. The reflection of the latter shock before it reaches the jet edge can clearly be seen. At the higher stagnation pressure ratio this was only just visible because the shock was almost perpendicular to the knife edge, the density change thus becoming undetectable. A further feature of Plate 15a is the dark line almost tangent to the surface between the two oblique shocks emanating from the surface. This line designates the edge of a separated zone and also appears as a black line when the knife edge is placed such as to cut off

the other side of the image of the light source (Plate 16a). This line is a shadowgraph effect denoting a rapid change of the second derivative of the density. A similar shadowgraph effect is visible at the jet edge near the nozzle of Plate 15b. The dark line that appears for about 20^0 also appears dark when the image of the light source is cut off from the opposite side, Plate 16b. The features of Plate 15b are similar to those at the higher stagnation pressure ratio with the addition of a light line at the surface of the Coanda during the first compression. This shows the separated region.

Plate 17 shows a further decrease in the stagnation pressure ratio to 0.267. Plate 17a shows a further increase in the maximum thickness of the jet after the nozzle exit and the non-uniform flow at the nozzle exit. The oblique shock emanating from the nozzle lip reaches the surface at the increased angle of 14^0 (Plate 17b). The dark region at the nozzle lip in this Plate also appears as a dark region when the knife edge is reversed and is a shadowgraph effect not a region of compression. The first oblique shock leaves the surface at about 17^0, an angle very similar to the previous stagnation pressure ratio. Its reflection from the free surface can clearly be seen in Plate 17b as the white line representing an expansion along the jet. The shadowgraph showing the separated region is clearly visible in Plate 17a, the separation region being larger than the previous stagnation pressure ratio. The region within the separation zone is of the same light intensity as the quiescent air outside the jet, indicating that no density changes take place within the region. The second of the two oblique shocks seen in the previous two plates no longer exists. However the first shock is reflected at the jet edge as an expansion which is in turn reflected from the edge of the separation zone

as a shock. At this intersection the flow at the edge of the separation is turned away from the surface. This shock in turn is again reflected from the jet edge as a further expansion region. The jet can be seen to reattach itself to the surface in Plate 17b at about 70^0 round the surface.

Plate 18 shows the jet at a stagnation pressure ratio of 0.241, a ratio just above breakaway. The features in the jet are similar to the previous Plate. The dark region at the nozzle lip in Plate 18b is again a shadowgraph effect. The point of separation is at a similar angle to the previous stagnation pressure ratio, although the jet moves further away from the surface before it is turned back. Plate 18b clearly shows that the flow is again turned away from the surface at about 55^0 round the Coanda, the point at which the region of expansion arrives at the edge of the separation. The point at which the jet fully reattaches to the surface is hard to determine, but is about 80^0 round the Coanda.

Plate 19 shows the jet at the breakaway stagnation pressure ratio. The jet leaves the Coanda surface at approximately 10^0 and continues as a free jet. Plate 19b shows the jet has become a classical free jet by the end of the first shock cell, with alternating regions of expansion and compression. Within the first shock cell the compression starts earlier at the Coanda, initiated by the shock wave turning the flow away from the surface. This wave is clearly visible in Plate 19a, the jet pattern again resembling that of a classical free jet after the first shock cell.

7.3 SPARK SCHLIEREN

7.3.1 Experimental Method

The optical system was converted to a Schlieren system as described in Section 5.3.2. The spark Schlieren source was set to a rapid low

intensity flash for the purposes of setting up the system. The required image at the camera was obtained and the image focused as in Section 7.2.1.

A series of spark Schlieren photographs were taken of the 2 mm, 4 mm and 8 mm slot widths. Photographs were taken with the knife edge horizontal and vertical. The spark source was set to give a flash rate of 2 Hz and the shutter speed set to 1/2 a second. The camera was manually triggered, the ratio of the shutter speed to the source spark rate ensuring a single spark was received by the film. A combination of the medium-range spark of 1.25 μJ, whose duration was 4 μ seconds, with a film speed of 125 ASA produced the best results. A range of stagnation pressure ratios down to separation were photographed at each slot width. In addition some photographs were taken of the separated jet as the stagnation pressure ratio was increased to the reattachment ratio.

7.3.2 Results

Plates 20 and 21 show a jet from a 4 mm slot at two different stagnation pressure ratios before breakaway. The main regions of expansion and compression are the same as those found in the continuous Schlieren photographs and for the presentation of these the reader is referred to Section 7.2.2. The growth of the turbulent shear layer is clearly visible in both plates. The initial expansion region at the nozzle exit is almost unaffected by the shear layer. However the shear layer starts encroaching into the potential core such that up to a third of the core has been lost by the angle at which the shock from the leading edge of the separation region reaches the outer edge of the jet. After this angle the potential core diminishes very rapidly and at a stagnation pressure ratio of 0.244 (Plate 21), it has almost disappeared by the angle that the expansion,

resulting from the reflection of the separation shock from the outer edge, reaches the inner surface.

At a stagnation pressure ratio near breakaway of a jet from a 2 mm slot, the potential core is similar to the 4 mm slot. The angle at which the separation shock reaches the surface is closer to the nozzle, but by this angle approximately one-third of the potential core has disappeared. The encroachment of the shear layer into the core of a jet from an 8 mm slot is very small, compared to the jet width, at the angle where the separation shock reaches the free surface. However the core quickly disappears after this angle, similar to the jets from 2 mm and 4 mm slots.

Plate 22 shows a jet from a 4 mm slot at the breakaway stagnation pressure ratio. The encroachment of the shear layer is minimal during the first shock cell, but then the potential core rapidly diminishes, the whole jet being turbulent by the end of the third shock cell. As the stagnation pressure ratio is increased from the breakaway ratio the jet becomes unstable before reattaching. This reattachment was usually sudden, but occasionally at the 4 mm slot a bistable jet occurred before reattachment. This jet could last for up to about five seconds before full reattachment resulted with no further increase in the stagnation pressure ratio. A jet of this type is shown in Plate 23. It is possible to see two distinct jets, the split occurring after the initial nozzle expansion is over. The turbulence created extends over a wide area after the jet has departed from the Coanda. Buffeting of the jet could be felt on a hand placed in the jet, the jet appearing to flick between the two positions indicated by the photographs. However this flicking, was at a frequency of the order of 1 Hz, but the photographs show that both jets are visible within 4 μ seconds. The latter suggests that both jets occur simultaneously, although the

photographs give no indication of the position of the jets across the slot breadth. No indication of this lateral position of the jets could be felt by hand, although it was impossible to get close to the nozzle due to the force of the jet. One speculative explanation of this effect is that the flow at the side walls tries to reattach before the central portion of the jet, the air at the surface which is entrained into the jet being more difficult to replace at the walls. This gives the appearance of two jets, the flicking of the jet felt by a hand placed in the jet being gross turbulence.

7.4 INTERFEROMETRY

7.4.1 Experimental Method

The optical apparatus was set up for the interferometric technique as described in Section 5.3.1. The focusing and size of the final image at the camera were achieved as described in Section 7.2.1 and the number and direction of the fringes adjusted by movement of lens L2 and rotation of mirror M2 (Figure 5.4). Initial observations showed that the fringes in the final picture at the plane of the camera became blurred even at stagnation pressure ratios near unity. However fringes could occasionally be distinguished outside the jet where the air was still. As the stagnation pressure ratio was reduced, the periods during which these fringes could be distinguished became infrequent until they were never visible at stagnation pressure ratios below 0.55. Initial photographs, taken at a shutter speed of 1/1000th second, showed clear fringes throughout the flow field at stagnation pressure ratios near unity. As the stagnation pressure ratio was reduced, fringes in sections of the jet became blurred. The clearest fringes were obtained when the photograph was taken while the fringes in the still air could be distinguished. Clear

interferograms could be obtained over a range of stagnation pressure ratios down to 0.55.

Interferograms were taken at three slot widths, 2 mm, 4 mm and 8 mm, over a range of stagnation pressure ratios down to 0.55. The optical apparatus was set and a zero flow photograph was taken. The test stagnation pressure ratio was then set and a series of photographs taken when the fringes in the still air became visible. The stagnation temperature and both atmospheric pressure and temperature were recorded. The rig was then shut down and the process repeated at a different stagnation pressure ratio. A completed film was then developed and the negatives inspected to ensure a clear interferogram had been obtained at each stagnation pressure ratio tested. Where no such frame existed, the test was repeated until a clear interferogram was obtained.

The width of the fringes set up before a test was a compromise between two conflicting criteria. An increase in the number of fringes results in an increase in the number of points in the jet where the fringe shift can be measured and the density derived. However as the number of fringes is increased, the physical distance that a fringe moves for a given shift reduces. This results in a decrease in the accuracy with which the shifts can be measured. A fringe spacing of approximately 12 fringes per centimetre allowed the fringe shifts to be measured to 1/10th fringe width (Section 7.4.3).

7.4.2 Photographic Results

Plates 24 and 25 show interferometric pictures of two jets from a 4 mm slot. Plate 24 was taken at a stagnation pressure ratio fo 0.654 and Plate 25 at 0.579. The photographs obtained from the 2 mm and 8 mm slots

are similar and are not presented here. Undisturbed fringes can be seen at the top of each photograph to the right of the nozzle, where the density is atmospheric. These fringes are shifted near the Coanda and upstream of the nozzle exit by densities that differ from atmospheric density. A region of constant fringe shift corresponds to a constant density (Section 4.1) and a shift to the right corresponds to a density greater than that of atmospheric.

The fringes upstream of the nozzle exit have been shifted to the right from their no flow position, showing the higher densities caused by the large static pressures. As the flow accelerates towards the slot exit, where the static pressure is atmospheric, the fringes become closer to each other (Plate 24). Thus each successive fringe has been shifted by a decreasing distance from its no-flow position, indicating the density decreases towards the slot exit. In addition, the deflection near the curved nozzle is less than that near the Coanda indicating a decrease in density corresponding to the lower pressure balancing the centripetal forces. This variation of density across the exit plane of the slot was also observed in the Schlieren photographs (Section 7.2).

The fringes just downstream of the nozzle exit of Plate 24 are deflected by approximately 3 fringes near the outer edge of the jet. This increase in density from atmospheric is caused by the lower static temperature of the jet, the stagnation temperature being near atmospheric temperature. The shift of the fringe then decreases towards the Coanda, indicating the decrease in density caused by the lower pressures balancing the centripetal forces. Further downstream the fringes are initially shifted slightly to the left as they enter the jet. This decrease in density is caused by the acceleration of atmospheric air as it is entrained

into the jet. The fringe is then moved to the right by the colder air of the jet. The maximum fringe shift decreases and the distance required to reach this maximum increases further downstream. This is an indication of the growth of the outer shear layer. The extent of the potential core of the jet decreases downstream, shown by the position of the maximum fringe shift moving towards the Coanda.

The features discussed above are also visible at the lower stagnation pressure ratio of 0.579 (Plate 25). The maximum fringe shifts obtained downstream of the slot exit are greater, caused by the greater expansion.

7.4.3 Processing of Photographs

The negatives were enlarged and printed onto 10" by 8" photographic paper such that the fringe width was approximately 5 mm. These photographs were digitised by use of an ICL PERQ computer in conjunction with an ADMEL Zodiac digitising tablet. The 6' by 4' tablet has a rectangular mesh of wires such that the position of the cursor from the PERQ computer is recorded in x and y coordinates with a resolution of 0.1 mm. A screen displayed an image of the points as they were recorded, thus allowing spurious points to be immediately recognised. These could then be edited out at a later date.

The fringes on a photograph were numbered, the first full black fringe downstream of the nozzle being arbitrarily numbered as 21. The fringe number was progressively increased downstream of this fringe and decreased upstream in the nozzle. The photographs were then placed on the digitising tablet and positioned such that the top parts of the first few fringes downstream of the nozzle lay parallel to the y axis. These first few fringes rather than the nozzle edge were chosen to align the photograph because the nozzle edge was often obscured by a region of destructive

interference and because it simplified the analysis of the shifts, an undeflected fringe having a constant value of x on digitisation.

The fringes were individually recorded starting upstream of the nozzle, both the position of the change from white to dark and vise versa being recorded. Five values of the position of the fringe side at the top of the photograph (Plate 24) were recorded and the cursor then run down the fringe side to the Coanda, several points being individually recorded during this process. The average of the five initial values, which are in the undisturbed part of the photograph were used in the processing program to locate the zero shift position of a fringe side. After a fringe side had been digitised, the cursor was placed on the digitising tablet such as to record a large value of x. This value was used by the processing program to recognise the end of a fringe side. After the fringes had been digitised, the Coanda surface and the nozzle positions were digitised and stored in a separate file, although the nozzle edge was hard to define when it coincided with a region of destructive interference.

Several fringe sides were digitised twice to enable the accuracy of the digitisation to be evaluated. These studies showed the eye could place the fringe side to within 0.3 mm. Thus the digitisation is accurate to better than 1/10th fringe. The digitised points were then recorded on an 8" floppy disk and transfered to the IBM 4341/1 mainframe computer for the analysis.

A Fortran IV program was written to read the data of the position of the fringes and to output the shift of the fringe at set y values from a maximum value down to the Coanda. The zero position of the fringe sides were averaged from the five initial data points of a fringe side. The zero position of the fringes leading to the nozzle edge were not known because

the nozzle itself obscured their position. These zero positions were estimated from the fringe spacing just downstream of the nozzle, with the assumption that the fringe spacing was constant in this region. Analysis of zero flow interferograms showed that this assumption was correct. The data was digitised such that a fringe that undergoes no shift, has a constant value of x for all y. The program linearly interpolated the value of x of a fringe side at a preset value of y from the data points either side of the y value preset. This x value was compared with an array containing the zero shift values of the fringes and a shift calculated.

The centre of the Coanda circle, and its radius in digitised units, had to be determined so that the fringe shift at set angles round the Coanda could be determined. This was achieved by an interactive program, the radius first being estimated from the photograph. An estimate was made of the centre and the distance from this estimate to the known data points of the Coanda compared with the estimated radius. The estimate of the radius and the coordinates of the centre of the Coanda were renewed and the process repeated. It was found to be possible to select a radius and centre of the circle such that all the data points lay within 0.3% of a radius from the arc produced by the estimated centre and radius of the Coanda. The coordinates of lines leaving the Coanda at set angles round the Coanda and perpendicular to the tangent at that point were then calculated. The fringe shifts at set points along these lines were then interpolated from those calculated earlier.

7.4.4 Results of Density Distributions

Figures 7.1 to 7.4 show density distributions through the jet along normals of selected tangents to the Coanda. The fringe shifts

corresponding to the densities are also shown, the latter being calculated from the fringe shifts using equations 4.1 and 4.8. Figures 7.1 and 7.2 show distributions through a jet from a 4 mm slot at stagnation pressure ratios of 0.654 and 0.579 respectively and Figures 7.3 and 7.4 show distributions through a jet from an 8 mm and 2 mm slot respectively, the stagnation pressure ratio being nominally 0.65.

The density at the exit of a 4 mm slot at a stagnation pressure ratio of 0.654 is nearly uniform (Figure 7.1). It is greater than atmospheric density because the jet is at a lower temperature, the stagnation temperature being nearly equal to atmospheric temperature. As the jet flows round the Coanda, two separate regions can be distinguished. Firstly there exists an inner potential region where the density falls as the surface is approached and secondly an outer region where the density falls to atmospheric density. This latter region corresponds to the free shear layer which not only grows away from the Coanda, but also into the potential region. At the outer edge there is a region where the density is lower than atmospheric, caused by the acceleration of ambient air into the jet. This is discussed in Section 8.6.

As the stagnation pressure ratio is reduced (Figure 7.2) the density at the slot exit is increased and the profile is distorted. This distortion is due to the centripetal forces resulting from the acceleration round the curvature on the nozzle. The density profiles further downstream are similar to those of the higher stagnation pressure ratio, although the maximum densities are increased.

The effect of altering the slot width is shown in Figures 7.3 and 7.4. At the larger slot width the potential region is less affected by the outer shear layer at a set angle round the Coanda. However, at the 2 mm

slot, the potential region has virtually disappeared by an angle of 30^0 round the Coanda. These results are discussed further and compared with other measurements in Section 8.6.

The errors involved in the use of the interferometric technique can be broadly placed into two classifications. The first classification is that of measurement. These include errors in the measurement of stagnation and atmospheric conditions, both reading errors and systematic errors, and errors in the measurement of the fringe shifts. The temperatures were measured to 0.1^0 and so the error in their measurement is insignificant, as is the error in the measurement of atmospheric pressure. The stagnation pressure is accurate to 0.01 bar, thus giving an uncertainty in the stagnation density of 1%. The error in the measurement of the fringe shift is 0.1 of a fringe (Section 7.4.3).

The second class of error in interferometry is the uncertainty in what has been measured. These types of errors, discussed by Tanner (1957) and by Hammond et al (1977), include uncertainty as to the two-dimensionality of the flow, temperature changes of the windows, refraction of the light beam and those caused by external convection currents. The latter were eliminated by enclosing the light paths with wooden covers, (Section 5.4) which ensured the beams were undisturbed outside the working section. There are no methods available to correct for refraction errors (Hammond et al (1977)), although as the density gradients measured were small, these errors are probably insignificant. The minimum temperatures reached in the jet were of the order of 220 K which, assuming a recovery factor of 0.9 through the side wall boundary layer, indicates the temperature of the air neighbouring the window was between 5^0 and 10^0 below atmospheric temperature. Tanner (1957) shows a change of temperature of 1^0

will produce a fringe shift of 0.2 of a fringe through a sheet of glass 1" thick. An attempt was made to reduce this error by taking the flow photograph as soon as possible after the jet was established. However this was not always possible due to the vibrating of the optical rig. This error, if present, should increase as the stagnation pressure ratio is reduced and as the slot width is increased, both resulting in a lowering of the minimum temperature in the jet. Finally, the secondary flows at the side walls will result in an alteration of the optical path length. These secondary flows will have a greater effect as the slot width is increased as they will increase in size.

CHAPTER 8

DISCUSSION

8.1 QUASI TWO-DIMENSIONAL FLOW

Guitton and Newman (1977) identified two main causes for the departure from two-dimensionality of a jet flowing over a convex surface in their study of an incompressible self-preserving wall jet. The first was related to the conditions in the plenum chamber and in particular at the slot lip and the second due to the secondary flows in the boundary layers on the side walls downstream of the slot.

On a convex downstream surface any irregularities in the slot width are amplified further downstream. A thick region at a certain lateral position will grow relative to a thin region because the surface static pressure under the former is lower, which results in lateral flow from the thin region to the thick one. Guitton and Newman designed their rig with these difficulties in mind, the rig consisting of a straight wall, free from obstructions, leading to a carefully ground slot lip which was shaped like a knife edge. However lateral traverses across the slot revealed variations in the total pressure of up to 20% at a position fifty slot widths downstream of the slot. These variations were unaltered by changing conditions in the plenum chamber, but a dramatic improvement was observed when the knife edge was honed flat such that the slot lip became right-angled. The manufacture of this slot was much more easily controlled than that of the knife edge slot lip. The slot lip of the rig of the present work is also right-angled and no variations of the total head were observed away from the side walls at a position of 40^0 round the Coanda (Figure 6.4), a position that was about ten slot widths downstream of the 2 mm slot.

The second cause of the departure from two-dimensional flow is that of secondary flows at the side walls. Launder and Rodi (1983) give two methods of minimising the effects of these secondary flows. The first is to use a small slot height to breadth ratio and the second is to bleed off the side wall boundary layers. Guitton and Newman designed their side walls as a series of small plates, arranged in a ladder formation such that each succeeding plate was placed further into the flow and thus cutting off the boundary layer formed immediately upstream of it. This solution, and that of sucking off the boundary layers, were not possible on the present rig because the side walls consisted of the high quality optical flats necessary for the interferometry.

The directions of the secondary flows on the side wall (Plate 7) and at its corner with the Coanda (Plate 6) were also observed by Guitton and Newman. Using smoke they observed that the secondary flow near the curved surface was directed towards the side wall, where it then split into two directions. The first was towards the Coanda surface and the second was away from the surface, contributing to a rapid expansion of the boundary layer flow and creating a U-shaped wall jet further downstream. This outflow was not explained by Guitton and Newman.

The secondary flow towards the Coanda can be predicted by the radial momentum equation. The pressure gradient in the mainstream is preserved through the side wall boundary layer according to Prandtl's boundary layer hypothesis. As the velocity drops at the side wall the radius of curvature of the flow decreases and the flow moves towards the Coanda. At the Coanda the pressure rises and the flow is forced away from the side wall along the Coanda. The effect of this vortex on the breakaway process is thought to be negligible because the largest encroachment of the vortex by the

second band of oil (Section 6.2) is approximately 2 mm (or 3% of the slot breadth) at a stagnation pressure ratio just above breakaway of a jet from an 8 mm slot. The vortex grows rapidly after the second band of oil and in Plate 4 has encroached approximately 8 mm into the jet by the transition from the convex curvature to the downstream flat. The static pressure tappings are 25 mm from the side walls and are thus positioned well away from the vortices. However it is possible that the vortices caused a blockage of the flow. This would cause an acceleration of the flow over the pressure tappings, resulting in a reduction of the static pressures at the tappings from those that would be recorded by truely two-dimensional flow. The surface static pressure measurements, discussed in Section 8.3 show no evidence of a drop in pressure as the jet flows round the Coanda and thus it can be assumed that any blockage of the flow by the side wall vortices is small.

8.2 DISCHARGE COEFFICIENT

The results obtained from the present investigation are plotted in Figure 8.1, together with various results cited in the literature. The geometry of the slot is altered in a complex manner as the slot width is increased; firstly the area ratio of the settling tube to the slot width is decreased, secondly the ratio of the radius of curvature of the nozzle to the slot width decreases, thirdly the ratio of the streamwise length of the slot to its width decreases, fourthly the aspect ratio (slot breadth to slot width ratio) decreases, and fifthly the ratio of the slot width to downstream radius increases. All of these changes in the geometry can be expected to affect the behaviour of the coefficient of discharge as the slot width and stagnation pressure ratio are altered.

Norwood (1962) shows the theoretical effect of increasing the slot width of the sharp-edged nozzle shown in Figure 2.5a, is to increase the discharge coefficient at a set stagnation pressure ratio (Figure 8.1). These results also show an increase in the discharge coefficient of a set slot width as the stagnation pressure ratio is reduced. The measured values of the present tests follow the same trends as those predicted by Norwood, although the actual values of the discharge coefficients are higher. These higher values can be attributed to the effect of the curvature of the nozzle. (However results from the 2 mm slot at stagnation pressure ratios below 0.3 are dubious which is probably due to an error in the measurement of the leakage flow rate (Section 6.3.2)). The theoretical results of Alder (1979) from nozzles of differing convergence angle (Figure 2.5c) are also shown in Figure 8.1. The curve for the angle of convergence of 15^0 is an approximation from only three points given by Alder. These results show an increase in the coefficient of discharge at a set stagnation pressure ratio as the angle of convergence is reduced.

The present measured values suggest that the effect of the downstream radius and of changes in the aspect ratio are negligible. The results of Norwood show that the intersection of the sonic line at choking with a flat downstream surface is very close to the slot (Section 2.7). Thus it might be expected that the effects of the curvature of the Coanda on the discharge coefficient would be small because this curvature does not begin until the flow has passed through the slot. Similarly, the minimum aspect ratio tested was 7.5 and so the effect of the changes in this ratio are small.

8.3 SURFACE STATIC PRESSURES

The results of the surface static pressure measurements from an incompressible jet are shown in Figure 6.13 to 6.18 and are presented in Section 6.5.2. At each slot width the non-dimensional pressure coefficient distributions over the range of stagnation pressure ratios tested collapse onto a single curve. This is predicted by equation 2.13 and gives confidence that the pressure tappings were all accurately recording the static pressures. The results are replotted in the form suggested by Newman (1961) in Figure 8.2, each line representing the mean pressure coefficient measured at a set slot width. The experimental line obtained by Newman for fully turbulent jets at Reynolds numbers greater than 4×10^4 is also shown. Newman suggests the jet can be considered fully turbulent after a distance of 20 slot widths downstream of the nozzle.

Figure 8.2 shows that the pressure coefficient rises with an increase in slot width. The result obtained from the 1.0 and 1.5 mm slots lie below the experimental curve of Newman. These jets can be considered fully turbulent by 40^0 and 60^0 respectively, but their Reynolds numbers lie below the critical number of 4×10^4 (Section 2.4). The maximum Reynolds number tested at the 1 mm slot was 2.5×10^4 and at the 1.5 mm slot was 3.0×10^4. Despite this the results from the larger slot width are close to those of Newman after 60^0, where the jet is fully turbulent, and before the adjustment for the downstream flat.

The jet from a 2 mm slot becomes fully turbulent at about 80^0, and thus only after the jet has started adjusting for the downstream flat. The largest Reynolds number tested at this slot was 3.5×10^4 and although this is still below the critical number, the results are close to those obtained by Newman. However, as the slot width is further increased, there is a

marked increase in the pressure coefficient. Although these jets have Reynolds numbers above the critical number, they do not become fully turbulent until a position downstream of the start of the flat. This increase in the coefficient with slot width is predicted by equation 2.13 which is derived from potential flow theory. In each case the theoretical pressure coefficient is higher than the measured value as would be expected.

The results of the surface static pressure measurements of a compressible jet are shown in Figures 6.19 to 6.21 and are presented in Section 6.5.3. As the stagnation pressure ratio is reduced a shock cell structure can be seen growing near the slot. This structure, also observed by Roderick (1961), is damped out further downstream and the coefficient becomes constant. This constant tends to increase in jets from a 2 mm and 4 mm slot as the stagnation pressure ratio is reduced, the effect being obscured in the jet from the 8 mm slot because the shock cell structure is maintained until the downstream flat at a stagnation pressure ratio of 0.536. This increase of the pressure coefficient plotted as the stagnation pressure ratio is reduced is expected because it does not include the effect of compressibility. The effects of compressibility increase as the stagnation pressure ratio is reduced, the increase in the pressure coefficient being predicted by equation 2.14. The results obtained at stagnation pressure ratios of approximately 0.61 and 0.52 are plotted in Figures 8.3 and 8.4 respectively to show the effect of increasing the slot width. The theoretical coefficients predicted by equation 2.14 are also shown together with the results obtained by Roderick (1961), at the largest slot width he tested. The slot width to downstream radius ratio of this slot is only a nominal value because no account has been taken of any warping of the nozzle during its manufacture (Section 2.4). This warping

tended to increase the slot width at its centre which was also the plane of the static pressure tappings on the downstream surface. Roderick gives no data of the warping of this slot plotted, although data is given at the smallest slot he tested. If it is assumed that the largest slot warped by a similar amount, the actual slot width to downstream radius ratio of his results plotted is about 0.072.

The pressure coefficients plotted in Figures 8.3 and 8.4 show a decrease as the slot width is increased, in each case the coefficient being greater than that predicted by equation 2.14. The agreement between the results obtained at the 2 mm slot and those obtained by Roderick (1961) agree within the limitations discussed above.

The surface static pressures of jets from a nominally choked nozzle are shown in Figures 6.22 to 6.26 and are presented in Section 6.5.4. At each slot width a shock cell structure can be seen, the peak at the end of the first cell initially increasing as the stagnation pressure ratio is reduced. As the stagnation pressure ratio is further reduced a region of constant pressure grows after the initial expansion from the nozzle has finished and the peak pressure reached after the pressure recovery at the end of the first shock cell is reduced and moves further downstream. This region of constant pressure and the following pressure rise correspond to a region of separation from and to a region of reverse flow on the Coanda surface respectively. The growth of this separation bubble as the stagnation pressure ratio is reduced is discussed and compared with photographs and flow visualization experiments in Section 8.4.1. The measured surface static pressures are also compared with those predicted by the method of characteristics in Section 8.5.

The shock cell pattern and its growth as the stagnation pressure ratio is reduced is similar at all the slot widths tested and seems to be almost unaltered by the introduction of the flat before the curvature on the Coanda (nozzle B, Figure 5.3). In each case the peak pressure after the rise at the end of the first shock cell has reached a position of 80^0 round the Coanda just before the breakaway stagnation pressure ratio is reached. Thus this is an indication that breakaway is imminent from this particular surface and nozzle configuration.

8.4 SEPARATION FROM THE COANDA

8.4.1 Growth of the Separation Bubble

The existence of a separation bubble at stagnation pressure ratios well above that required for breakaway is shown by Schlieren and shadowgraph photographs, by the static pressure distributions and by the flow visualization experiments. Moreover the latter experiments also revealed a region of reverse flow on the surface within the separation bubble. The growth of this region as the stagnation pressure ratio is reduced is shown in Figures 8.5 to 8.7, showing the 4 mm, 8 mm and 2 mm slot widths respectively. The graphs show the initial angle of separation, the angle of the upstream edge of the region of reverse flow within the bubble and the angle at which the jet reattaches. The graphs show data from all the experiments mentioned above.

The angles measured from the flow visualization are accurate to 1^0 at Coanda angles of less than 40^0 and to 2^0 at Coanda angles greater than this. The angles measured from the static pressure distributions are accurate to 3^0. The initial angle of separation is taken as the angle at which the surface static pressure becomes constant, the upstream edge of

the region of reverse flow taken as the angle at which the pressure starts to rise and the reattachment angle as the angle of the peak of this pressure rise. The angles of separation measured from the photographs are accurate to 2^0 but the accuracy of the reattachment point, which becomes difficult to determine especially at stagnation pressure ratios near breakaway, is no better than 5^0.

The three graphs all show similar features. The angle of the separation, which initially increases as the stagnation pressure ratio is reduced, becomes constant as the stagnation pressure ratio is reduced to that required for breakaway. At the 8 mm slot width it appears to decrease just before breakaway. The angle at which separation occurs at a set stagnation pressure ratio increases with slot width. For the 2 mm and 4 mm slots the angle of the upstream edge of the region of reverse flow within the separation zone increases as the stagnation pressure ratio is reduced. The rate of increase becomes more rapid as breakaway is approached. However for the 8 mm slot this angle appears to become constant as breakaway is approached but the number of data points is small. An increase in the reattachment angle of all the jets tested can be seen as the stagnation pressure ratio is reduced. In all three cases this increase becomes more rapid as breakaway is approached. At a stagnation pressure ratio near breakaway the reattachment angle is approximately 80^0 for both the 4 mm and 8 mm slots and 70^0 for the 2 mm slot, the increase in the angle being large for a small change in the stagnation pressure ratio near breakaway at this latter slot.

The results presented in Figures 8.5 to 8.7 show that the determination of the above angles are, within the measurement error, consistent between the various methods of their measurement. In

particular, the region of constant surface static pressure after the initial expansion corresponds to the stationary separated region and the pressure rise after this constant pressure region corresponds to the region of reverse flow detected by the flow visualization. The Figures also show that the reattachment curve can be used to estimate the breakaway stagnation pressure ratio. It would be expected that a Coanda surface which turned the flow through a smaller angle than the present rig would breakaway at a higher stagnation pressure ratio, and breakaway of a larger turning angle Coanda surface would be at a lower stagnation pressure ratio. This trend is confirmed by the experiments of Sadler (1983).

8.4.2 Breakaway and Reattachment

The breakaway stagnation pressure ratios of both nozzles tested are replotted in Figure 8.8, together with results from previous experiments. The results obtained from both nozzles are identical, indicating that the nozzle profile has no effect on the breakaway stagnation pressure ratio. Similar conclusions were reached by Gilchrist (1981) and Savin (1982) in their experiments on a plane two-dimensional rig. However the latter found that the inclusion of a step between the slot and the Coanda surface decreased the breakaway stagnation pressure ratio at a set slot width. Figure 8.8 shows that the upstream stagnation pressures at which breakaway occurred on the present apparatus are higher than those obtained by Gilchrist (1981). There are two possible reasons for this; firstly there were inaccuracies in the measurement of the slot width in the rig of Gilchrist (1981) and secondly the side walls of that rig did not extend fully round the downstream circular section. The latter reason leads to the possibility that breakaway was triggered by a three-dimensional effect,

in particular an interaction between the separation bubble (Section 8.4.1) and the downstream atmospheric air.

Figure 8.8 shows that the present results are very close to those obtained by Sadler (1983) on a downstream section that turned the flow by 90^0, the present rig turning the jet through 100^0. This is expected from the observations of the growth of the separation bubble (Figures 8.5 to 8.7), the angle of the reattachment being near the end of the Coanda just before breakaway. The results obtained by British Petroleum (1979) in their tests on an axisymmetric flare are also plotted in Figure 8.8. The stagnation pressures required for breakaway for this flare at a set slot width to downstream radius ratio are higher, the absolute difference compared to the plane rigs being almost constant over the entire range of slot widths tested. This increase in the breakaway stagnation pressure is expected because the radial outflow on the axisymmetric flare effectively thins out the jet.

The stagnation pressure ratios at which the jet reattached to the Coanda surface after breakaway are replotted in Figure 8.9. The results obtained from both nozzles are similar with the exception of the scatter at small slot widths of nozzle A (Figure 5.3). This indicates that the reattachment stagnation pressure is independent of the nozzle profile, a conclusion also reached by Gilchrist (1981). The absolute stagnation pressures obtained by the latter are again lower than the present results at a set slot width to downstream radius ratio for the reasons outlined above. Figure 8.9 shows that the present results are almost identical to those obtained by Sadler (1983), who also concluded that the reattachment stagnation pressure ratio is independent of the turning angle of the Coanda. There is no data available on the effect of the inclusion of a

step between the nozzle and the Coanda surface, or on the effect of the additional curvature of the axisymmetric flare, on the reattachment stagnation pressure ratio.

8.5 JET STRUCTURE AND PREDICTION

8.5.1 Method of Characteristics Prediction

In Chapter 3 a computer program using the method of characteristics to solve the potential flow equations is presented, together with results from this program. The predicted surface static pressure distributions are compared with those measured in Figure 8.10 to 8.15 and the jet structure compared with Schlieren photographs in the overlays on Plates 14 and 17.

Figure 8.10 shows the predicted and measured static pressure distributions of a jet from a 4 mm slot at a stagnation pressure ratio of 0.407. The agreement is close during the initial Prandtl-Meyer expansion, a process that is complete by an angle of 7^0. The method of characteristics then predicts a greater expansion after this point than the measured expansion. The following static pressure rise predicted is of a similar rate to the measured one, although the predicted peak is higher. The separated region of this jet extends from 15^0 to 30^0 (Figure 8.5). This separated region reduces the expansion, after the initial Prandtl-Meyer expansion, of the real jet. This region grows both into the jet and in the streamwise direction as the stagnation pressure ratio is reduced (Figure 8.5 and Plates 14 to 18) and its effect on the static pressure distribution becomes increasingly pronounced. Figure 8.11 shows the predicted and measured distributions from a 4 mm slot at a stagnation pressure ratio of 0.311 and as before the agreement is close during the initial Prandtl-Meyer expansion, which is complete by an angle of 13^0.

However the real jet then separates from the surface and the following expansion predicted does not occur. The predicted positive pressure gradient following this is greater than the real jet.

As the stagnation pressure ratio is further reduced towards breakaway (Figures 8.12 and 8.13) similar discrepancies between the predicted and measured profiles occur. Whilst the angle by which the Prandtl-Meyer expansion is complete increases as the stagnation pressure ratio is reduced, the separation point remains at a constant angle. Thus by a stagnation pressure ratio of 0.289 the separation point occurs before the Prandtl-Meyer expansion is complete. The predicted pressure rise further downstream has a steeper gradient than the measured one, although the angle at which this starts is similar.

Figures 8.14 and 8.15 each show two comparisons of the predicted and measured static pressure distributions from the 8 mm and 2 mm slots respectively. The discrepancies between the predicted and measured distributions are similar to those of the 4 mm slot. The angle at which the jet from an 8 mm slot separates is always greater than that of the end of the Prandtl-Meyer expansion. However at the 2 mm slot the separation angle has moved upstream of the end of the Prandtl-Meyer expansion before breakaway. The predicted positive pressure gradients further downstream are also much greater than those measured. Figure 8.15b shows the effect of foldback of the characteristics at the start of this pressure rise.

The overlays on Plates 14 and 17 show the predicted jet structure at stagnation pressure ratios of 0.370 and 0.267 respectively. The overlays show the predicted jet edge and the Prandtl-Meyer expansion waves from the nozzle lip together with their subsequent reflections.

The free edge of the real jet is difficult to define, the shear layer growing as the jet flows downstream. The predicted jet edge at a stagnation pressure ratio of 0.370 (Plate 14) lies in the middle of the shear layer throughout the first shock cell and thus can be considered to predict the outer edge well. In the Schlieren photograph two shocks initiated at the surface appear, the upstream shock coming from the point of separation. The second shock is coincident with the shock at the end of the first shock cell predicted by the method of characteristics. Thus it appears that the shock initiated at the point of separation, and the small separated zone, do not have a large effect on the flow at this stagnation pressure ratio. Thus despite the fact that the method of characteristics predicts a lower minimum static pressure, it predicts the first shock cell fairly accurately.

However, as the stagnation pressure ratio is reduced the separation bubble grows and increasingly affects the flow. The overlay at a stagnation pressure ratio of 0.267 (Plate 17) shows the predicted jet edge is only accurate in the initial section of the jet. The predicted jet edge then gradually moves closer to the surface than the real jet edge, the separation bubble causing the real jet to move away from the surface. The shock wave initiated at the upstream edge of the separation zone is coincident with the reflection from the surface at the last Prandtl-Meyer expansion wave. This shock is subsequently reflected from the free surface and the structure of the jet is no longer similar to that predicted by the method of characteristics. Similar results were obtained at the 2 mm and 8 mm slots.

Thus the method of characteristics accurately predicts the first shock cell at stagnation pressure ratios where the separation bubble is

small. However as the stagnation pressure ratio is reduced the bubble grows and affects the flow such that a potential solution that ignores the bubble becomes inaccurate beyond the initial Prandtl-Meyer expansion. Thus the interaction between the boundary layer and the potential flow is strong which implies a potential solution cannot be used directly to provide the boundary conditions for a boundary layer calculation. The two solutions must be coupled to provide an accurate solution.

An attempt was made to calculate the initial boundary layer using the method of Bradshaw-Ferriss-Atwell for the calculation of thin shear layers (Bradshaw and Unsworth (1974)). The Navier-Stokes equations are closed using the turbulent kinetic energy equation, three empirical terms being defined in this equation. The resultant set of equations is parabolic and solved by the method of characteristics (Section 2.2). The program was successfully run with the test cases supplied and also on some measured experimental boundary layers cited in the literature. It was hoped to run this program on the present boundary layer, using the static pressure profiles predicted by the potential flow, to predict any separation of the jet. However all attempts to run the program failed it now being apparent that the boundary layer is laminar up to the point of the separation bubble. This method cannot be used in cases of reversed flow and thus cannot be used to predict the behaviour of the separation bubble.

8.5.2 Inverse Method of Characteristics

The predictions of the modified computer program discussed in Section 3.4 are shown in Figures 8.16 to 8.20, each figure consisting of two graphs. The top graph shows the predicted jet shape, the Coanda surface and the initial Prandtl-Meyer expansion waves and their reflections. The second graph shows the predicted static pressure distribution and both the

measured data points and those guessed by the author to ensure a reasonable interpolated fit (Section 3.4).

Figure 8.16 shows a jet from a nominally 4 mm slot at a stagnation pressure ratio of 0.337. The predicted jet separates from the surface at an angle of approximately 13^0, after the Prandtl-Meyer expansion is over. The jet then continues to expand, but not sufficiently to remain fully attached, until the reflections from the outer edge of the jet of the initial Prandtl-Meyer waves again reach the surface. The arrival of these compression waves coincides with the start of the static pressure rise at about 23^0 round the surface. These waves turn the flow further round the surface, but insufficiently to reattach the jet to the Coanda. The last of these compression waves, after their reflection from the inner layer, coalesce into an oblique shock near the outer edge of the jet. Further downstream the jet continues to move away from the surface. As the absolute peak value of the static pressure at 42^0 is unknown, several predictions of jets were made, each with a different peak value. The resultant jets were very similar to the one shown in Figure 8.16 and are not shown.

Figure 8.17 shows the predicted jet at a stagnation pressure ratio of 0.289. The separation point is coincident with the arrival of the last Prandtl-Meyer expansion wave at the surface. The reflections of the last two waves from the surface converge, which suggests the presence of a weak shock. The static pressure at the inner edge of the jet remains constant from the separation point until the compressive reflections from the outer surface of the initial Prandtl-Meyer expansion waves arrive at the inner surface. The static pressure then rises and the flow is turned towards the surface. However the jet does not reattach to the Coanda.

Figure 8.18 shows the jet at a stagnation pressure ratio just above that required for breakaway. The separation point has moved upstream of the arrival of the last Prandtl-Meyer expansion waves at the Coanda surface, the reflection of these last waves coalescing into a shock near the outer edge of the jet. The features of the jet are similar to the previous two jets and in particular the jet does not reattach to the Coanda surface. Figures 8.19 and 8.20 show jets from an 8 mm and 2 mm slot respectively, the stagnation pressure ratios being just above that required for breakaway. The features are similar to those of the jets from the 4 mm slots, the jets never reattaching after the initial separation.

The overlays over Plates 15 and 18 compare the predicted and photographed jets from a nominally 4 mm slot. Plate 15 shows the outer edge within the first shock cell and the position of the shock at the end of the cell are accurately predicted by the inverse method of characteristics. The inner edge of the jet is also accurately predicted until the flow is turned back towards the Coanda by the compression waves resulting from the reflections of the initial Prandtl-Meyer expansion. The real jet is turned further towards the Coanda than the predicted jet by the last of these compression waves. One possible cause for this is that the reflections of the expansion and compression waves from the outer edge are altered by the shear layer. The growth of this layer and its effect on the flow are ignored by the potential flow model.

Plate 18 and the overlay shows the jet at a stagnation pressure ratio just above that required for breakaway. The separation point is before the last Prandtl-Meyer expansion wave has reached the surface, the shocks initiated at this point being accurately predicted. The outer edge of the jet within the first shock cell and the position of the shock at the end of

it are also accurately predicted. However, although the initial inner layer is accurately predicted, the predicted inner layer is turned through a smaller angle near the end of the first shock cell than the real jet.

The results obtained from the 8 mm and 2 mm slots are similar. Thus the inverse method of characteristics accurately predicts the features of the first shock cell. However the real jet moves closer to the wall after the first shock cell and eventually reattaches, and a potential solution becomes inaccurate. The potential solution ignores the presence of the outer shear layer of the real jet. This layer grows as the jet flows round the Coanda and increasingly affects the reflections of expansion and compression waves from this edge of the jet. This causes the inaccuracies after the first shock cell in the potential prediction of the jet.

8.6 INTERFEROMETRY

The development of an optical system to measure the density changes in the jet as it flows round the Coanda is described in Section 5.2. Interferometric pictures were only possible at stagnation pressure ratios above 0.55 although it is thought that improvements in the system, discussed in Section 5.4, would allow pictures to be taken at lower ratios. The interpretation of the interferometric pictures is discussed in Section 7.4.

An approximate growth of the outer shear layer is plotted in Figure 8.21. The width of the shear layer is defined as the distance between the maximum density in the jet to the point where it first reaches atmospheric density (Figures 7.1 to 7.4). These widths are plotted against the arc length whose radius is the radius of the Coanda plus the slot width. The width of the shear layer from a set slot was found to be independent of the

stagnation pressure ratio. Figure 8.21 shows the growth rates of the shear layers from different slot widths are similar. These growth rates are larger than for an uncurved mixing layer (Reynolds (1974)), which is expected due to the destabilising nature of the curvature. It is also expected that the growth of the shear layers from the different slots would be similar because the radius of curvature is similar. No further flow properties can be derived from the known densities of the shear layers because the flow is not isentropic in this region.

At the outer edge of the jet there is a region where the density is lower than atmospheric, caused by the acceleration of ambient air into the jet. If it is assumed that this acceleration from atmospheric conditions is isentropic, the measured density drop shows these velocities are between 30 m/s and 40 m/s.

The growth of an incompressible shear layer can be written as

$$V_2 - V_1 = -\frac{1}{\rho}\frac{dm}{dx} \qquad \ldots(8.1)$$

where V is positive moving away from the Coanda (Plate 24) and condition 1 is in the core of the jet and condition 2 is atmospheric. If it is assumed that the density is constant through the shear layer, the velocity profile is linear and that V_1 is negligible, the entrainment velocity can be written as

$$V_2 \approx -\frac{1}{2} U_1 \frac{d\delta}{dx} \qquad \ldots(8.2)$$

where δ is a measure of the thickness of the shear layer. Substituting values for the main core velocity and the growth of the shear layer (Figure 8.21) gives entrainment velocities of 23 m/s. These are lower than those measured but given the broad assumptions above (both in the theoretical and

measured velocities) they are of the same order of magnitude.

The flow within the inner potential region is isentropic and the densities are related to the upstream density by the Mach number. The other properties of the flow can also be derived from the known stagnation conditions and the Mach number (Section 2.1). The total velocity at a point is thus known, although the direction of the velocity is impossible to determine. Figure 8.22 shows the variation of a 'pseudo' discharge coefficient, C_D', with both the slot width and stagnation pressure ratio. The measured mass flow is obtained from an integral across the slot exit of the multiple of the density and the square of the total velocity. The real mass flow rate will be lower because the assumption that the velocity is normal to the slot exit is inaccurate. The values obtained of the 'pseudo' discharge coefficient are within 1% of unity, thus showing, as expected, that the static pressure across the slot exit is atmospheric. The values of the coefficient of discharge measured by an orifice plate are less than unity (Section 8.2).

Figure 8.23 shows the static pressure variation in the potential region of two jets from a 4 mm slot width. The static pressure variation across a potential jet whose streamlines form concentric circles and whose outer edge is fully expanded is also shown. These pressures are obtained from equation 2.15. The static pressure profiles are similar at all angles round the Coanda, the pressure falling as the Coanda is approached. The rate of change of pressure with distance from the Coanda is smaller than that required for the streamlines to form concentric circles. The smaller centripetal force is an indication that the real flow is following a radius of curvature that is larger than the Coanda. Figure 8.24 shows static pressure profiles of jets from 2 mm and 8 mm slots, the stagnation pressure

ratio being nominally 0.65. These are similar to those of the 4 mm slot, the centripetal forces again being too small for the flow to follow concentric circles round the Coanda.

The surface static pressures obtained from the interferometry are plotted in Figures 8.25 to 8.27, the slot widths being 8 mm, 4 mm and 2 mm respectively. The static pressures measured by the static pressure tappings and the theoretical pressure that would be measured if an inviscid flow followed concentric circles (equation 2.14) are also plotted. The agreement between the interferometric static pressures and those measured by the static pressure tappings is good in jets from an 8 mm slot (Figure 8.25). The measured pressures are generally above those that would be recorded if the flow followed concentric circles. However, as the slot width is decreased, a discrepancy between the interferometric static pressures and those from the static pressure tappings becomes apparent. The interferometric static pressures are lower, the discrepancy being approximately equivalent to 0.4 of a fringe shift at the 4 mm slot (Figure 8.26) and 0.7 of a fringe shift at the 2 mm slot width (Figure 8.27). The interferometric static pressures are almost equal to those of a jet that follows concentric circles at the 4 mm slot and are lower at the 2 mm slot.

The errors involved in the interferometric technique are discussed in Section 7.4.4. The results from the 8 mm slot give confidence that any errors of the measurement type are insignificant, and the derivation of the other jet properties from the densities is also accurate. The surface static pressures of jets obtained from the 4 mm and 2 mm slots are thus hard to explain. The density gradients of these jets are of the same order as those in the jets from an 8 mm slot and so diffraction errors are eliminated. The errors caused by the side wall boundary layers and by the

cooling of the windows should increase as the slot width is increased. Thus it is unlikely that these are the causes for the consistent discrepancies between the interferometric measurements and the surface static pressure measurements of the 4 mm and 2 mm slots. The discrepancies thus remain unexplained.

CHAPTER 9

CONCLUSIONS

9.1 CONCLUSIONS

A plane two-dimensional model flare, based on the Kaldair I8-H-AS Coanda flare, has been designed and commissioned. The features of the model include an interchangeable nozzle, a variable slot width and surface pressure tappings on the Coanda surface. In addition the jet can be viewed following the Coanda surface through two side windows. These windows can be interchanged between perspex or high quality optical glass, the latter allowing optical measurements of the jet. The rig is supplied by an air line that filters the incoming air and both controls and measures the flow rate.

Flow visualization tests indicate the presence of secondary flows at the side walls that are inherent in the design of the rig. The vortices do not approach the static pressure tappings, although it is possible that they act as a blockage to the flow. This would result in the acceleration of the flow over the pressure tappings which would in turn result in a decrease in the static pressure. Static pressure measurements did not reveal a decrease in the static pressure as the jet flowed round the Coanda surface and thus it is believed any blockage of the flow by the side wall vortices is small.

An optical system capable of shadowgraph, spark and continuous Schlieren and interferometric techniques has been developed. A feature of the system is that it requires minimal adjustment to switch from one technique to another. After the system had been initially set up, it required no further major adjustments during the tests.

Photographs of good quality have been obtained of jets flowing round the Coanda surface using all four optical techniques. No limitations on the use of the shadowgraph or both Schlieren techniques were discovered. However it was found impossible to obtain clear interferometric pictures at stagnation pressure ratios below 0.55. An investigation into possible reasons for this shows that the probable cause is vibrations from the mechanical rig are transfered via the floor into the optical rig.

The phenomenon of breakaway of the jet from the Coanda has been investigated. Two nozzles were tested, one designed such that the slot exit coincided with the start of the curvature on the Coanda surface and the other designed such that there was a short flat section on the Coanda surface between the slot exit and the start of the curvature. There is no detectable difference in the breakaway properties of the two nozzles. The breakaway stagnation pressure ratio decreases as the slot width is decreased, as is the ratio at which the jet reattaches after breakaway. The hysteresis between breakaway and reattachment increases as the slot width is reduced.

The existence of a separation bubble at stagnation pressure ratios above that required for breakaway has been established. The boundary layer up to the point of separation is laminar. Shadowgraph and Schlieren photographs, together with flow visualization and surface static pressure measurements, show the streamwise length and the extent of its encroachment into the jet increase as the stagnation pressure ratio is reduced. Surface flow visualization shows that the separation bubble contains a region of strongly reversed flow. This reverse flow coincides with a strong adverse pressure gradient caused by reflections of the Prandtl-Meyer expansion at the nozzle lip. At all the three slot widths tested, it was observed that

the reattachment point at the end of the separation bubble reaches a point approximately 80^0 round the Coanda surface at a stagnation pressure ratio just above that required for breakaway.

Measurements of the mass flow rate through the slot were taken. The coefficient of discharge at a set stagnation pressure ratio was found to increase as the slot width was decreased. At all slot widths tested, the coefficient of discharge increased as the stagnation pressure ratio was decreased. There is some doubt about the validity of the results obtained at the 2 mm slot width below a stagnation pressure ratio of 0.3, the coefficient of discharges being greater than unity. It is believed that the reason for these high values results from an error in the estimation of the leakage flow rate at the low stagnation pressure ratios.

Measurements were taken of the surface static pressure on the Coanda surface over a range of stagnation pressure ratios. At ratios close to unity, when the flow was entirely incompressible, the non-dimensional pressure coefficient, C_p, , was found to increase with slot width. At large slot widths the jet does not fully develop, the rise in the pressure coefficient, C_p, , as the slot width is increased being predicted by potential flow theory. As the stagnation pressure ratio was decreased below the critical value a wave-like variation, corresponding to a shock cell structure, was observed. As the stagnation pressure ratio was further reduced a region of constant pressure was observed after the initial expansion. This region of constant pressure corresponds to the first section of the separation bubble.

Interferometric pictures of jets at stagnation pressure ratios above 0.55 were taken and analysed. An approximate measurement of the width of the outer shear layer shows that its growth is independent of the total jet

width. The surface static pressures derived from the interferometric pictures of jets from an 8 mm slot agree with those measured at the static pressure tappings. However the interferometric surface static pressures of jets from both 4 mm and 2 mm slots are lower than those measured by the tappings. This difference has not been explained and merits further investigation.

A computer program has been developed to model an inviscid supersonic jet flowing over the Coanda surface. The method of characteristics is employed and the finite difference equations solved by the Euler predictor-corrector method. The initial program models a jet that remains fully attached to the Coanda surface. This accurately predicts the jets free edge and the surface static pressure only during the initial Prandtl-Meyer expansion. The solution then becomes inaccurate due to the strong interaction between the separation bubble and the potential flow.

A modification to the program replaces the condition that the jet remains fully attached to the Coanda surface with one that the inner edge is solved to a known static pressure. These static pressures are interpolated from measured values. The main features of the jet shown by shadowgraph and Schlieren photographs are accurately predicted over the first shock cell, the accuracy then deteriorating after this as the outer shear layer of the jet grows and begins to affect the potential region.

9.2 IMPLICATIONS FOR FUTURE WORK

The optical system developed in this work has performed well in the shadowgraph and Schlieren modes. However, vibrations prevented interferometric pictures being taken of jets below the critical stagnation pressure ratio. It is believed that further development aimed at isolating

the mechanical and optical rigs will allow interferometry over a wider range of stagnation pressure ratios, thus allowing the properties of critical jets to be determined. This work should focus in particular at the bolting of the mechanical rig to the floor with the aim of preventing the transmission of vibrations from the rig to the floor.

The mechanism of breakaway of a plane model of a Coanda flare has been established. An initially laminar boundary layer separates near the slot exit, the separation being precipitated by a pressure rise imposed on the boundary layer by the outer potential flow. There follows a strong interaction between the separation bubble and the outer potential flow, the latter also being affected by the outer shear layer. This interaction determines whether or not the jet reattaches. The inclusion of a step between the slot exit and the Coanda is a proven method of delaying breakaway. This step ensures the initial boundary layer on the Coanda surface is turbulent, which increases the ability of the boundary layer to withstand the adverse pressure gradient imposed upon it by the outer flow. This in turn will reduce the size of the separation bubble and lead to a decrease in the breakaway stagnation pressure ratio at a set slot width to downstream radius ratio.

It can be assumed that the mechanism for breakaway on an axisymmetric flare is similar, with a separation bubble growing as the stagnation pressure ratio is reduced. A simple method of confirming the existence of this separated region would be through surface flow visualization. This would also reveal any regions of reverse flow and the point at which the jet reattaches, the latter being of particular interest near the breakaway stagnation pressure ratio. Surface static pressure measurements would also be useful to tie up any separated region with the shock cell structure.

The existence of the separation bubble has important implications for the theoretical prediction of any supersonic jet flowing over a convex surface and for the theoretical prediction of breakaway in particular. The strong interaction between the separation bubble and the potential flow requires a coupling of the two regions immediately downstream of the slot exit. The method chosen to solve the boundary layer must also allow reverse flow. The critical region of the jet that determines breakaway is the reattachment of the jet at the end of the separation bubble. This reattachment occurs downstream of the first shock cell, where the potential flow has also been affected by the outer shear layer. Thus, in addition to being coupled to the boundary layer solution, the potential solution must be coupled to a solution of the outer shear layer.

Calculation methods that attempt to solve the total jet are beginning to be developed. This present work shows the boundary layer is an important region of the jet and its growth, separation and reattachment must be included in any calculation method of the total jet. However once an accurate calculation technique has been developed this will not only aid flare designers but will also be useful in fields such as aerofoil control, where jets are used to re-energise the boundary layer and prevent separation of the mainstream flow and the resultant loss of lift.

REFERENCES

Abbett, M. (1971), Mach disk in underexpanded exhaust plumes, AIAA, J. Vol. 9, p512.

Alcaraz, E., Charnay, G., Mathieu, J. (1977), Measurements in a wall jet over a convex surface, Phys. of Fluids, Vol. 20, p203.

Alder, G.M. (1976), Transonic flow through sharp-lipped convergent nozzles, Ph.D. Thesis, University of Edinburgh.

Alder, G.M. (1979), The numerical solution of choked and supercritical ideal gas flow through orifices and convergent conical nozzles, J.Mech.Eng. Sci., Vol. 21, p197.

Andrews, J.R., Netzer, D.W. (1976), Laser Schlieren for study of solid-propellant deflagration, AIAA, J. Vol. 4, p410.

Arzoan, Y., Ben-Dor, G. (1985), Fully computerized evaluation of interferograms from fluid flow investigations, Int. J. Heat & Fluid Flow, Vol. 6, p133.

Bakke, P. (1957), An experimental investigation of a wall jet, J.F.M., Vol. 2, p467.

Ben-Dor, G., Whitten, B.T., Glass, I.I., (1979), Evaluation of perfect and imperfect gas interferograms by computer, Int. J. Heat and Fluid Flow, Vol. 1, p77.

Benson, R.S., Poole, D.E., (1965a), Compressible flow through a two-dimensional slit, Int. J. Mech. Sci. Vol. 7, p315.

Benson, R.S., Poole, D.E., (1965b), The compressible flow discharge coefficients for a two-dimensional slit, Int. J. Mech. Sci. Vol. 7, p337.

Born, M., Wolf, E., (1959), Principles of Optics, Pergamon Press, London.

Bradbury, L.J.S., Wood, M.N. (1965), An exploratory investigation into the deflection of thick jets by the Coanda effect, RAE, T.R. 65235.

Bradshaw, P. (1973), Effects of streamline curvature on turbulent flows. AGARDograph 169.

Bradshaw, P. Cebeci, T., Whitelaw, J.H. (1981), Engineering calculation methods for turbulent flow, Academic Press, London.

Bradshaw, P., Ferriss, D.H. (1971), Calculation of boundary-layer development using the turbulent energy equation : compressible flow on adiabatic walls, J.F.M., Vol. 46, p83.

Bradshaw, P., Ferriss, D.H., Atwell, D.H. (1967), Calculation of boundary-layer development using the turbulent energy equation, J.F.M., Vol. 28, p593.

Bradshaw, P., Gee, M.T. (1960), Turbulent wall jets with and without an external stream, A.R.C., R&M 3252.

Bradshaw, P., Unsworth, K. (1974) An improved Fortran program for the Bradshaw-Ferriss-Atwell method of calculating turbulent shear layers, I.C.Aero. Report 74-02 (Revised 1980).

British Petroleum (1979), Private communication. Boden, J., B.P. Research Centre, Sunbury-on-Thames, Middlesex.

British Petroleum (1980), Private communication. Boden, J., B.P. Research Centre, Sunbury-on-Thames, Middlesex.

British Petrleum (1982), Private Communication. Boden, J., B.P. Research Centre, Sunbury-on-Thames, Middlesex.

Brown, E.F. (1968), Compressible flow through convergent conical nozzles with emphasis on the transonic region, Ph.D. Thesis, University of Illinois.

Carpenter, P.W., Green, P.N. (1983), Noise sources in external Coanda-type gas flares, AIAA-83-0758, 8th Aeroacoustics Conference, April 11-13, Atlanta, Georgia.

Cebeci, T., Smith, A.M.O. (1974), Analysis of turbulent boundary layers, Academic Press, London.

Chang, I.S., Chow, W.L. (1974), Mach disk from underexpanded axisymmetric nozzle flow, AIAA J. Vol. 12, p1079.

Chevalerias, R., Latron, T., Veret, C. (1957), Methods of interferometry applied to the visualization of flows in wind tunnels, J. Opt. Soc. Amer., Vol. 47, p703.

Chow, C-Y (1979), An introduction to computational fluid mechanics, Wiley, New York.

Chow, W.L., Chang, I.S. (1972), Mach reflection from overexpanded nozzle flows, AIAA J., Vol. 10, p1261.

CRC Handbook of Chemistry and Physics (1984-5), 65th edition, Ed. Weast R.C., CRC Press Inc., Cleveland, Ohio.

Dash, S.M., Beddini, R.A., Wolf,, D.E., Sinha, N. (1983), Viscous/Inviscid analysis of curved sub-or supersonic wall jets, AIAA-83-1679.

Dash, S.M., Thorpe, R.D. (1981), Shock-capturing model for one- and two-phase supersonic exhaust flow, AIAA J., Vol. 19, p842.

Dash, S.M., Wilmoth, R.G., Pergament H.S. (1979), Overlaid viscous/inviscid model for the prediction of near-field jet entrainment, AIAA J. Vol. 17, p950.

Deckker, B.E.L., Chang, Y.F., (1965-6), An investigation of steady compressible flow through thick orifices, Proc. Instn. Mech. Engineers, Vol. 180, Pt 3J, p312.

Dew, G.D. (1964), A method for the precise evaluation of interferograms, J.Sci.Inst., Vol. 41, p160.

Fekete, G.I. (1963), Coanda flow of a two-dimensional wall jet on the outside of a circular cylinder, McGill Univ., MERL Rept. No. 63-11.

Fernholz, H. (1964), Umlenkung von Freistrahlen an gekrümmten Wänden, Jahrbuch der W.G.L.R., p149.

Fernholz, H. (1971), The deflection of free jets at convexly curved walls (Coanda Effect), Can. NRC-TT-1504.

Fox, J.H. (1974),On the structure of jet plumes, AIAA J., Vol. 12, p105.

Gilchrist, A.R. (1981), Flow from a thin slot over a curved downstream section, Internal Rep., Dept. Eng., University of Durham.

Glauert, M.B. (1956), The wall jet, J.F.M., Vol. 1, p625.

Goldstein, R.J. (1965), Interferometer for aerodynamic and heat transfer measurements, Rev. Sci. Instrum., Vol. 36, p1408.

Green, P.N. (1982), Private Communication, Exeter University.

Gregory-Smith, D.G., Robinson, C.T. (1982), The discharge from a thin slot over a surface of convex curvature, Int. J. Mech. Sci., Vol. 24, p329.

Grigull, U., Rottenkolber, H. (1967), Two-beam interferometer using a laser, J.Opt.Soc. Amer., Vol. 57, p149.

Guderley, K.G. (1962), The theory of transonic flow, Pergamon, Oxford.

Guitton, D.E., Newman, B.G. (1977), Self-preserving turbulent wall jets over convex surfaces, J.F.M., Vol. 81, p155.

Hammond, G.P., Fung, W.S., O'Callaghan, P.W., Probert, S.D. (1977), Interferometric study of the temperature field created by a quasi-plane cold air jet and an adjacent flat plate, J.Mech.Eng.Sci., Vol. 19, p47.

Hauf, W., Grigull, U. (1970), Optical methods in heat transfer, Advances in Heat Transfer, Vol. 6, Ed. Harnett, J.P., Irvine, T.F., Academic Press, London.

Heflinger, L.O., Wuerker, R.F., Brooks, R.F. (1966), Holographic Interferometry, J.Appl. Phys., Vol. 37, p642.

Hoffmann, J.D. (1973), Accuracy studies of the numerical method of characteristics for axisymmetric steady supersonic flow, J. Comp. Phys., Vol. 11, p210.

Holder, D.W., North, R.J. (1952), A Schlieren apparatus giving an image in colour, Nature, Vol. 169, p466.

Holder, D.W., North, R.J., Wood, G.P. (1956), Optical methods for examining the flow in high-speed wind tunnels, AGARDograph, No. 23.

Houstoun, R.A. (1957), Physical Optics, Blackie and Son Ltd., London.

Hunt, B.L., Lamont, P.J. (1976), The impingement of underexpanded axisymmetric jets on wedges, J.F.M., Vol. 76, p307.

Hunt, B.L., Lamont, P.J. (1980), The impingement of underexpanded axisymmetric jets on perpendicular and inclined flat plates, J.F.M., Vol. 100, p471.

Jennions, I.K., Hunt, B.L. (1982), The axisymmetric impingement of supersonic air jets on cones, Aero. Quart., Vol. 31, p26.

Kamutzki, B.H., Griffiths, R.T. (1970), A polarization interferometer for density measurements in compressible flow, Proc. Inst. Mech. Eng., Vol. 184, p665.

Keller, H.B. (1978), Numerical methods in boundary-layer theory, Ann. Rev. Fluid Mech., Vol. 10, p417.

Keshavan, N.R. (1975), Separation of turbulent boundary layer on a lifting cylinder, AIAA J., Vol. 13, p252.

Korbacher, G.K. (1962), The Coanda effect at deflection surfaces detached from the jet nozzle, Can. Aero. Sp. J., Vol. 8, p1.

Kraushaar, R. (1950), A diffraction grating interferometer, J.Opt.Soc.America., Vol. 40, p480.

Kreyszig, E. (1972), Advanced Engineering Mathematics, 3rd Ed., John Wiley and Sons, London.

Kuehn, T.H., Goldstein, R.J. (1976), An experimental and theoretical study of natural convection in the annulus between horizontal concentric cylinders, J.F.M., Vol. 74, p695.

Ladenburg, R.W. (1955), Physical measurements in gas dynamics and combustion, Pt. 1, Vol. IX:- high speed aerodynamics and jet propulsion, O.U.P., London.

Ladenburg, R., Van Voorhis, C.C., Winckler, J. (1949), Interferometric studies of faster than sound phenomenon Part II: Analysis of supersonic air jets, Physical Review, Vol. 76, p662.

Launder, B.E., Rodi, W. (1981), The turbulent wall jet, Prog. Aerospace Sci., Vol. 19, p81.

Launder, B.E., Rodi, W. (1983), The turbulent wall jet - measurement and modeling, Ann. Rev. Fluid Mech., Vol. 15, p429.

Lee, P.H., Woolsey, G.A. (1981), Versatile polarization and interferometer, Appl. Optics., Vol. 20, p3514.

Love, E.S., Grigsby, C.E., Lee, L.P., Woodling, M.J. (1959), Experimental and theoretical studies of axisymmetric free jets,NASA Tech.Rep.R-6.

MacCormack, R.W. (1982), A numerical method for solving the equations of compressible viscous flow, AIAA J., Vol. 20, p1275.

Mahgoub, H.E.H., Bradshaw, P. (1979), Calculation of turbulent-inviscid flow interactions with large normal pressure gradients, AIAA J., Vol. 17, p1025.

Maltby, R.L. (1962), Flow visualization in wind tunnels using indicators, Part 1. AGARDograph 70.

McKeen, W.J., Tarasuk, J.D. (1981), Accurate method for locating fringes on an interferogram, Rev. Sci. Inst., Vol. 52, p1223.

McNally, W.D., Sockol, P.M. (1985), REVIEW - Computational methods for internal flows with emphasis on turbomachinery, Trans. ASME, Vol.107, p6.

Merzkirch, W.F. (1964), A simple Schlieren interferometer system, AIAA J., Vol. 3, p1974.

Merzkirch, W., (1974), Flow visualization, Academic Press, New York.

Merzkirch, W. (1981), Density sensitive flow visualization. Methods of experimental physics, Ed. Emrich, R.J., Vol. 18:- Fluid dynamics, Pt. A2, Academic Press.

Mesli, R., Ferendeci, A.M., Mawardi, O.K. (1981), Plasma-Beam-Hole interaction, I.E.E.E. Trans., Plasma Sci., Vol. PS-9, p58.

Metral, A., Zerner, F. (1948), The Coanda effect, British TIL/T4207 translation of French Pub. Sci. et Tech. du Min. de L'Air, 218.

Morrison, J.F. (1982), A study of an axisymmetric wall jet with streamline curvature and its application to the Coanda flare, Ph.D. Thesis, Dept. of Eng., University of Durham.

Murty, M.V.R.K., Shukla, R.P. (1976), Jamin type laser interferometers, Indian J. Phys., Vol. 50, p139.

Newman, B.G. (1961), The deflection of plane jets by adjacent boundaries - Coanda effect, Boundary layer theory and flow control, p232, Ed. Zachmann, G.V., Pergamon Press.

Newman, B.G. (1969), The prediction of turbulent jets and wall jets, Can. Aero. Spa. J., Vol. 15, p288.

Norwood, R.E. (1962), Two-dimensional transonic gas jets, Proc. 4th U.S. Nat. Cong. Appl. Mech., Vol. 2, p1359.

Oppenheim, A.K., Urtiew, P.A., Weinberg, F.J. (1966), On the use of laser light sources in Schlieren interferometer systems, Proc. Roy. Soc. Lond. A., Vol. 291, p279.

Patel, V.C. (1965), Calibration of the Preston tube and limitations on its use in pressure gradients, J.F.M., Vol. 23, p185.

Physics Handbook (1980), Ed. Nordling, C., and Osterman, J., Studentlitterator, Sweden.

Pollock, N. (1980), A simple laser interferometer for wind tunnel flow visualization, J. Phys. E. : Sci. Instrum., Vol. 13, p1062.

Rayleigh, Lord (1917), On the dynamics of revolving fluids, Proc. Roy. Soc. Lond. A., Vol. 93, p148.

Reynolds, A.J. (1974), Turbulent flows in engineering, John Wiley and Sons, London.

Roderick, W.E.B. (1961), Use of the Coanda effect for the deflection of jet sheets over smoothly curved surfaces, Part II - Some tests with supersonic over and under expanded jet sheets, U.T.I.A., T.N. No. 51.

Sadler, J.D. (1983), Breakaway tests on cylinderical Coanda surface of varying turning angle, B.P. Internal Report.

Savin, R.A. (1982), Flow from a thin slot over a curved downstream section, Int. Rept., Dept. of Eng., University of Durham.

Schlichting, H. (1979), Boundary-layer theory, Seventh Edition, McGraw-Hill Book Co., New York.

Schwar, M.J.R., Weinberg, F.J. (1969), Laser techniques in combustion research, Combustion and Flame, Vol. 13, p335.

Schwarz, W.H., Cosart, W.P. (1960), Two-dimensional turbulent wall jet, J.F.M., Vol. 10, p481.

Settles, G.S. (1980), Colour Schlieren optics - A review of techniques and applications, Proc. International Symp. on Flow Viz., Bochum, 9-12 Sept.

Settles, G.S. (1985), Colour-coding Schlieren techniques for the optical study of heat and fluid flow, Int. J. Heat & Fluid Flow, Vol. 6, p3.

Shapiro, A.H. (1953), The dynamics and thermodynamics of compressible fluid flow, Vols. I and II, Ronald Press Company, New York.

Sharma, R.N. (1981), Experimental investigation of conical wall jets, AIAA J., Vol. 19, p28.

Smeaton, J. (1759), An experimental enquiry concerning the natural powers of water and wind to turn mills and other machines depending on a circular motion, J. Roy. Aero. Soc., Vol. 61, p156.

Smith, G.D. (1978), Numerical solution of partial differential equations: Finite difference methods, O.U.P., Second Edition.

Starr, J.B., Sparrow, E.M. (1967), Experiments on a turbulent cylindrical wall jet, J.F.M., Vol. 29, p495.

Tanner, L.H. (1957), The design and use of interferometers in aerodynamics, A.R.C., R&M 3131.

Tanner, L.H. (1965), Some laser interferometers for use in fluid mechanics, J.Sci.Instrum., Vol. 42, p834.

Tanner, L.H. (1966), The design of laser interferometers for use in fluid mechanics, J.Sci.Instrum., Vol. 43, p878.

Walker, J. (1984), The troublesome teapot effect or why a poured liquid clings to the container, Scientific American, Oct., p140.

Weinberg, F.J. (1963), Optics of Flames, Butterworths, London.

Weinberg, F.J., Wood, N.B. (1959), Interferometer based on flow diffraction gratings, J.Sci.Instrum., Vol. 36, p227.

Werner, F.D., Leadon, B.M. (1953), Very accurate measurement of fringe shifts in an optical interferometer study of gas flows, Rev. Sci. Inst., Vol. 24, p121.

Whelan, P.M., Hodgson, M.J. (1977), Essential pre-university physics, John Murray, London.

Whiffen, M.C., Ahuja, K.K. (1983), An improved Schlieren system and some new results on acoustically excited jets, J. Sound and Vibration, Vol. 86, p99.

Wilkins, J., Withridge, R.E., Desty, D.H., Mason, J.T.M., Newby, N., (1977), The design and development and performance of Indair and Mardair flares, Offshore Technology Conference, May 2-5, Houston, Texas, (OTC 2822).

Wille, R., Fernholz, H. (1965), Report on the first European Mechanics Colloquium on the Coanda effect, J.F.M., Vol. 23, p801.

Wilson, D.J., Goldstein, R.J. (1976), Turbulent wall jets with cylinderical streamwise surface curvature, J.Fluids.Eng., Trans ASME, Vol. 98, p550.

Young, T. (1800), Outlines of experiments and inquiries respecting sound and light, J. Roy. Aero. Soc., Vol. 61, p157.

Zucrow, M.J., Hoffman, J.D. (1976), Gas Dynamics, Vols. 1 and 2, John Wiley and Sons, New York.

APPENDIX A

EULER PREDICTOR-CORRECTOR METHOD

This appendix presents the Euler predictor-corrector method for the solution of an interior point in irrotational planar flow (Figure 3.2). The method is given in detail by Zucrow and Hoffman (1976). The conditions at points 1 and 2 are known, the solution point, point 3, being at the intersection of the characteristics from points 1 and 2. The characteristic and compatibility equations are rewritten here for convenience. They are respectively, in finite difference form

$$\Delta y_{\pm} = \lambda_{\pm} \Delta x_{\pm} \qquad \ldots(A1)$$

and

$$Q_{\pm} \Delta u_{\pm} + R_{\pm} \Delta v_{\pm} = 0 \qquad \ldots(A2)$$

where

$$Q = (u^2 - a^2) \qquad \ldots(A3)$$

$$R = 2uv - (u^2 - a^2)\lambda \qquad \ldots(A4)$$

The equations A1 can be rewritten

$$(y_3 - y_1) = \lambda_- (x_3 - x_1)$$

$$(y_3 - y_2) = \lambda_+ (x_3 - x_2) \qquad \ldots(A5)$$

where initially

$$\lambda_- = \tan(\theta_1 - \alpha_1)$$

$$\lambda_+ = \tan(\theta_2 + \alpha_2) \qquad \ldots(A6)$$

The position and properties of points 1 and 2 are known and thus the equations of A5 can be solved simultaneously to give a prediction of point 3.

The equations A2 can be rewritten

$$Q_- u_3 + R_- v_3 = T_-$$

$$Q_+ u_3 + R_+ v_3 = T_+ \qquad \ldots(A7)$$

where initially

$$T_- = Q_- u_1 + R_- v_1$$

$$T_+ = Q_+ u_2 + R_+ v_2 \qquad \ldots(A8)$$

and

$$Q_- = (u_1^2 - a_1^2)$$

$$Q_+ = (u_2^2 - a_2^2) \qquad \ldots(A9)$$

$$R_- = 2u_1 v_1 - Q_- \lambda_-$$

$$R_+ = 2u_2 v_2 - Q_+ \lambda_+ \qquad \ldots(A10)$$

The properties of points 1 and 2 are known and so a prediction of the properties of point 3 can be made by the simultaneous solution of equations A7.

There are two methods of improving the prediction of the position and properties at point 3: the average property method and the average coefficient method. The average property method involves replacing the properties of equations A6, A9 and A10, initially assumed to be of points 1 and 2, by the averages of points 1 and 3 and points 2 and 3 respectively. Thus, for example, in equation A9 u_1 becomes $(u_1 + u_3)/2$ and a_1 becomes $(a_1 + a_3)/2$. The new coefficients Q, R, T and λ are calculated and equations A5 solved simultaneously to give a corrected prediction of point 3 and equations A7 solved simultaneously to give a corrected prediction of the properties at point 3. The corrector can then be reapplied until the change of the position and properties of point 3 from their previous estimate is sufficiently small.

The average coefficient method involves replacing the coefficients Q, R and λ by the average of the coefficients of points 1 and 3 and points 2 and 3. Thus, for example, in equation A9

$$Q_- = [(Q_-)_1 + (Q_-)_3]/2$$
$$= [(u_1^2 - a_1^2) + (u_3^2 - a_3^2)]/2$$
$$Q_+ = [(Q_+)_2 + (Q_+)_3]/2$$
$$= [(u_2^2 - a_2^2) + (u_3^2 - a_3^2)]/2$$

The values of the coefficients can then be used to obtain a new estimate of the position of point 3 from the simultaneous solution of equations A5 and of the properties from the simultaneous solution of equations A7. The corrector can then be reapplied until the desired convergence of the position and properties of point 3 has been obtained.

APPENDIX B

PARABOLIC INTERPOLATION

The values of the surface static pressure are known at three values of the angle round the Coanda, ϕ (points 1, 2 and 3). It is desired to interpolate for the value of the static pressure at an angle ϕ, where $\phi_2 < \phi < \phi_3$.

Kreyszig (1972) gives the Lagrange's interpolation formula as

$$f(\phi) \approx L_n(\phi) = \sum_{k=1}^{n} \frac{l_k(\phi)}{l_k(\phi_k)} \cdot f(\phi_k) \qquad \ldots(B1)$$

where $\phi_1 \ldots \phi_n$ are not necessarily equally spaced and

$$l_1(\phi) = (\phi - \phi_2)(\phi - \phi_3) \ldots (\phi - \phi_n)$$

$$l_k(\phi) = (\phi - \phi_1) \ldots (\phi - \phi_{k-1})(\phi - \phi_{k+1}) \ldots (\phi - \phi_n)$$

$$l_n(\phi) = (\phi - \phi_1)(\phi - \phi_2) \ldots (\phi - \phi_{n-1}) \qquad \ldots(B2)$$

In the present case n = 3, and thus equation B1 becomes

$$p = \frac{(\phi-\phi_2)(\phi-\phi_3)}{(\phi_1-\phi_2)(\phi_1-\phi_3)} p_1 + \frac{(\phi-\phi_1)(\phi-\phi_3)}{(\phi_2-\phi_1)(\phi_2-\phi_3)} p_2 + \frac{(\phi-\phi_1)(\phi-\phi_2)}{(\phi_3-\phi_1)(\phi_3-\phi_2)} p_3 \qquad \ldots(B3)$$

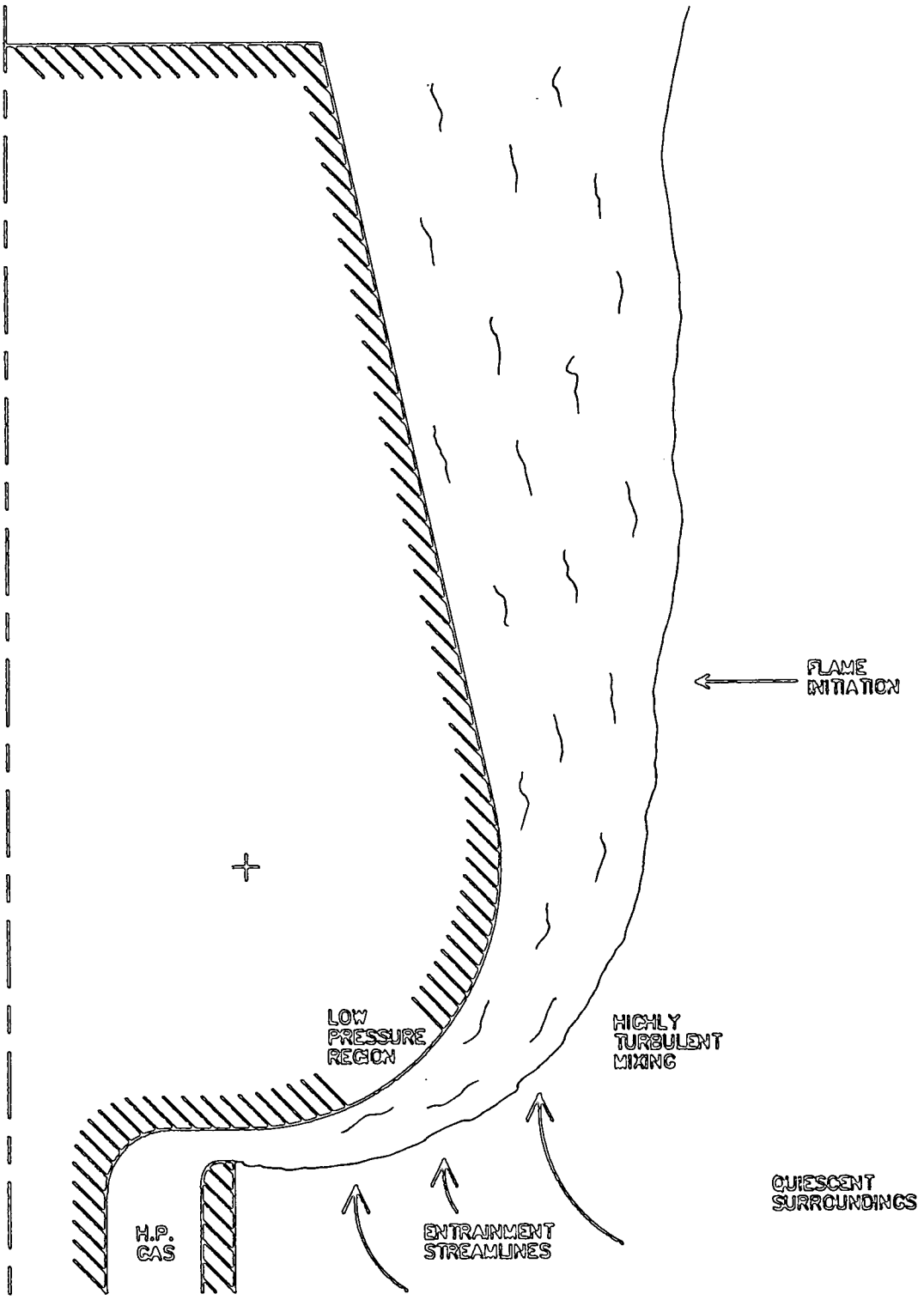

FIG 1.1 : PRINCIPLES OF THE COANDA FLARE

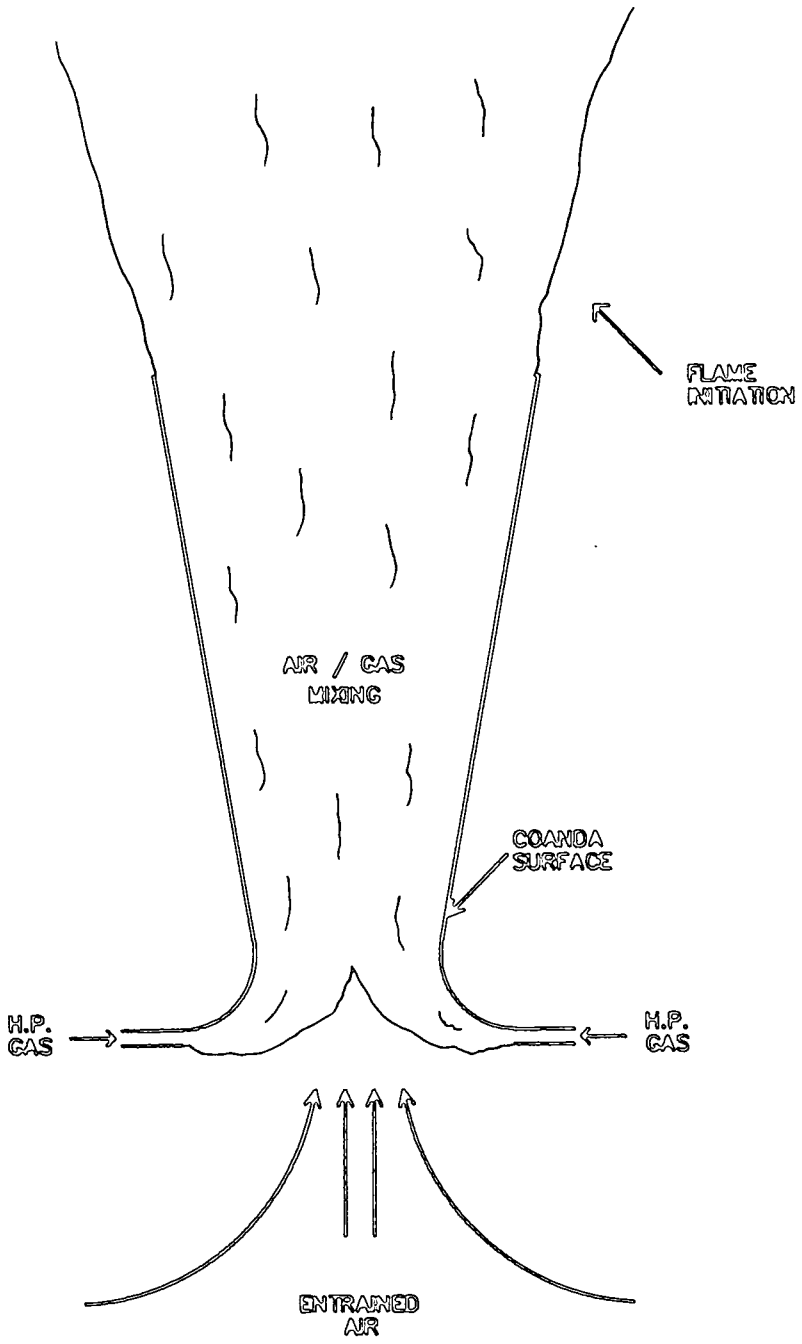

FIG 1.2 : PRINCIPLES OF THE MARDAIR FLARE

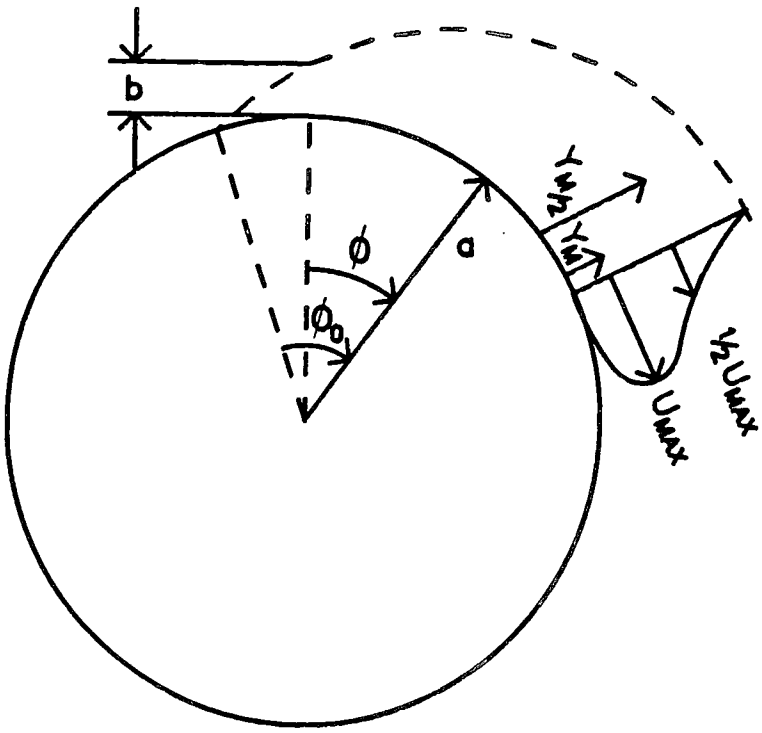

FIG 2.1 : CURVED JET

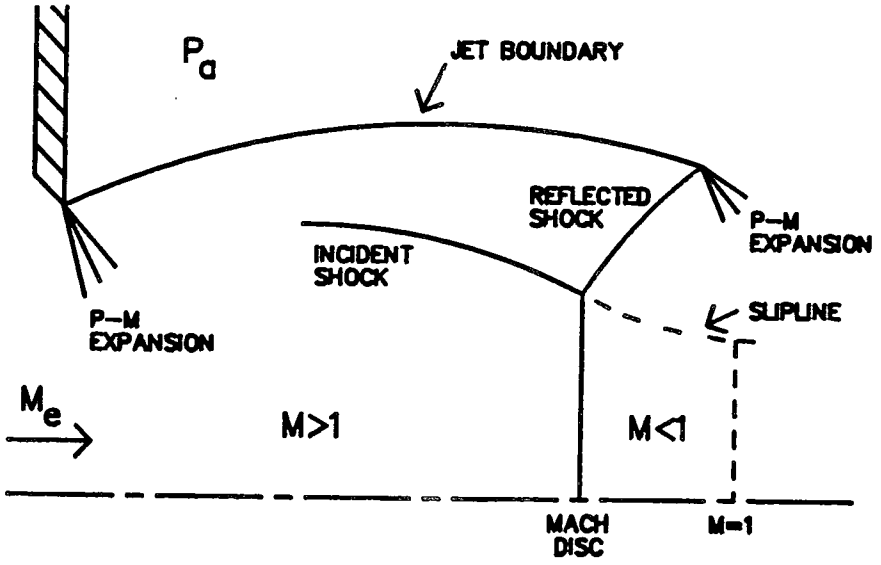

FIG 2.2 : SHOCK CELL STRUCTURE

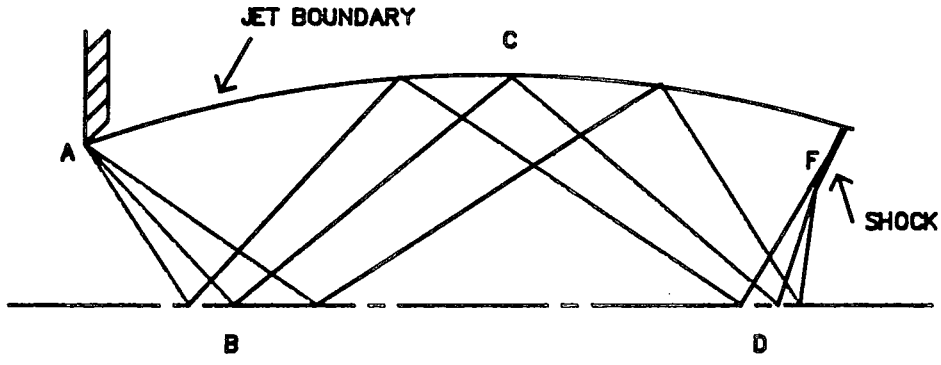

FIG 2.3A : WEAK SHOCK

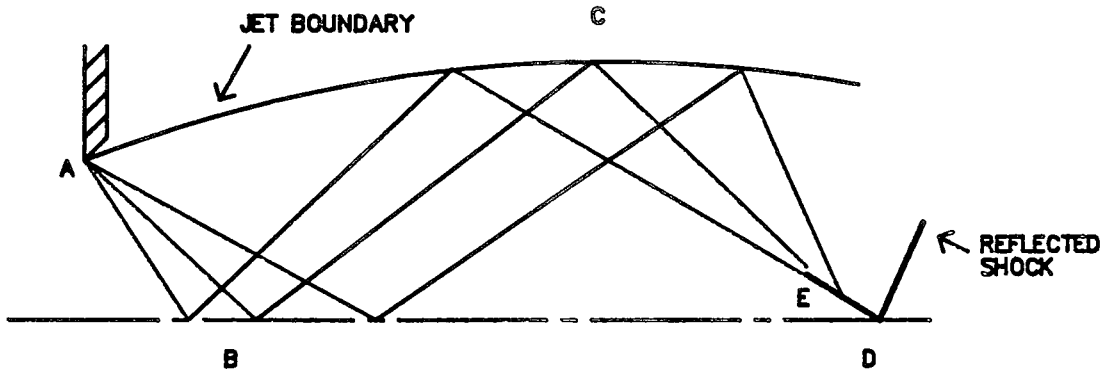

FIG 2.3B : STRONG REFLECTION

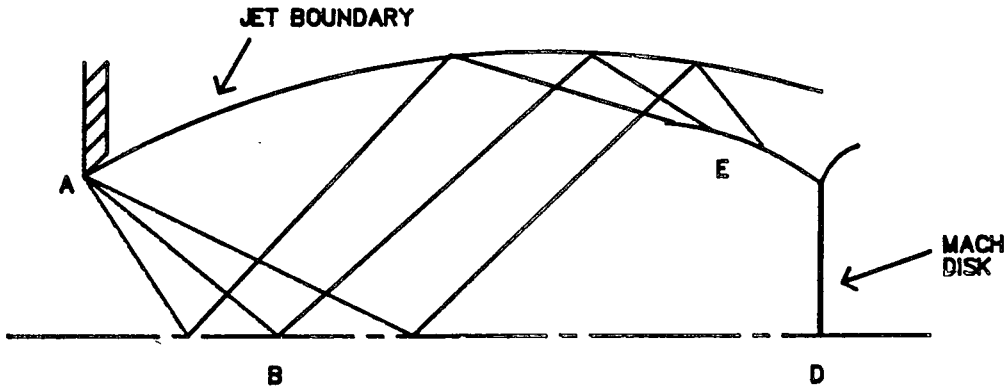

FIG 2.3C : MACH DISK

FIG 2.3 : SHOCK CELL SYSTEMS

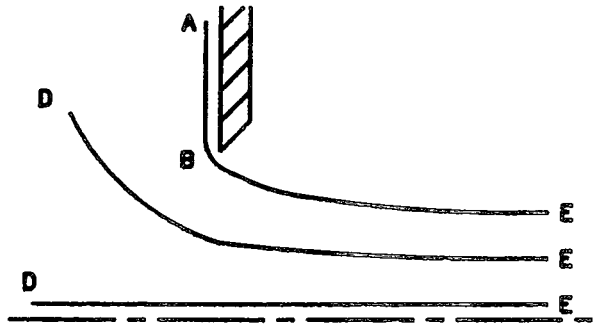

FIG 2.4A : SUBSONIC PRESSURE RATIO

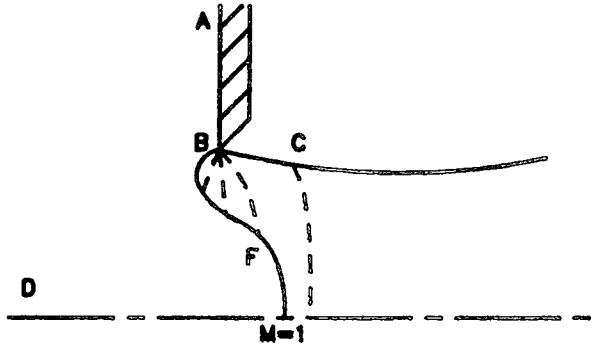

FIG 2.4B : SUBCRITICAL PRESSURE RATIO

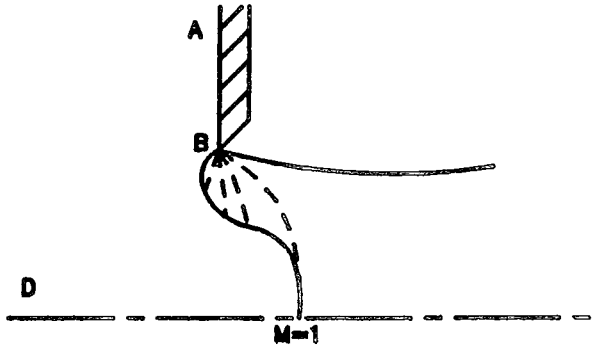

FIG 2.4C : CHOKED PRESSURE RATIO

FIG 2.4 : DISCHARGE THROUGH AN ORIFICE

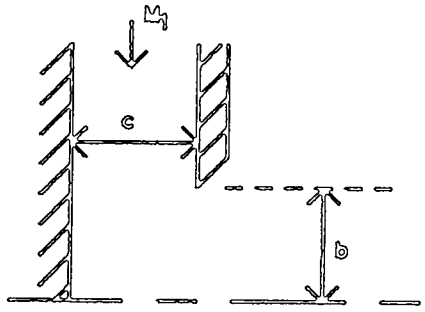

FIG 2.5A : NORWOOD (1962)

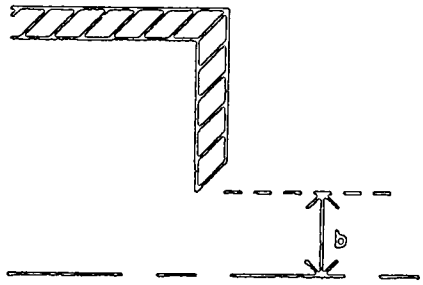

FIG 2.5B : BENSON AND POOLE (1965B)

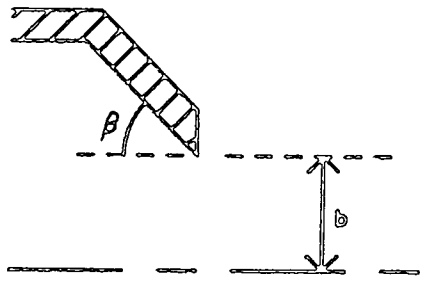

FIG 2.5C : ADLER (1979)

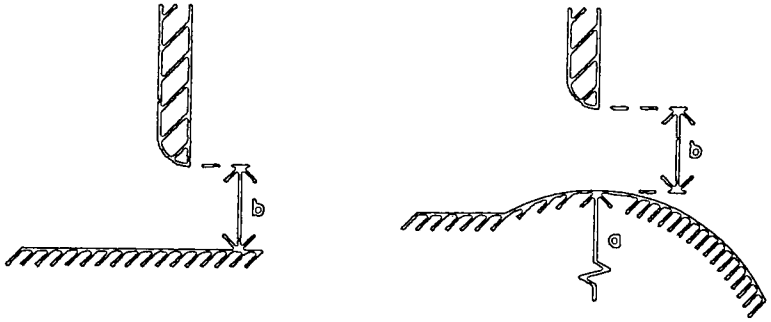

FIG 2.5D : GREGORY-SMITH AND ROBINSON (1982)

FIG 2.5 : PLANE SLOTS INVESTIGATED

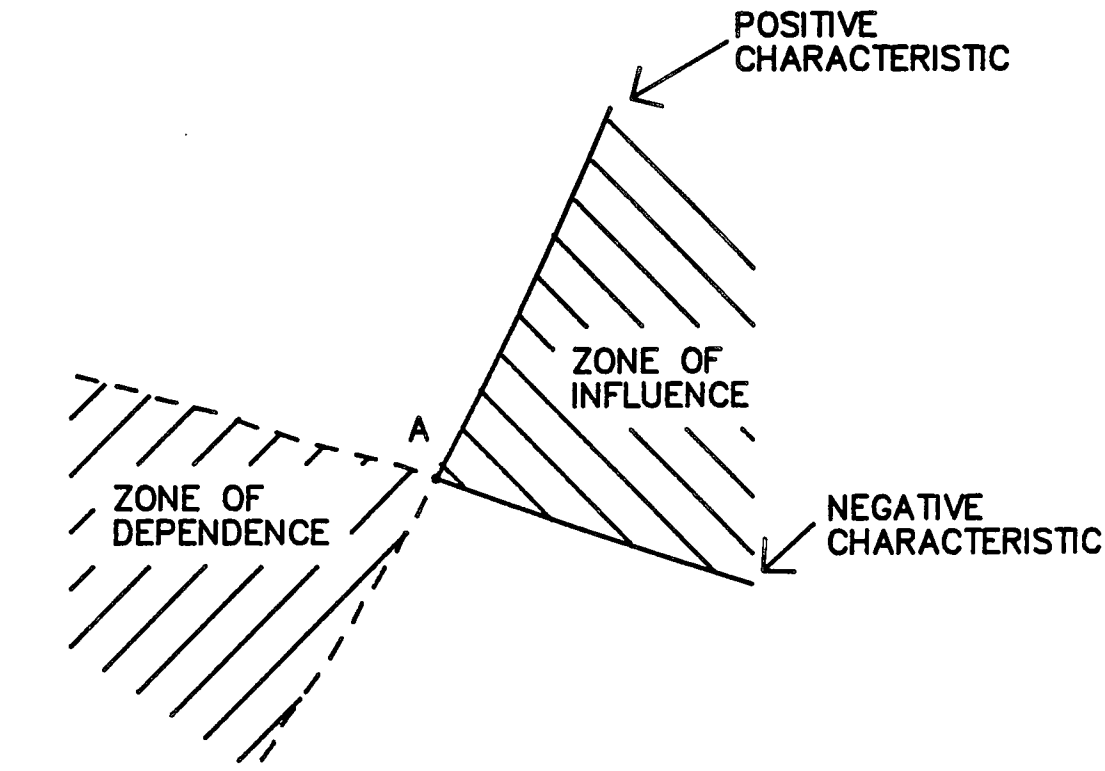

FIG 3.1A : REGIONS OF DEPENDENCE

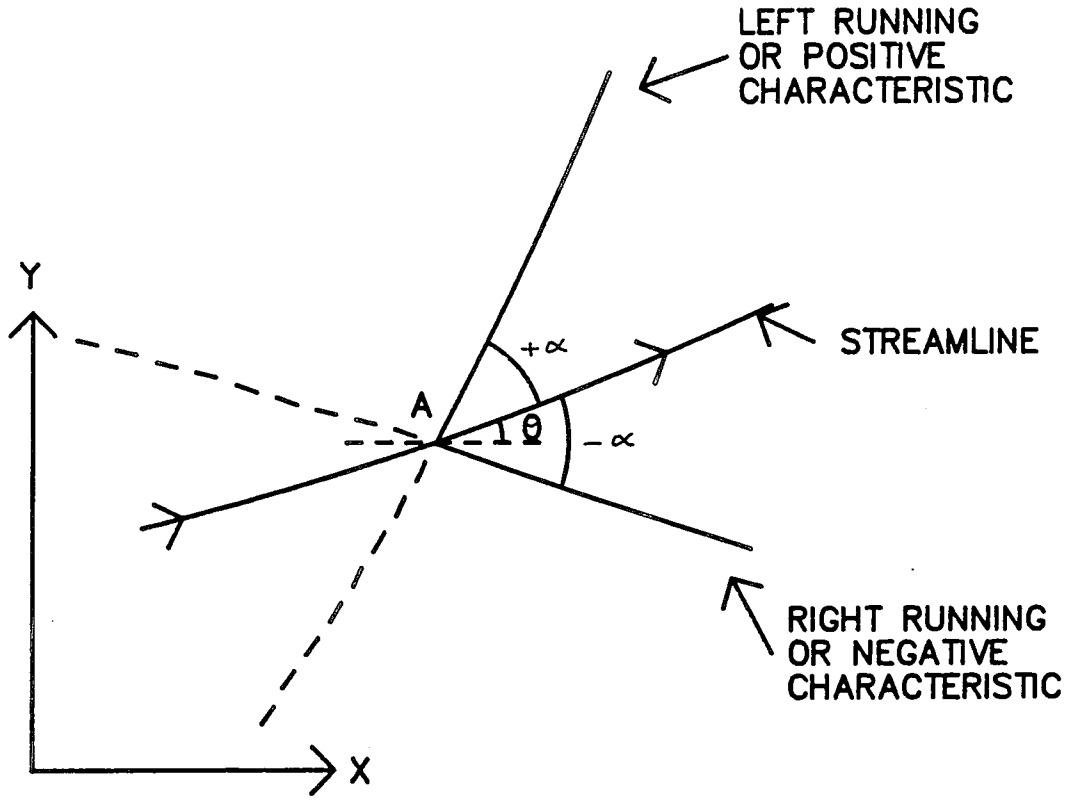

FIG 3.1B : ANGLES OF CHARACTERISTICS

FIG 3.1 : CHARACTERISTICS IN SUPERSONIC FLOW

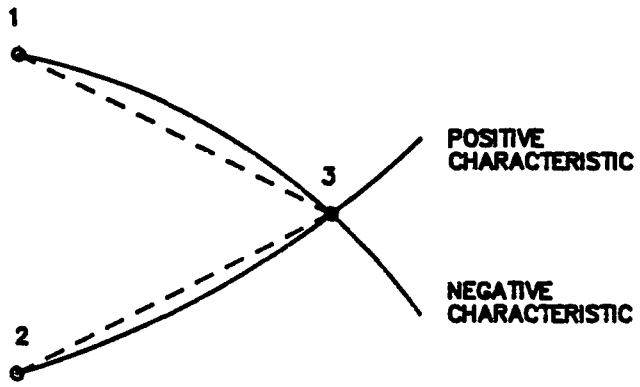

FIG 3.2 : INTERIOR POINT SOLUTION

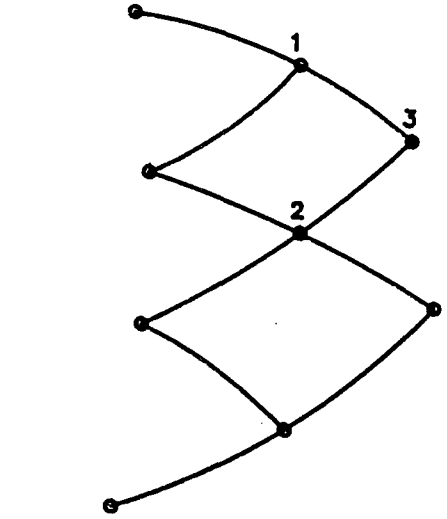

FIG 3.3A : DIRECT MARCHING

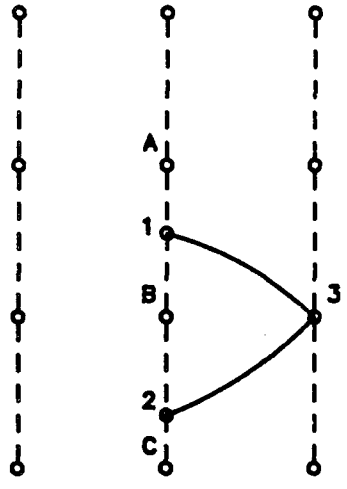

FIG 3.3B : INVERSE MARCHING

FIG 3.3 : MARCHING GRIDS IN IRROTATIONAL FLOW

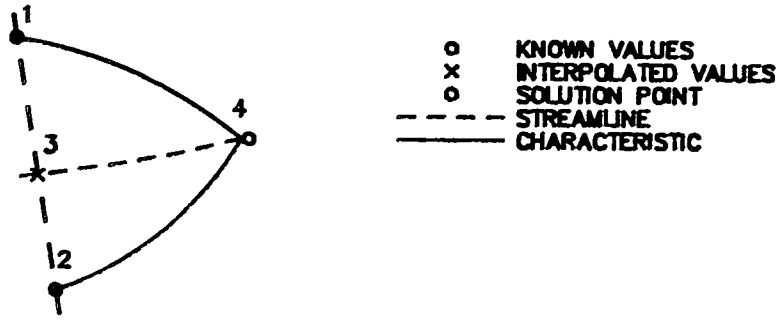

FIG 3.4 : MARCHING GRID IN ROTATIONAL FLOW

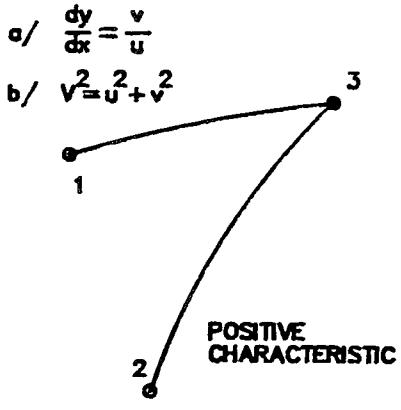

FIG 3.5A : UPPER BOUNDARY

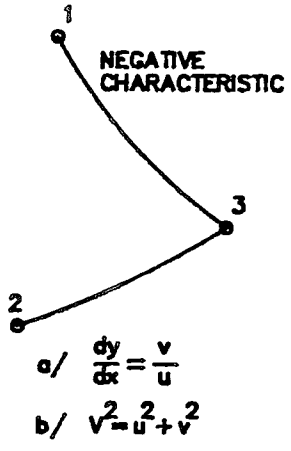

FIG 3.5B : LOWER BOUNDARY

FIG 3.5 : FREE PRESSURE BOUNDARY

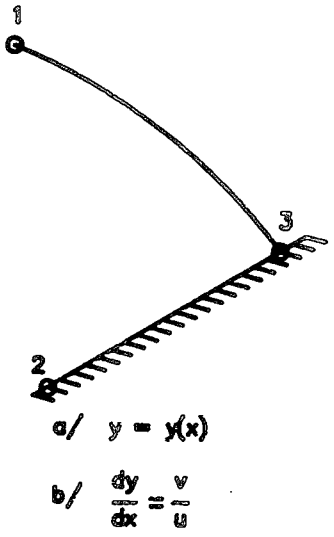

FIG 3.6 : SOLID BOUNDARY

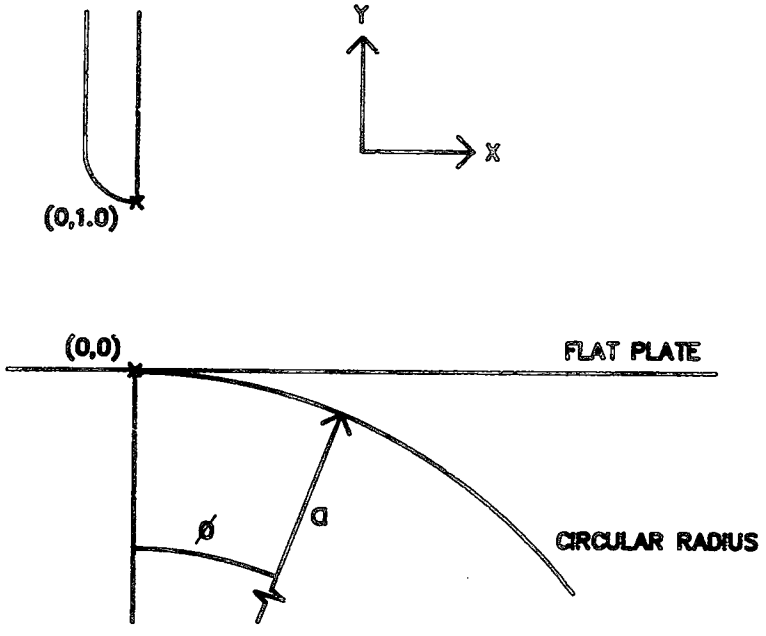

FIG 3.7 : COORDINATE SYSTEM

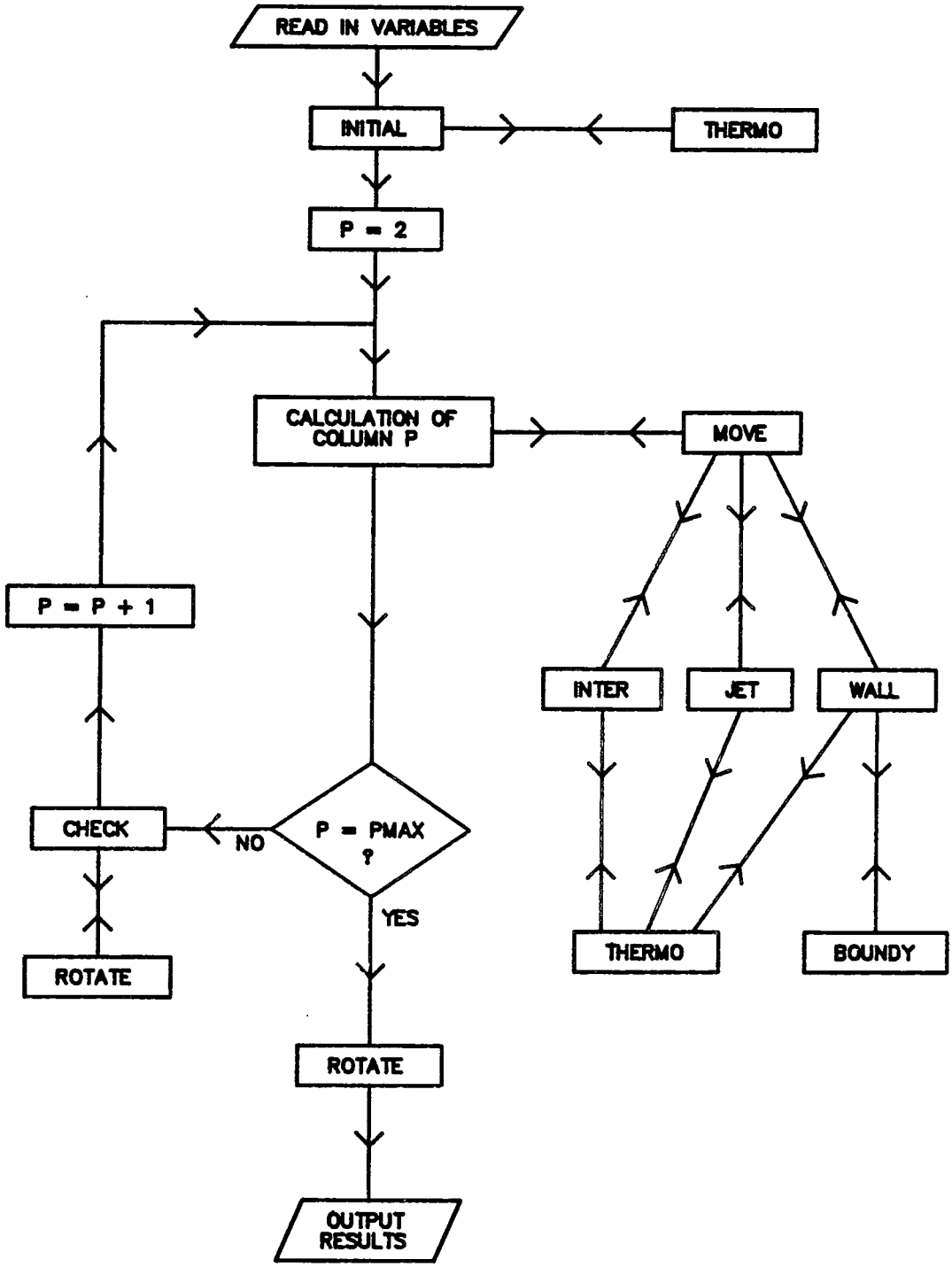

FIG 3.8 : FLOW CHART

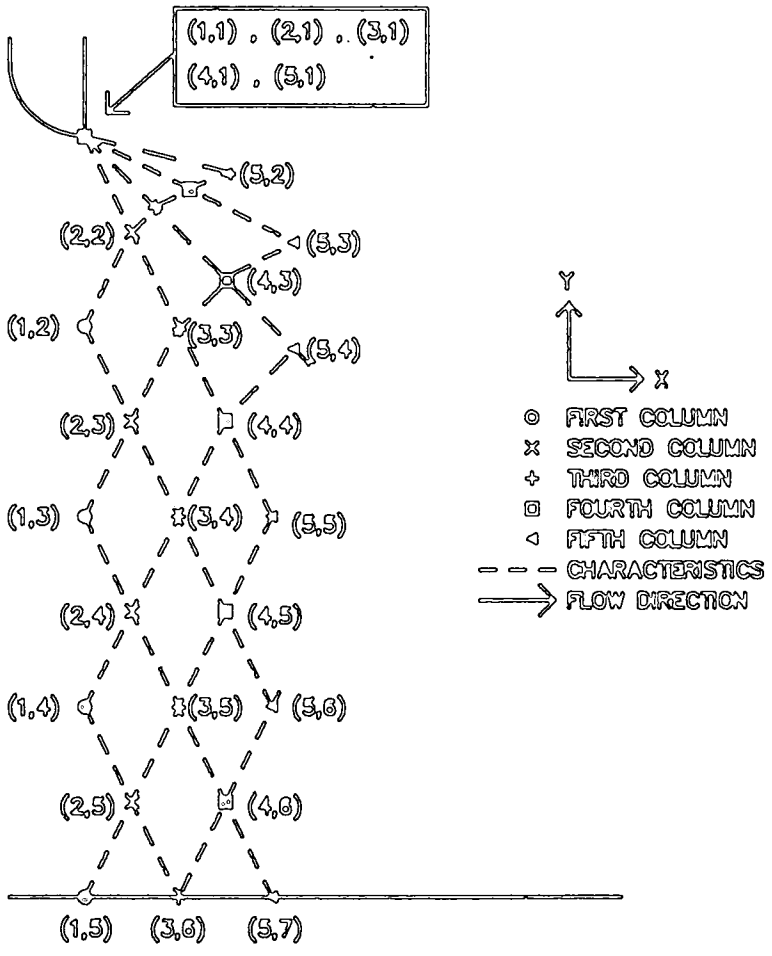

FIG 3.9 : PRANDTL–MEYER EXPANSION

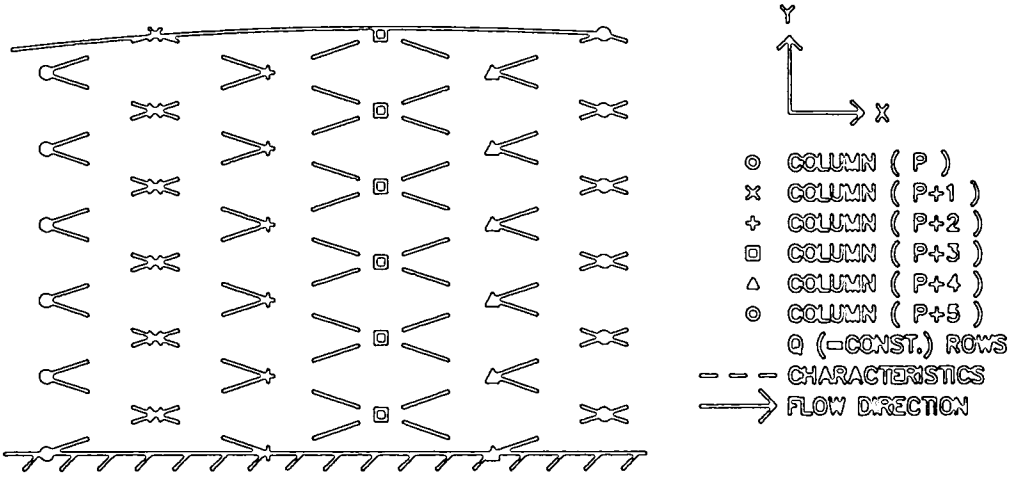

FIG 3.10 : MARCHING SCHEME

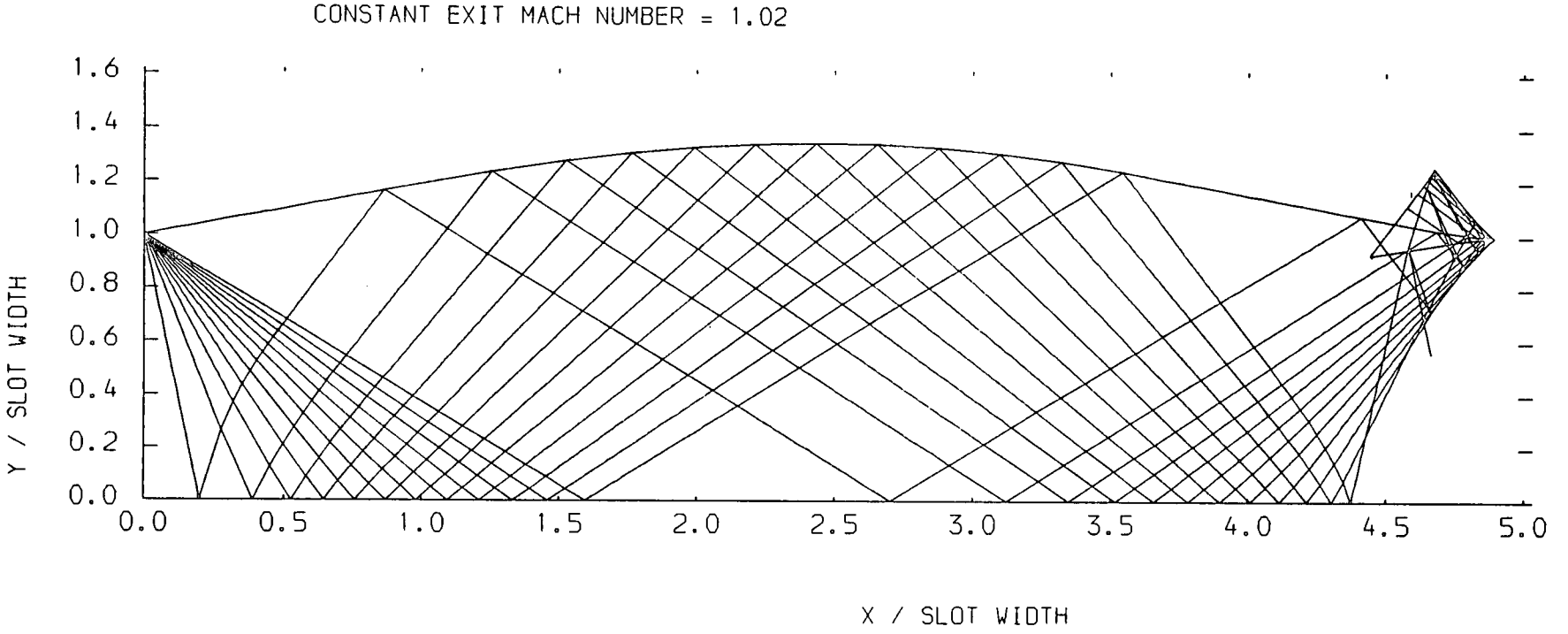

FIG 3.11 :- UNDEREXPANDED JET OVER A FLAT SURFACE , Pa/Po = 0.286

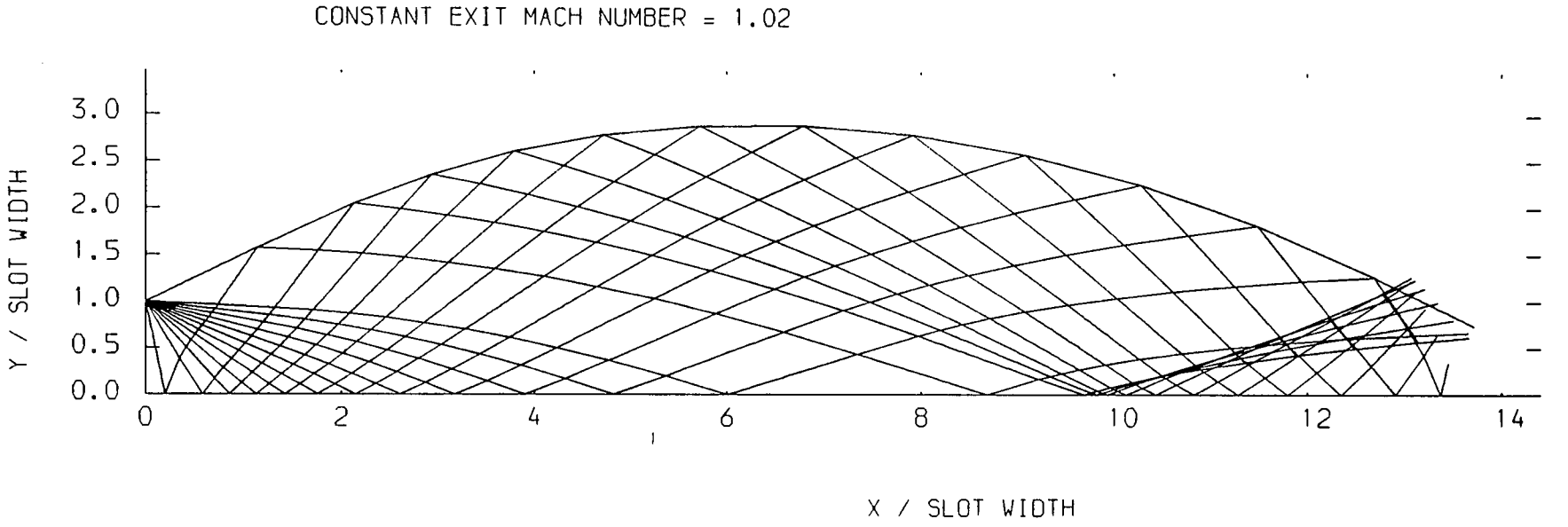

FIG 3.12 :- UNDEREXPANDED JET OVER A FLAT SURFACE , Pa/Po = 0.123

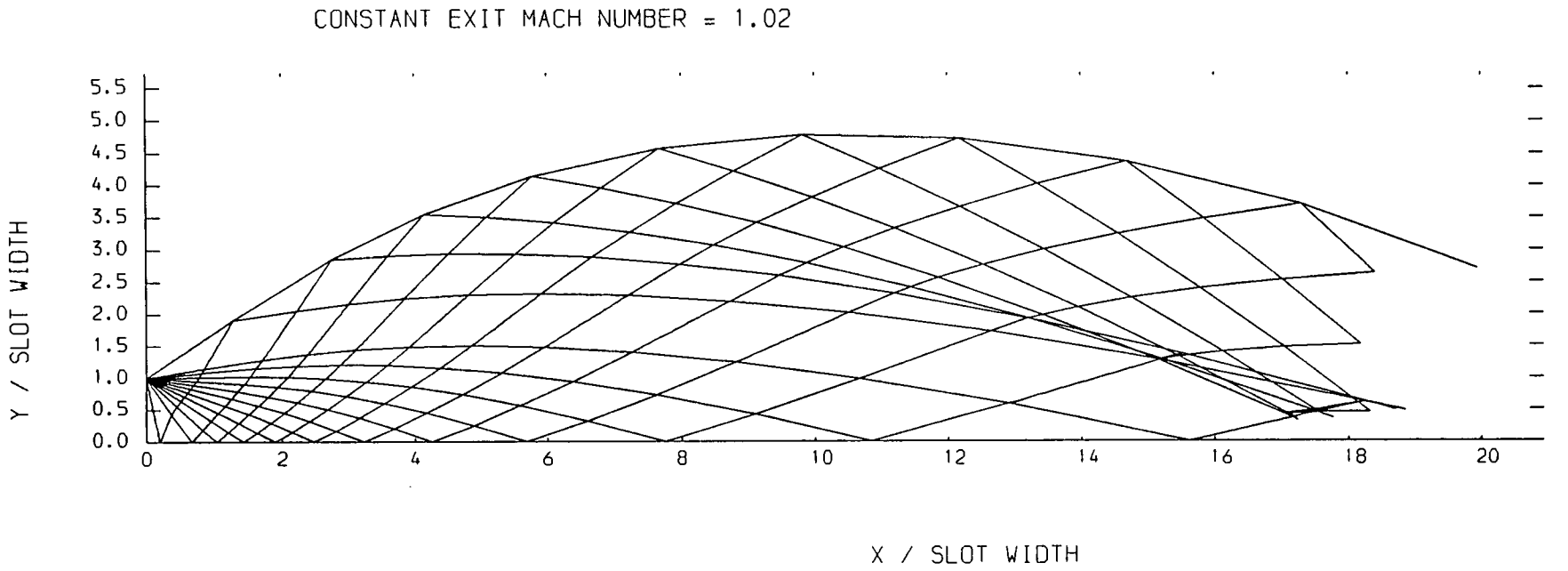

FIG 3.13 :- UNDEREXPANDED JET OVER A FLAT SURFACE , Pa/Po = 0.075

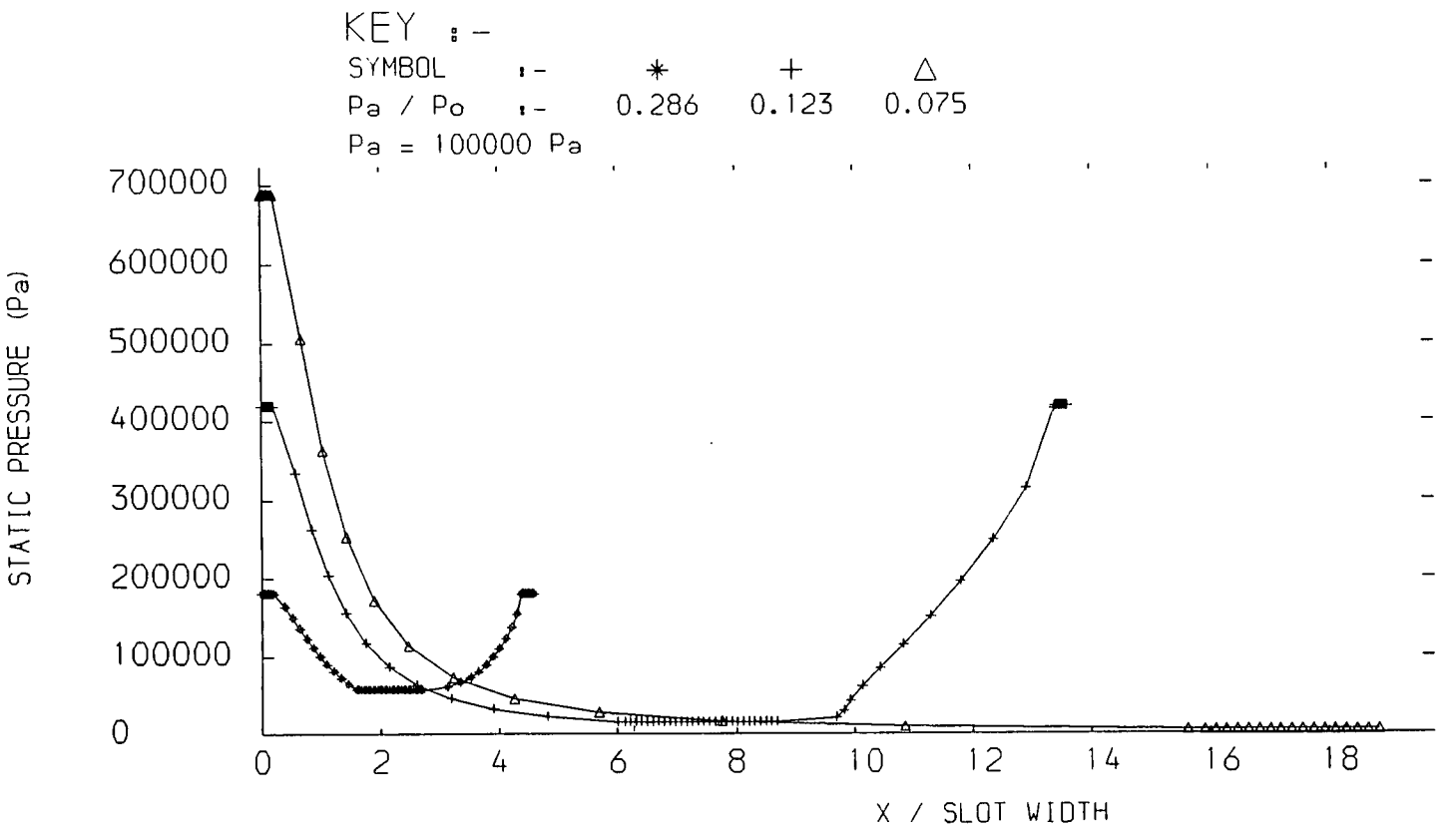

FIG 3.14 :- STATIC PRESSURE DISTRIBUTION OVER A FLAT PLATE

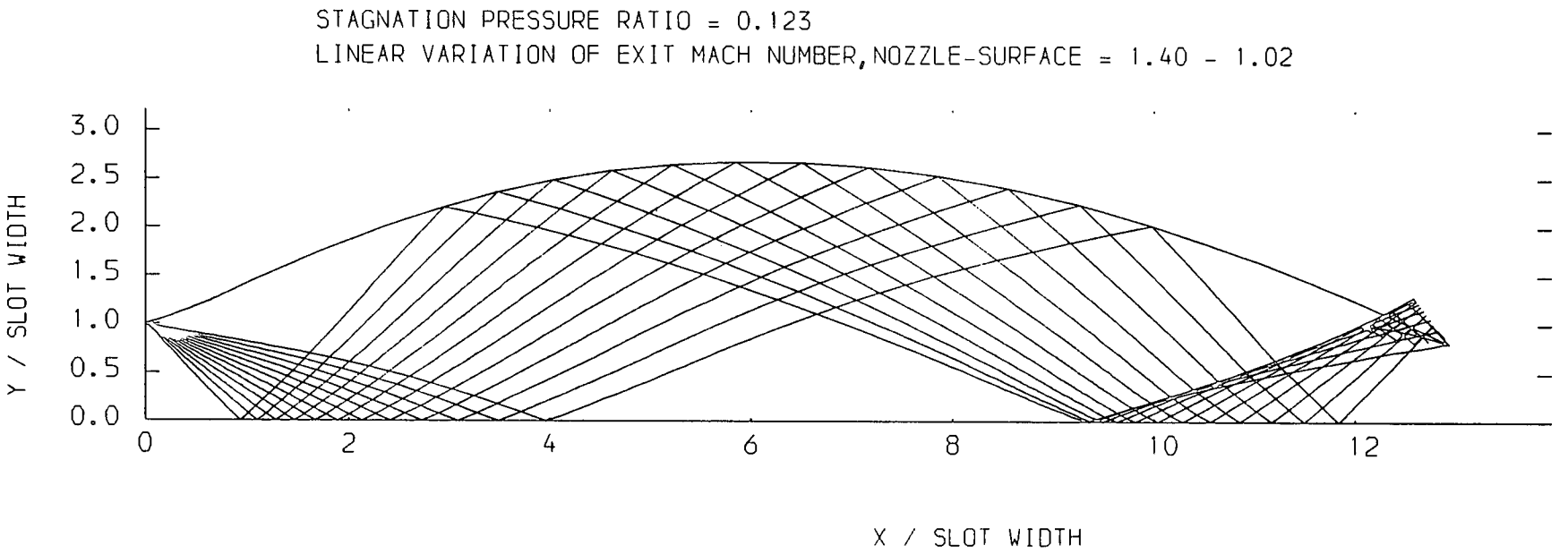

FIG 3.15 :- VARIATION OF EXIT MACH NUMBER

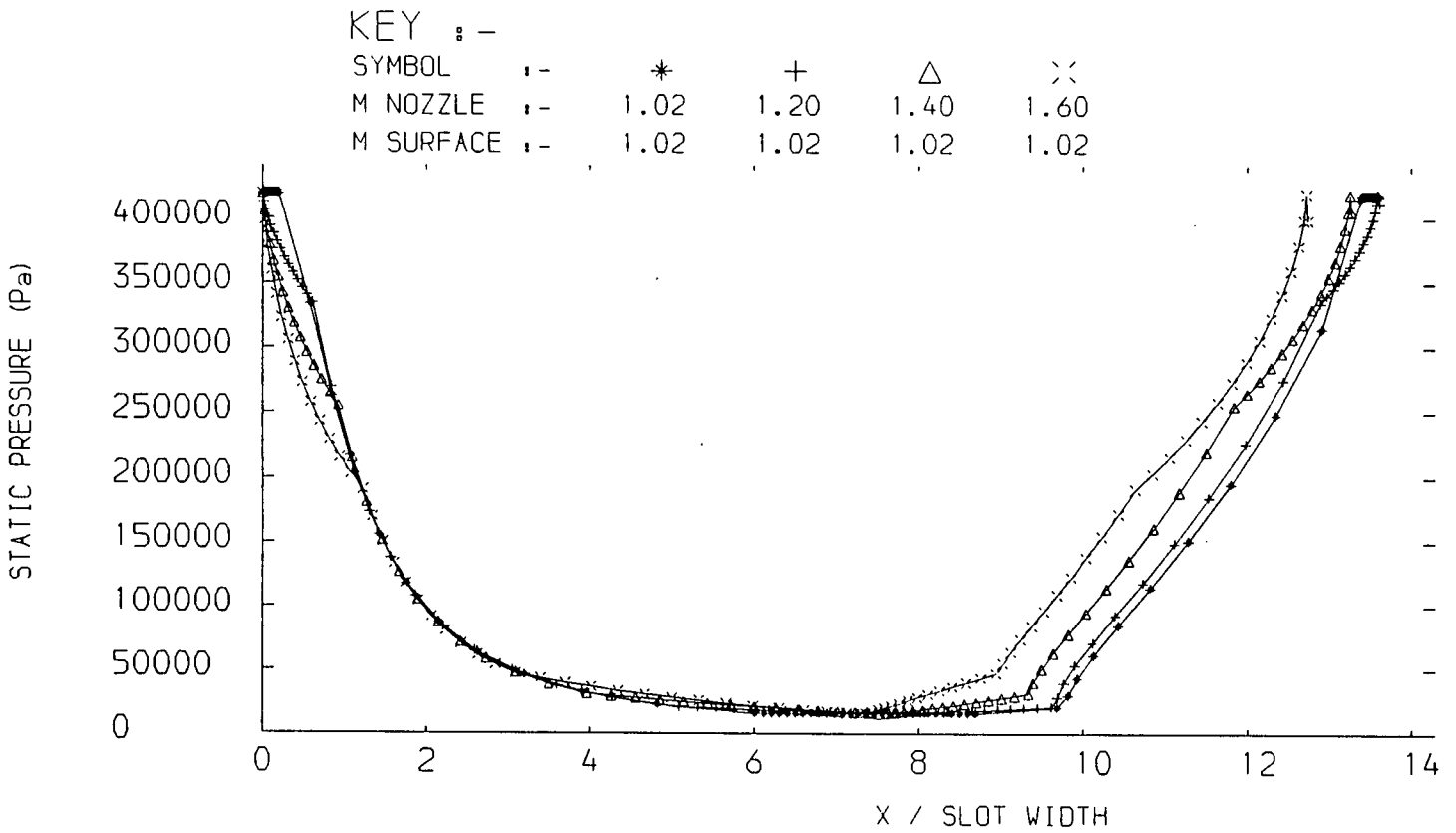

FIG 3.16 :- VARIATION OF EXIT MACH NUMBER , Pa/Po = 0.123

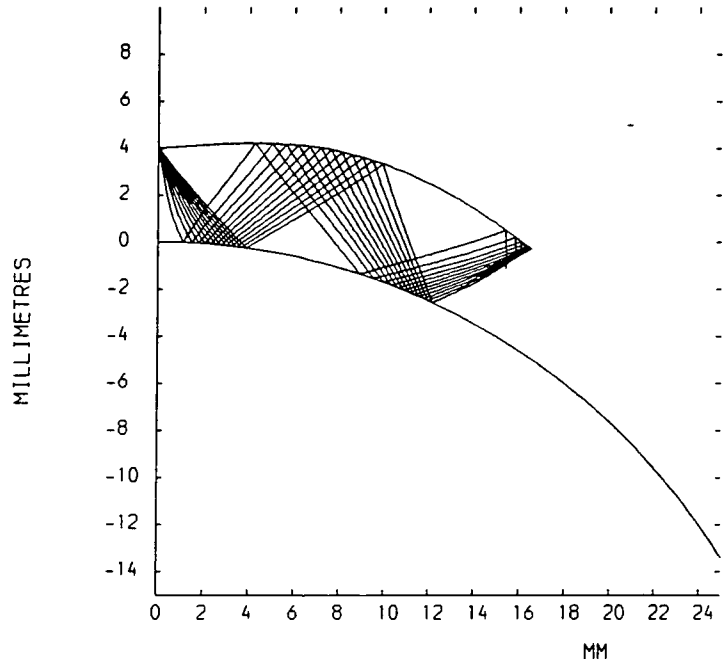

FIG 3.17A :- STAGNATION PRESSURE RATIO = 0.394

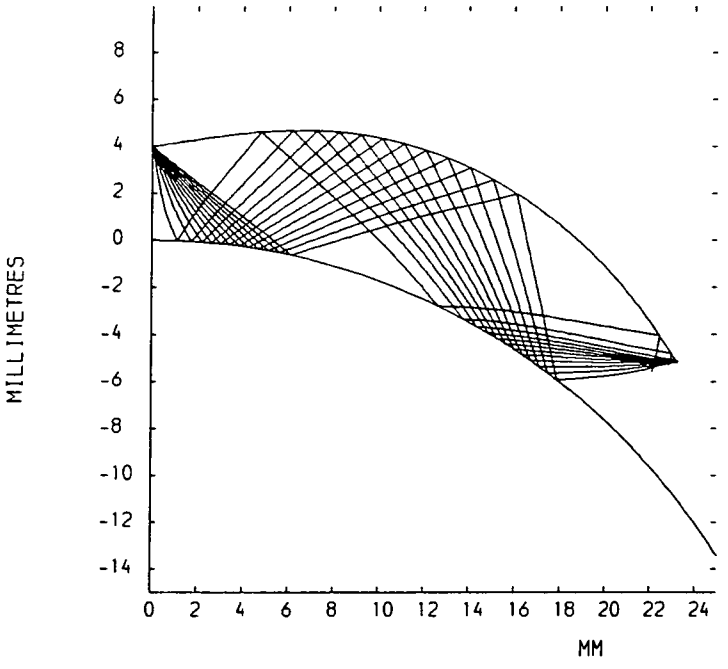

FIG 3.17B :- STAGNATION PRESSURE RATIO = 0.318

FIG 3.17 :- ATTACHED JET , SLOT WIDTH / RADIUS = 0.133

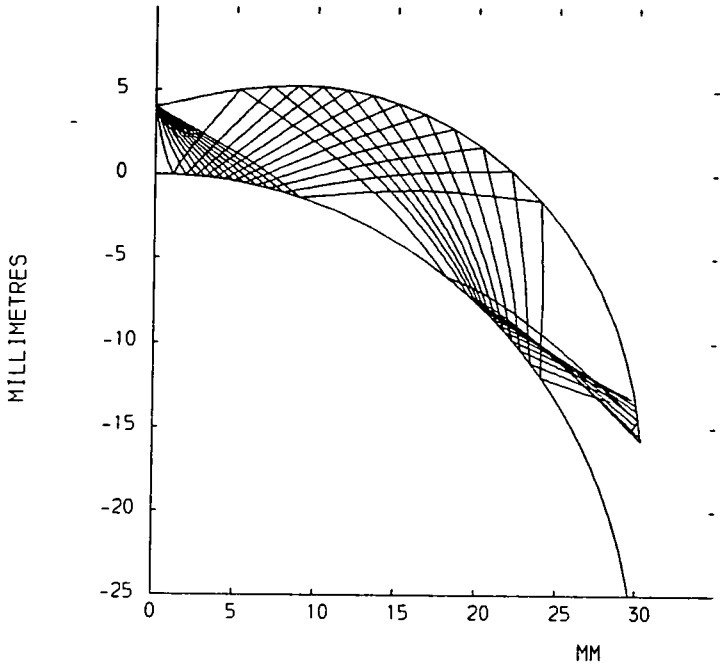

FIG 3.17C :- STAGNATION PRESSURE RATIO = 0.263

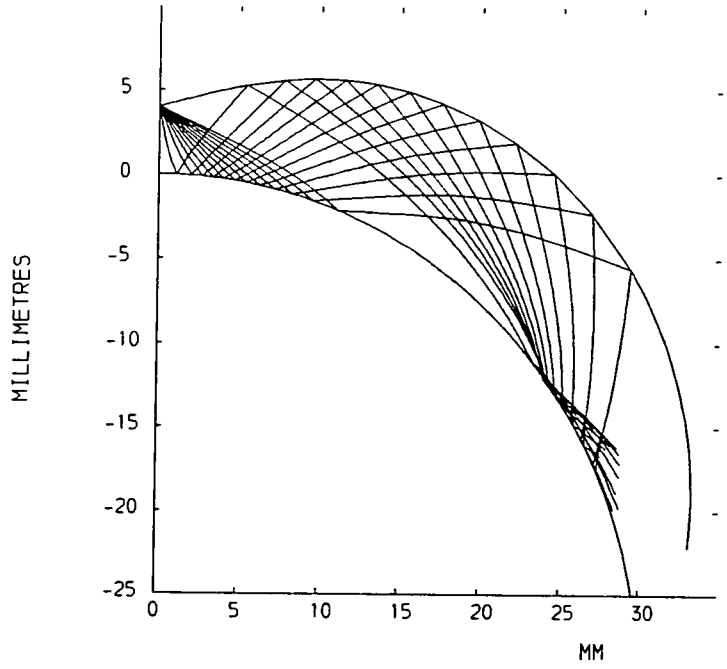

FIG 3.17D :- STAGNATION PRESSURE RATIO = 0.238

FIG 3.17 :- ATTACHED JET , SLOT WIDTH / RADIUS = 0.133

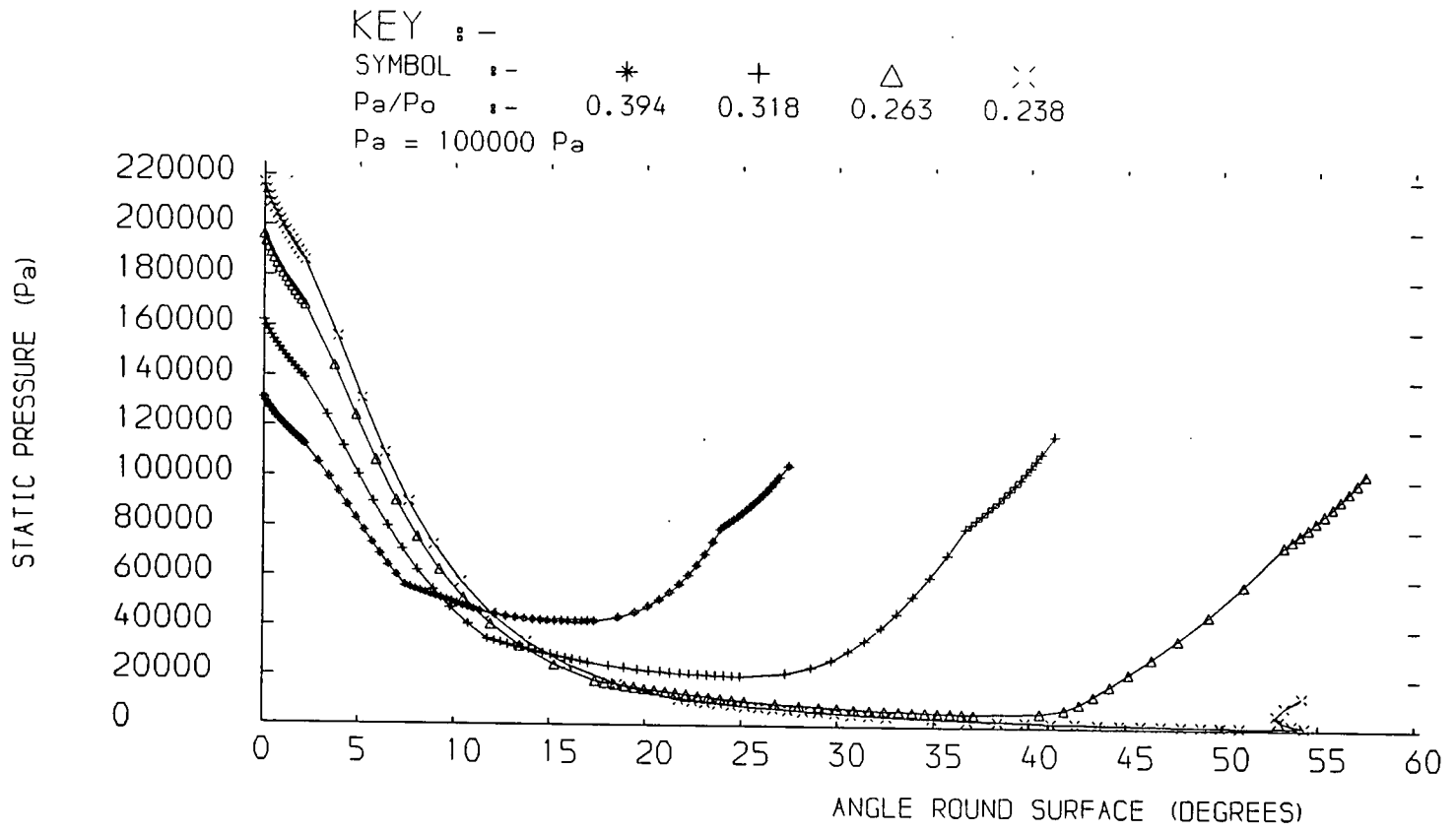

FIG 3.18 :- SURFACE STATIC PRESSURE DISTRIBUTION , b/a=0.133

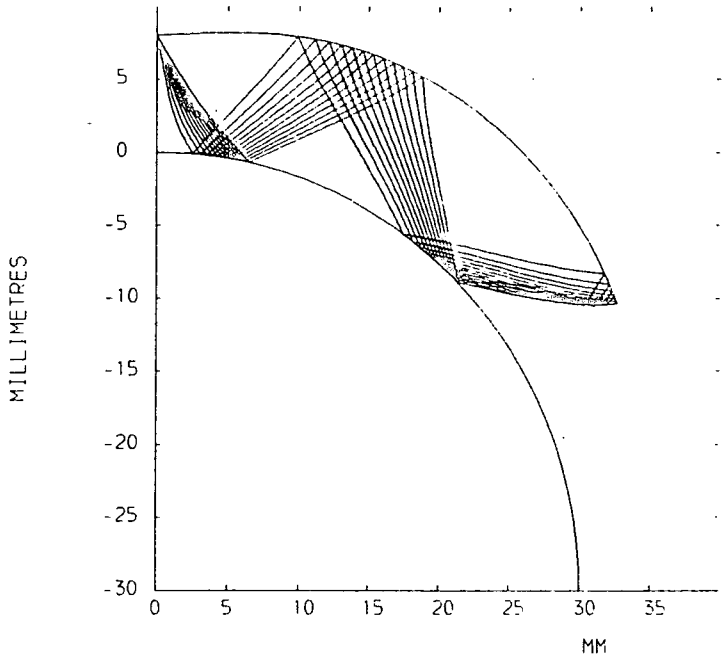

FIG 3.19A :- STAGNATION PRESSURE RATIO = 0.437

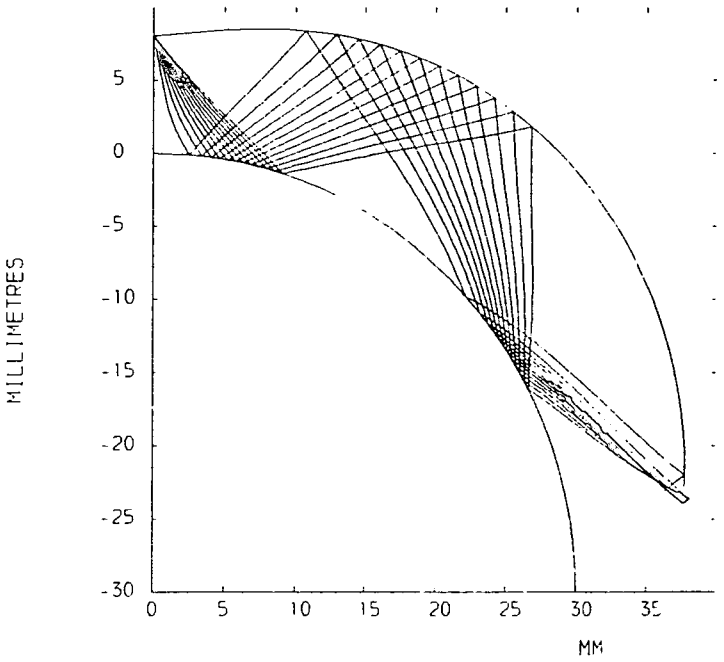

FIG 3.19B :- STAGNATION PRESSURE RATIO = 0.385

FIG 3.19 :- ATTACHED JET , SLOT WIDTH / RADIUS = 0.267

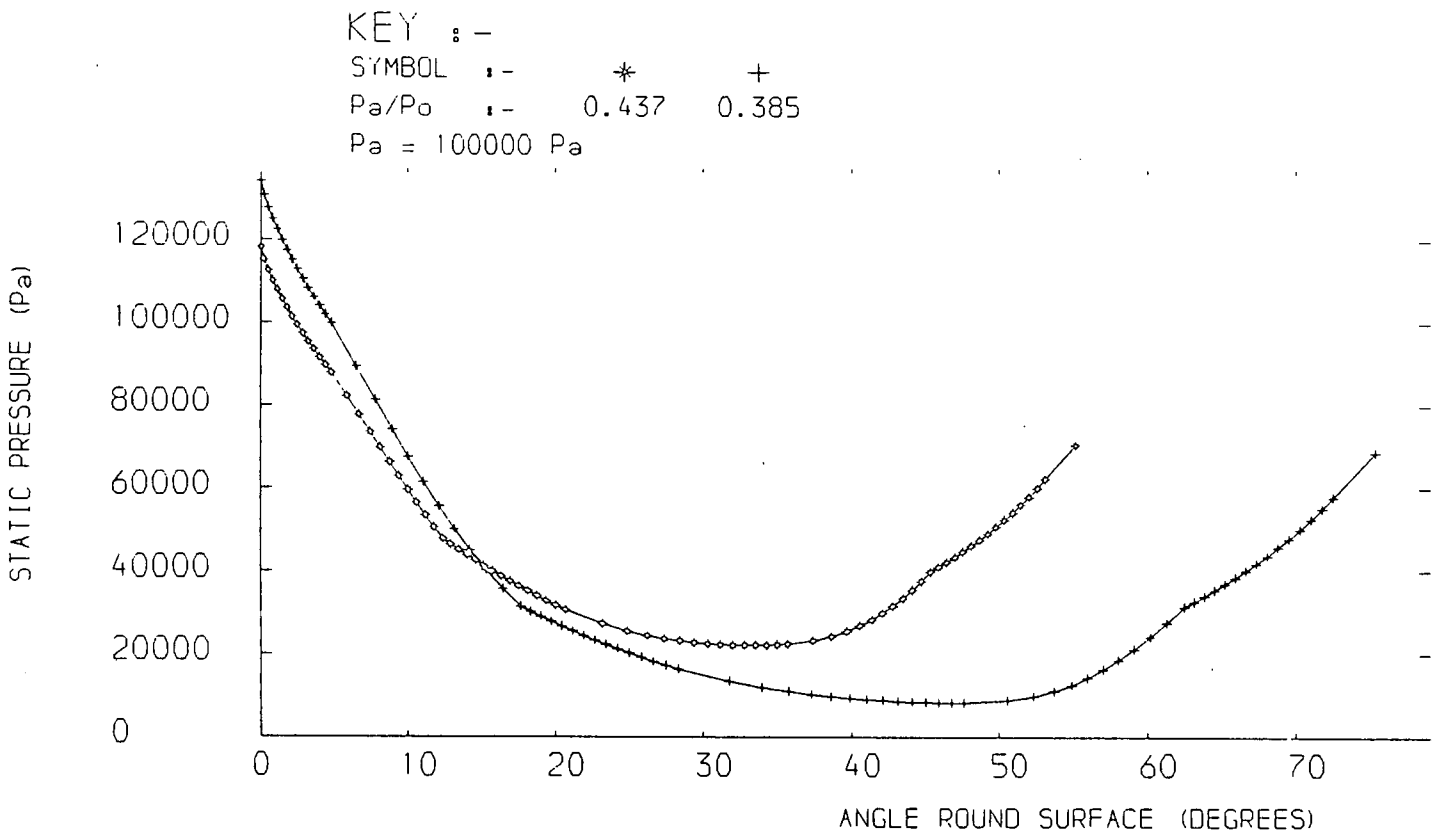

FIG 3.20 :- SURFACE STATIC PRESSURE DISTRIBUTION , b/a=0.267

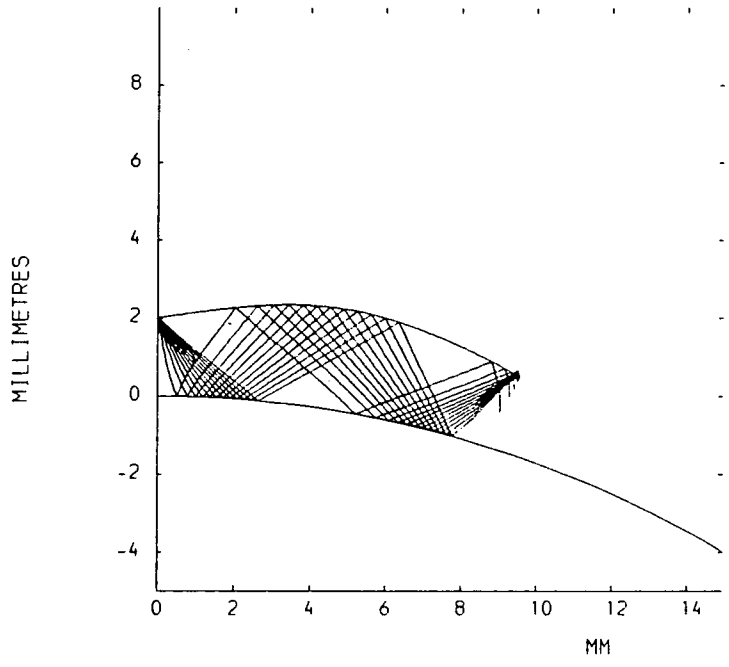

FIG 3.21A :- STAGNATION PRESSURE RATIO = 0.331

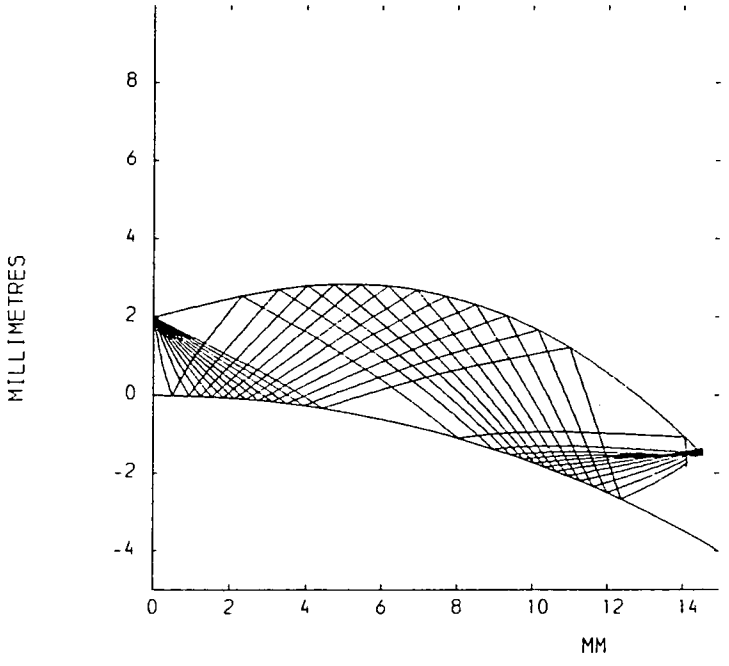

FIG 3.21B :- STAGNATION PRESSURE RATIO = 0.249

FIG 3.21 :- ATTACHED JET , SLOT WIDTH / RADIUS = 0.067

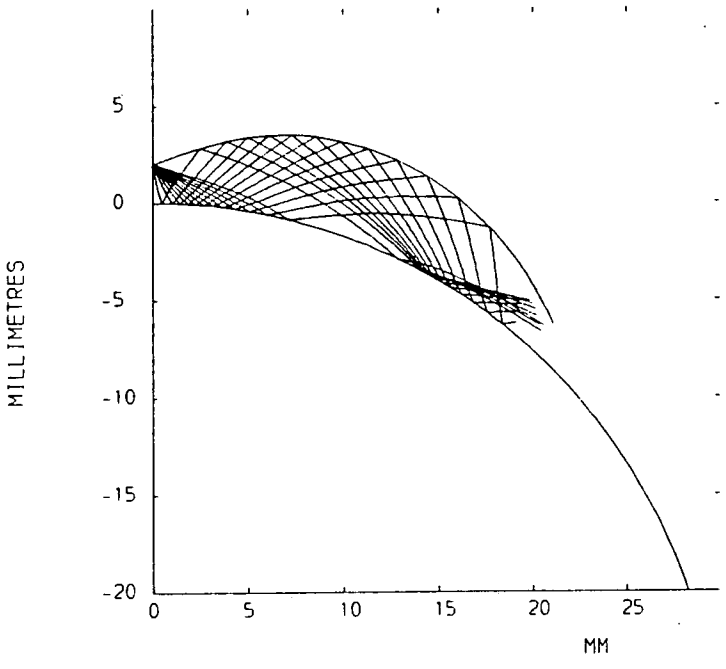

FIG 3.21C :- STAGNATION PRESSURE RATIO = 0.192

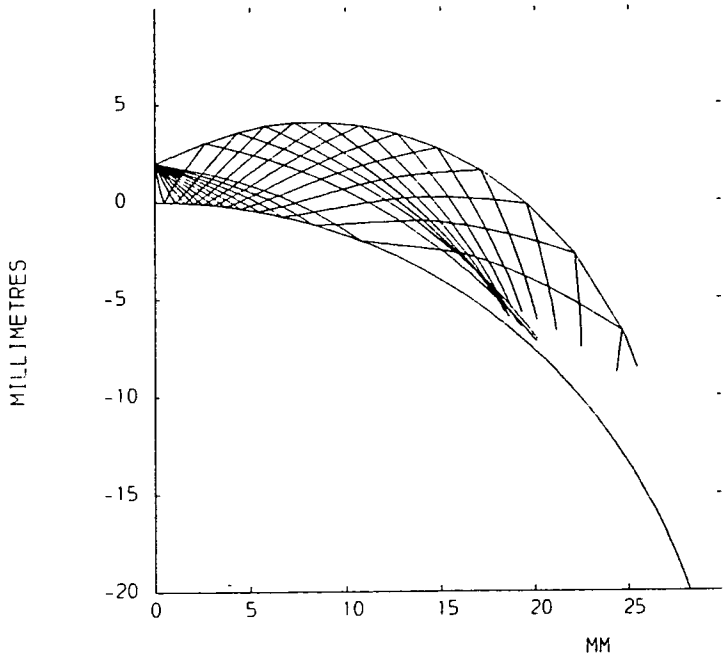

FIG 3.21D :- STAGNATION PRESSURE RATIO = 0.161

FIG 3.21 :- ATTACHED JET , SLOT WIDTH / RADIUS = 0.067

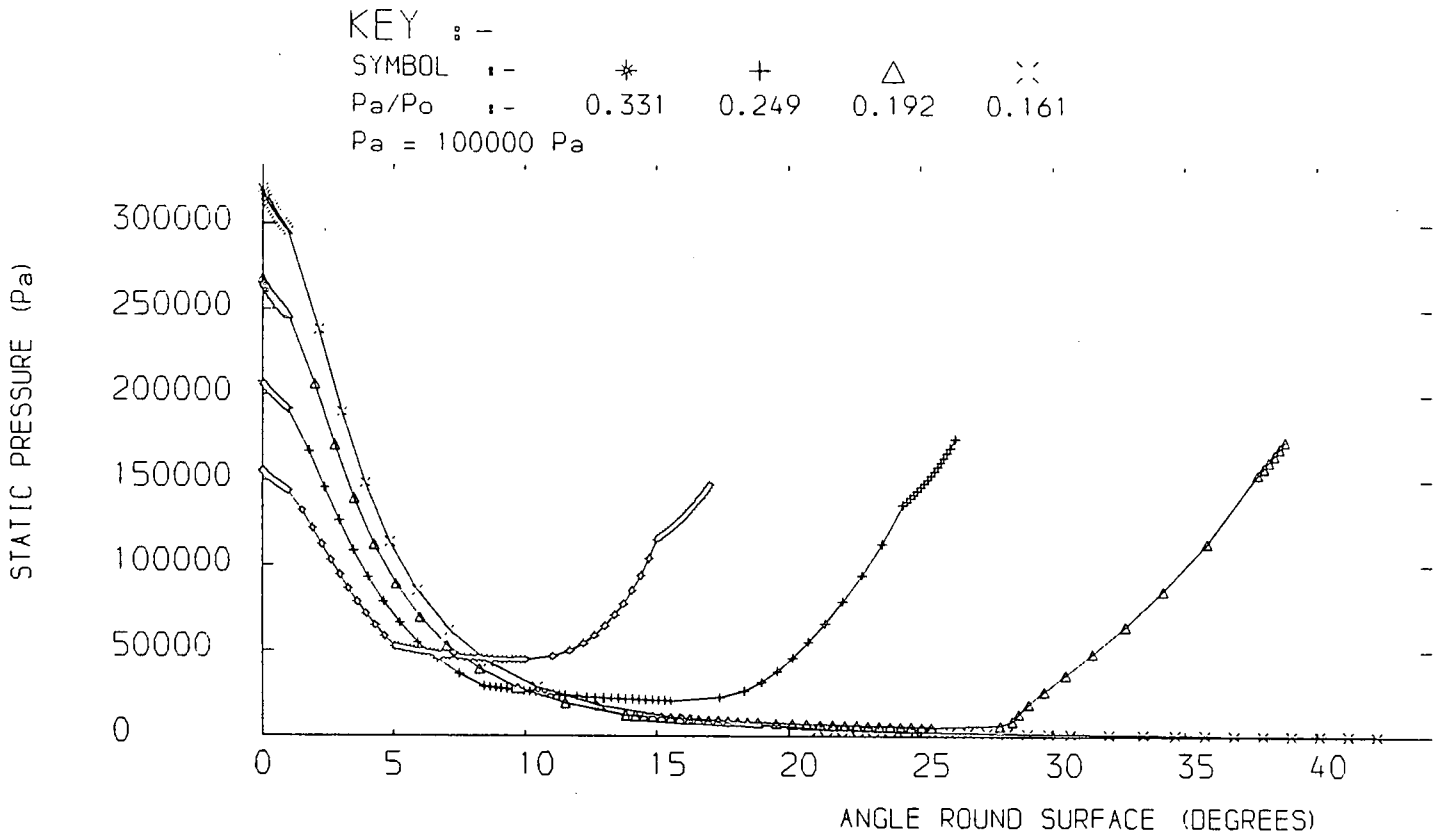

FIG 3.22 :- SURFACE STATIC PRESSURE DISTRIBUTION , b/a=0.067

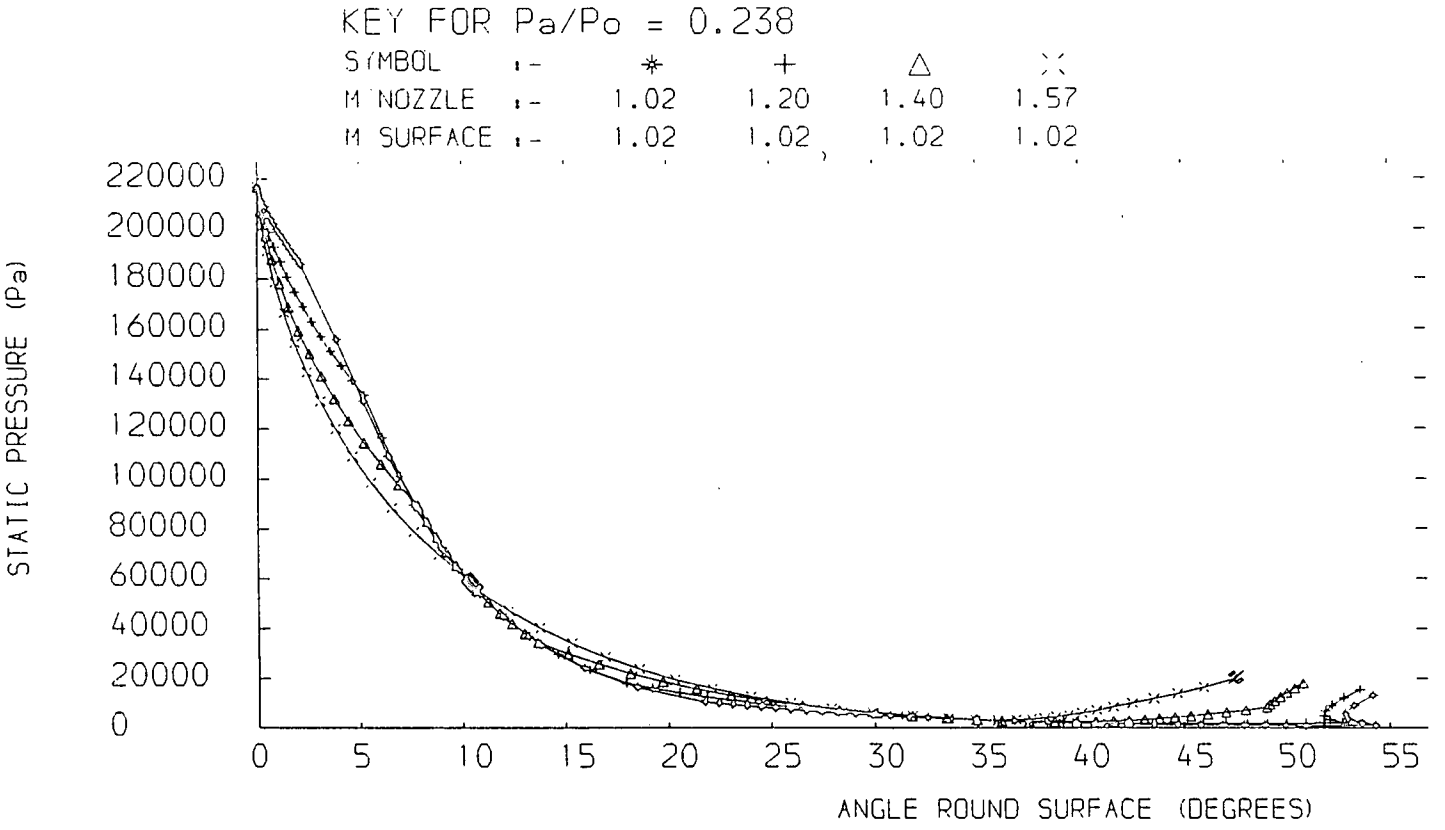

FIG 3.23 :- VARIATION OF EXIT MACH NUMBER , b/a = 0.133

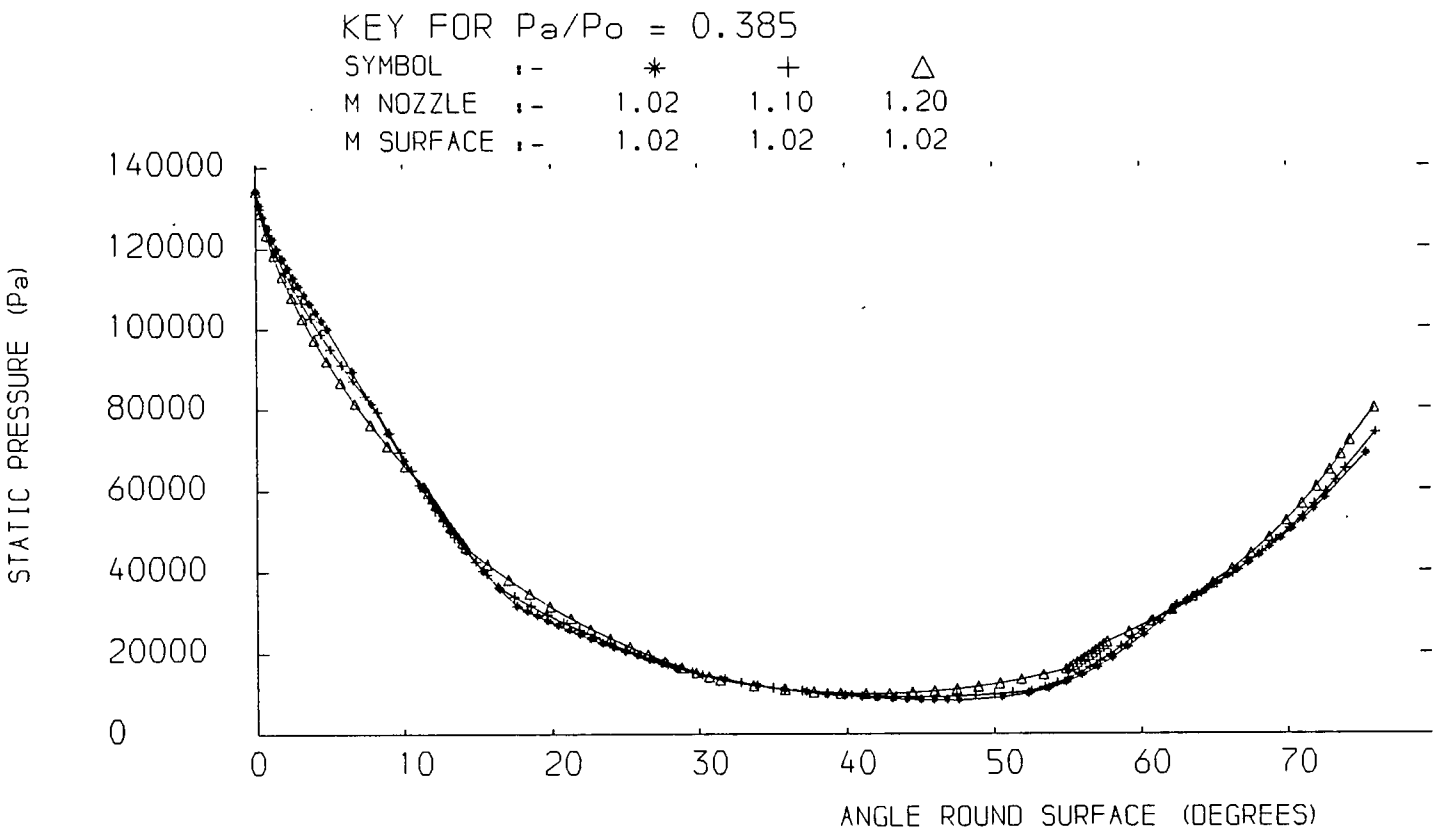

FIG 3.24 :- VARIATION OF EXIT MACH NUMBER , b/a = 0.267

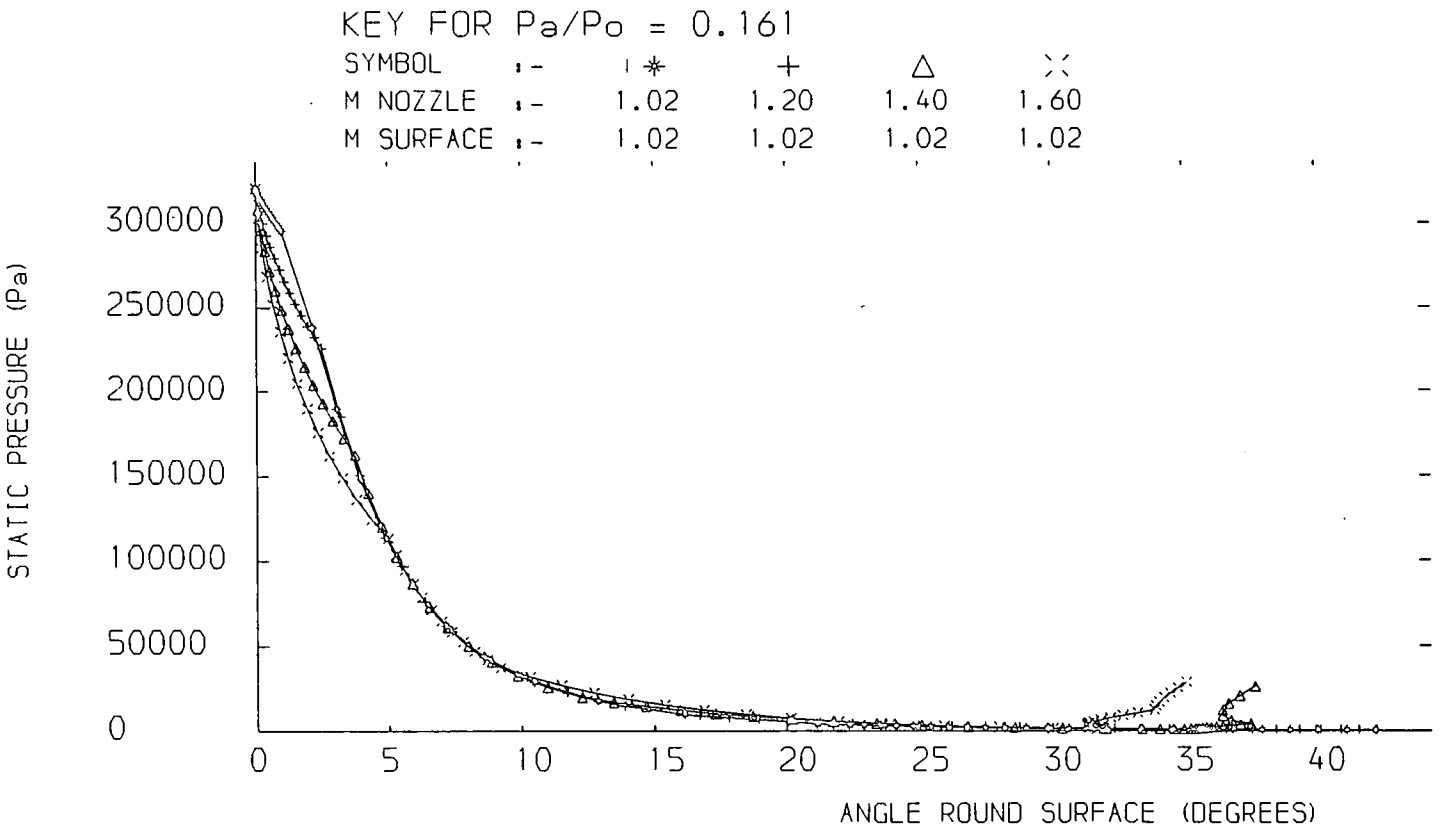

FIG 3.25 :- VARIATION OF EXIT MACH NUMBER , b/a = 0.067

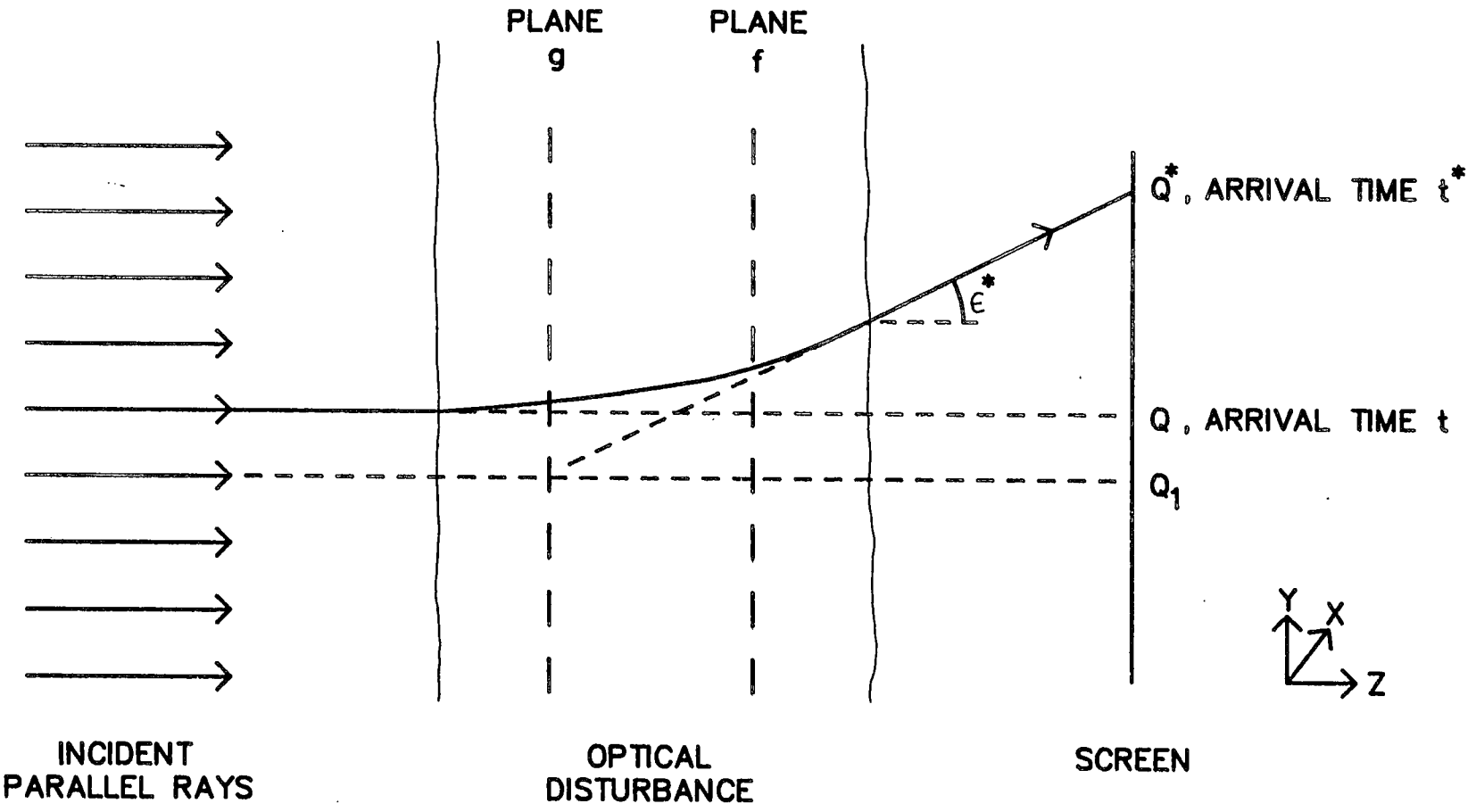

FIG 4.1 : BEHAVIOUR OF A LIGHT RAY IN AN OPTICAL DISTURBANCE

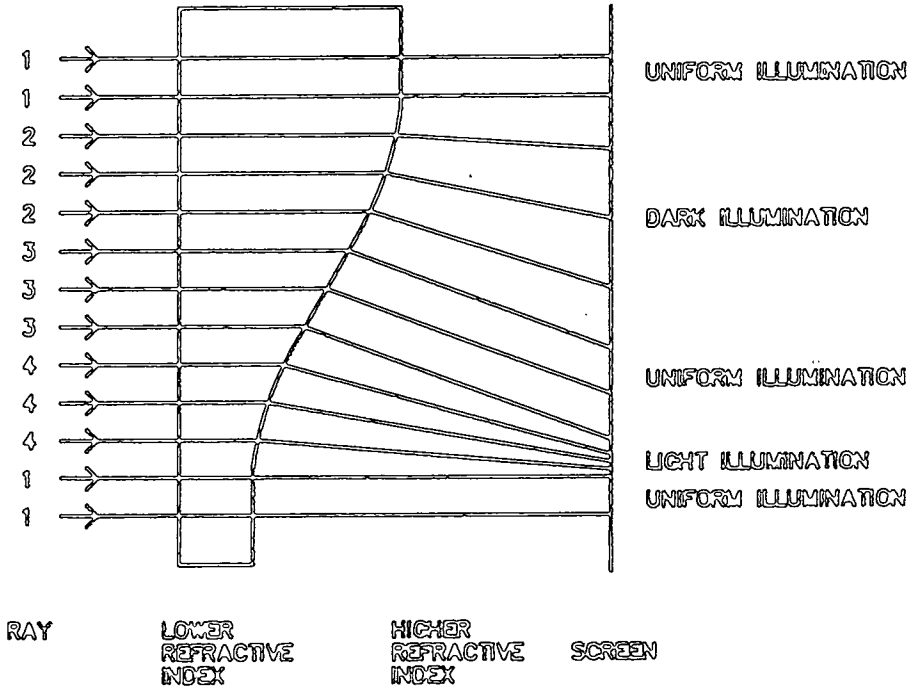

FIG 4.2 : PRINCIPLES OF SHADOWGRAPH

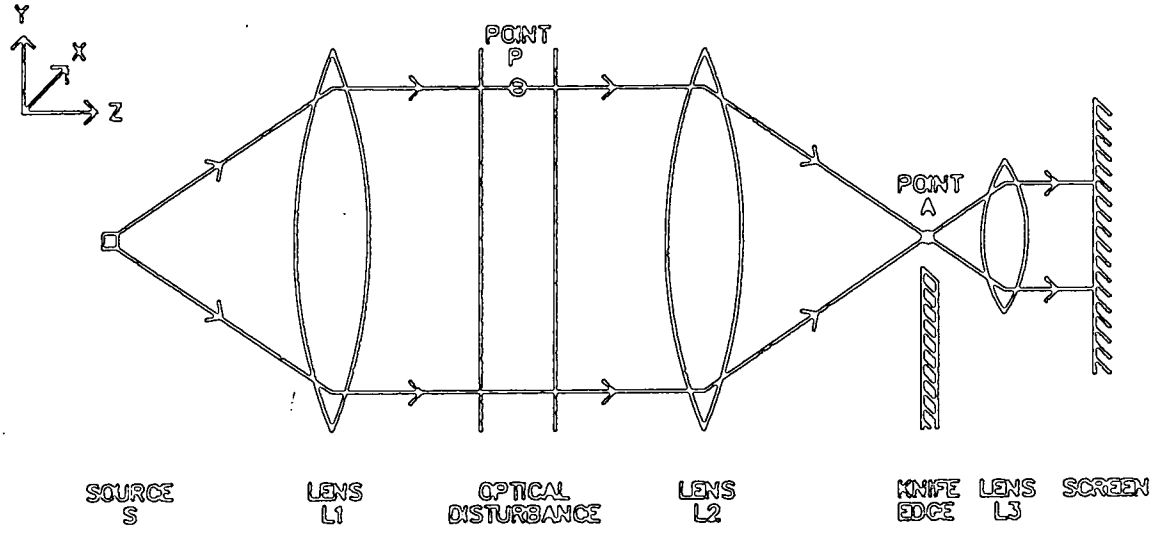

FIG 4.3 : TOEPLER SCHLIEREN SYSTEM

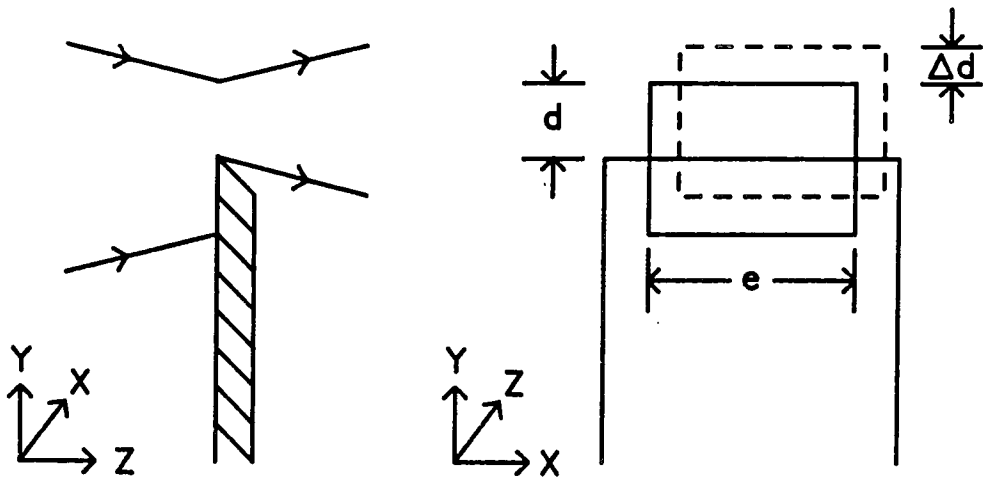

FIG 4.4 : SCHLIEREN CUT OFF

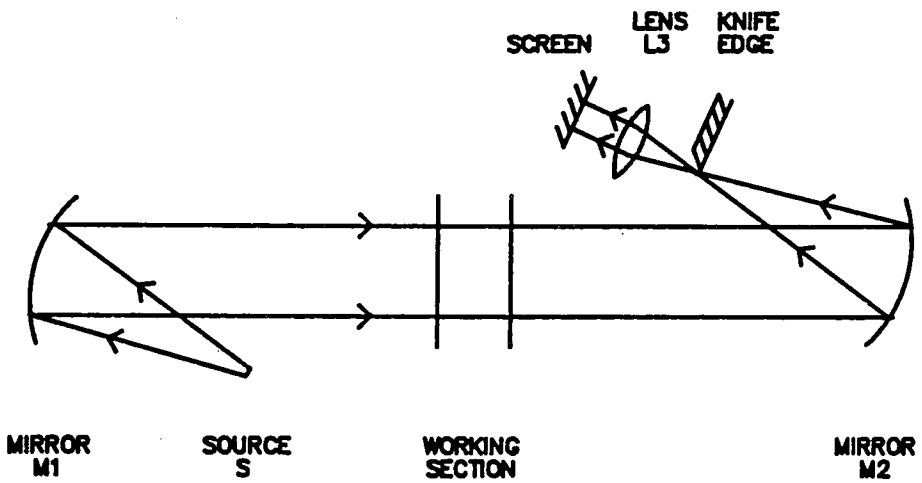

FIG 4.5 : Z–CONFIGURATION SCHLIEREN SYSTEM

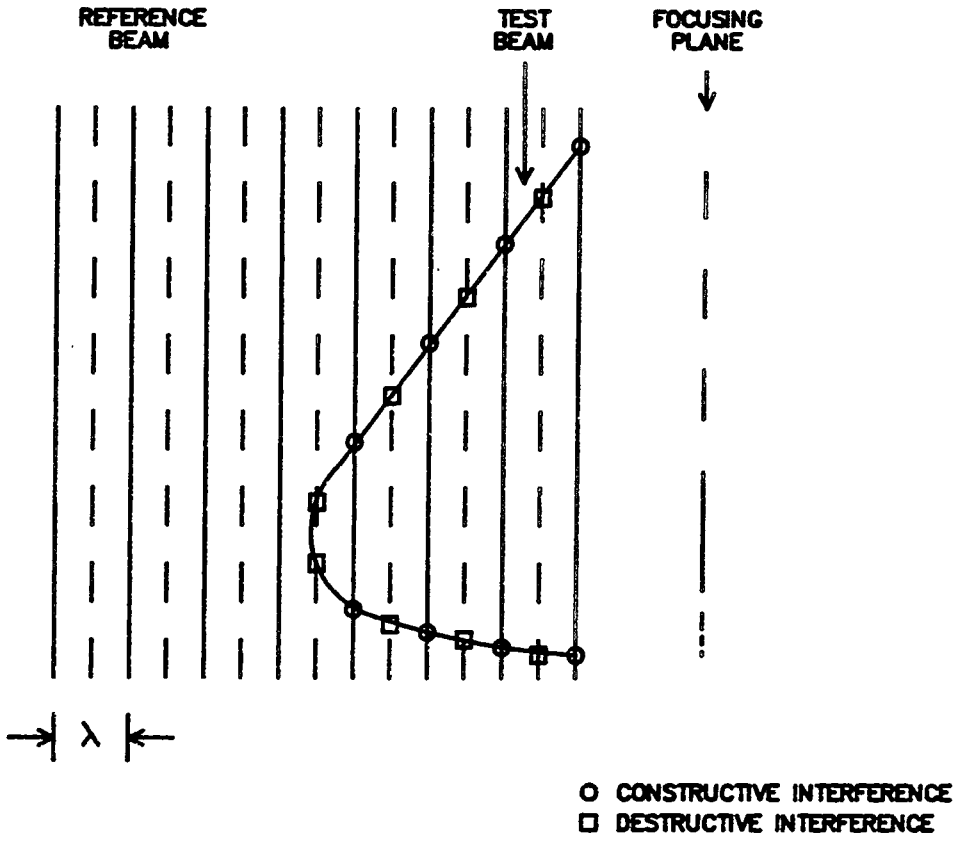

FIG 4.6A : NORMAL INTERFEROMETRY

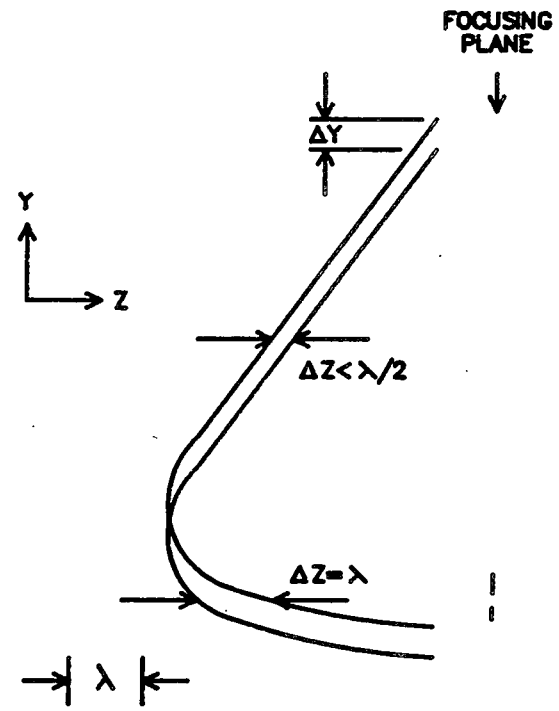

FIG 4.6B : DIFFERENTIAL INTERFEROMETRY

FIG 4.6 : PRINCIPLES OF INTERFEROMETRY

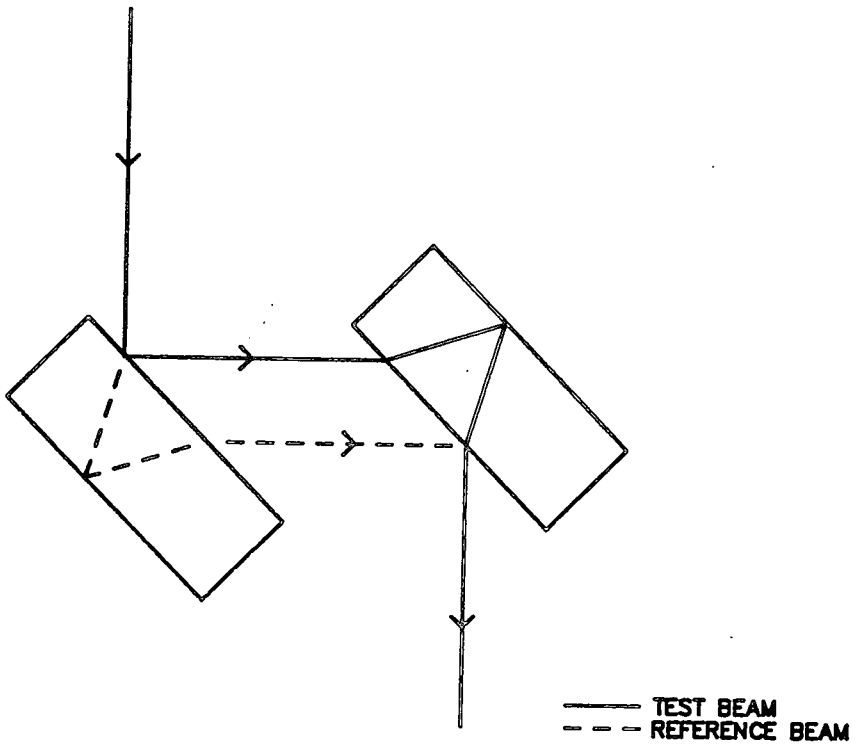

FIG 4.7 : JAMIN INTERFEROMETER

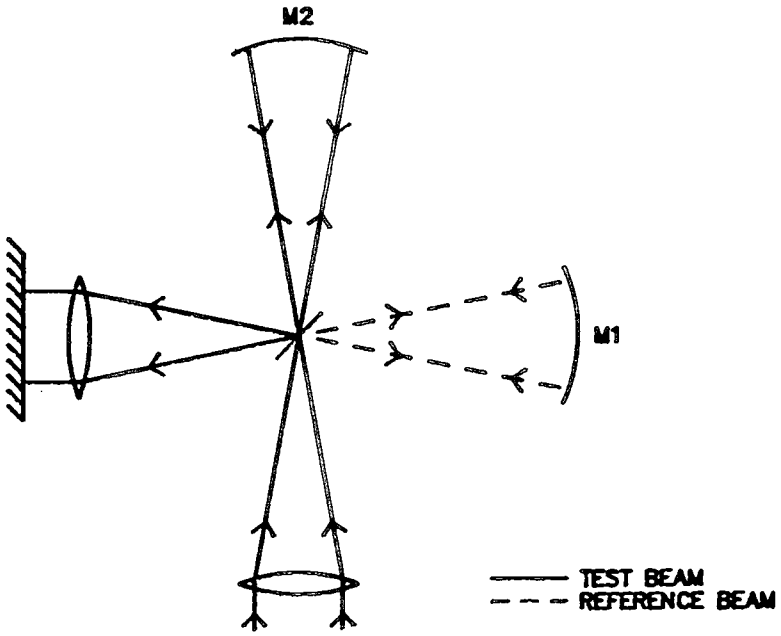

FIG 4.8 : MICHELSON INTERFEROMETER

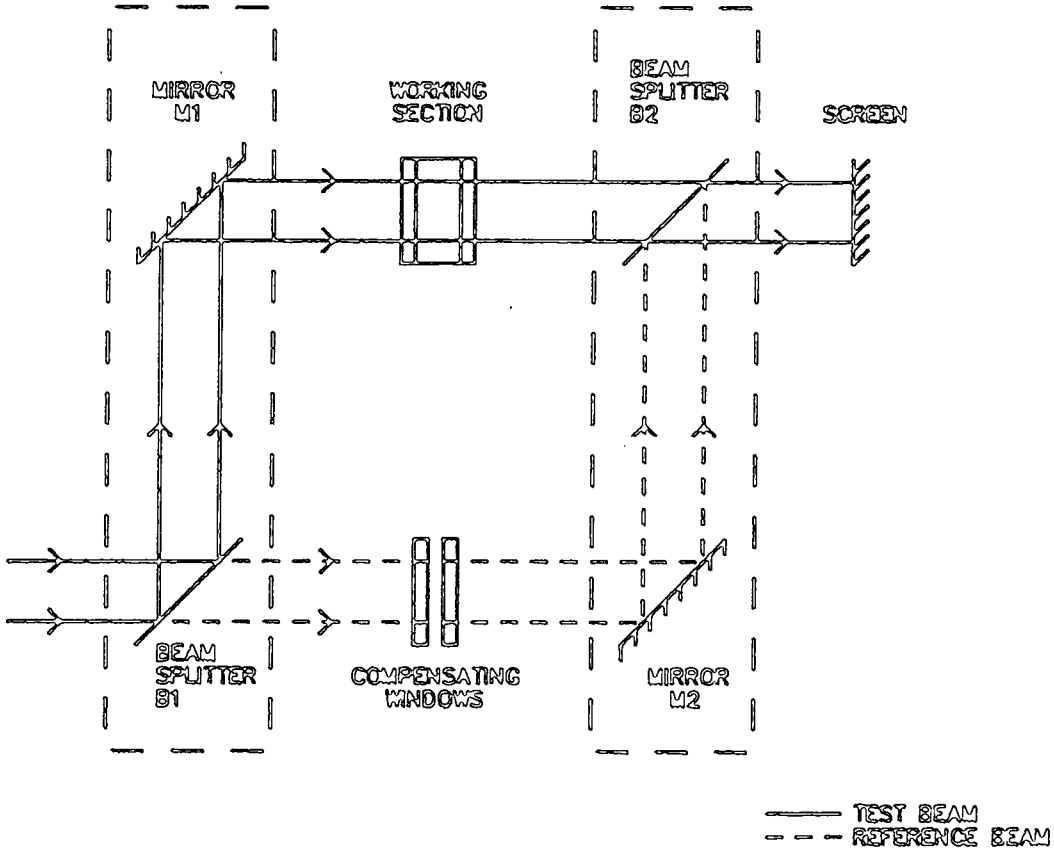

FIG 4.9 : MACH–ZEHNDER INTERFEROMETER

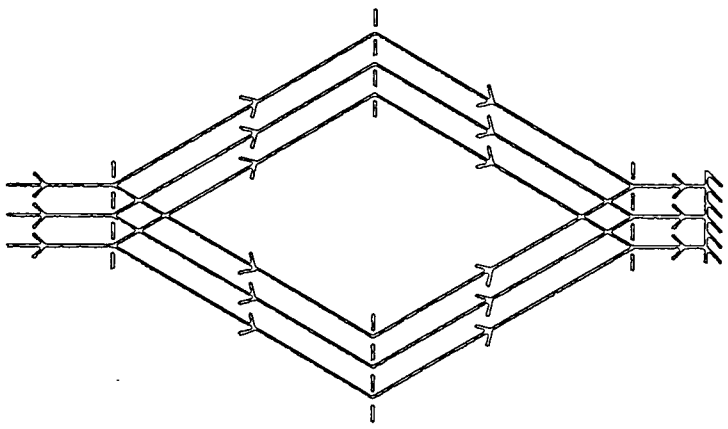

FIG 4.10A : WEINBERG AND WOOD (1959)

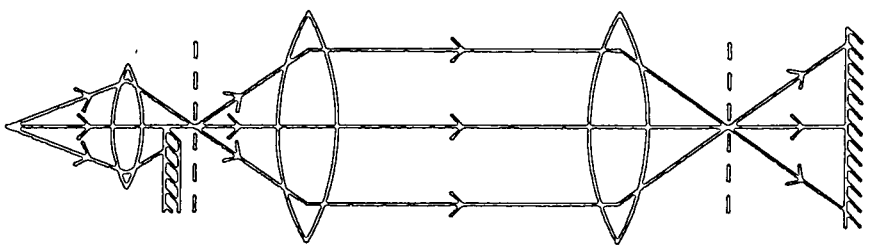

FIG 4.10B : KRAUSHAAR(1950)

FIG 4.10 : DIFFRACTION–GRATING INTERFEROMETERS

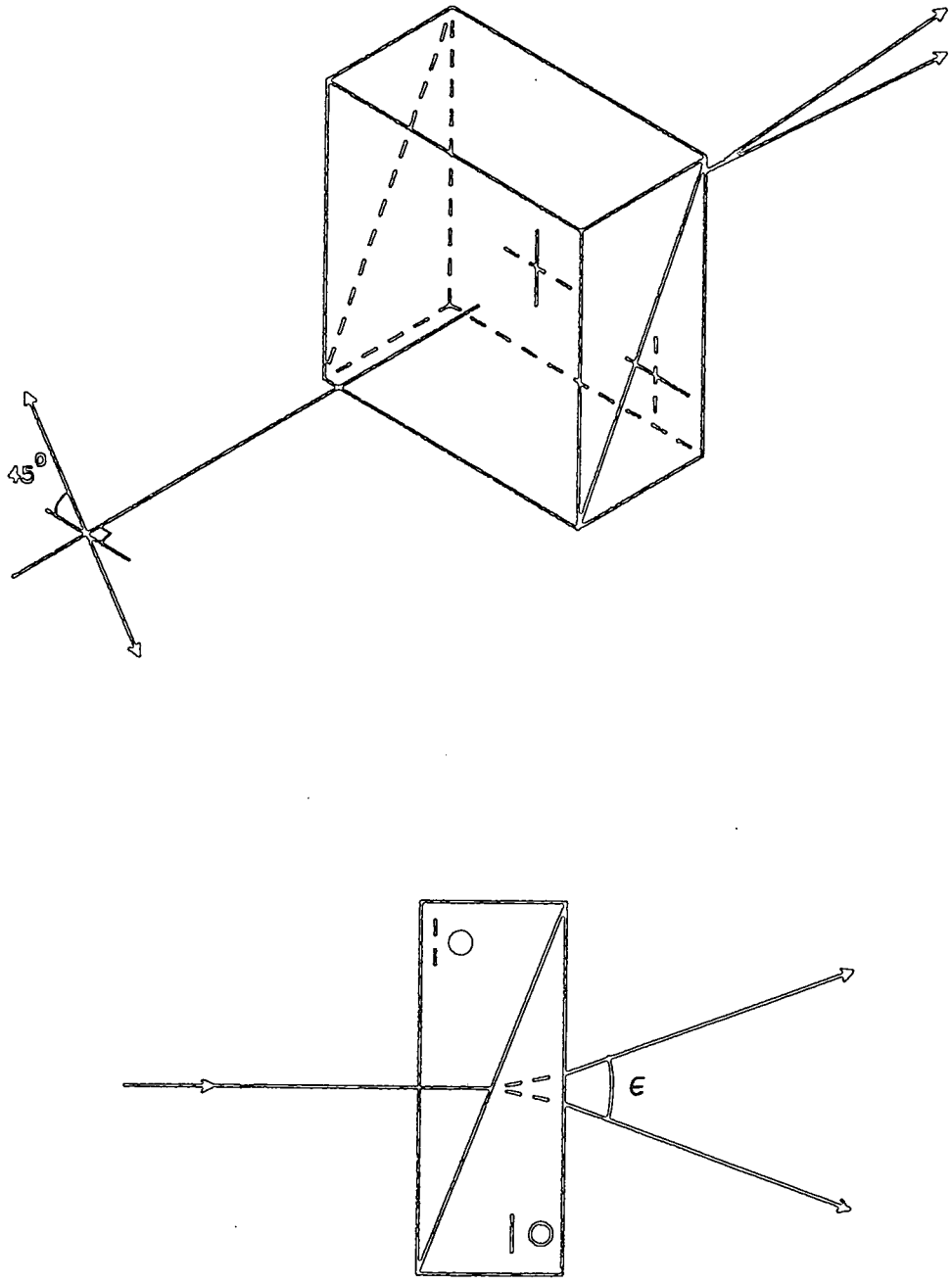

FIG 4.11 : PRINCIPLES OF WOLLASTON PRISM

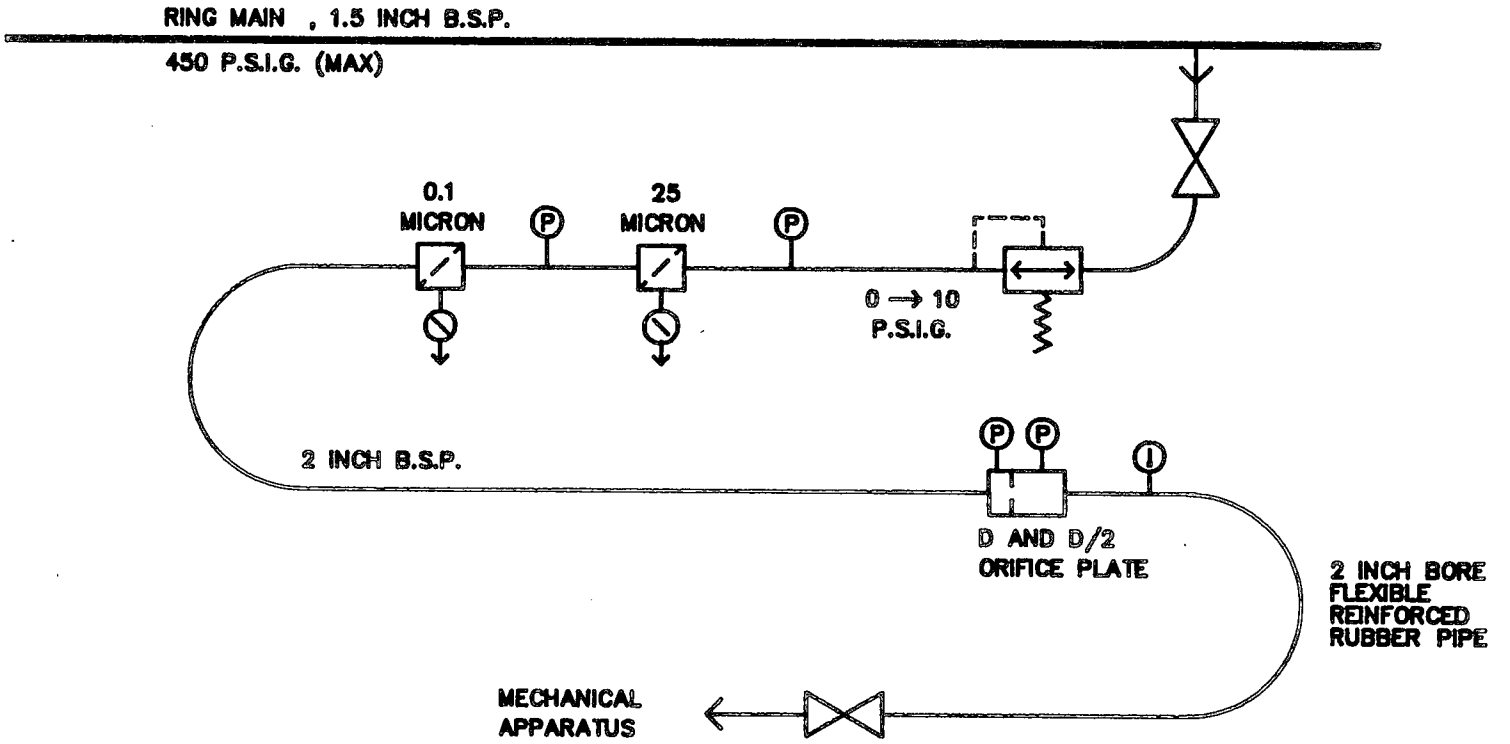

FIG 5.1 : INLET AIR LINE

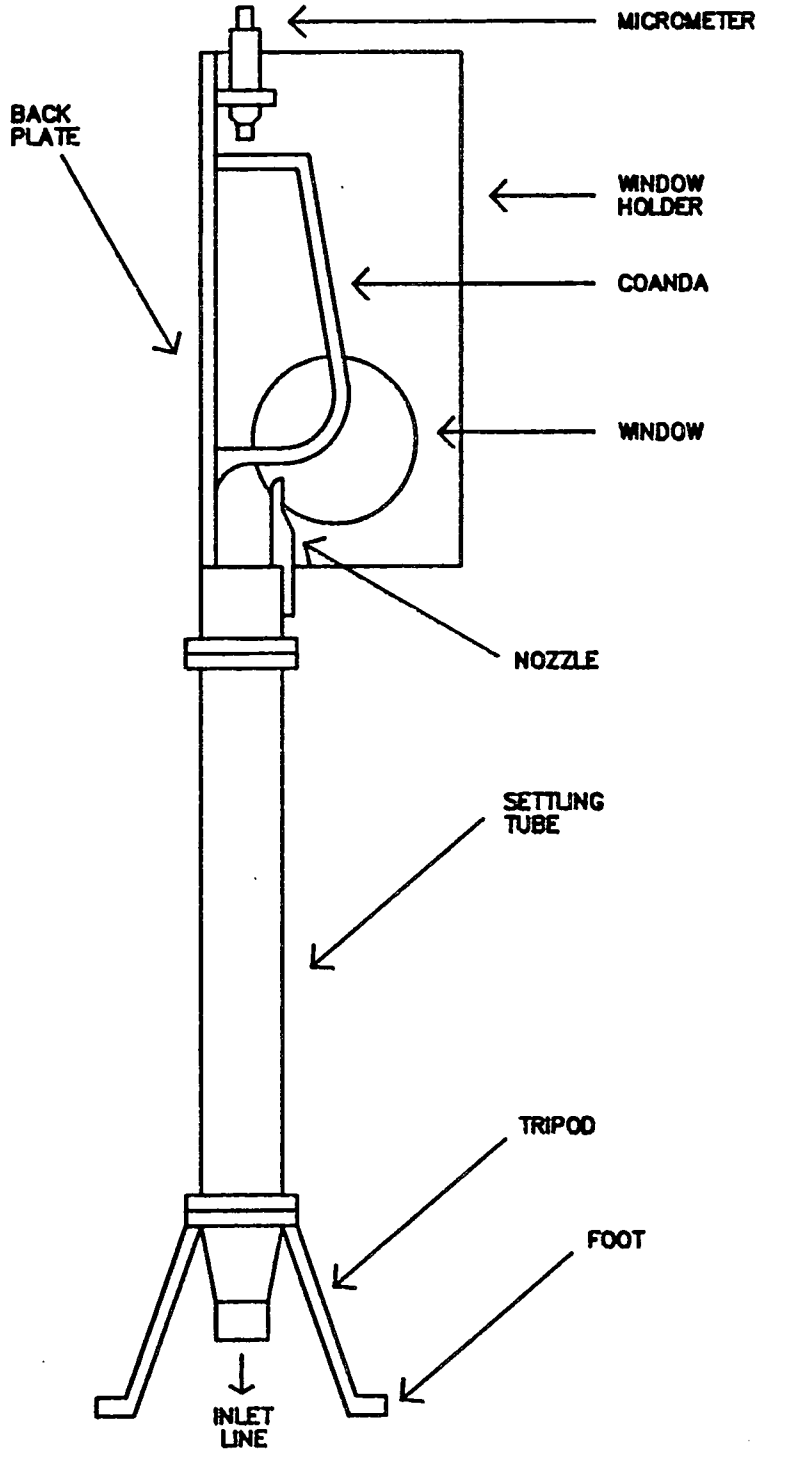

FIG 5.2 : NOMENCLATURE OF MECHANICAL RIG

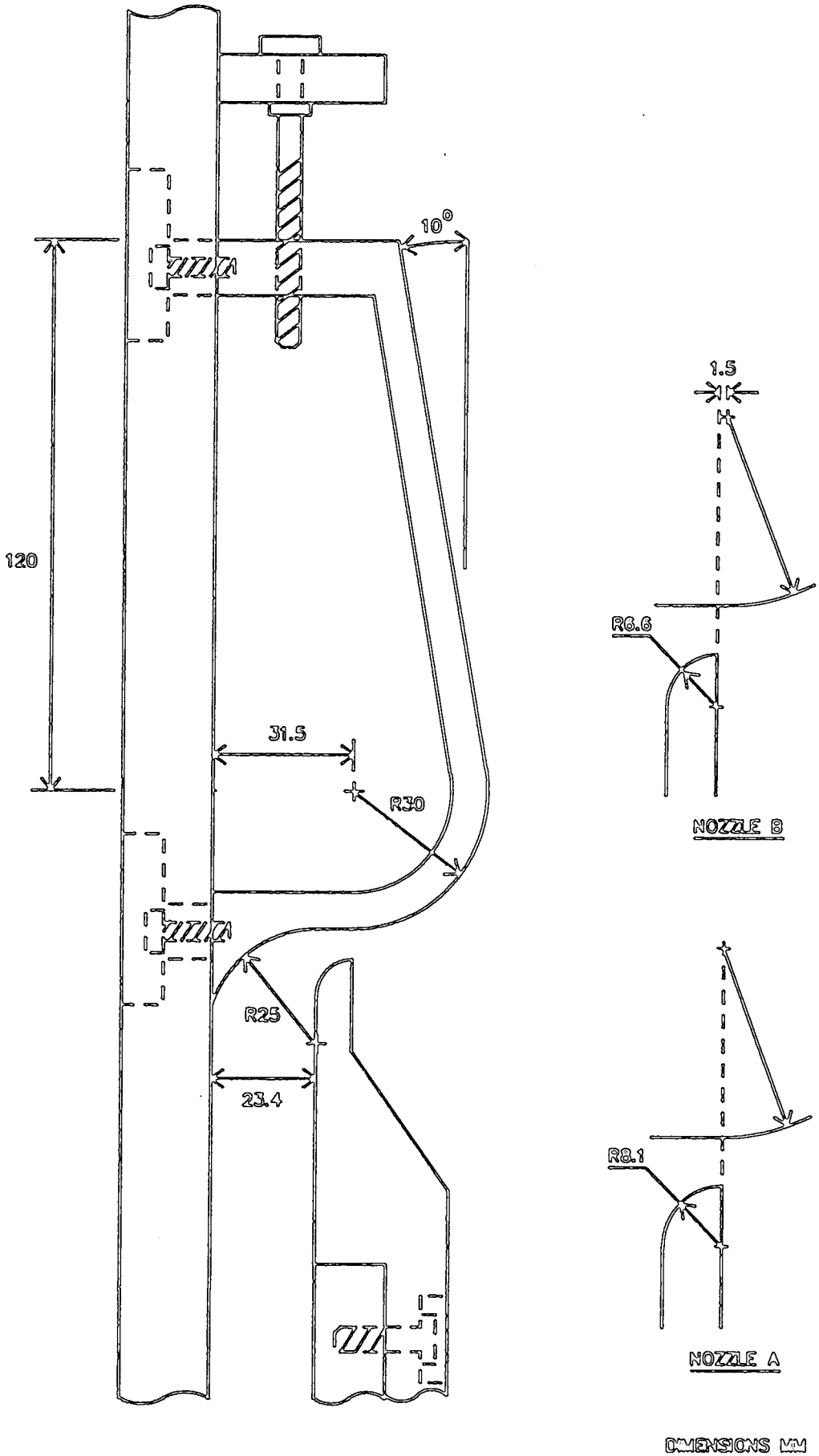

FIG 5.3 : COANDA SECTION

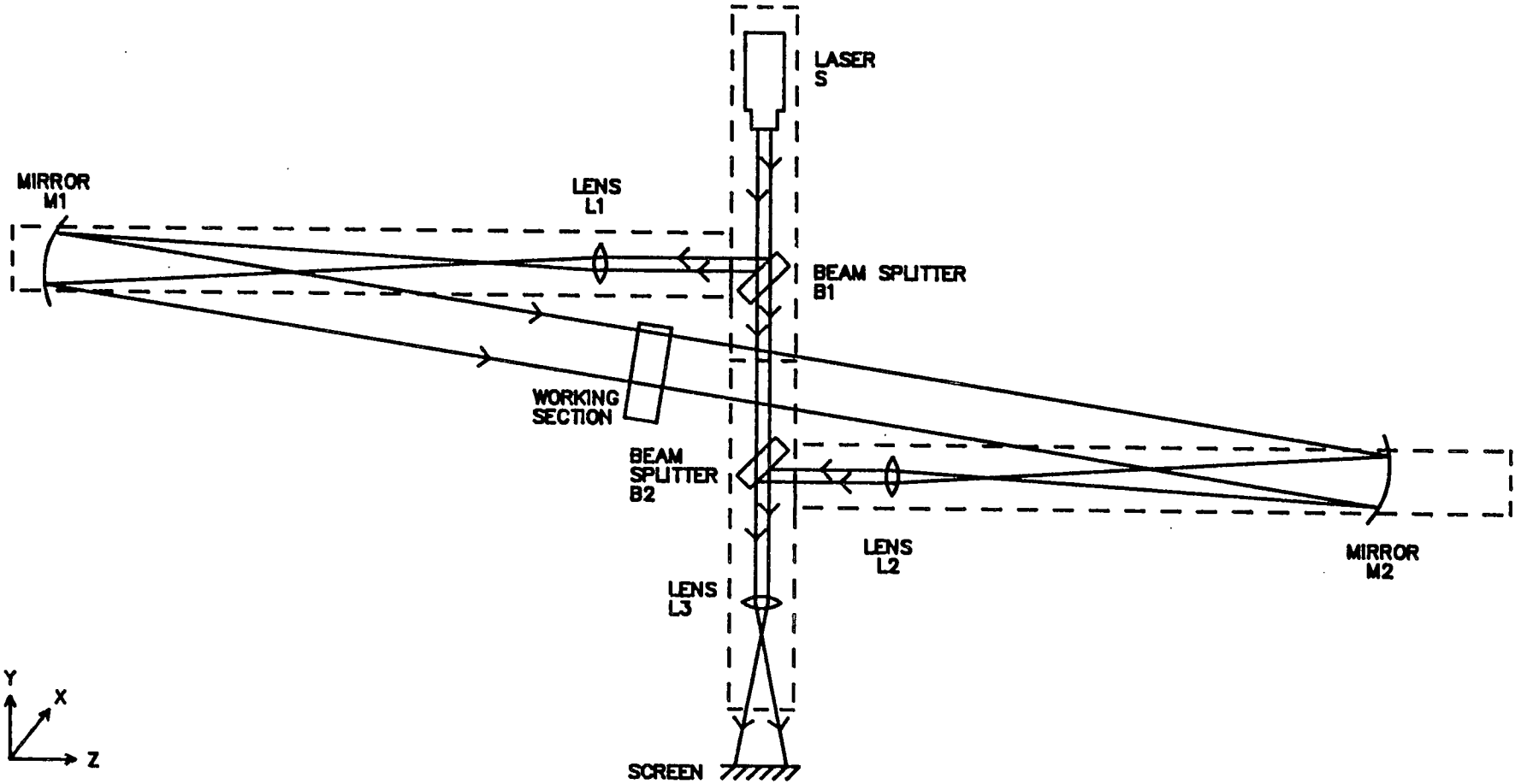

FIG 5.4 : CONFIGURATION OF OPTICAL SYSTEM , TYPE A

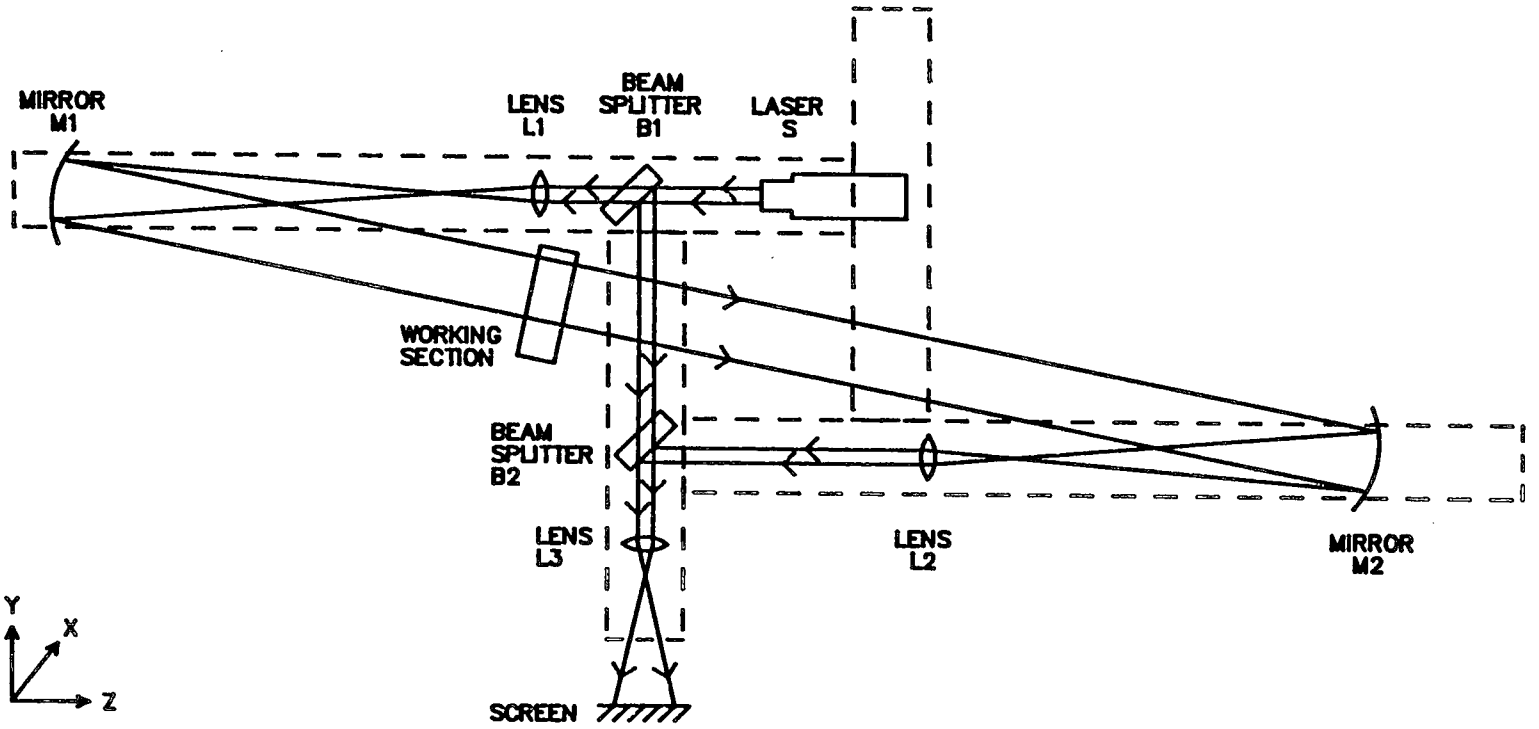

FIG 5.5 : CONFIGURATION OF OPTICAL SYSTEM , TYPE B

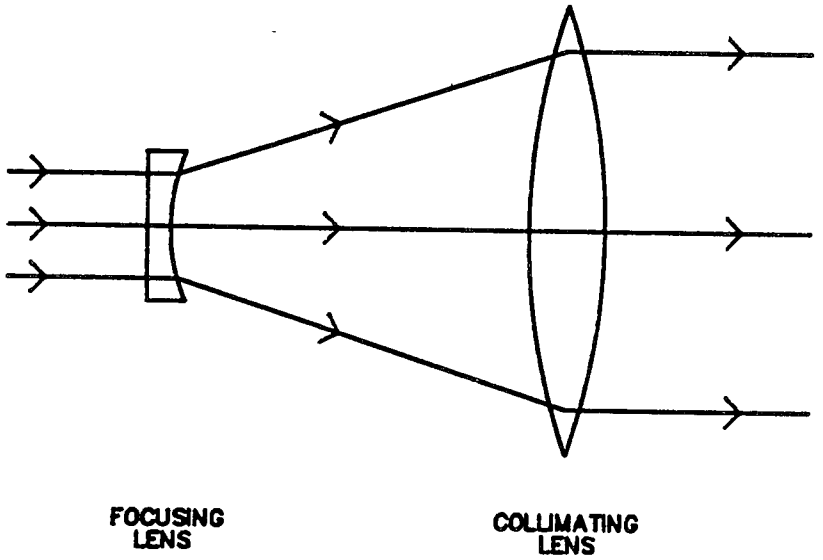

FIG 5.6A : BEAM EXPANDER

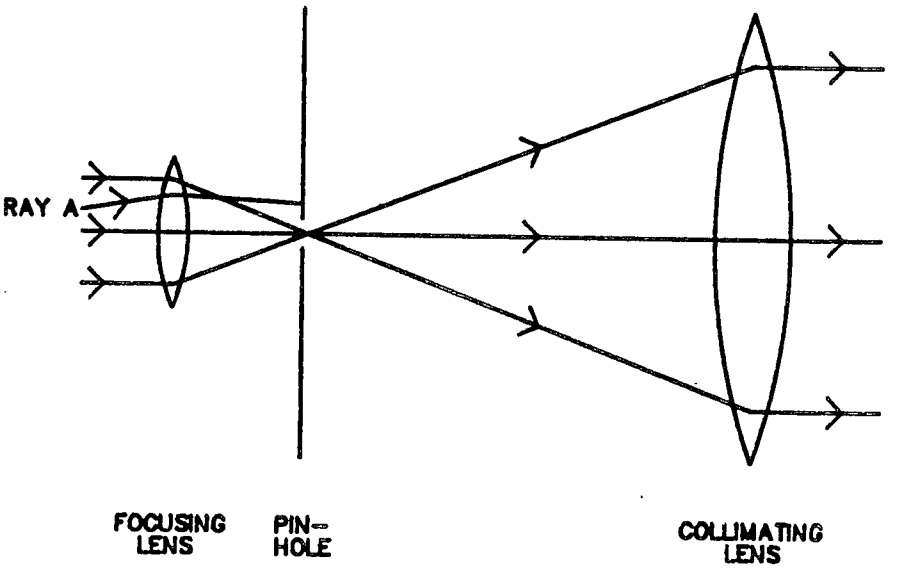

FIG 5.6B : SPATIAL FILTER

FIG 5.6 : EXPANSION OF LASER BEAM

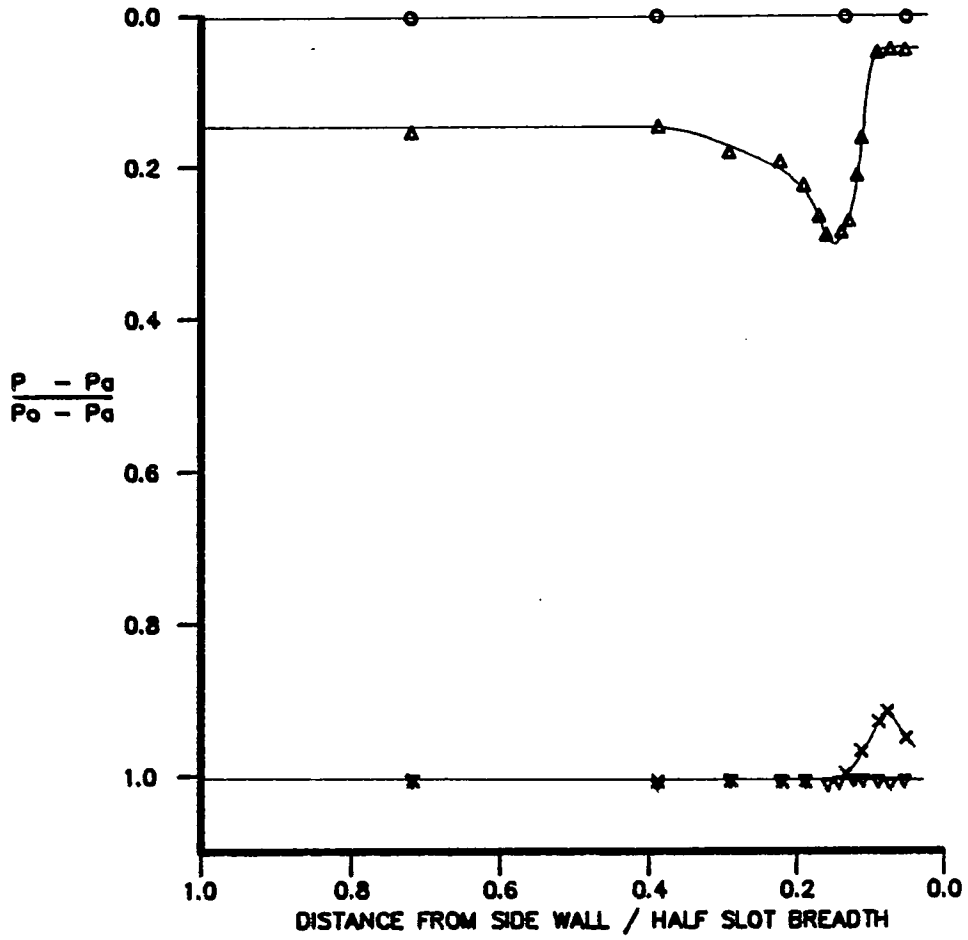

STAGNATION PRESSURE RATIO = 0.662

ANGLE ROUND COANDA = 20°

SLOT WIDTH = 4.00 mm

DISTANCE OF CENTRE-LINE OF TOTAL PRESSURE TUBE FROM COANDA SURFACE

- o 6.4 mm
- Δ 4.4 mm
- × 2.4 mm
- ▽ 0.4 mm

FIG 6.1 : TOTAL PRESSURE TRAVERSE AT 20 DEGREES

N.B. P is the total pressure measured by the probe and ignores any normal shock in front of the probe

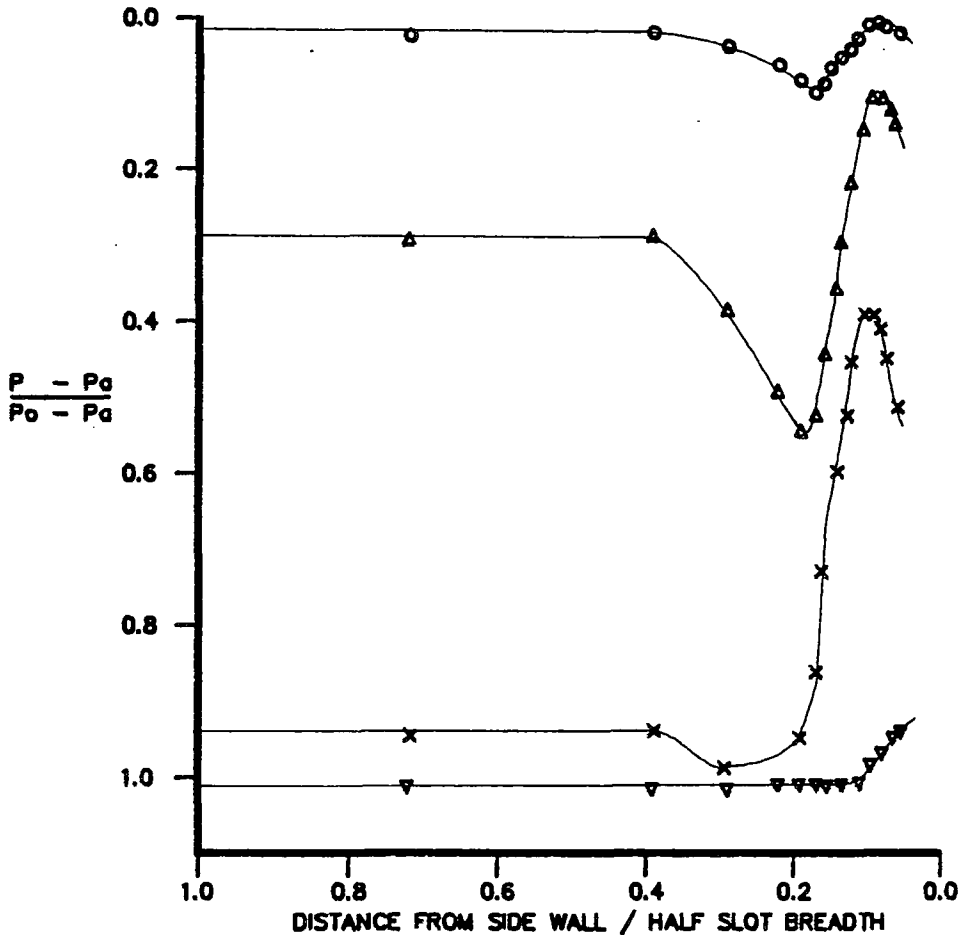

STAGNATION PRESSURE RATIO = 0.662

ANGLE ROUND COANDA = 40°

SLOT WIDTH = 4.00 mm

DISTANCE OF CENTRE-LINE OF TOTAL PRESSURE TUBE FROM COANDA SURFACE

o 6.4 mm
Δ 4.4 mm
+ 2.4 mm
▽ 0.4 mm

FIG 6.2 : TOTAL PRESSURE TRAVERSE AT 40 DEGREES

N.B. See note on FIG 6.1

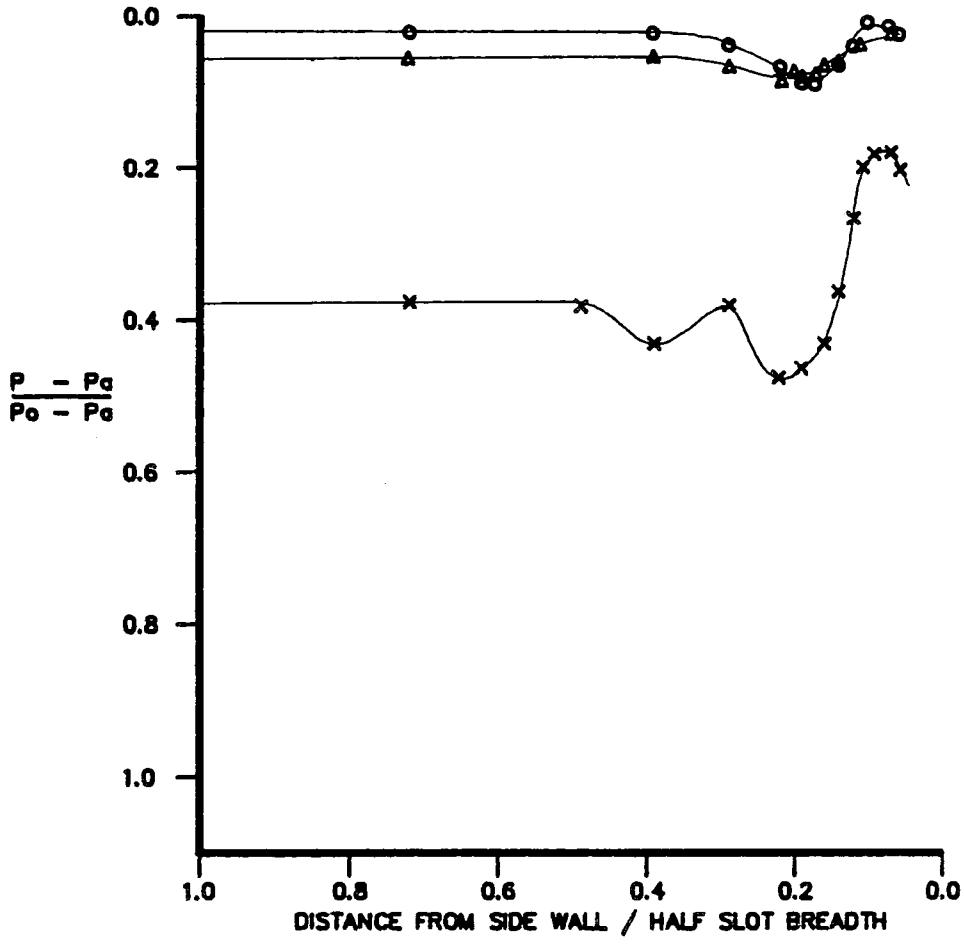

DISTANCE OF PROBE FROM COANDA SURFACE	= 6.4 mm	Pa/Po
ANGLE ROUND COANDA	= 40°	o 0.662 Δ 0.398 × 0.285
SLOT WIDTH	= 4.00 mm	

FIG 6.3 : EFFECT OF PRESSURE RATIO ON TRAVERSE

N.B. See note on FIG 6.1

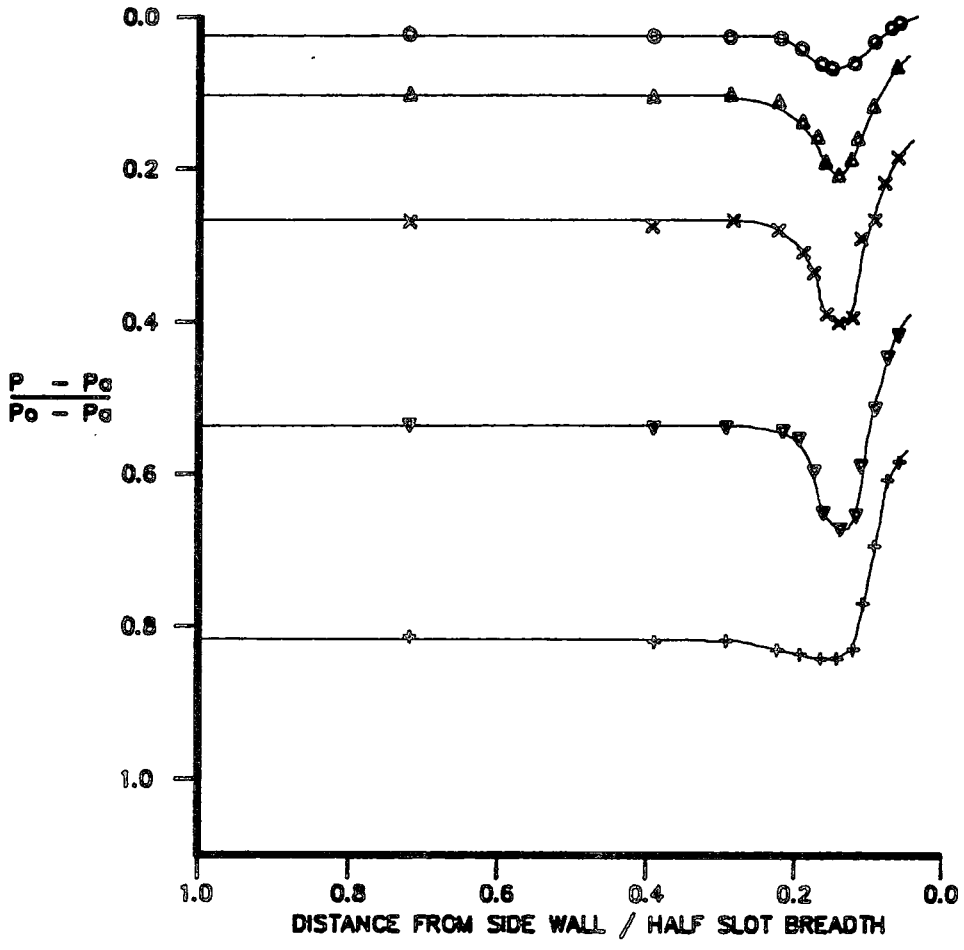

STAGNATION PRESSURE RATIO = 0.662

ANGLE ROUND COANDA = 40°

SLOT WIDTH = 1.96 mm

DISTANCE OF CENTRE-LINE OF TOTAL PRESSURE TUBE FROM COANDA SURFACE

○ 4.4 mm
△ 3.4 mm
× 2.4 mm
▽ 1.4 mm
+ 0.4 mm

FIG 6.4 : TOTAL PRESSURE TRAVERSE ON 2 MM SLOT JET

N·B See note on FIG 6.1

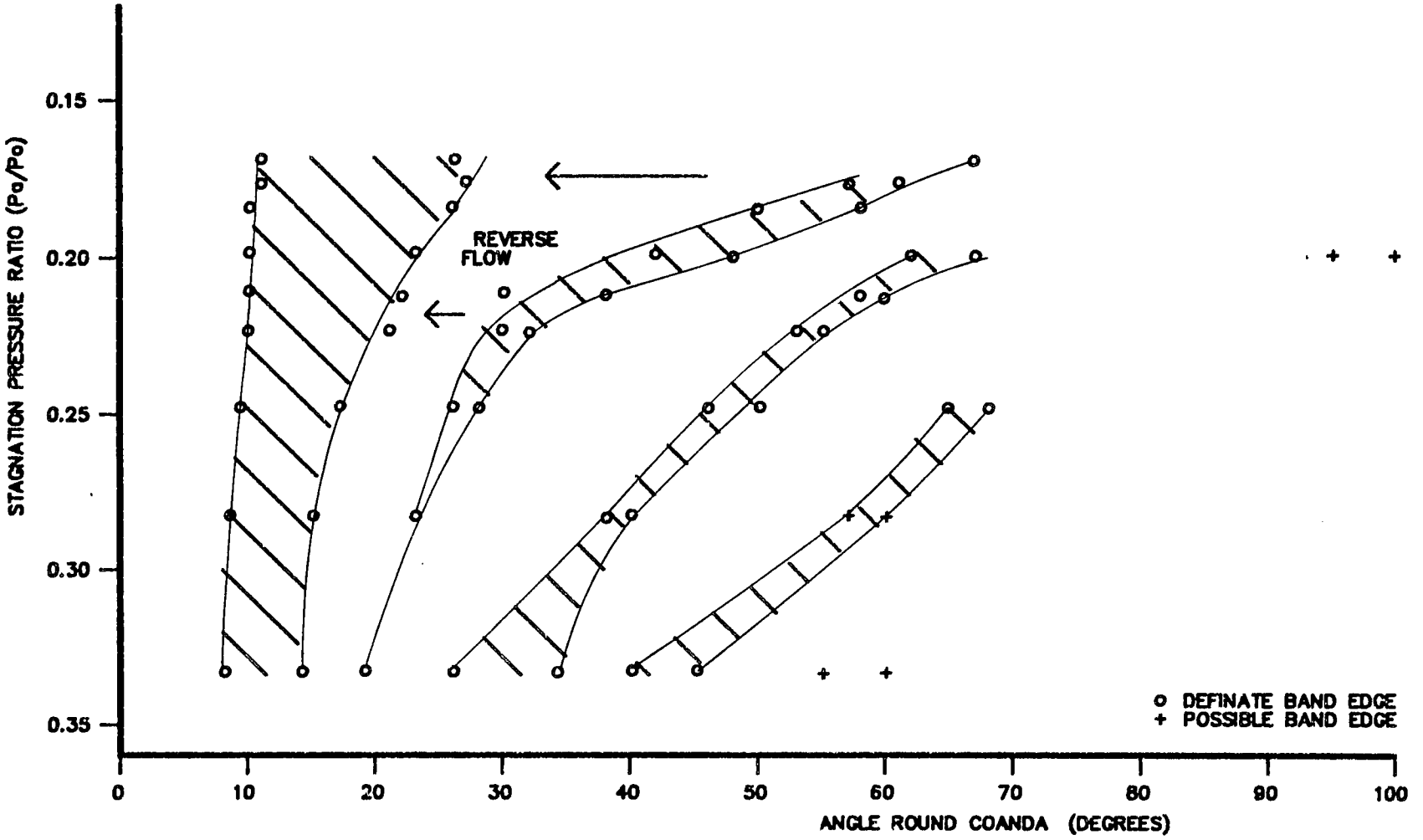

FIG 6.5 : 2 MM SLOT SURFACE OIL BANDS

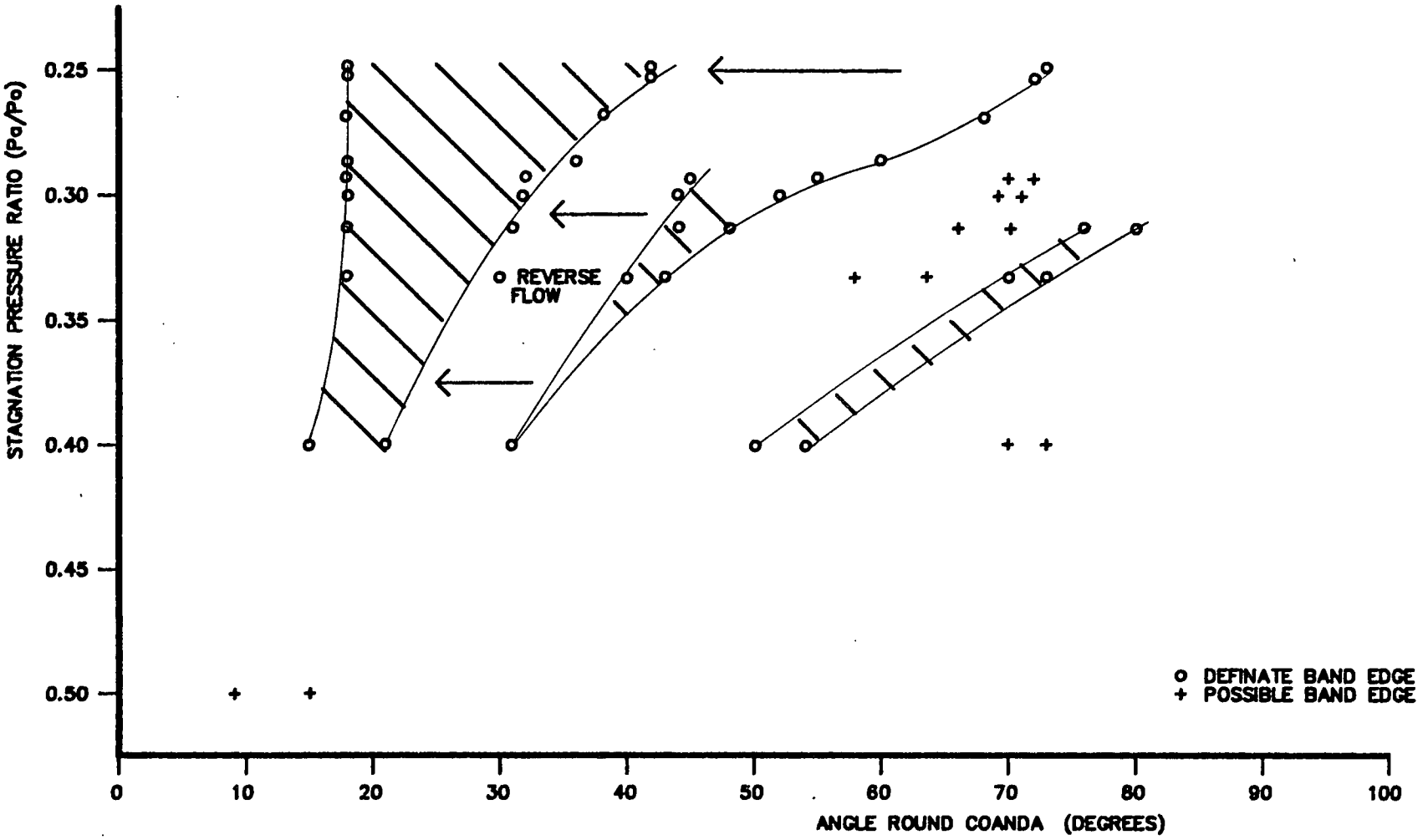

FIG 6.6 : 4 MM SLOT SURFACE OIL BANDS

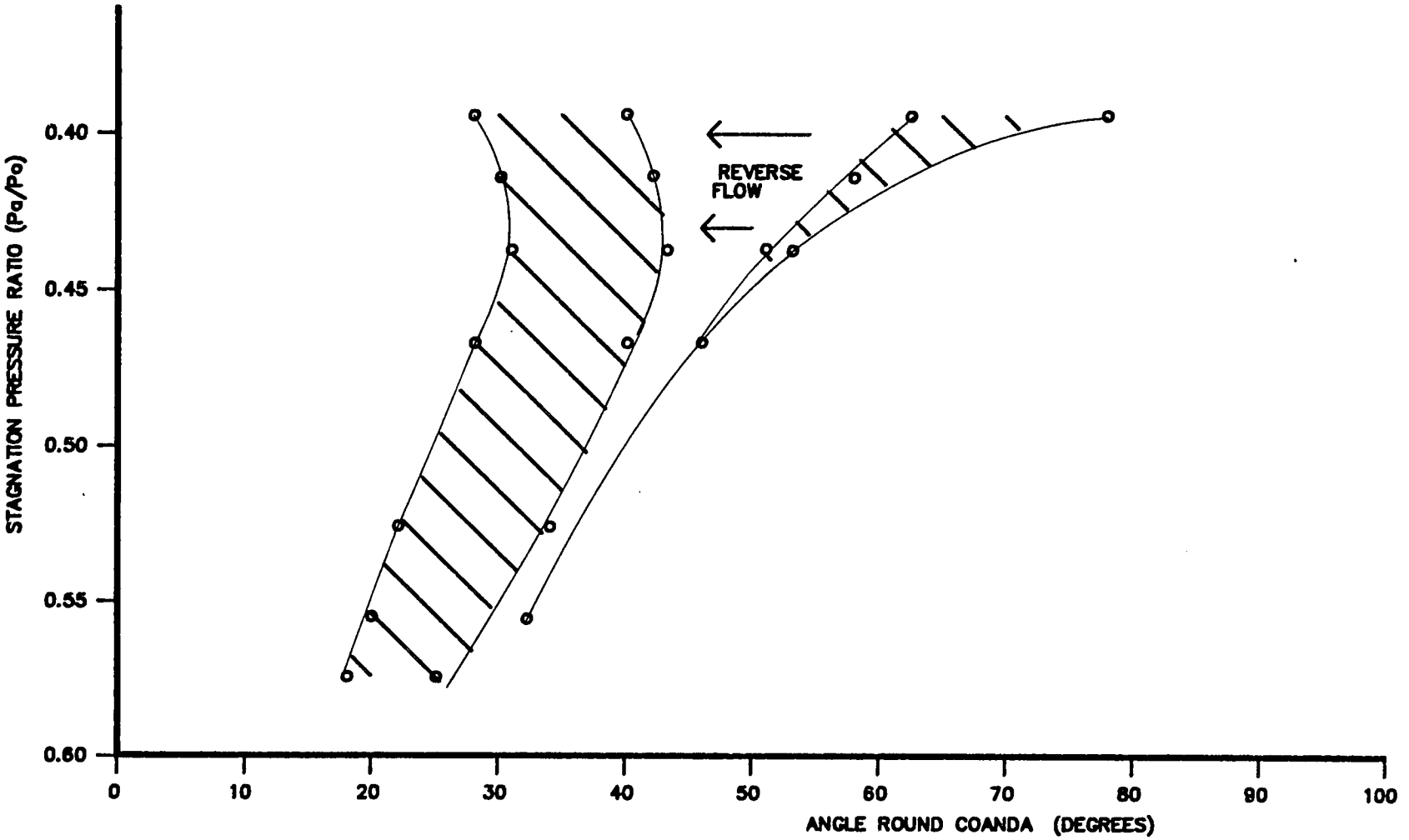

FIG 6.7 : 8 MM SLOT SURFACE OIL BANDS

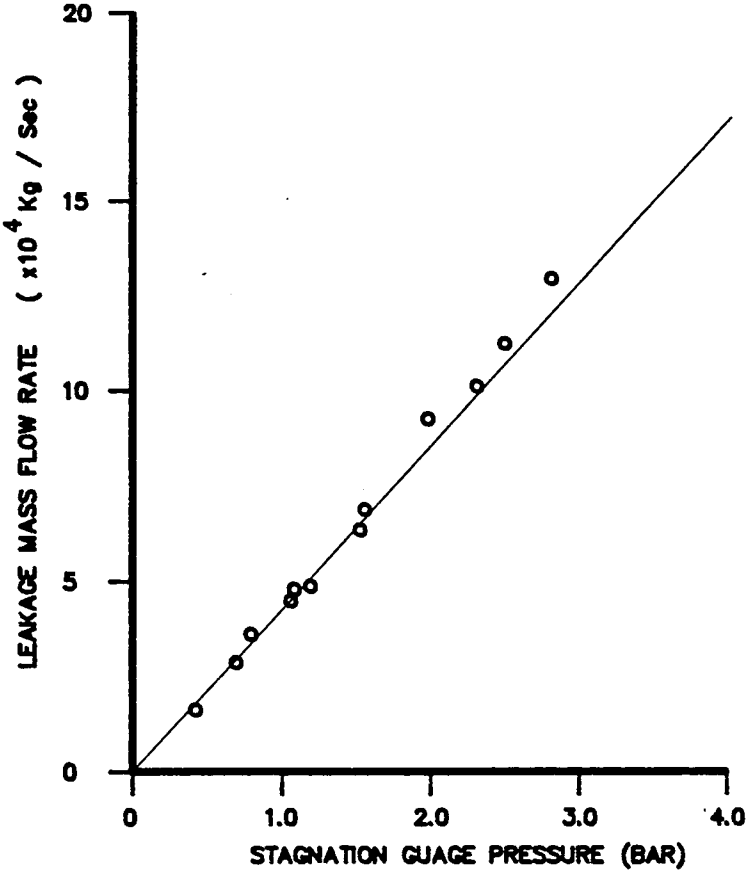

FIG 6.8 : LEAKAGE MASS FLOW RATE

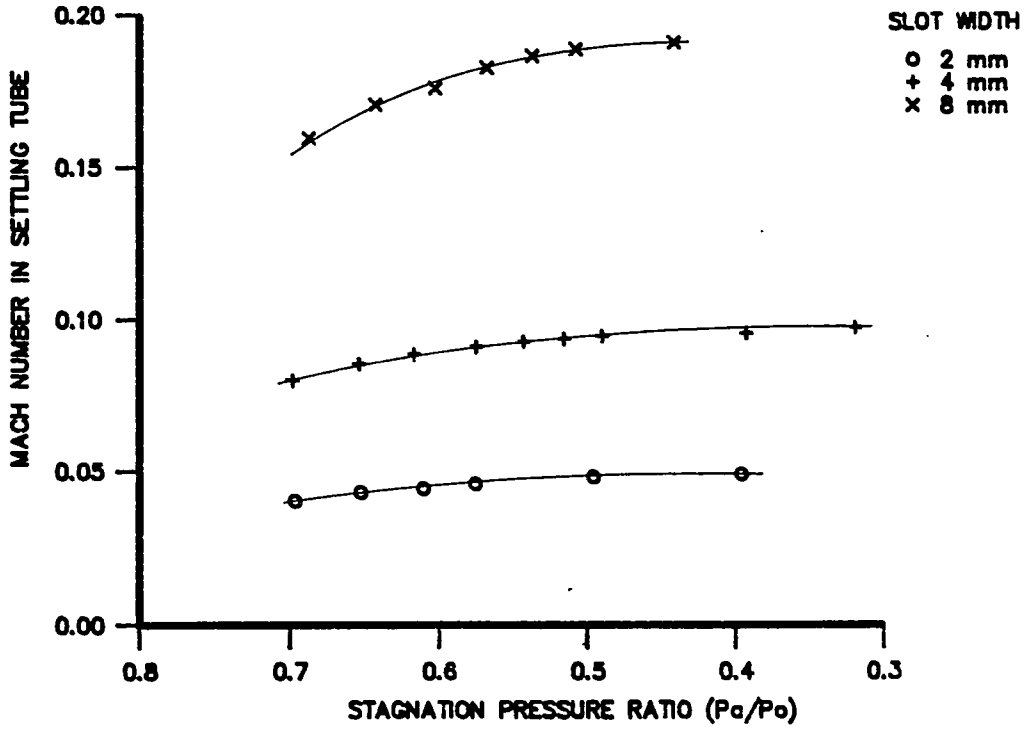

FIG 6.9 : SETTLING TUBE MACH NUMBER

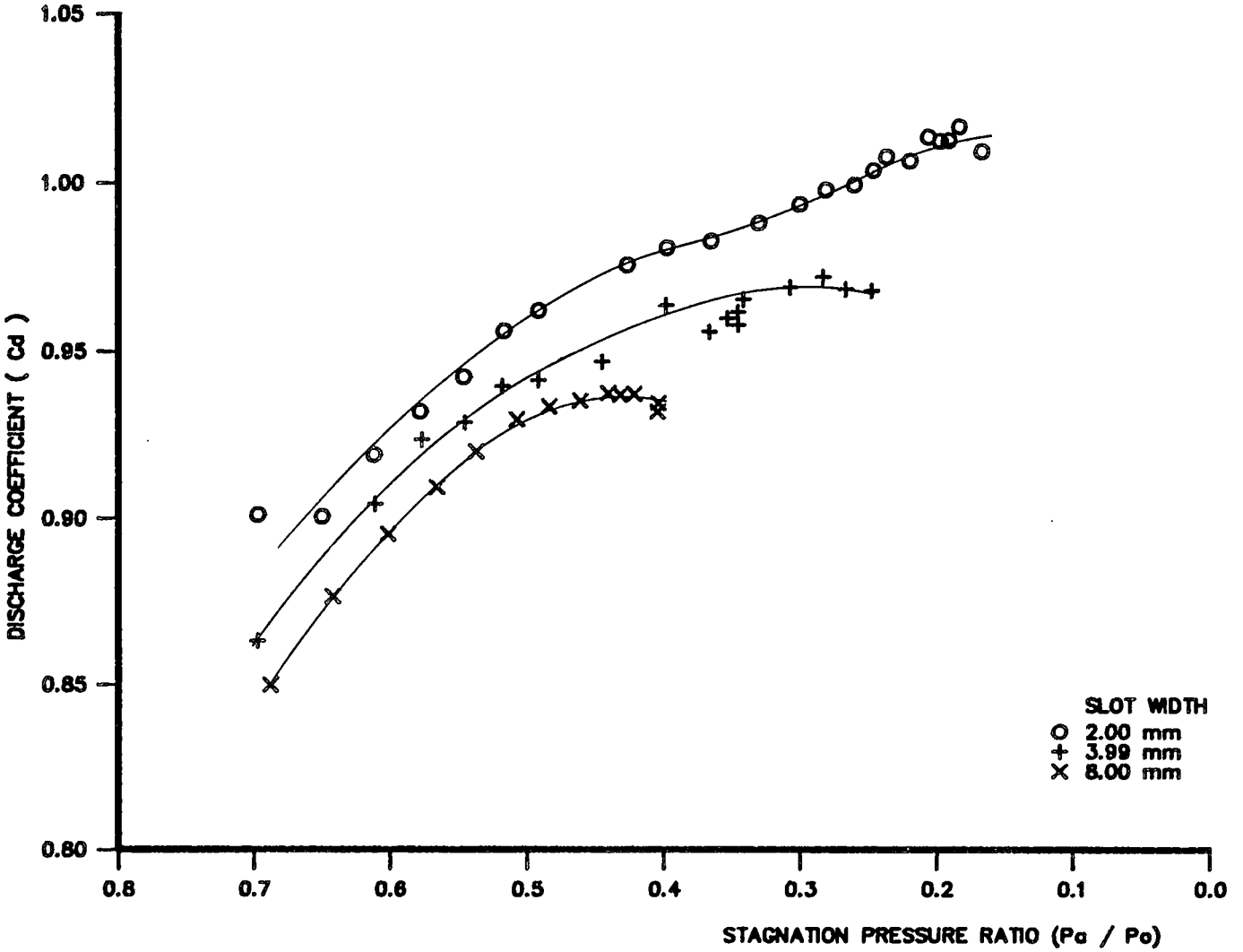

FIG 6.10 : COEFFICIENT OF DISCHARGE

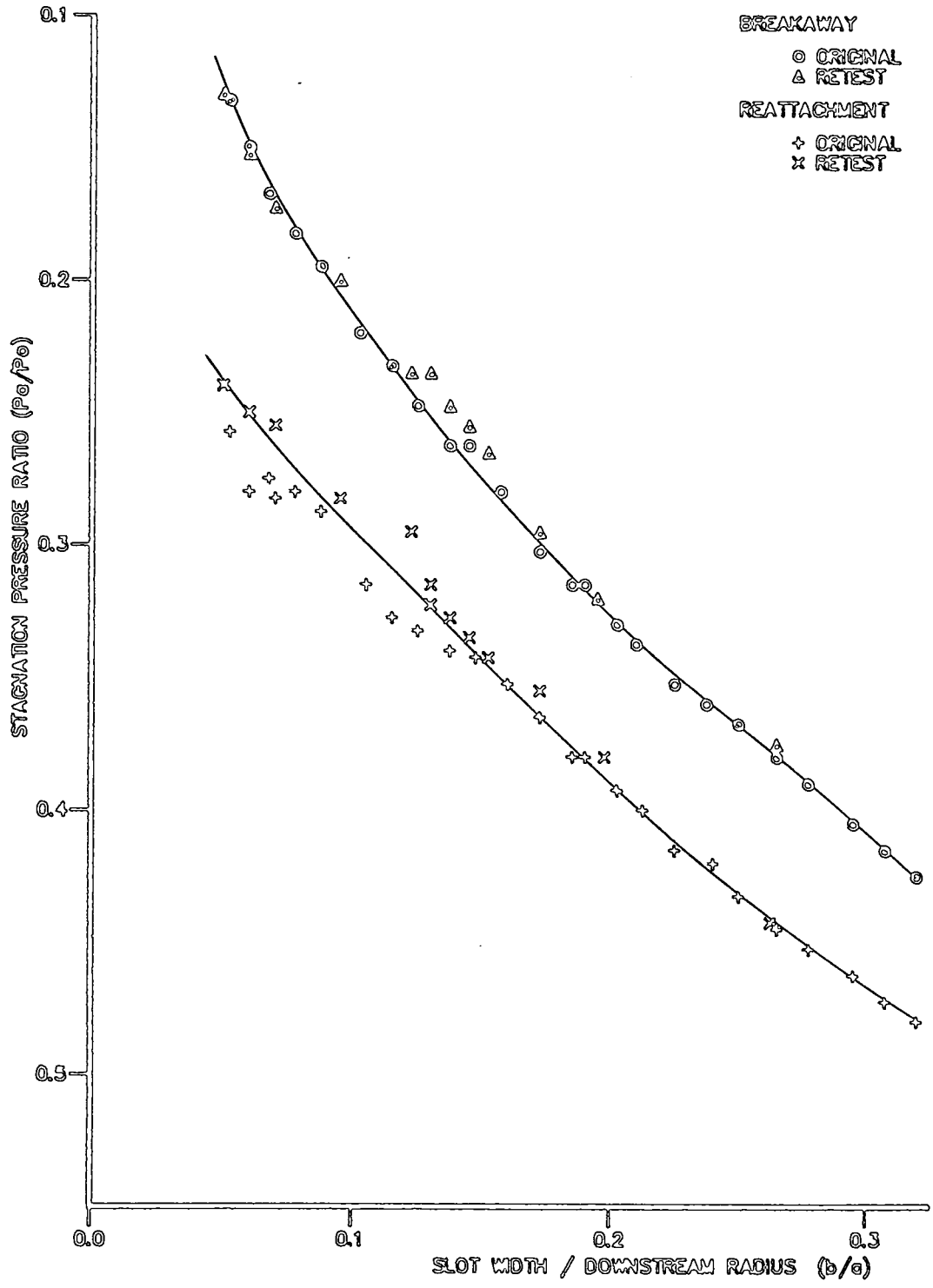

FIG 6.11 : BREAKAWAY / REATTACHMENT OF NOZZLE A

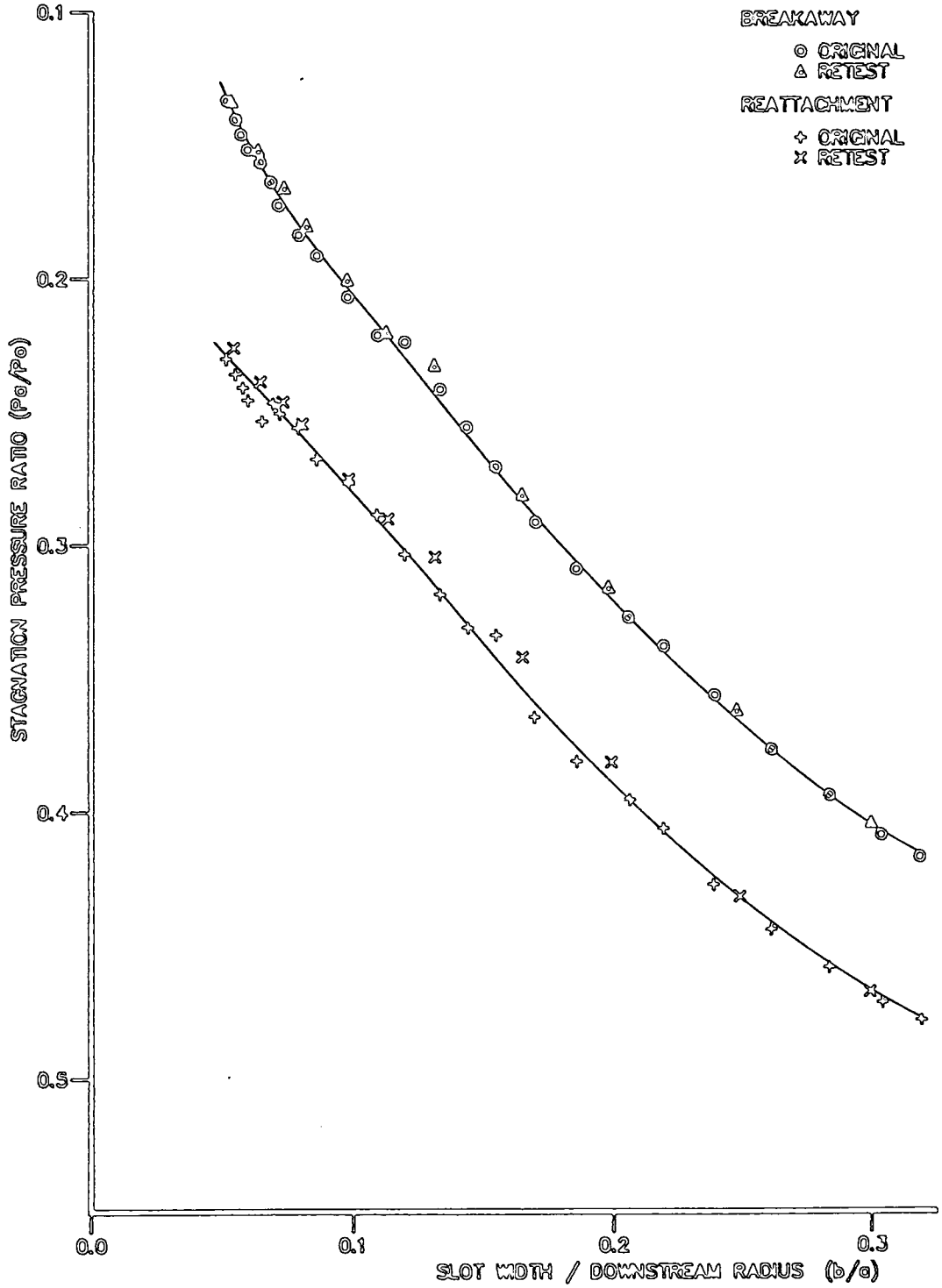

FIG 6.12 : BREAKAWAY / REATTACHMENT OF NOZZLE B

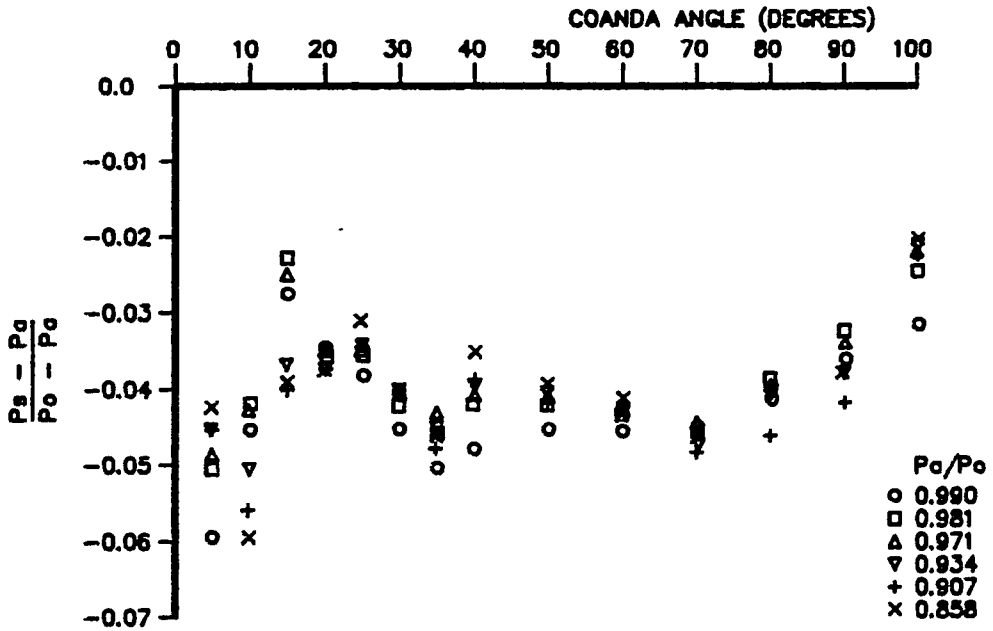

FIG 6.13 : INCOMPRESSIBLE SURFACE PRESSURE COEFFICIENT , 0.99 MM SLOT

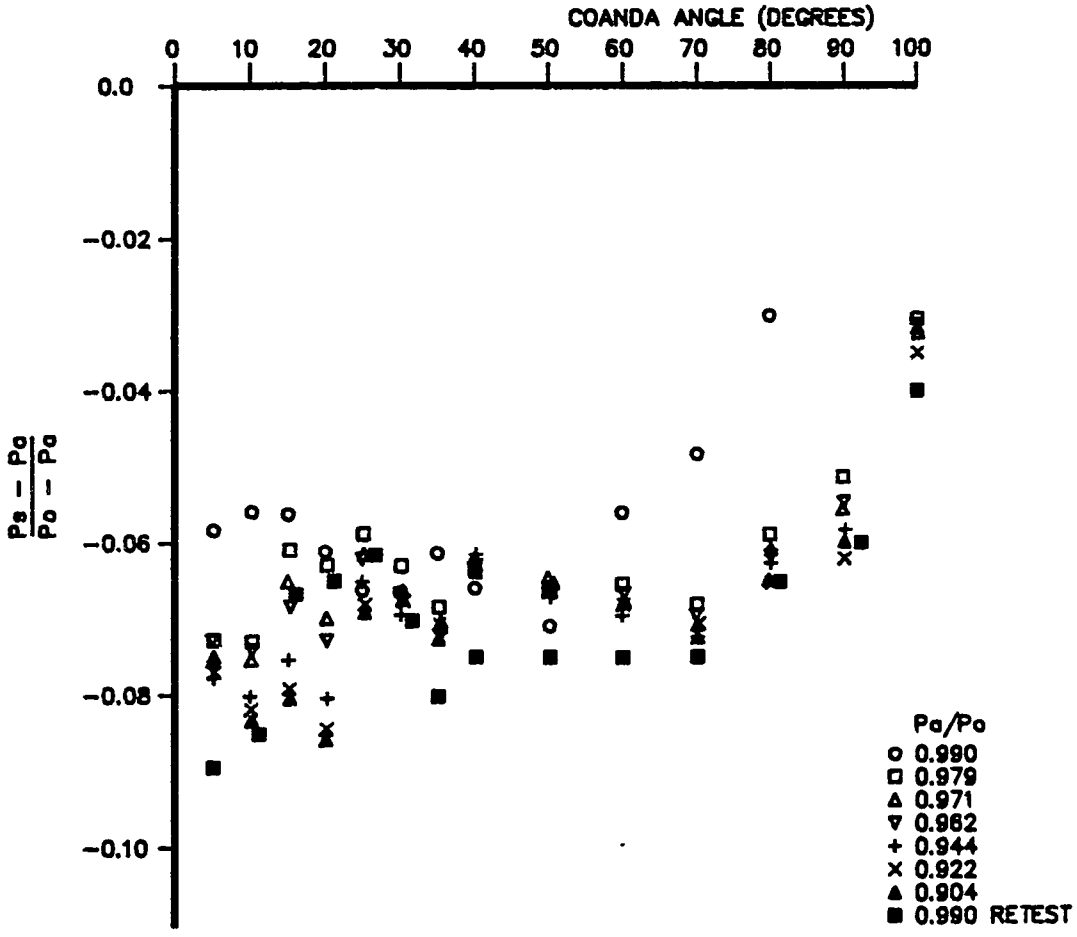

FIG 6.14 : INCOMPRESSIBLE SURFACE PRESSURE COEFFICIENT , 1.50 MM SLOT

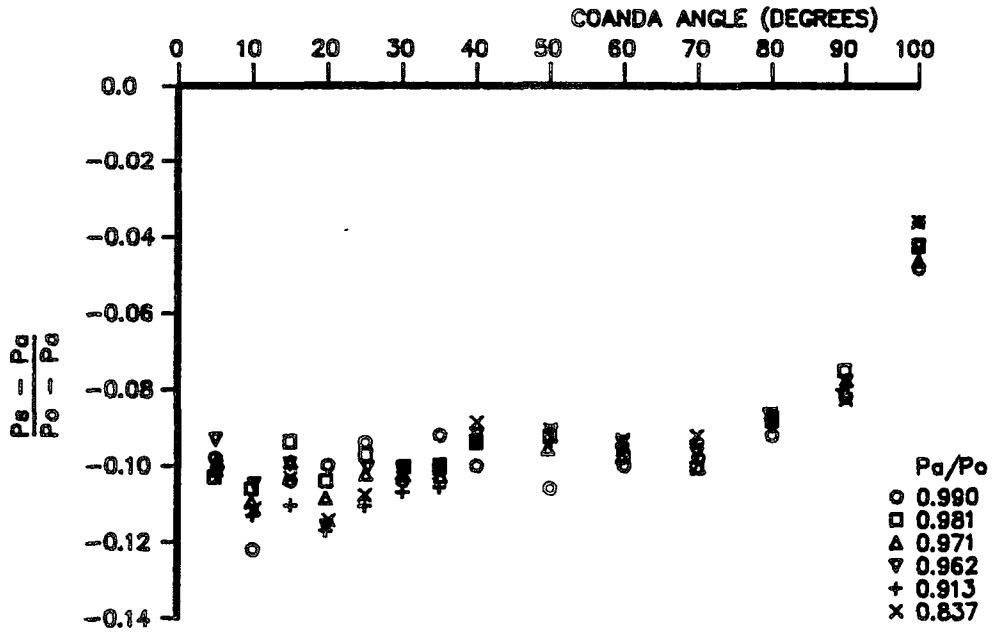

FIG 6.15 : INCOMPRESSIBLE SURFACE PRESSURE COEFFICIENT , 2.00 MM SLOT

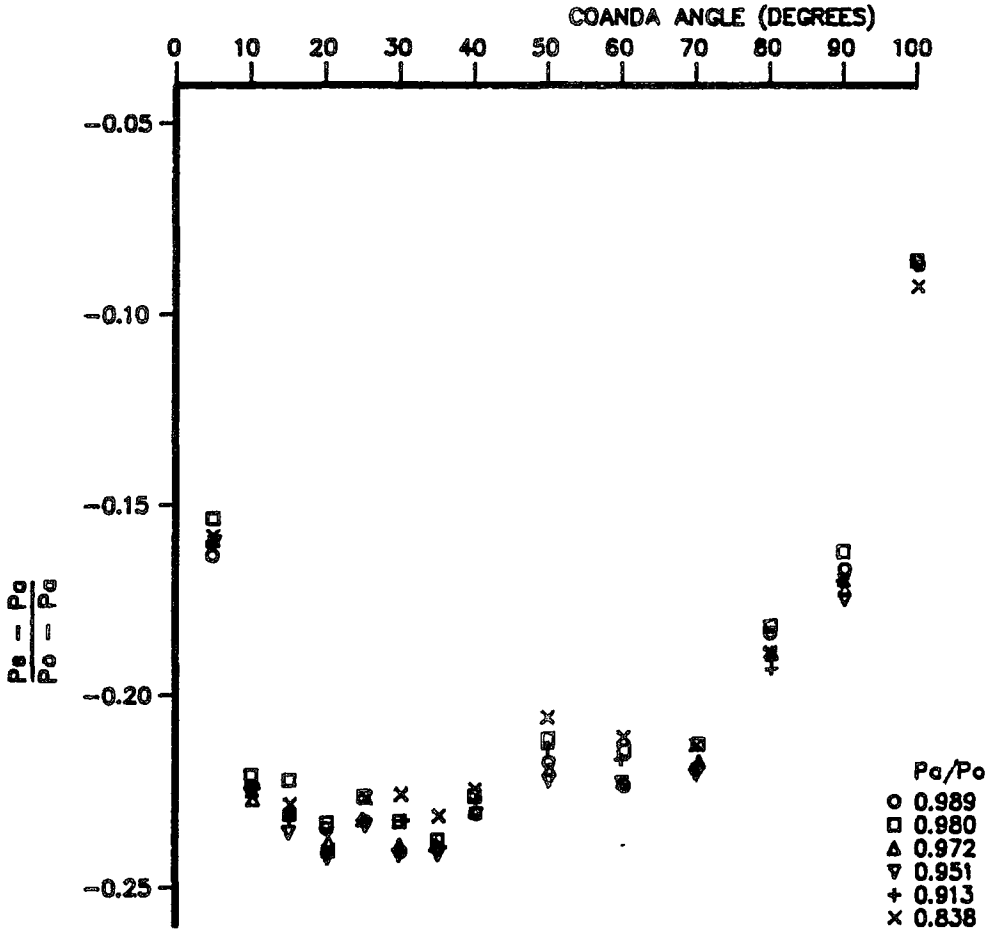

FIG 6.16 : INCOMPRESSIBLE SURFACE PRESSURE COEFFICIENT , 4.01 MM SLOT

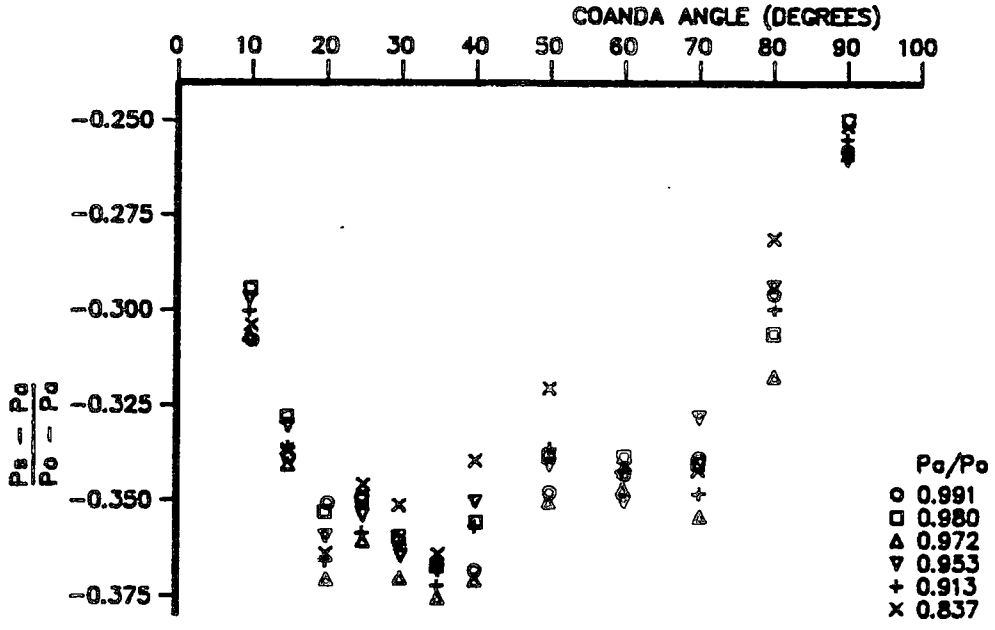

FIG 6.17 : INCOMPRESSIBLE SURFACE PRESSURE COEFFICIENT , 6.00 MM SLOT

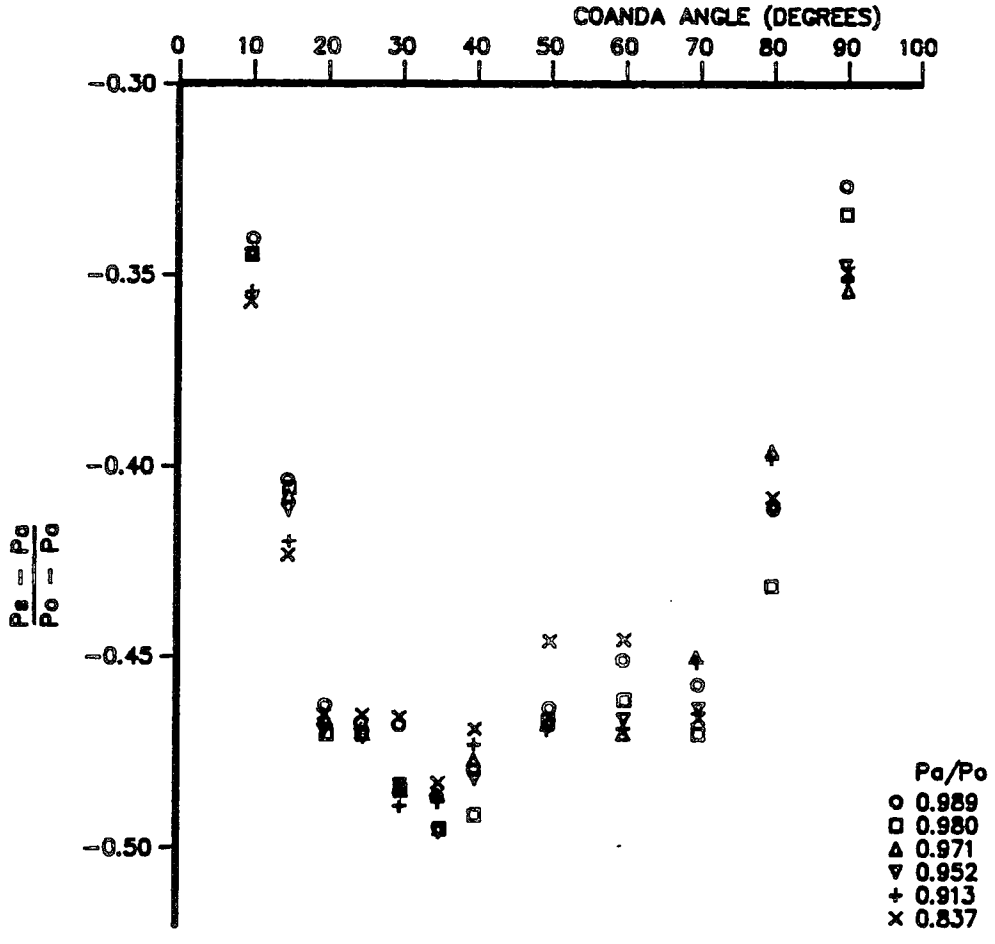

FIG 6.18 : INCOMPRESSIBLE SURFACE PRESSURE COEFFICIENT , 7.99 MM SLOT

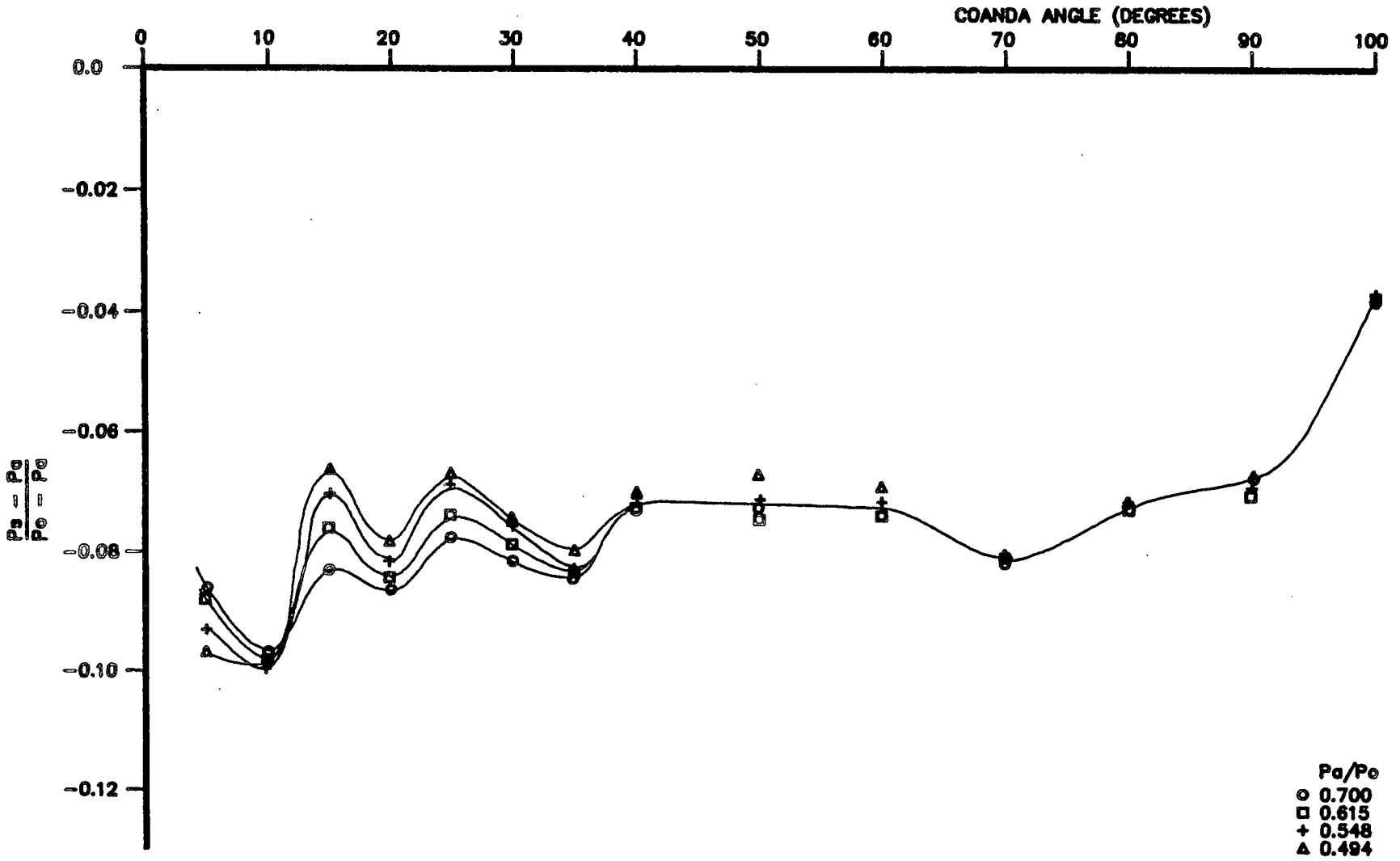

FIG 6.19 : COMPRESSIBLE SURFACE PRESSURE COEFFICIENT , 2 MM SLOT

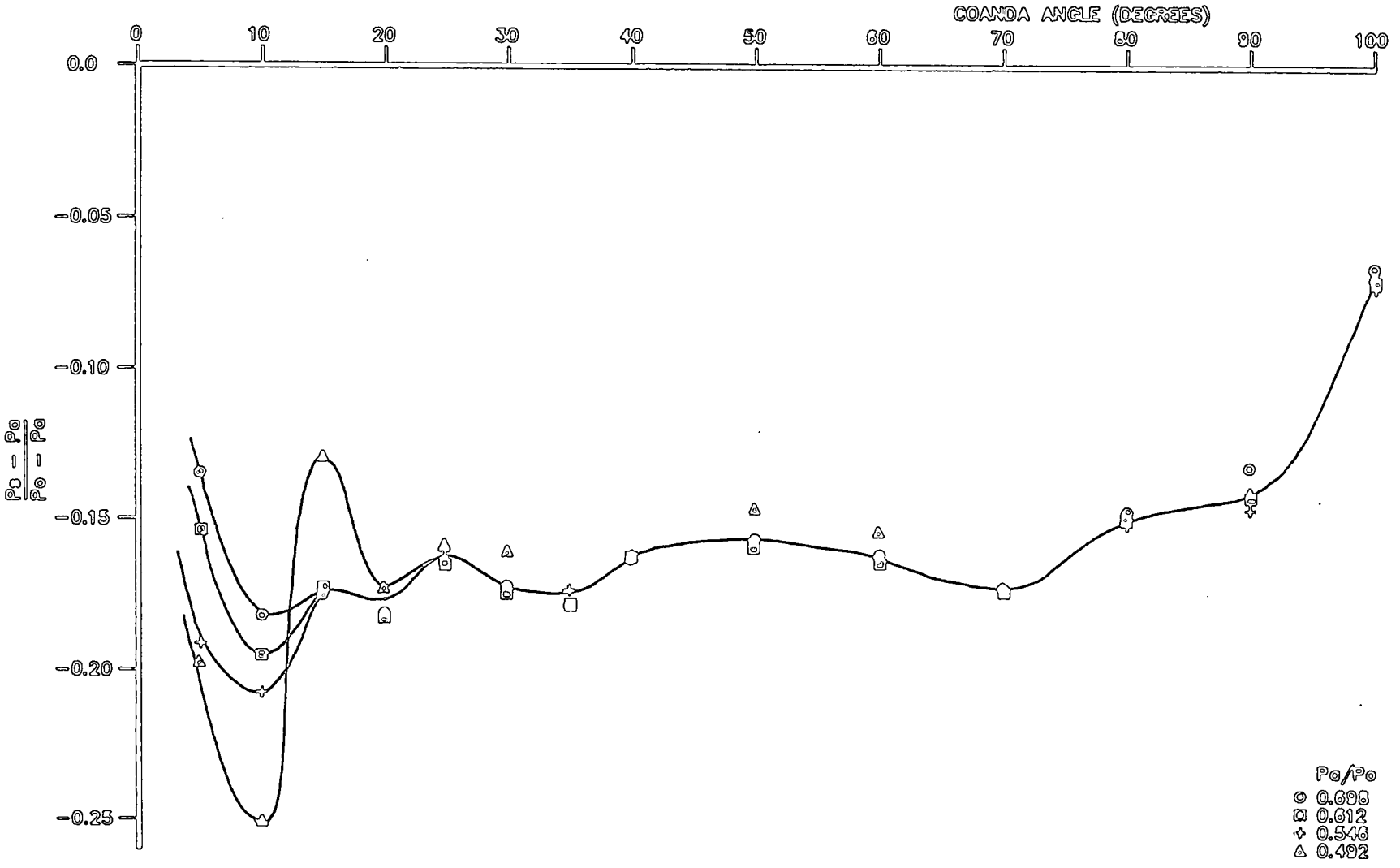

FIG 6.20 : COMPRESSIBLE SURFACE PRESSURE COEFFICIENT , 4 MM SLOT

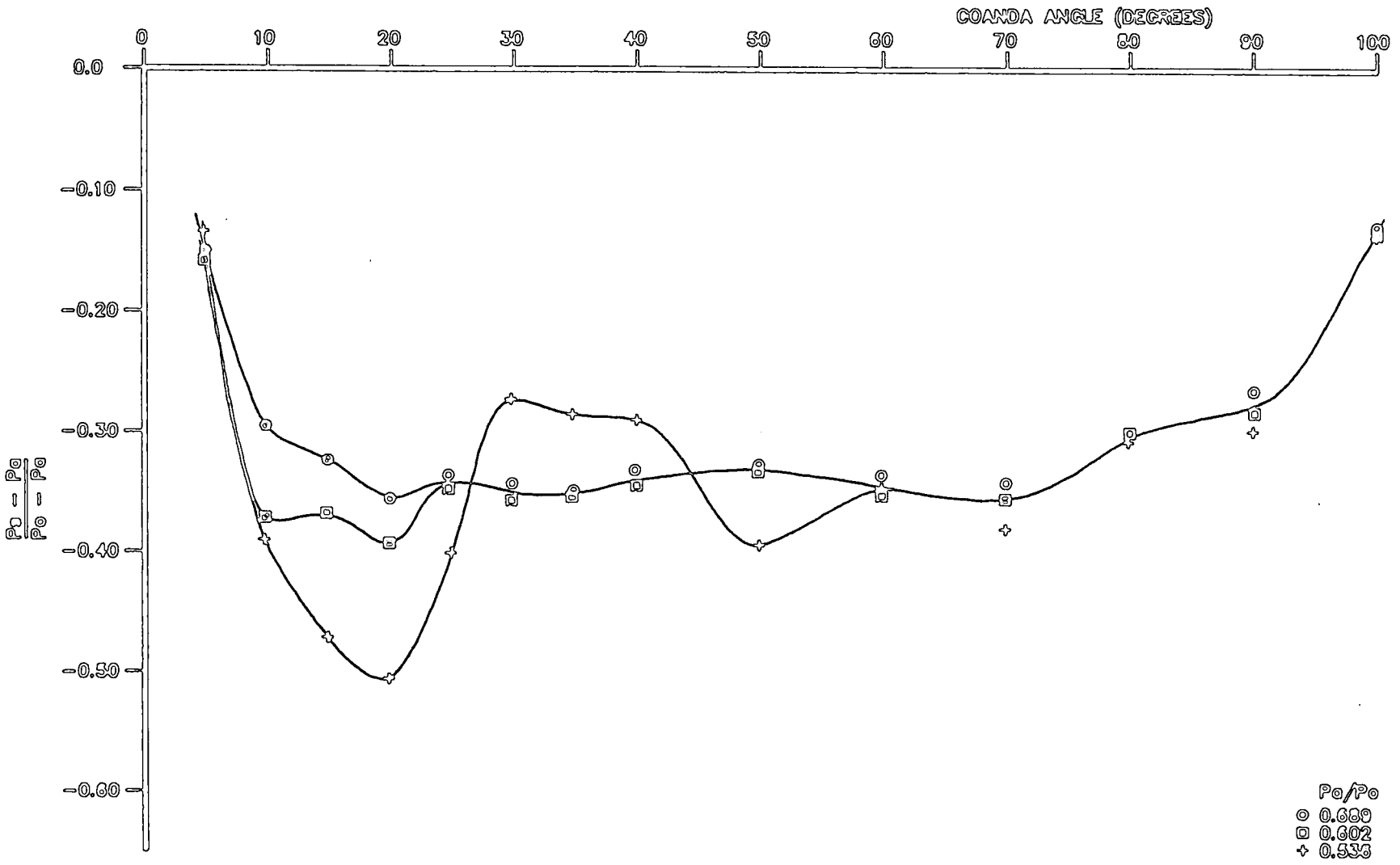

FIG 6.21 : COMPRESSIBLE SURFACE PRESSURE COEFFICIENT , 8 MM SLOT

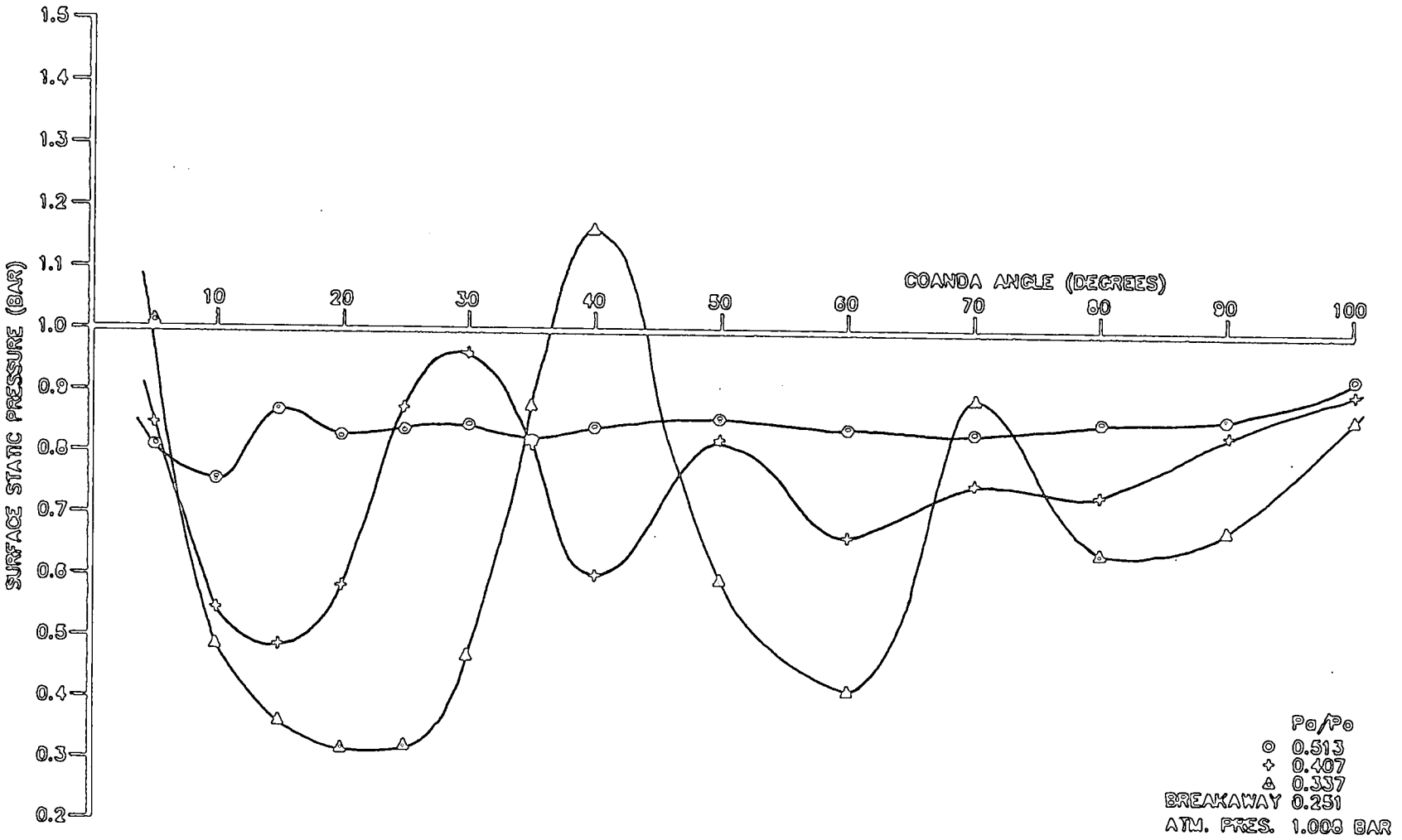

FIG 6.22A : SURFACE PRESSURES FROM CHOKED 4.15 MM SLOT

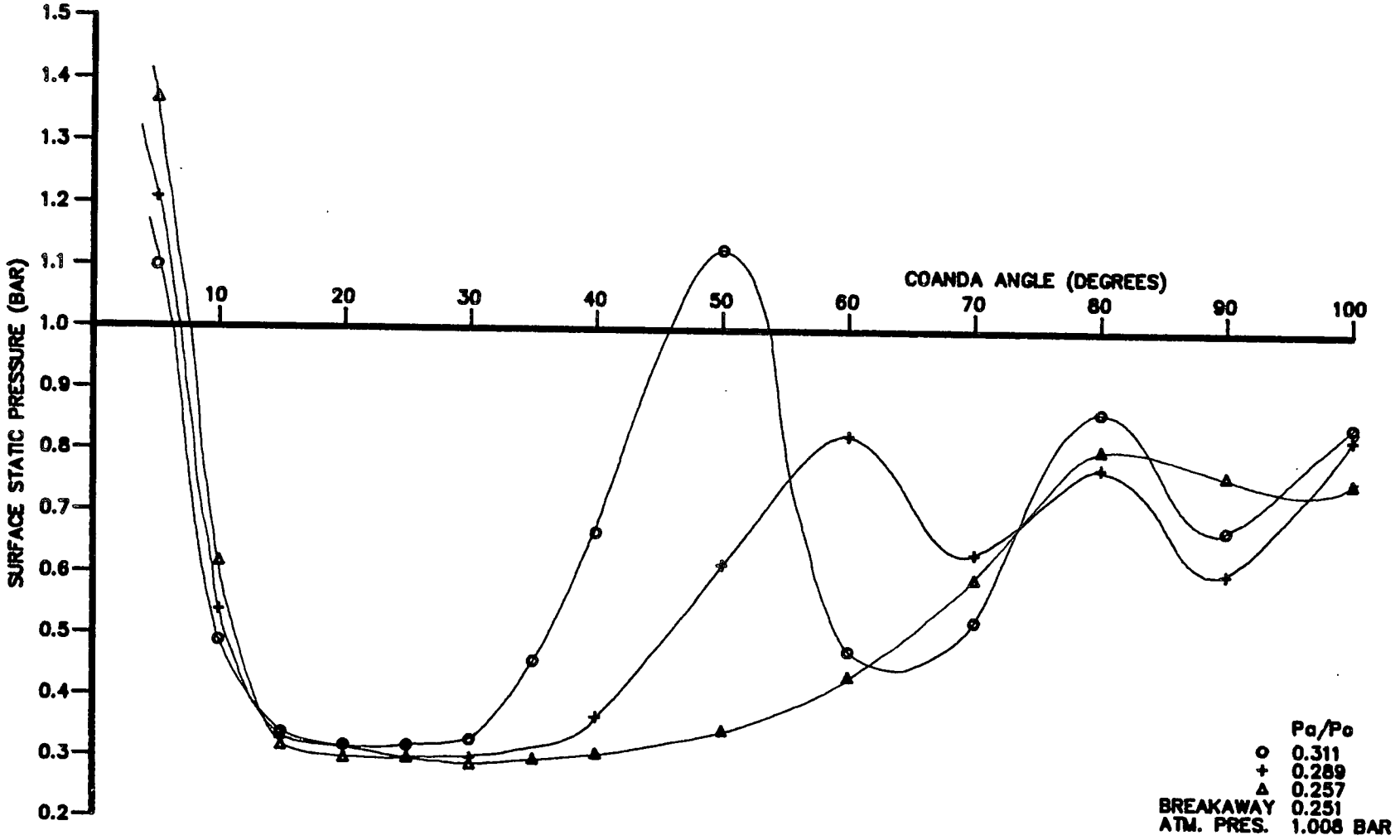

FIG 6.22B : SURFACE PRESSURES FROM CHOKED 4.15 MM SLOT

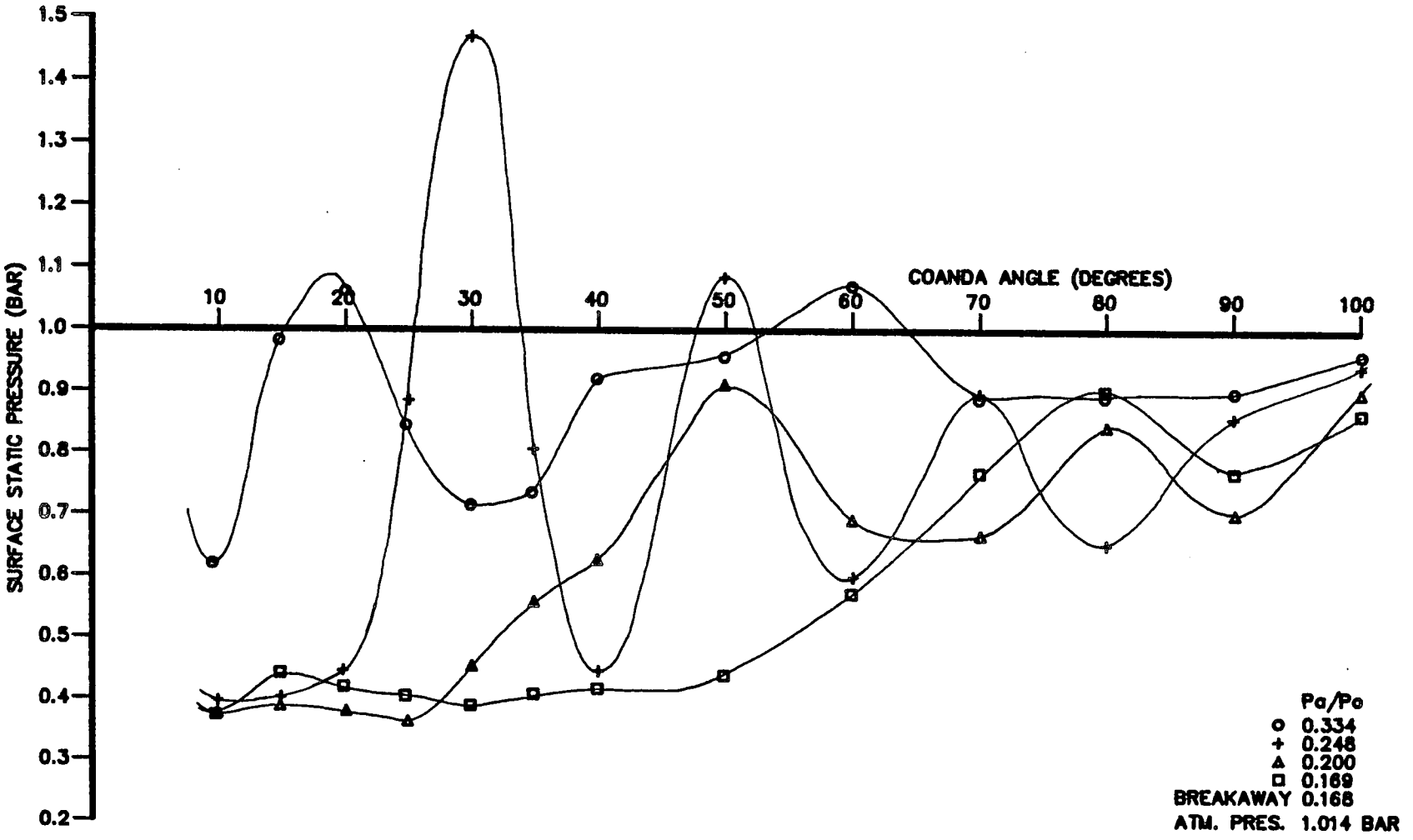

FIG 6.23 : SURFACE PRESSURES FROM CHOKED 1.99 MM SLOT

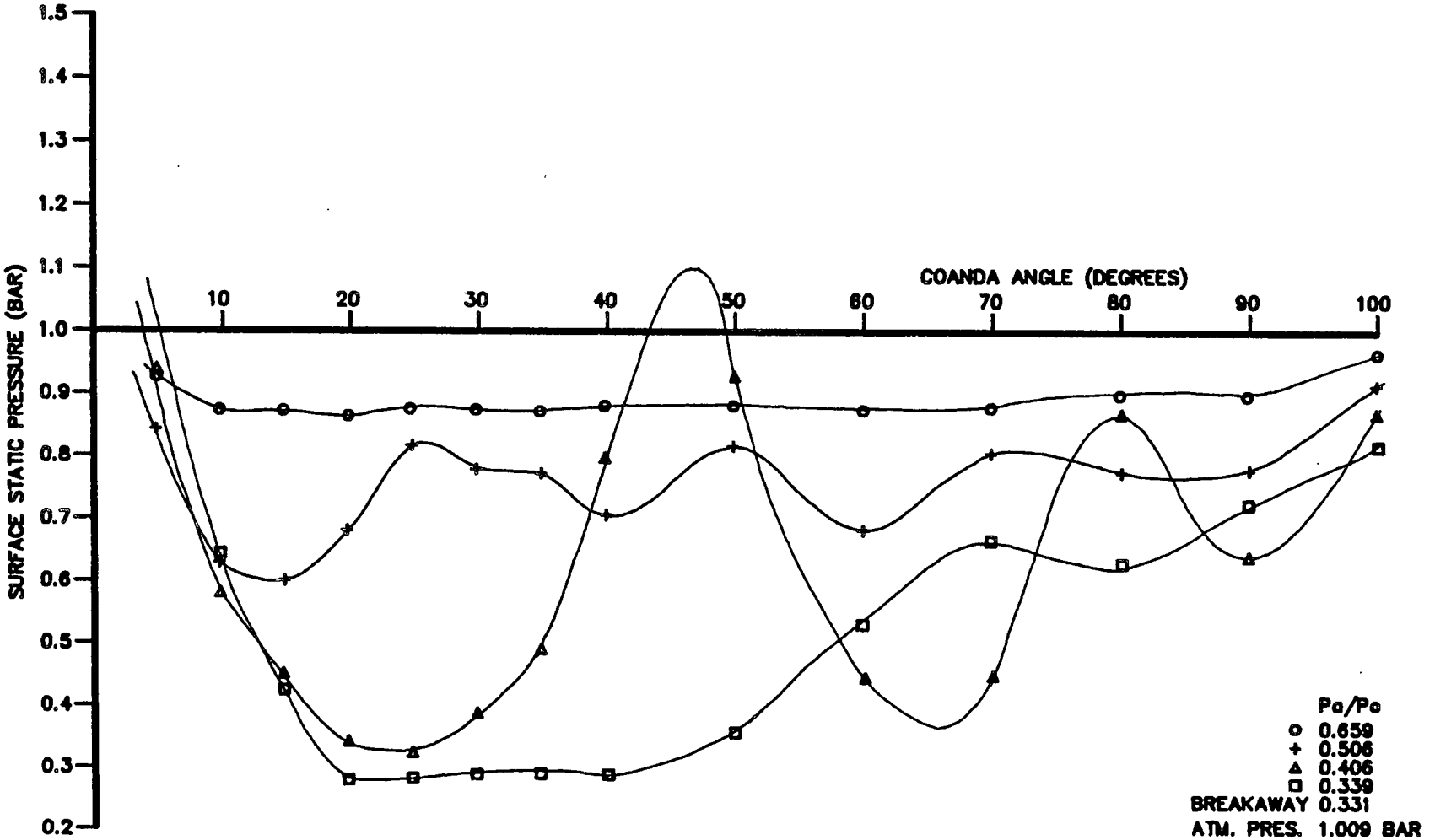

FIG 6.24 : SURFACE PRESSURES FROM CHOKED 6.00 MM SLOT

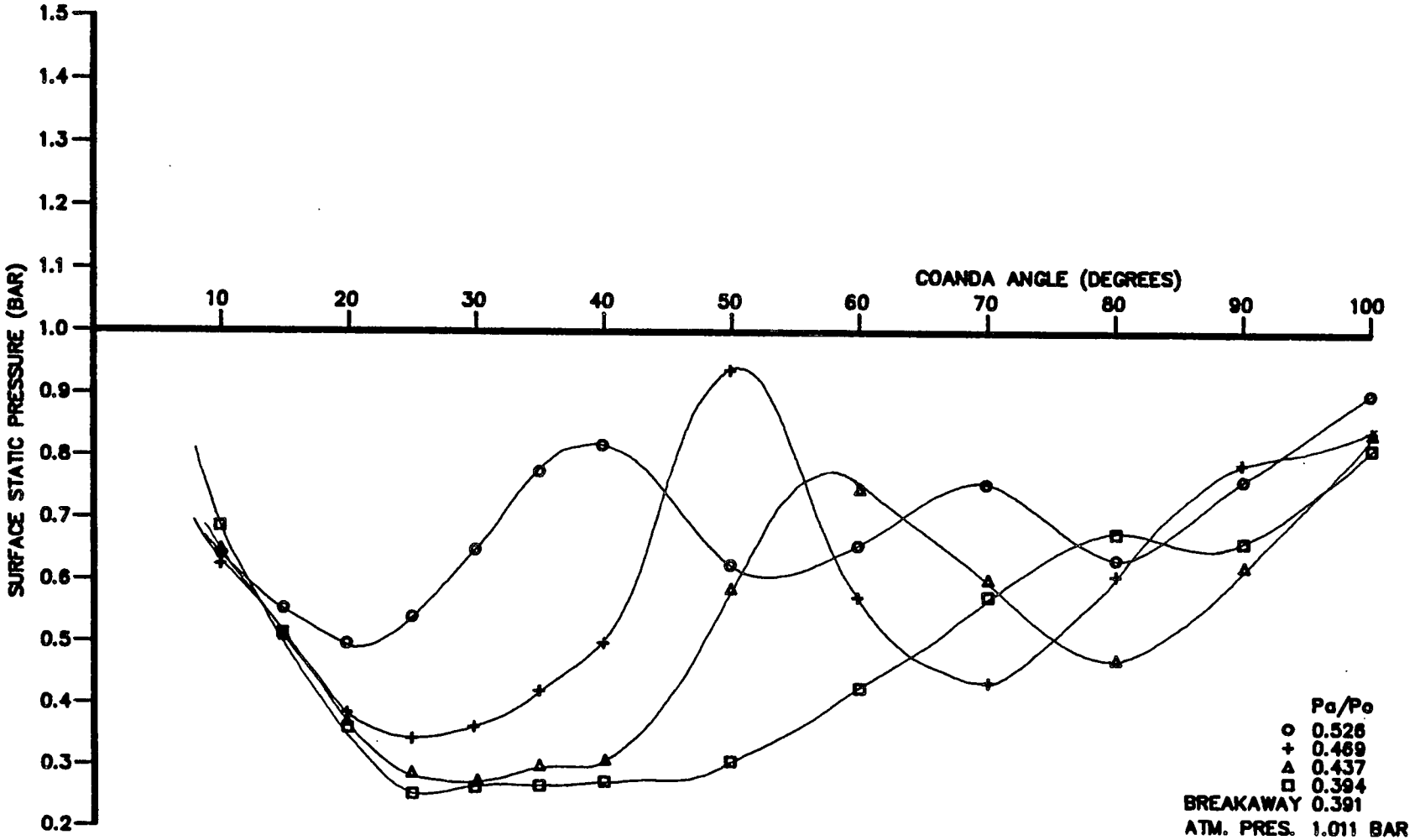

FIG 6.25 : SURFACE PRESSURES FROM CHOKED 7.99 MM SLOT

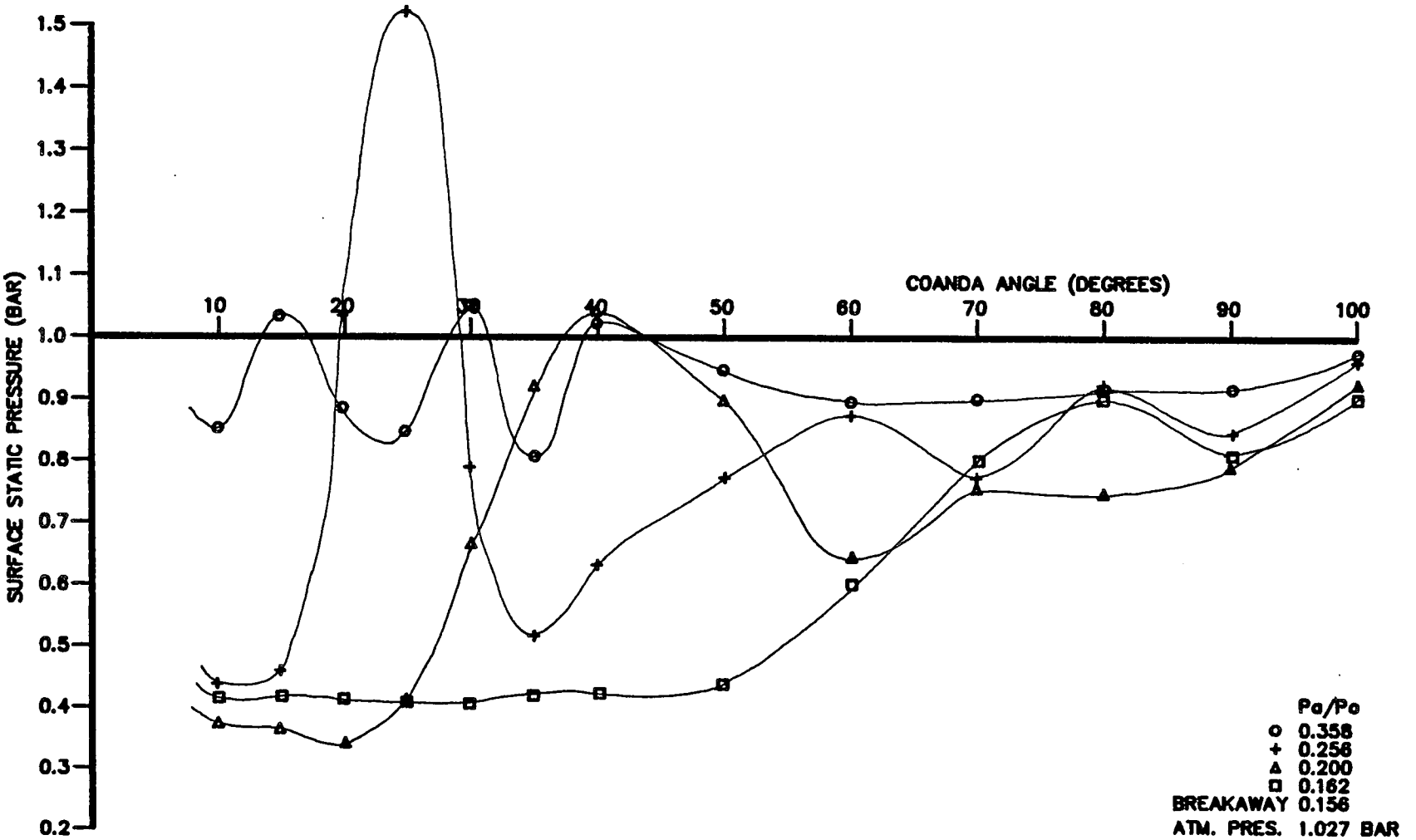

FIG 6.26 : SURFACE PRESSURES FROM 1.99 MM SLOT , NOZZLE B

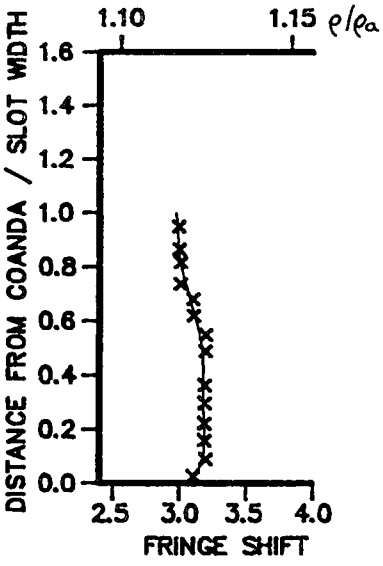

FIG 7.1A : SLOT EXIT

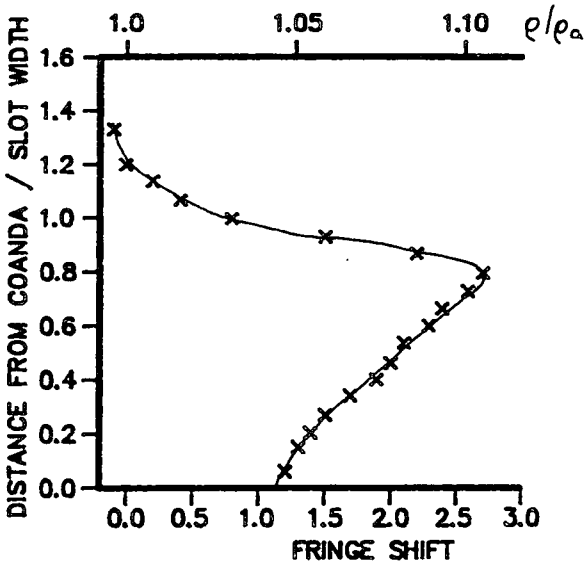

FIG 7.1B : 10° ROUND COANDA

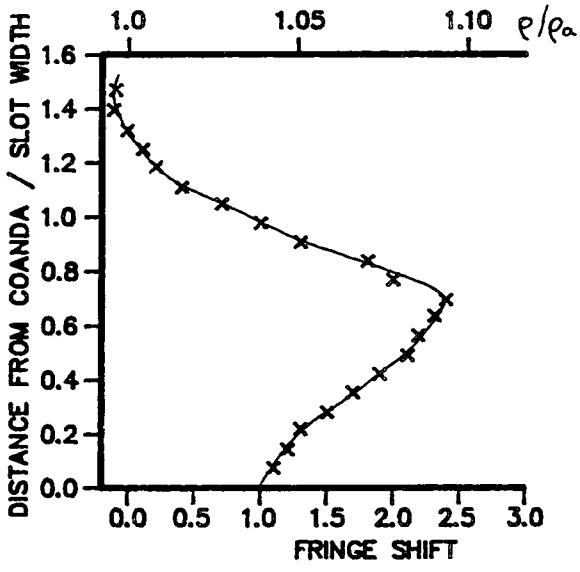

FIG 7.1C : 20° ROUND COANDA

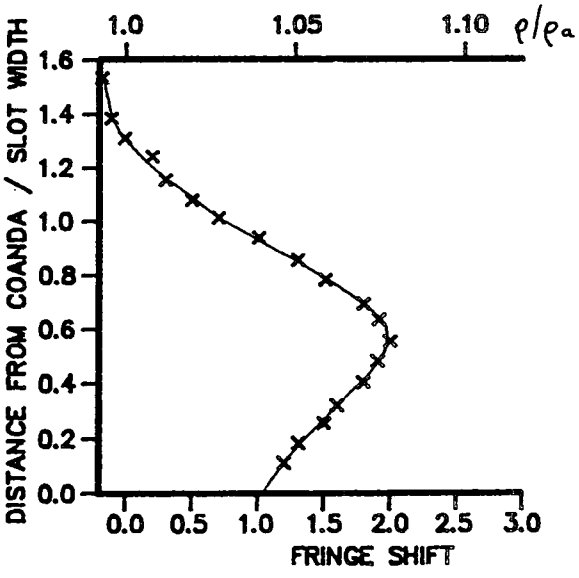

FIG 7.1D : 30° ROUND COANDA

FIG 7.1 : DENSITY DISTRIBUTION b/a = 0.133 , Pa/Po = 0.654

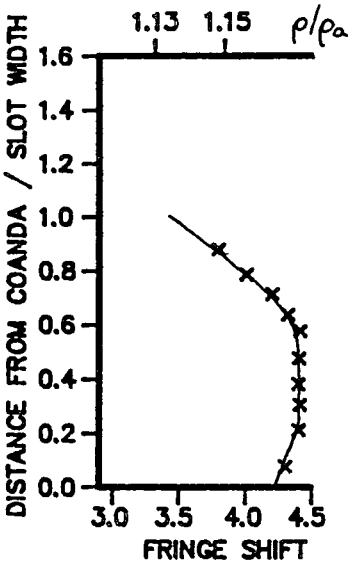

FIG 7.2A : SLOT EXIT

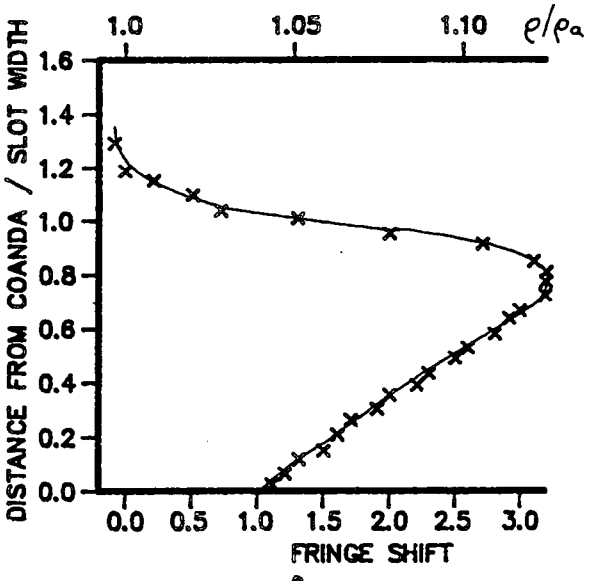

FIG 7.2B : 10^{0} ROUND COANDA

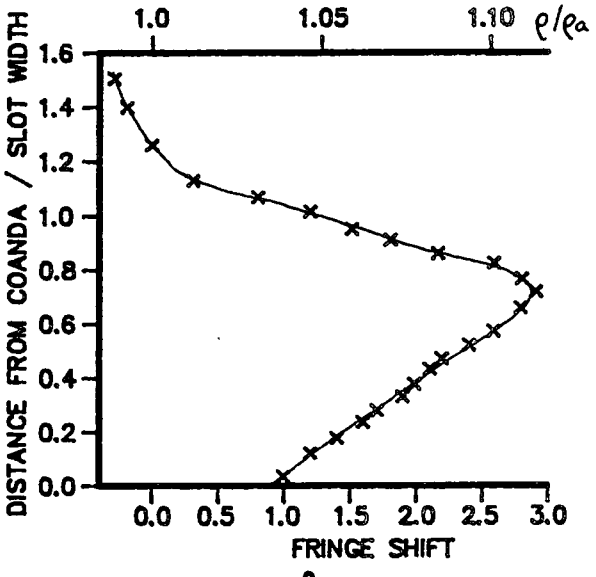

FIG 7.2C : 20^{0} ROUND COANDA

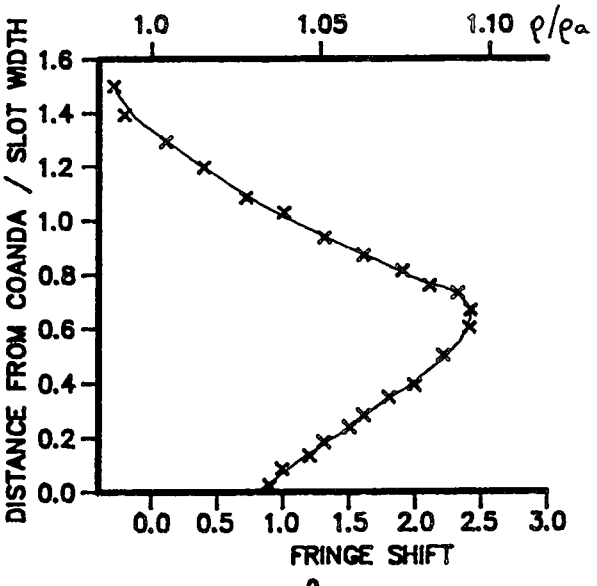

FIG 7.2D : 30^{0} ROUND COANDA

FIG 7.2 : DENSITY DISTRIBUTION b/a = 0.133 , Pa/Po = 0.579

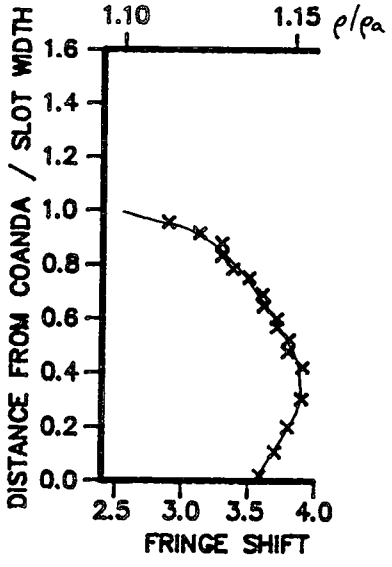

FIG 7.3A : SLOT EXIT

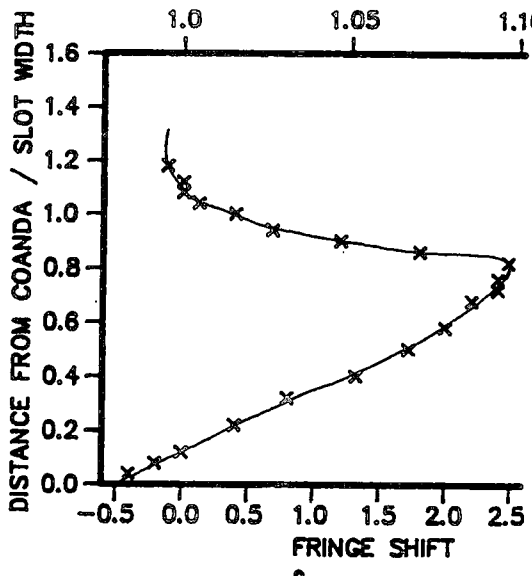

FIG 7.3B : 10^{0} ROUND COANDA

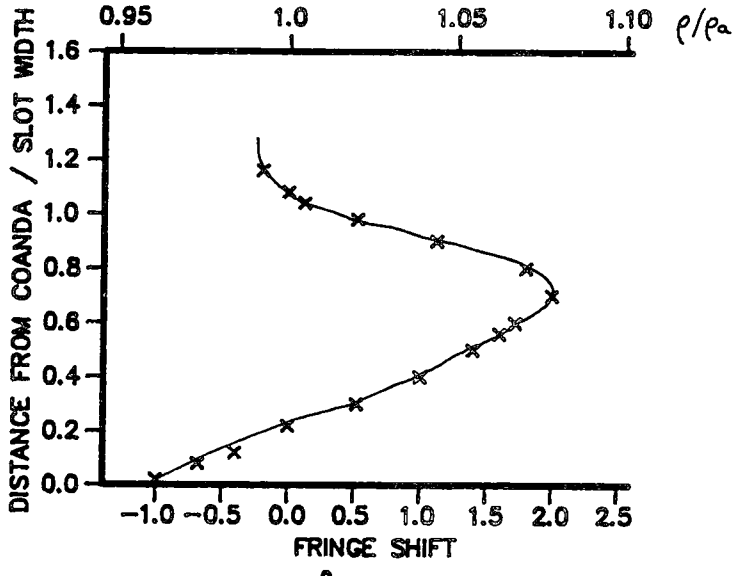

FIG 7.3C : 20^{0} ROUND COANDA

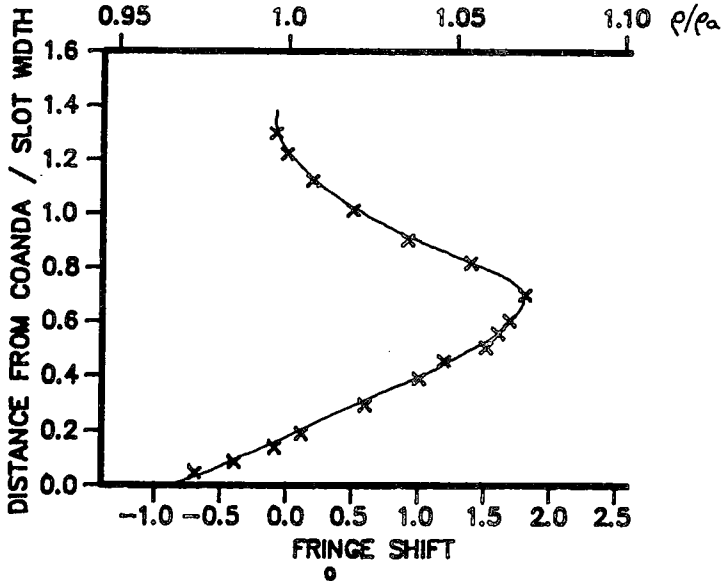

FIG 7.3D : 30^{0} ROUND COANDA

FIG 7.3 : DENSITY DISTRIBUTION b/a = 0.266 , Pa/Po = 0.644

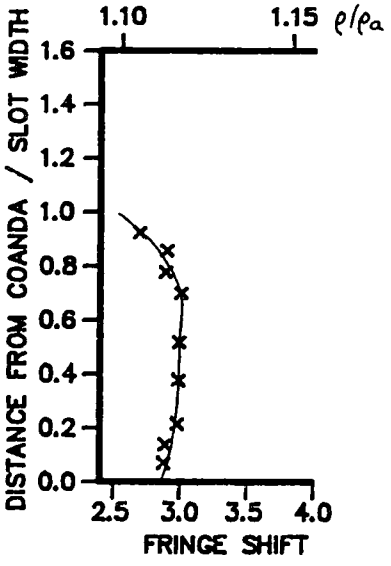

FIG 7.4A : SLOT EXIT

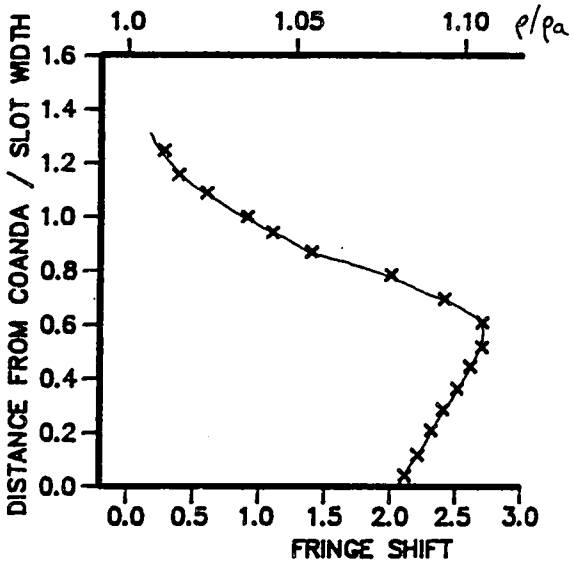

FIG 7.4B : 10° ROUND COANDA

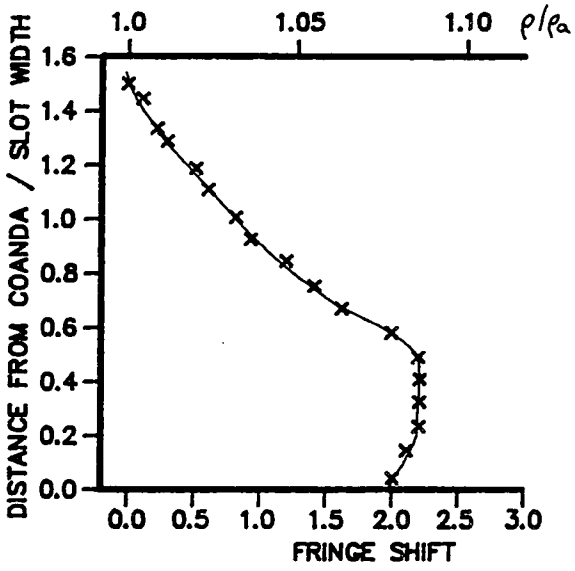

FIG 7.4C : 20° ROUND COANDA

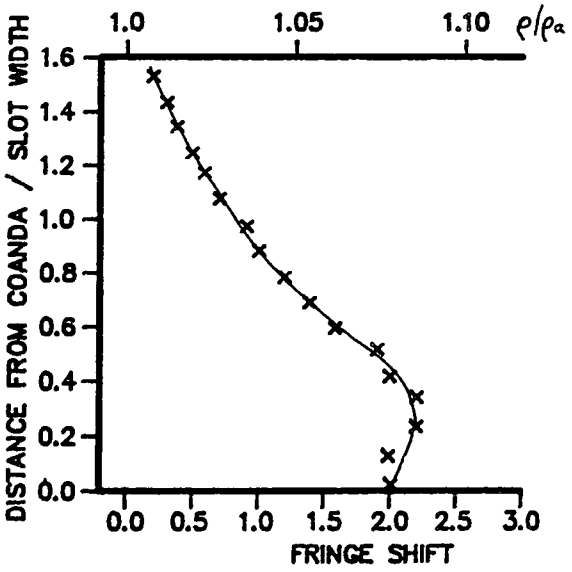

FIG 7.4D : 30° ROUND COANDA

FIG 7.4 : DENSITY DISTRIBUTION b/a = 0.067 , Pa/Po = 0.653

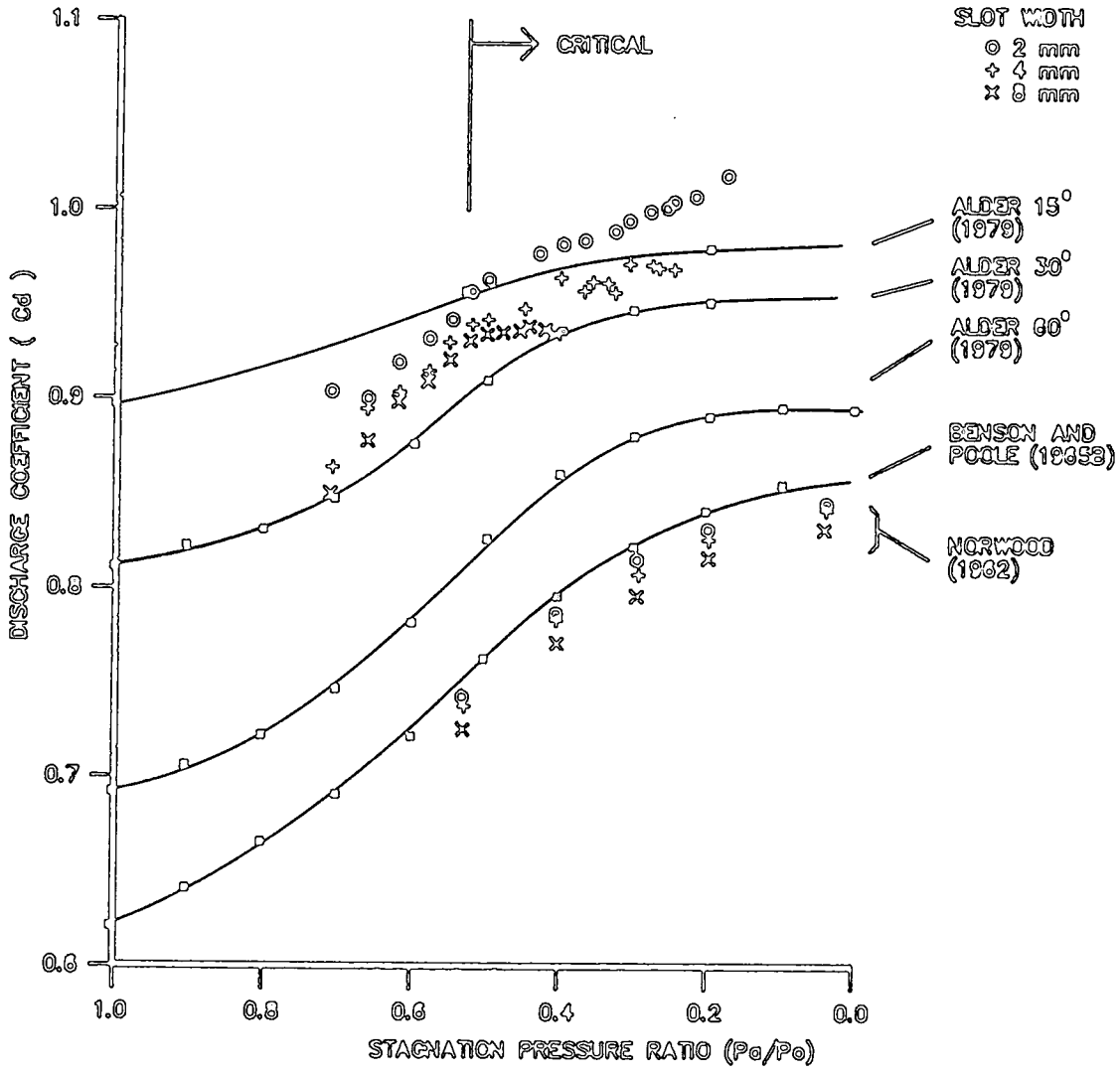

FIG 8.1 : COMPARISON OF DISCHARGE COEFFICIENT

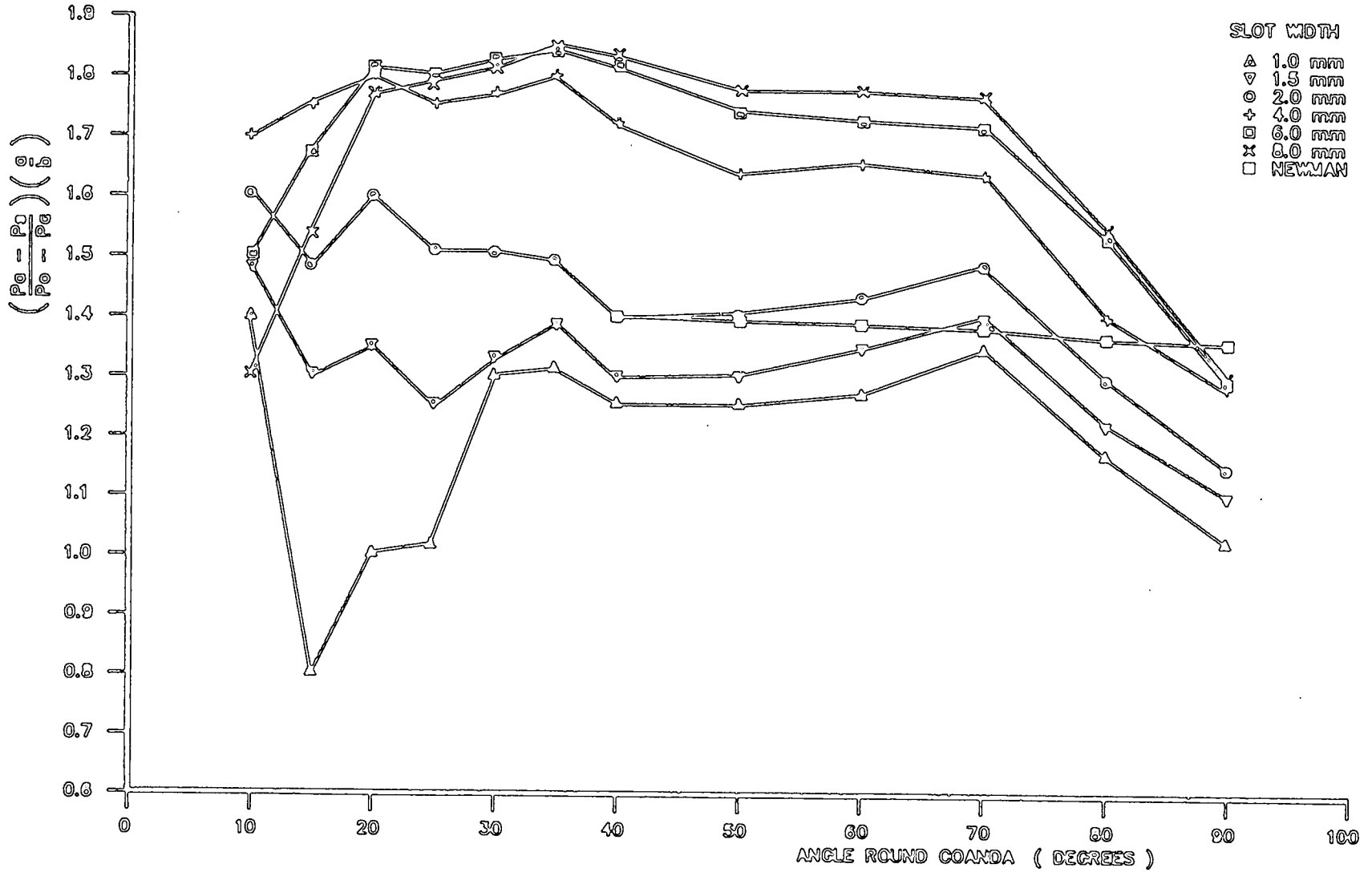

FIG 8.2 : INCOMPRESSIBLE SURFACE STATIC PRESSURES

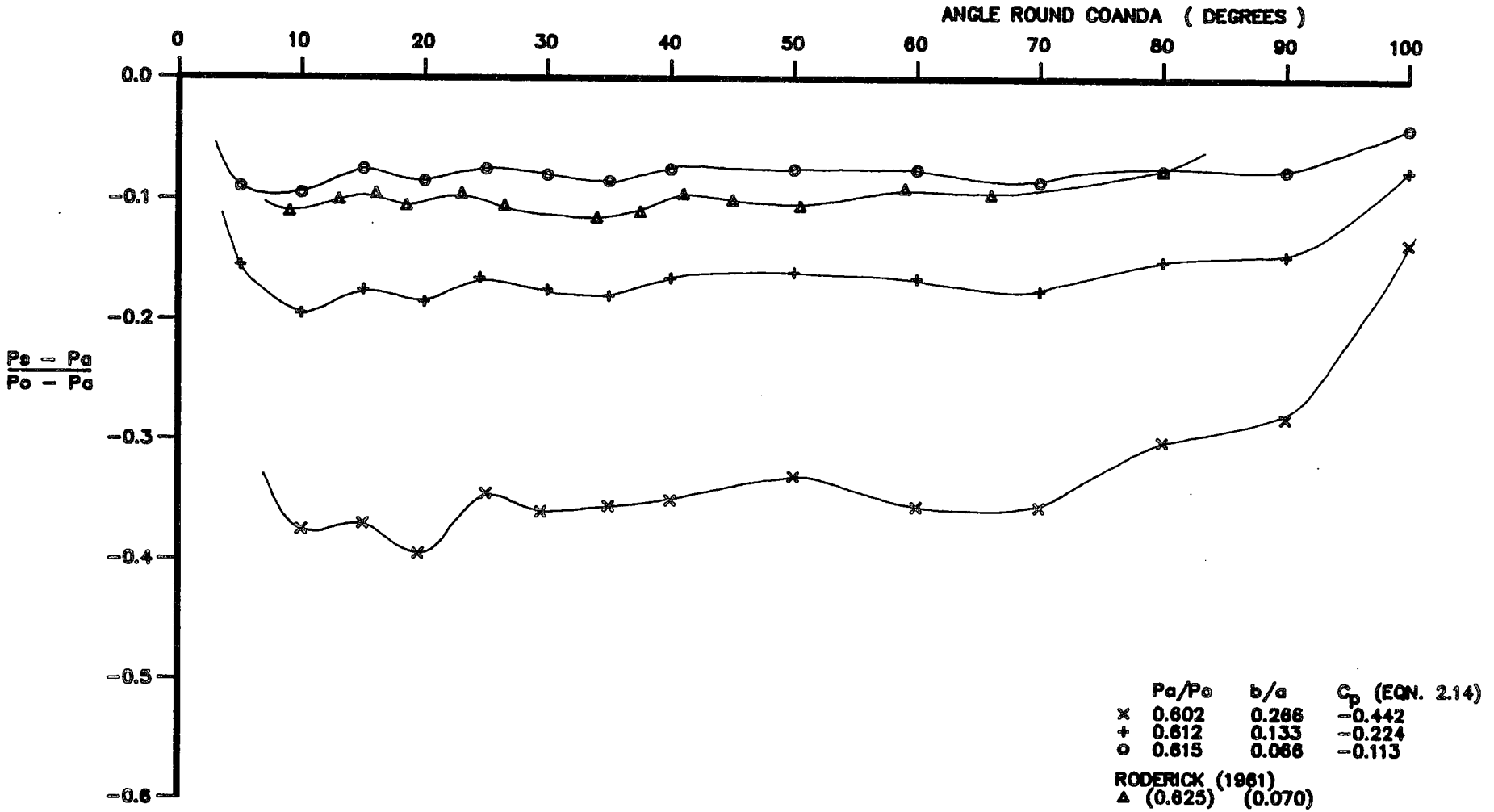

FIG 8.3 : COMPRESSIBLE SURFACE PRESSURES , Pa/Po = 0.61

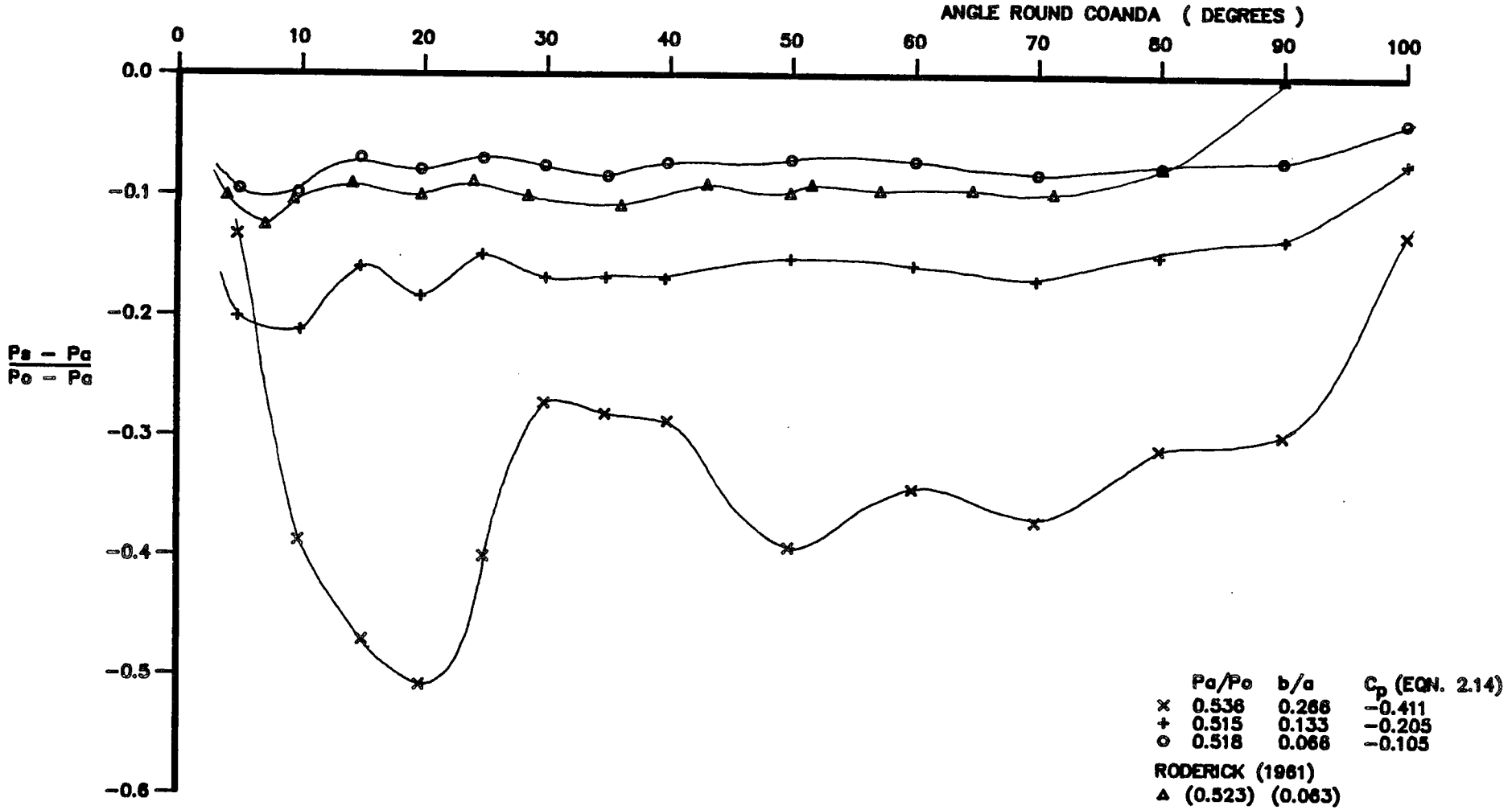

FIG 8.4 : COMPRESSIBLE SURFACE PRESSURES , Pa/Po = 0.52

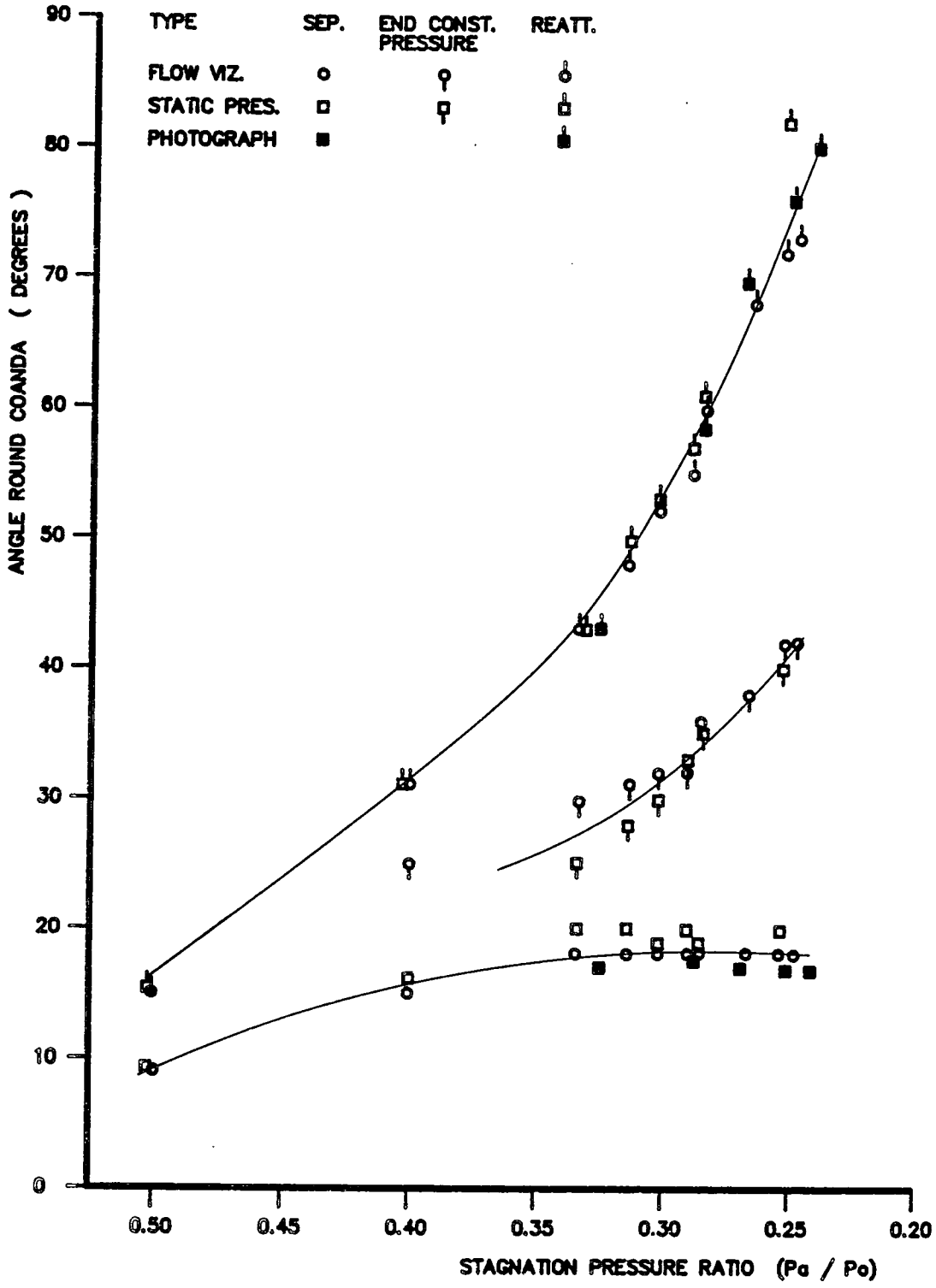

FIG 8.5 : CORRELATION OF SEPARATION BUBBLE , 4MM SLOT

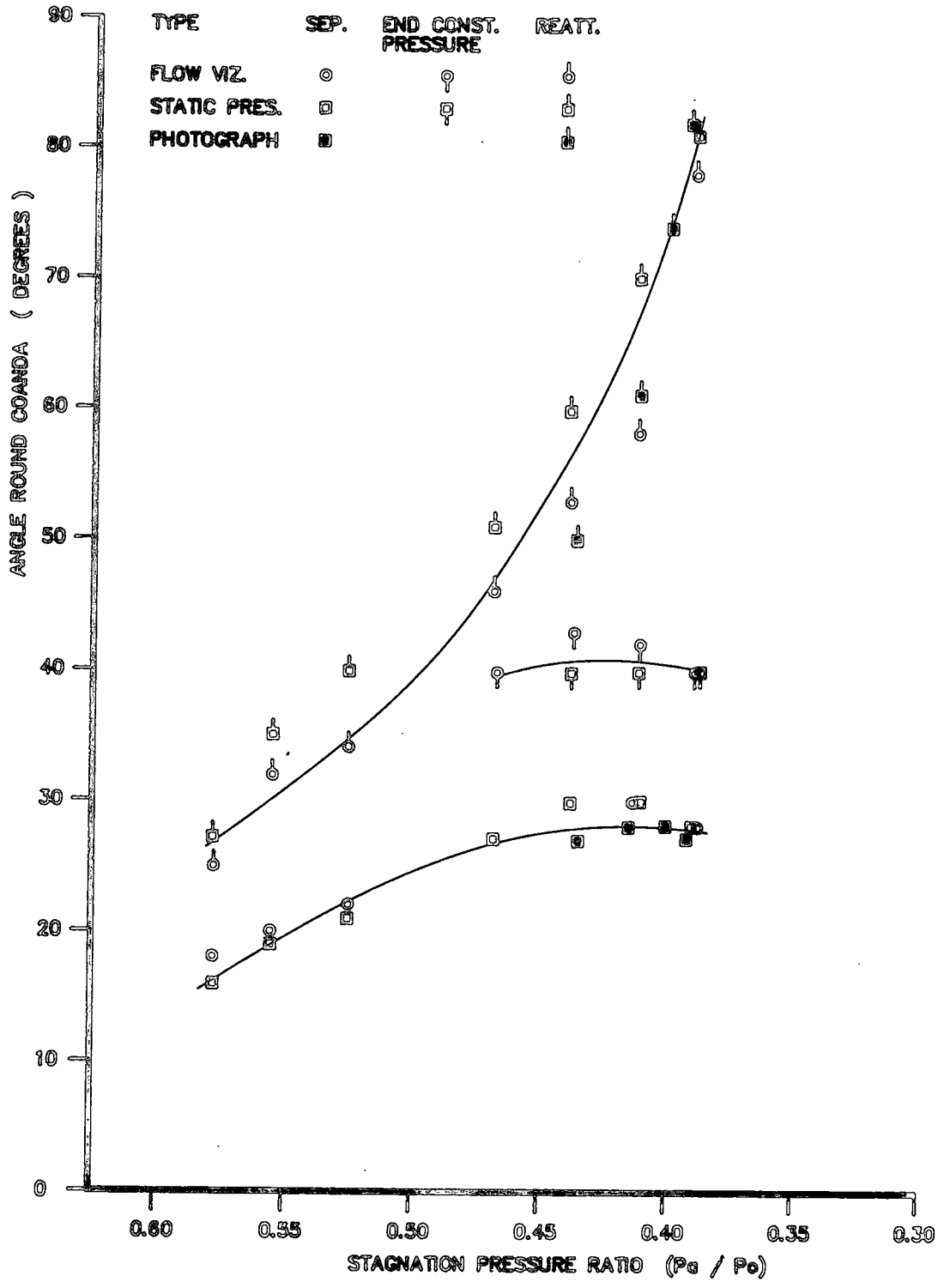

FIG 8.6 : CORRELATION OF SEPARATION BUBBLE , 8MM SLOT

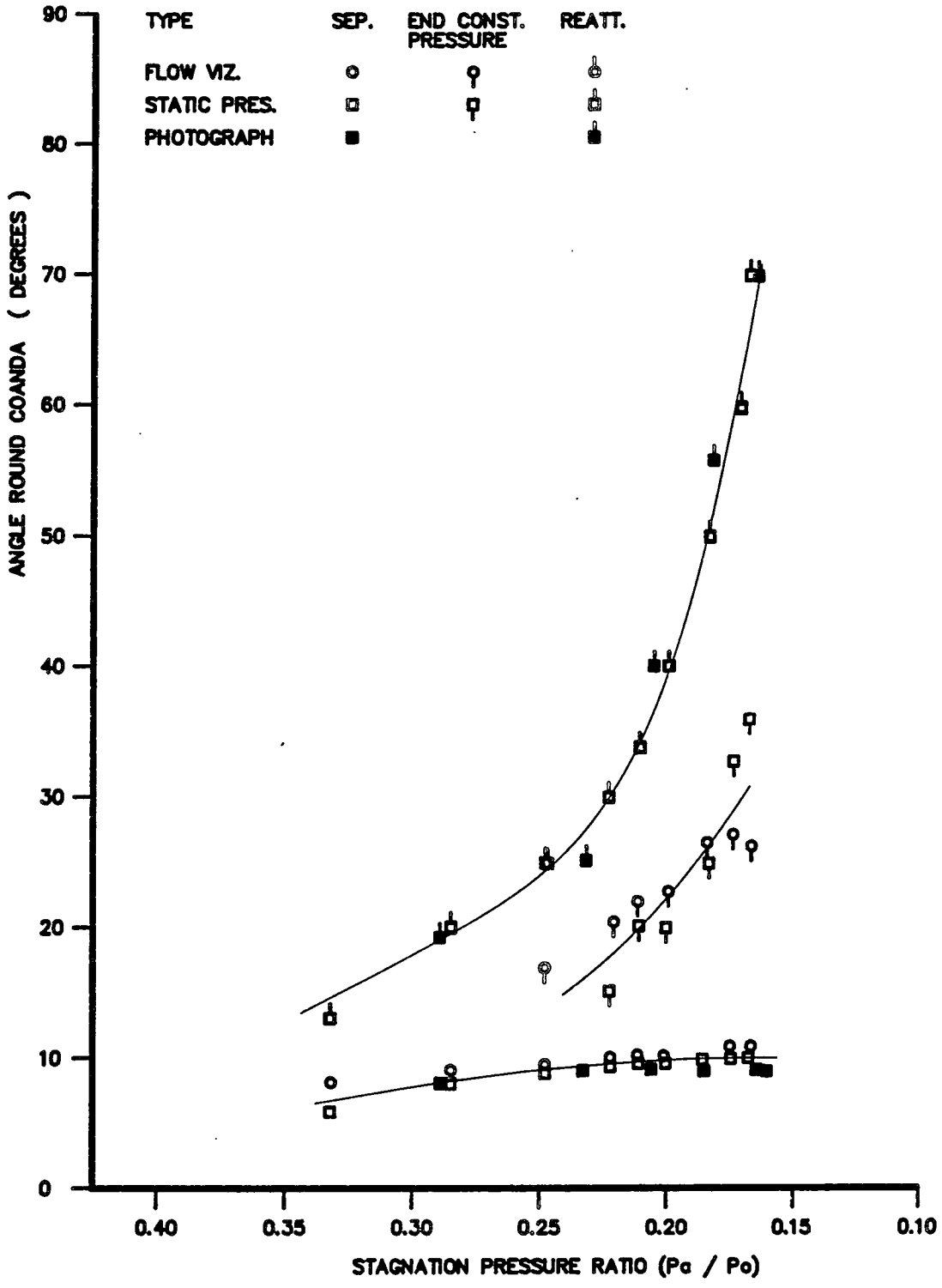

FIG 8.7 : CORRELATION OF SEPARATION BUBBLE , 2MM SLOT

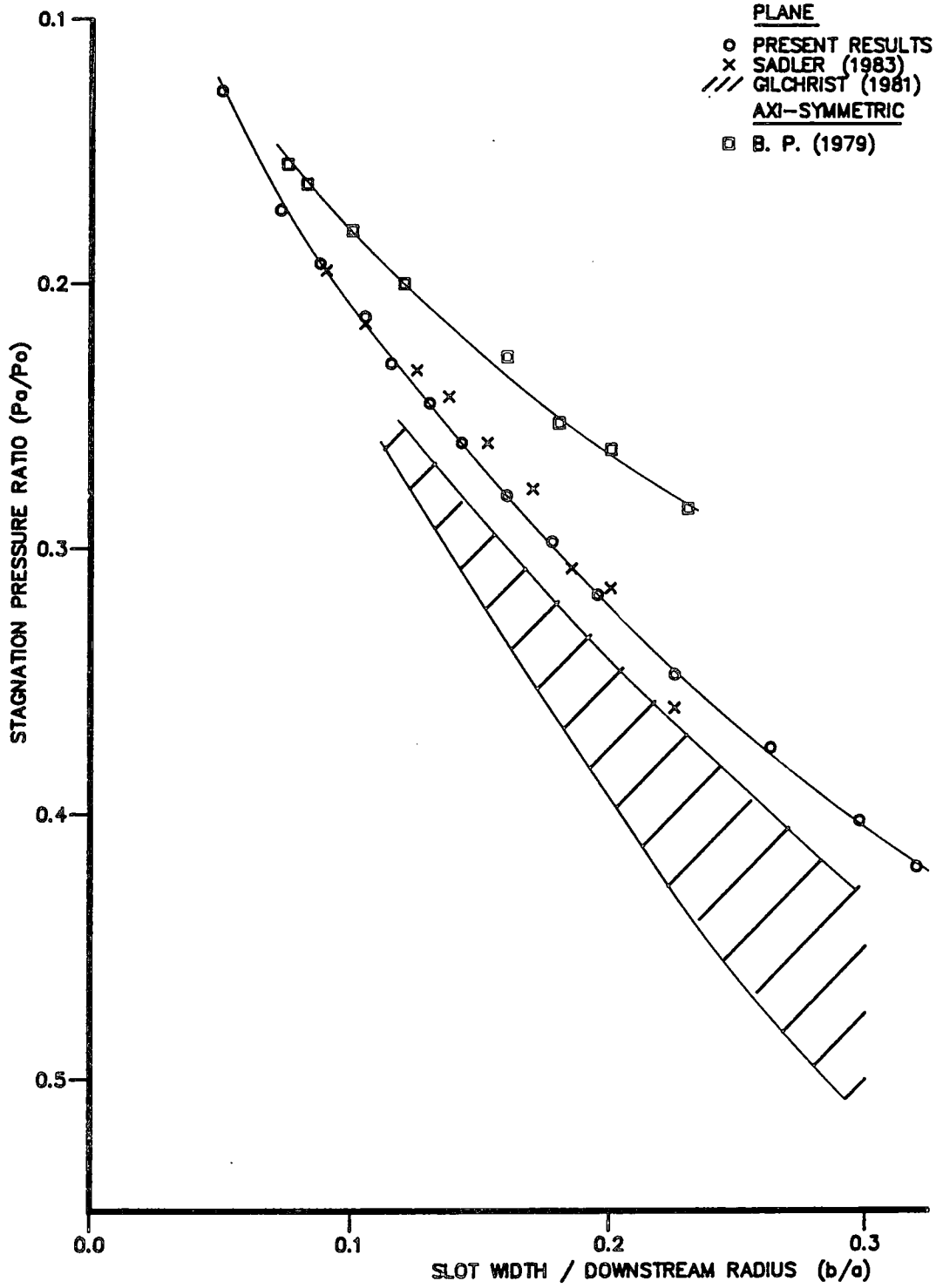

FIG 8.8 : COMPARISON OF BREAKAWAY

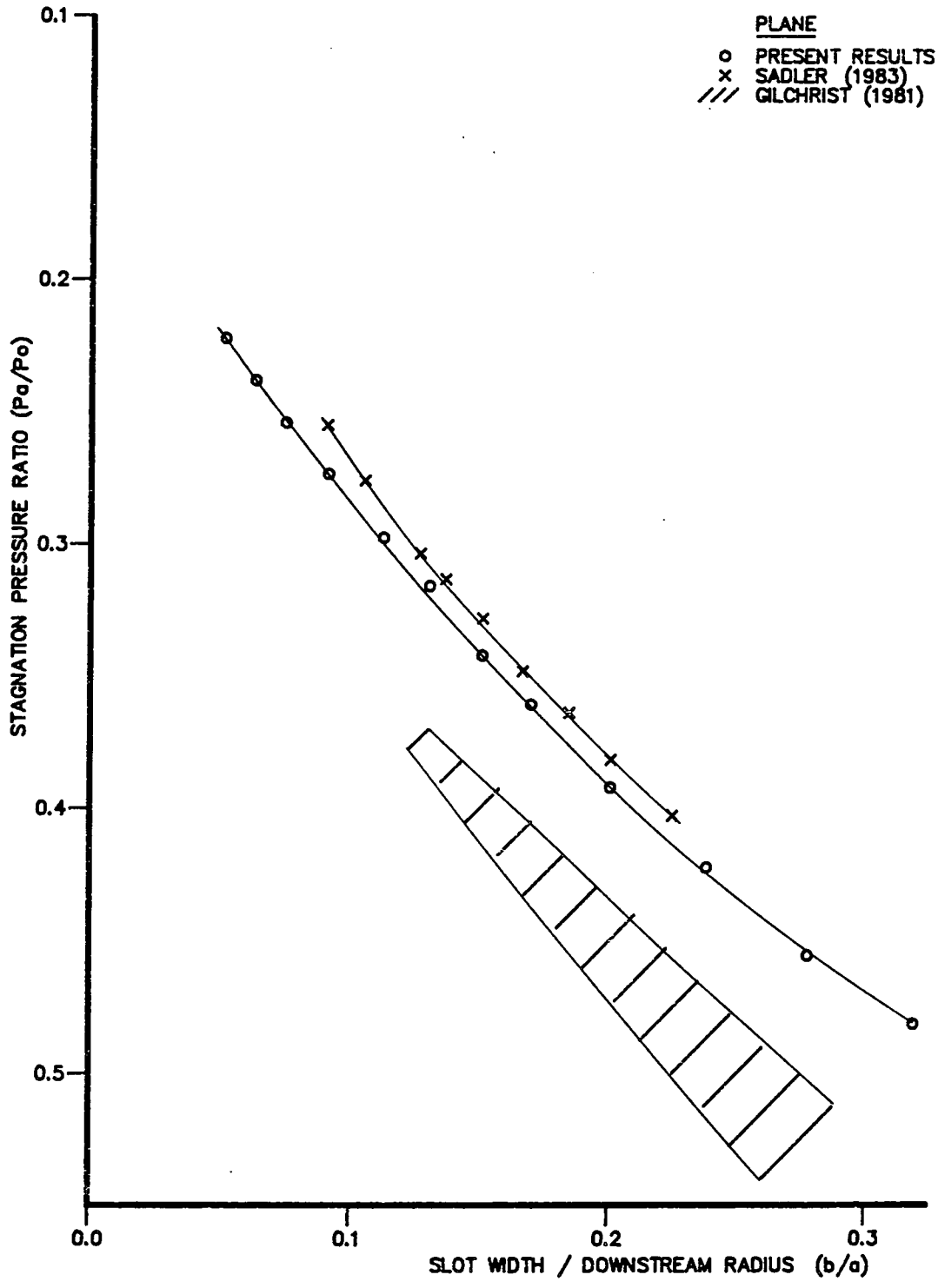

FIG 8.9 : COMPARISON OF REATTACHMENT

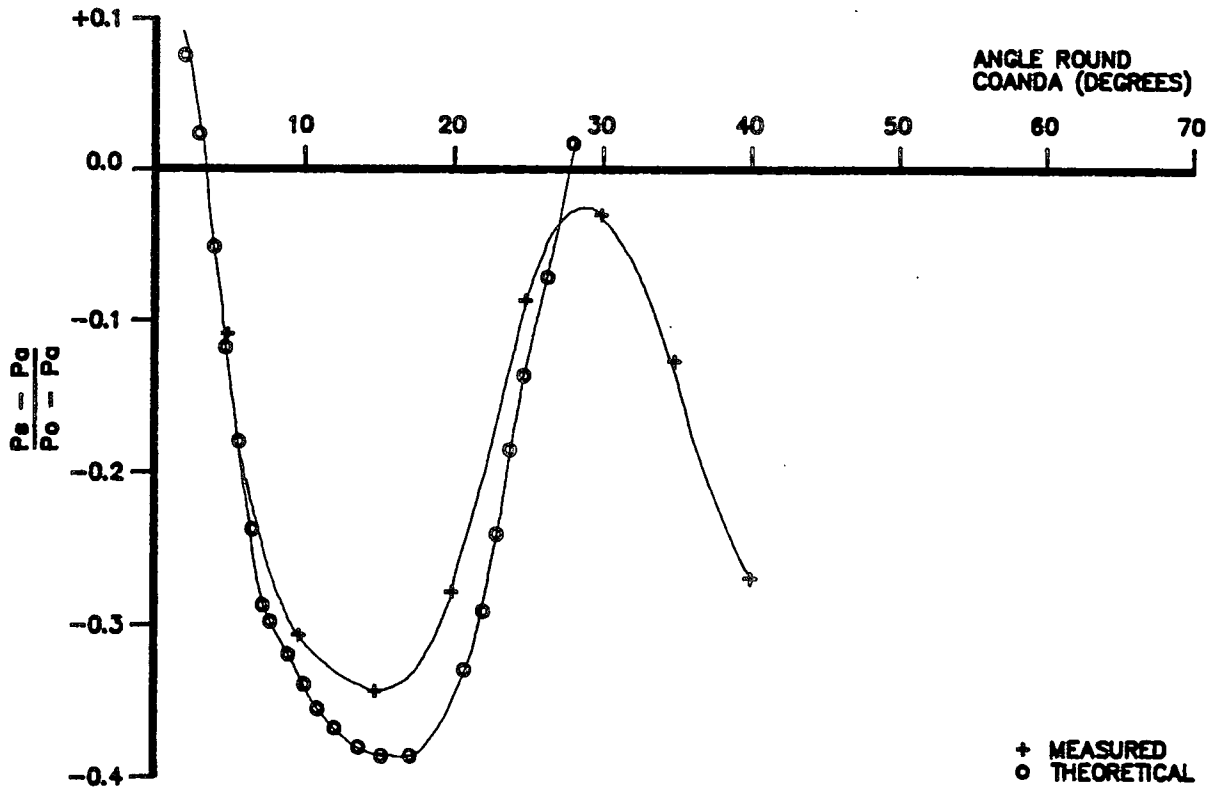

FIG 8.10 : COMPARISON OF SURFACE PRESSURE , Pa/Po = 0.407 , b/a = 0.138

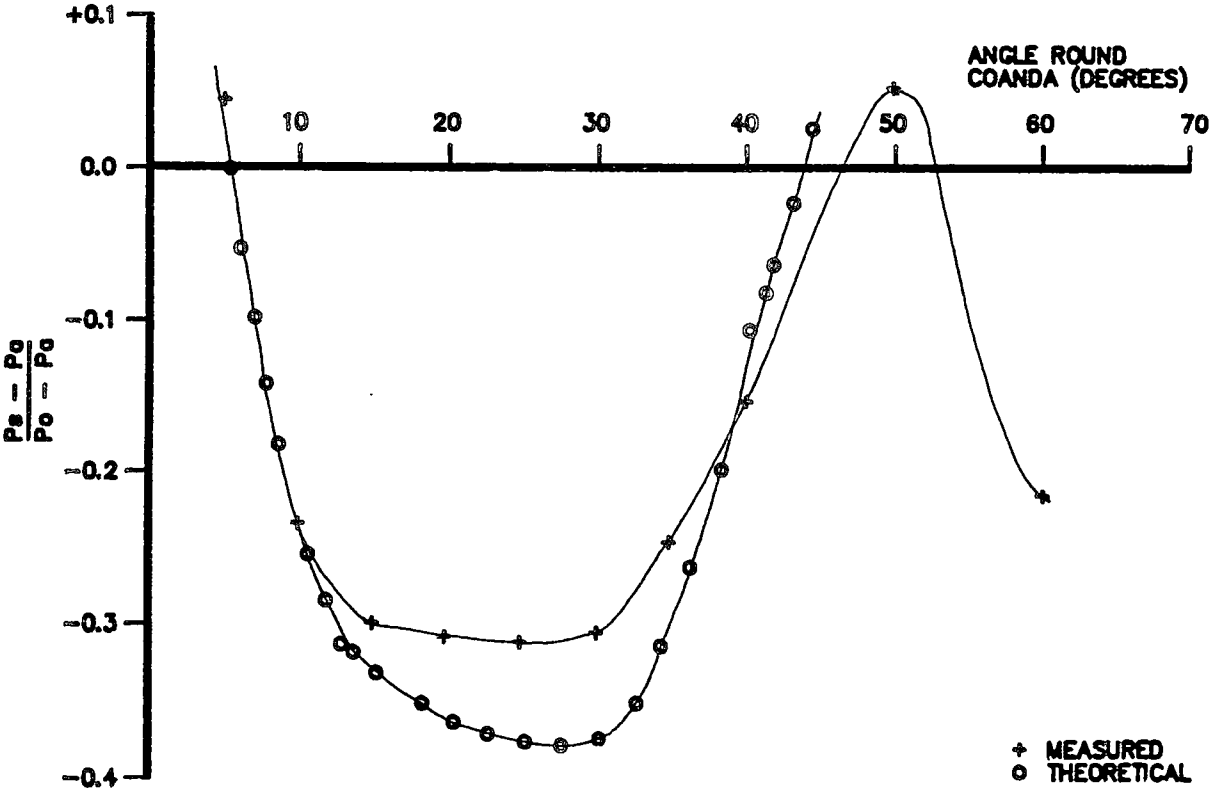

FIG 8.11 : COMPARISON OF SURFACE PRESSURE , Pa/Po = 0.311 , b/a = 0.138

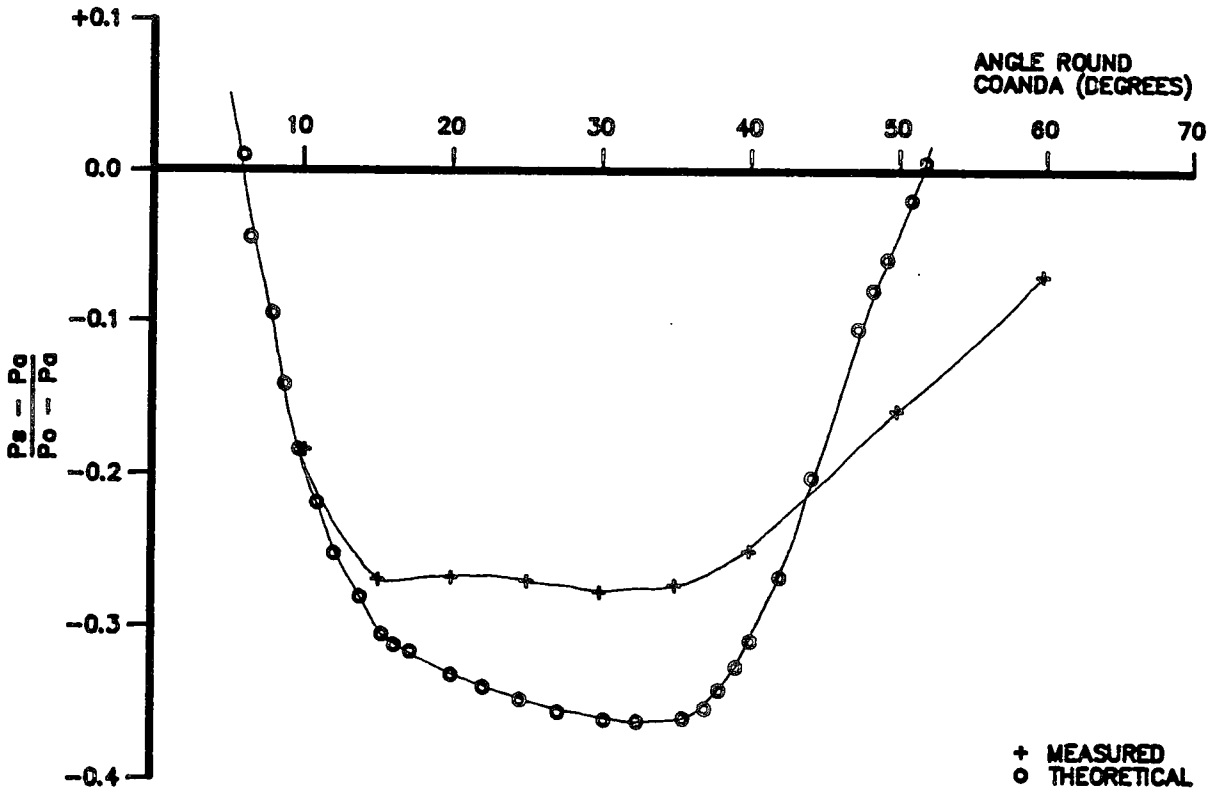

FIG 8.12 : COMPARISON OF SURFACE PRESSURE , Pa/Po = 0.289 , b/a = 0.138

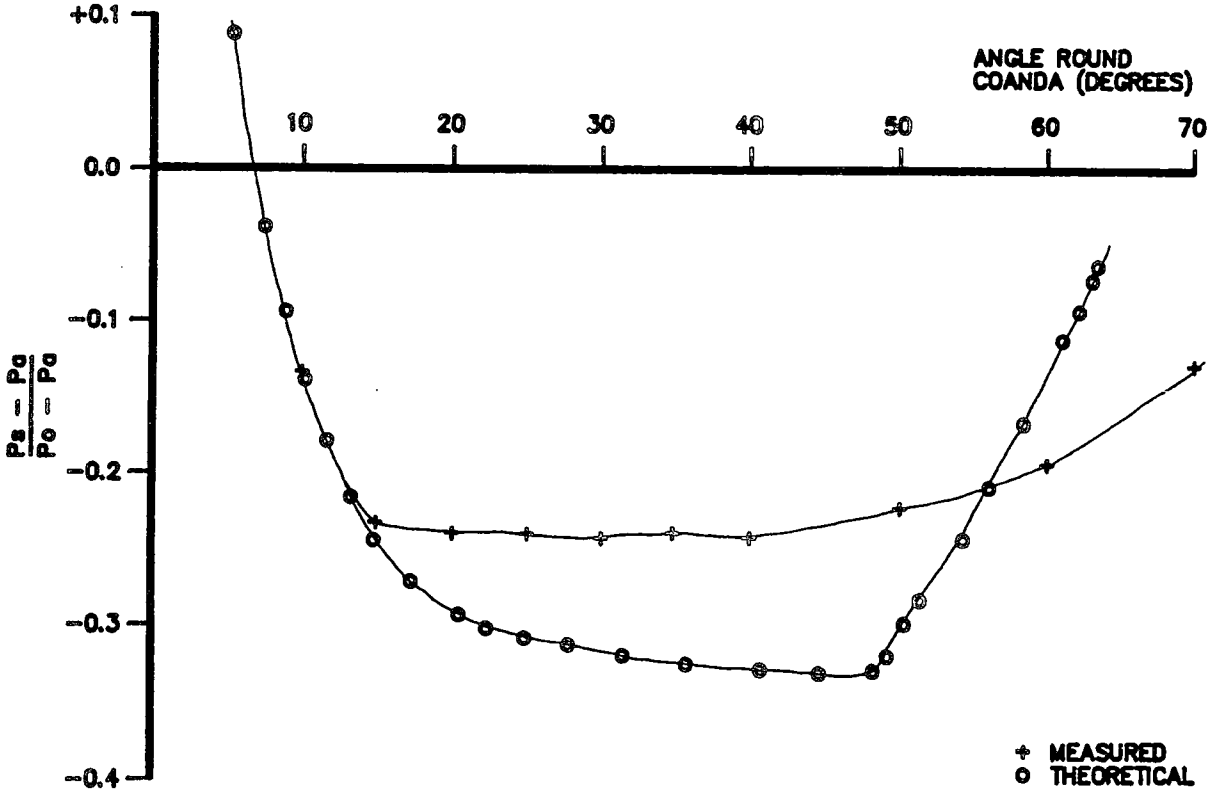

FIG 8.13 : COMPARISON OF SURFACE PRESSURE , Pa/Po = 0.257 , b/a = 0.138

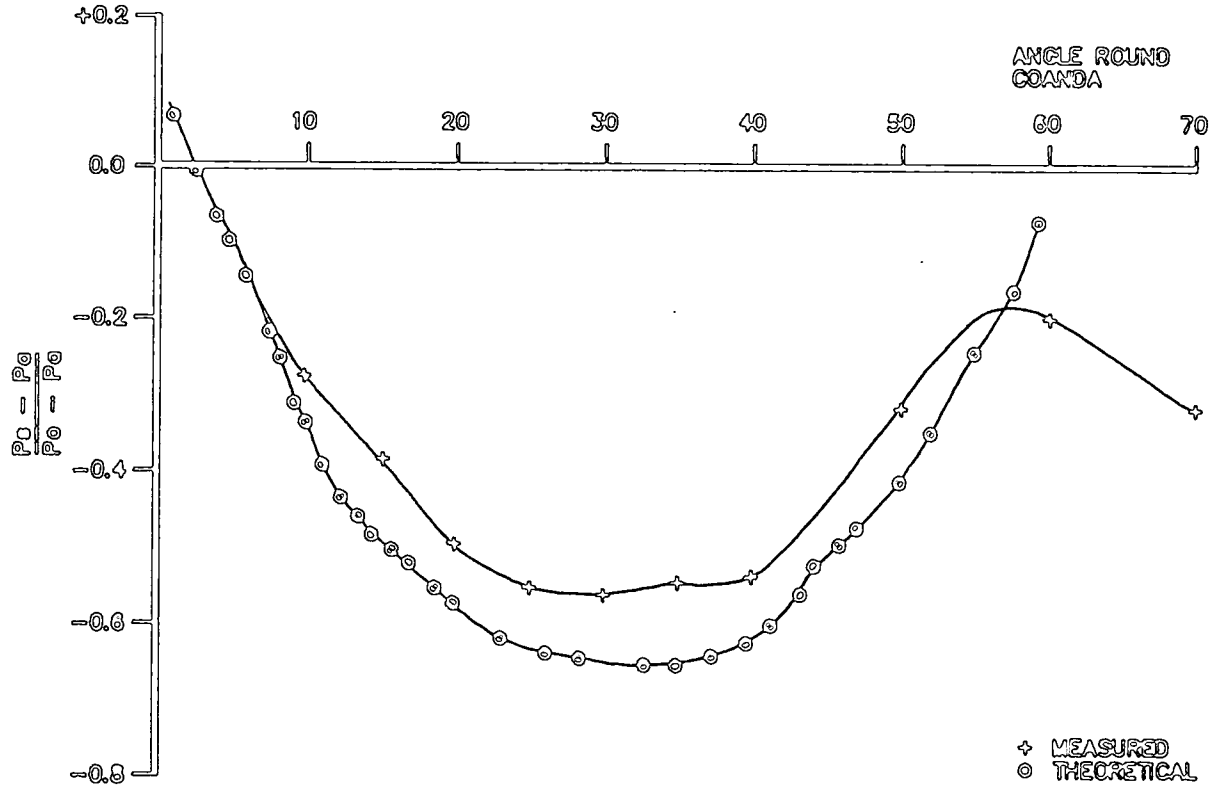

FIG 8.14A : Pa/Po = 0.437

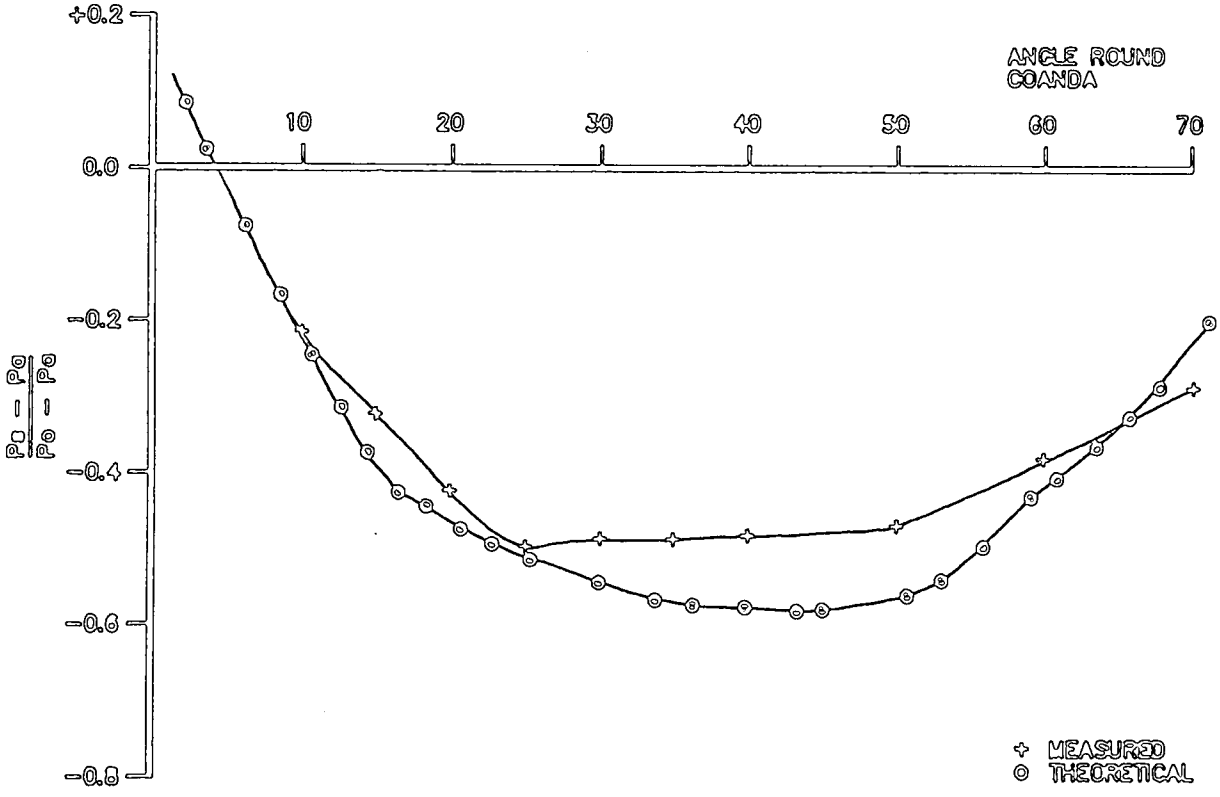

FIG 8.14B : Pa/Po = 0.304

FIG 8.14 : COMPARISON OF SURFACE PRESSURE , b/a = 0.267

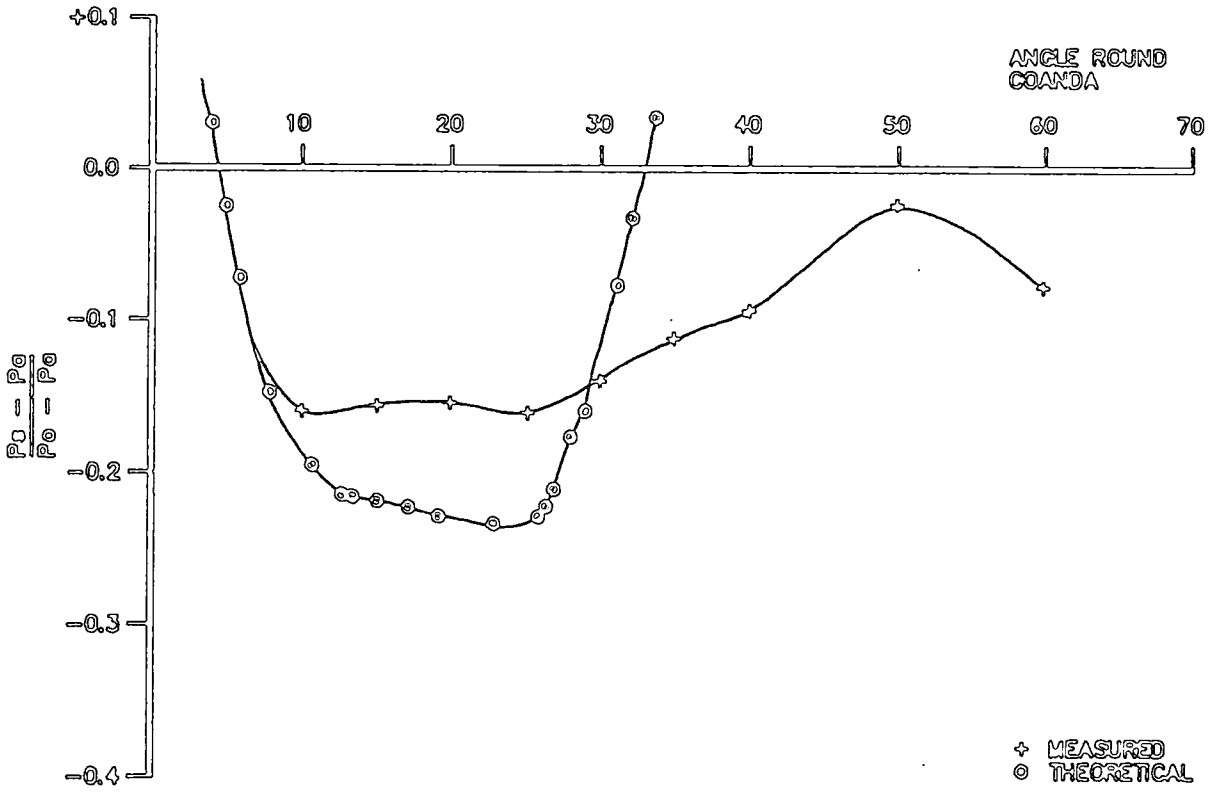

FIG 8.15A : Pa/Po = 0.200

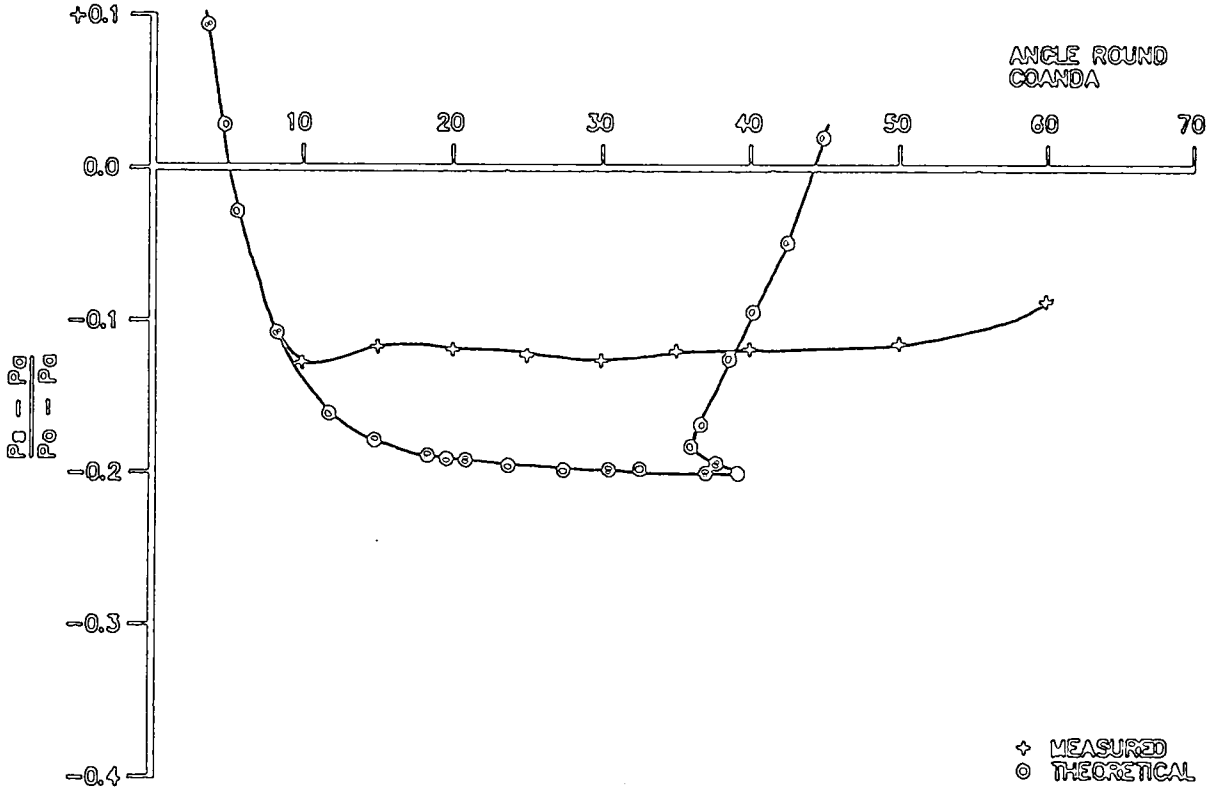

FIG 8.15B : Pa/Po = 0.169

FIG 8.15 : COMPARISON OF SURFACE PRESSURE , b/a = 0.037

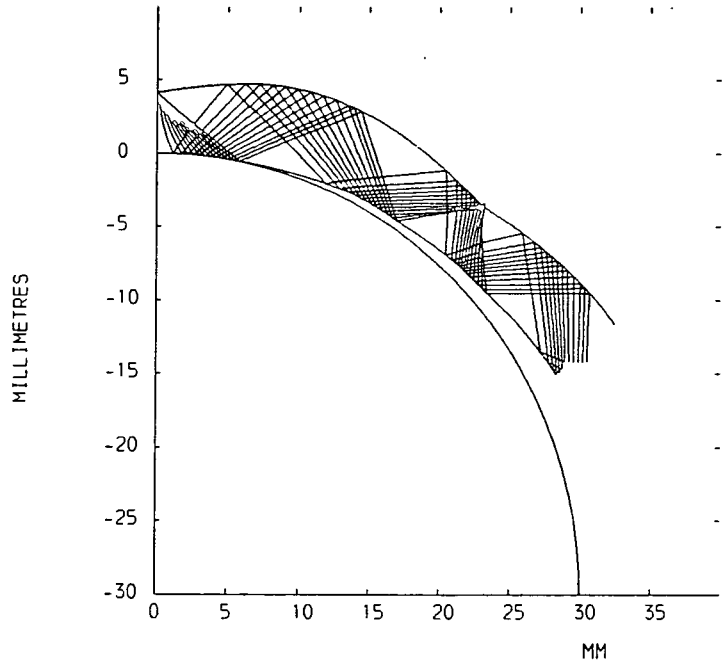

FIG 8.16A :- PREDICTED SEPARATED JET

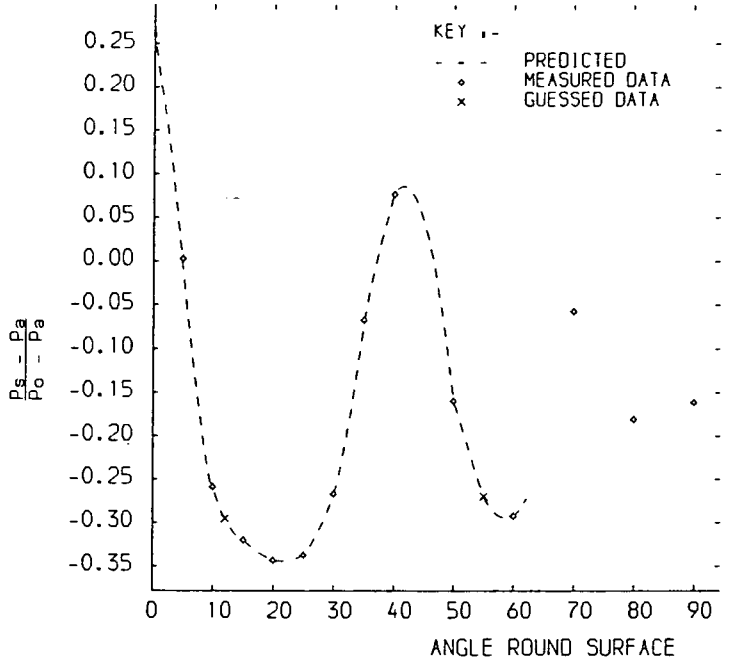

FIG 8.16B :- SURFACE PRESSURE DISTRIBUTION

FIG 8.16 :- SEPARATED JET , b/a = 0.138 , Pa/Po = 0.337

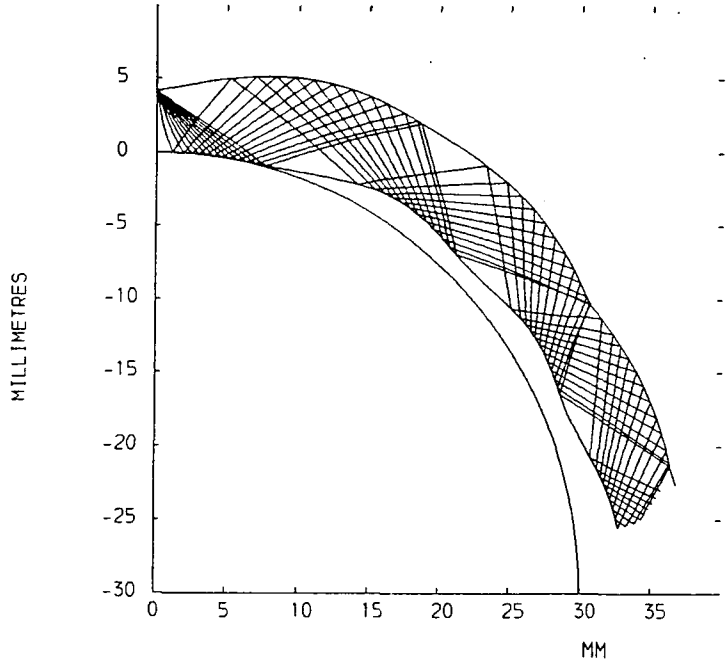

FIG 8.17A :- PREDICTED SEPARATED JET

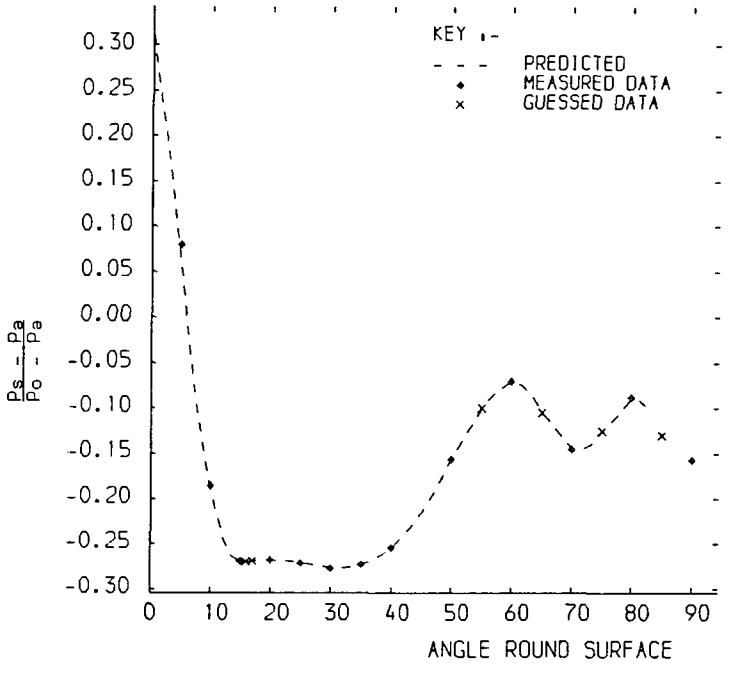

FIG 8.17B :- SURFACE PRESSURE DISTRIBUTION

FIG 8.17 :- SEPARATED JET , b/a = 0.138 , Pa/Po = 0.289

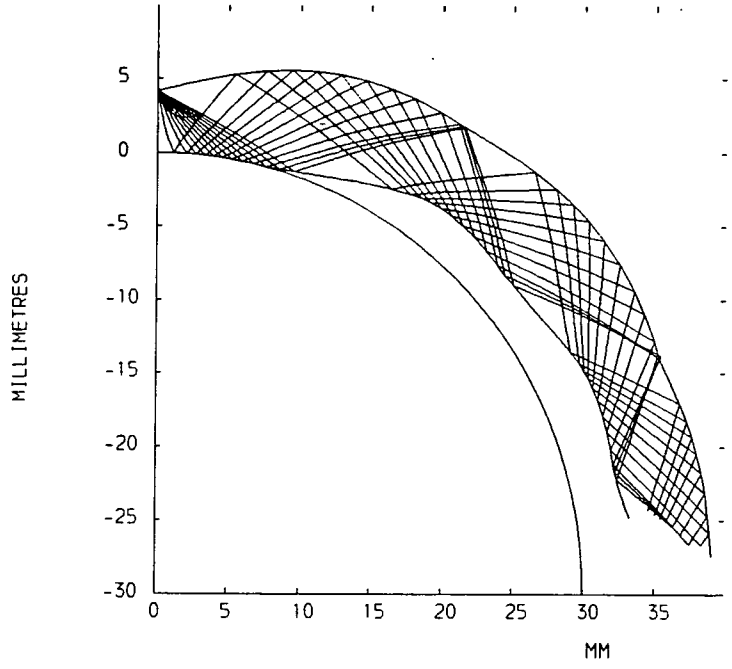

FIG 8.18A :- PREDICTED SEPARATED JET

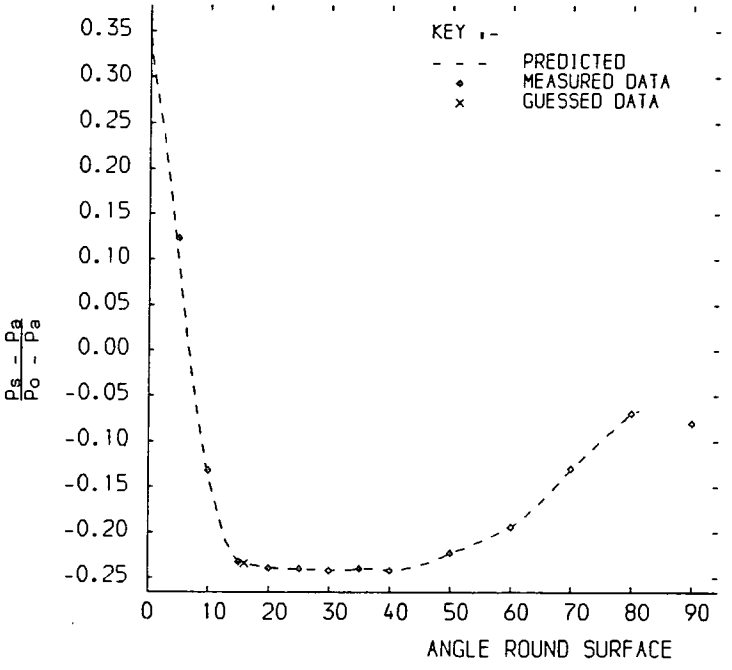

FIG 8.18B :- SURFACE PRESSURE DISTRIBUTION

FIG 8.18 :- SEPARATED JET , b/a = 0.138 , Pa/Po = 0.257

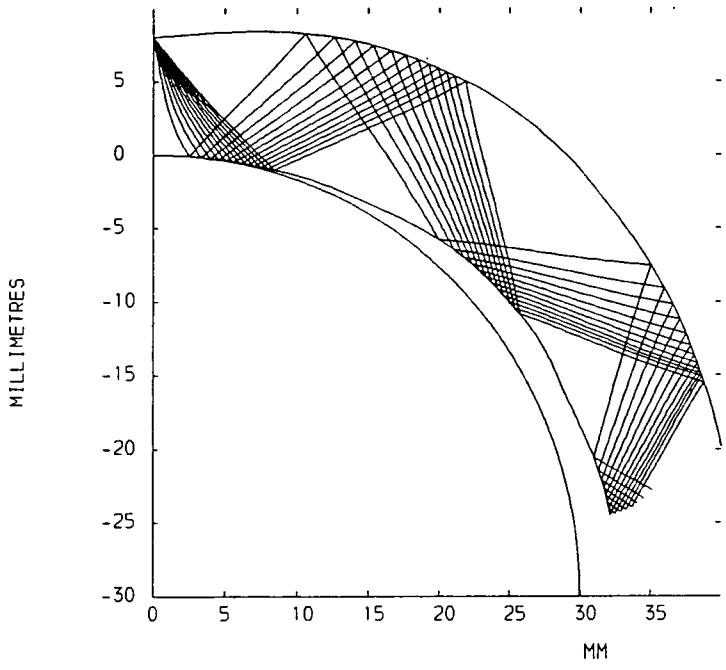

FIG 8.19A :- PREDICTED SEPARATED JET

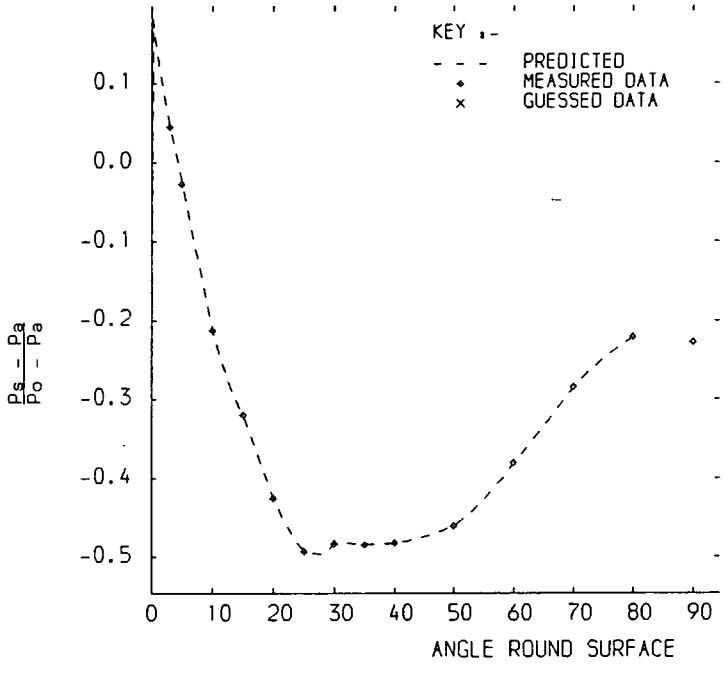

FIG 8.19B :- SURFACE PRESSURE DISTRIBUTION

FIG 8.19 :- SEPARATED JET , b/a = 0.266 , Pa/Po = 0.394

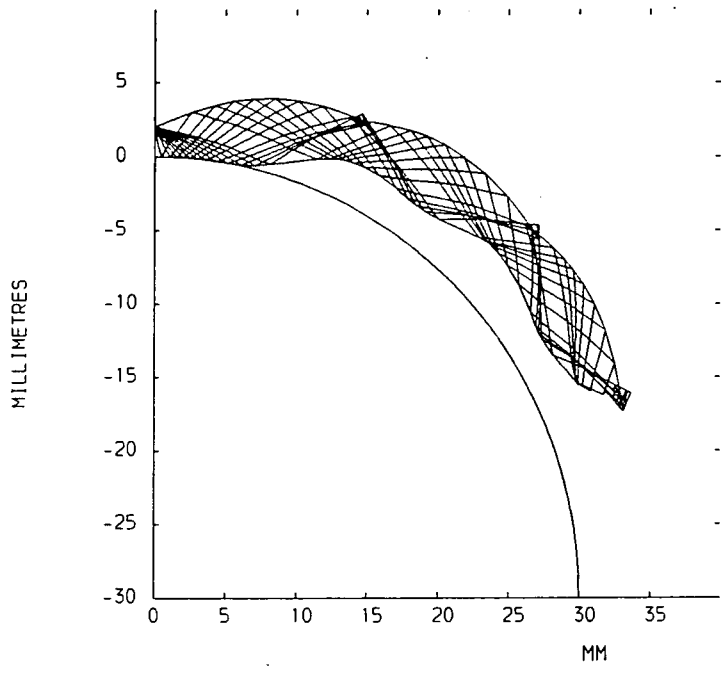

FIG 8.20A :- PREDICTED SEPARATED JET

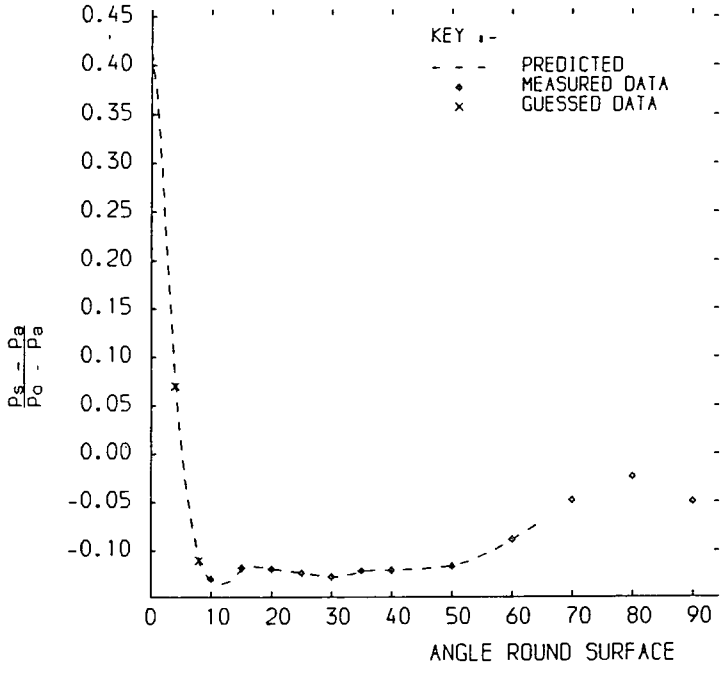

FIG 8.20B :- SURFACE PRESSURE DISTRIBUTION

FIG 8.20 :- SEPARATED JET , b/a = 0.066 , Pa/Po = 0.169

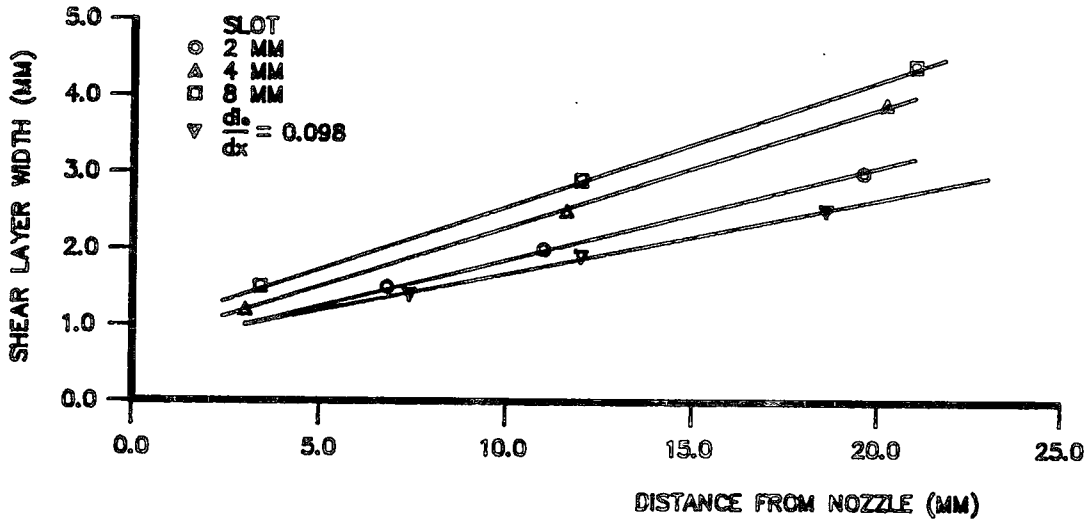

FIG 8.21 : GROWTH OF SHEAR LAYER

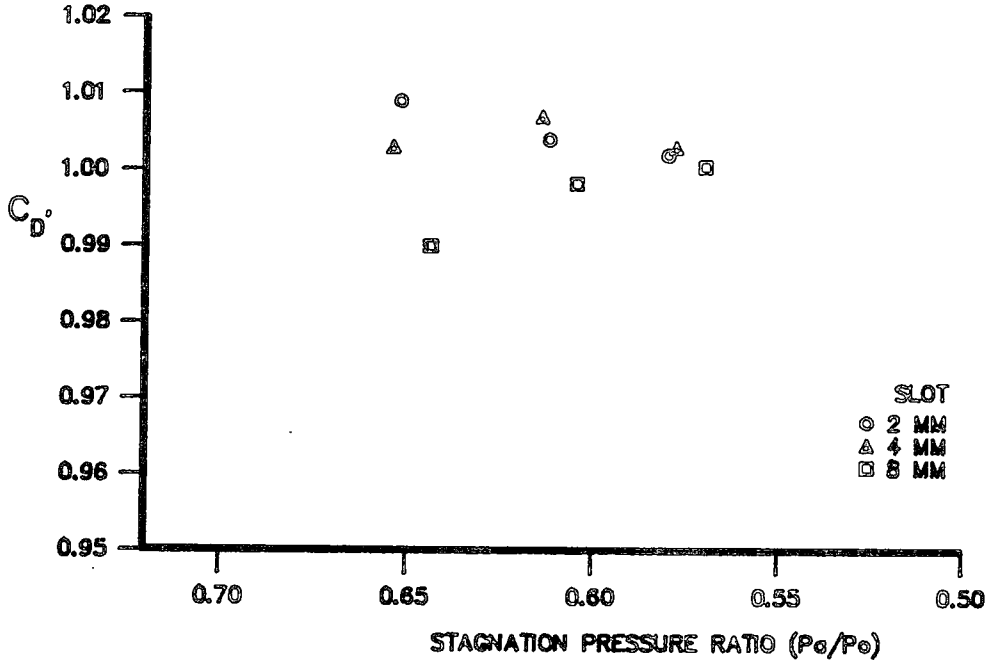

FIG 8.22 : INTERFEROMETRIC SLOT DISCHARGE

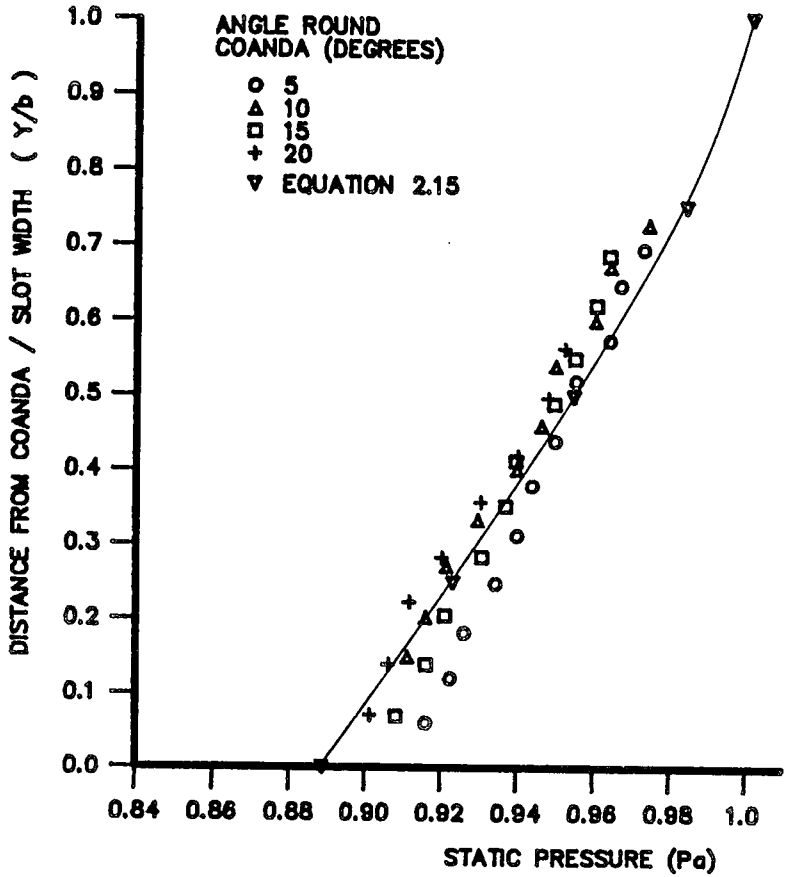

FIG 8.23A : Pa/Po = 0.654

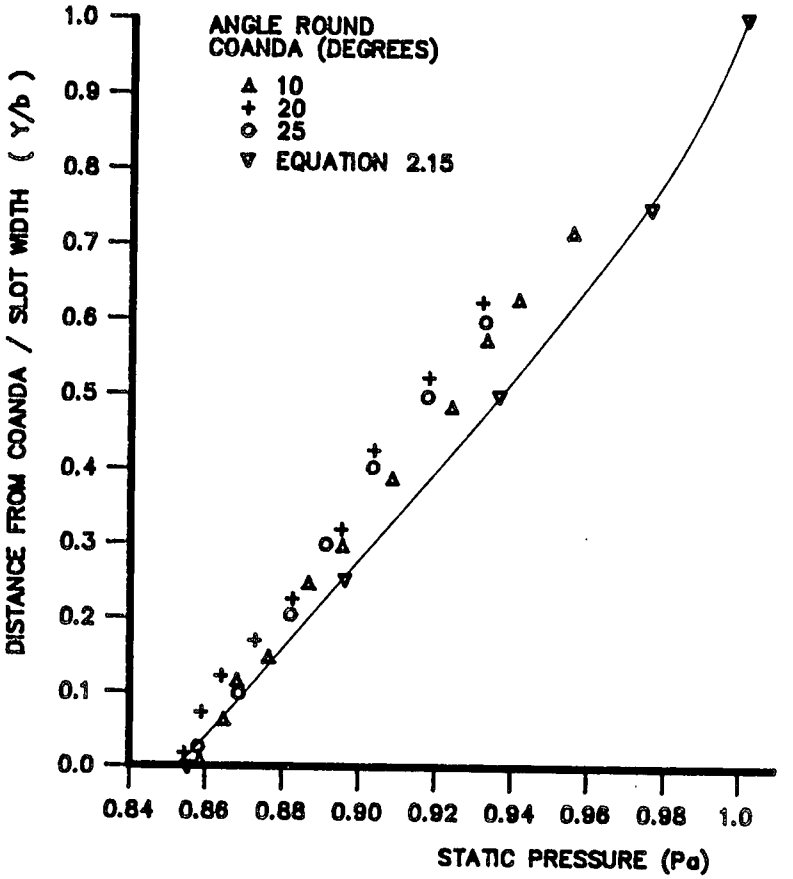

FIG 8.23B : Pa/Po = 0.579

FIG 8.23 : PRESSURE DISTRIBUTIONS THROUGH A 4 MM JET

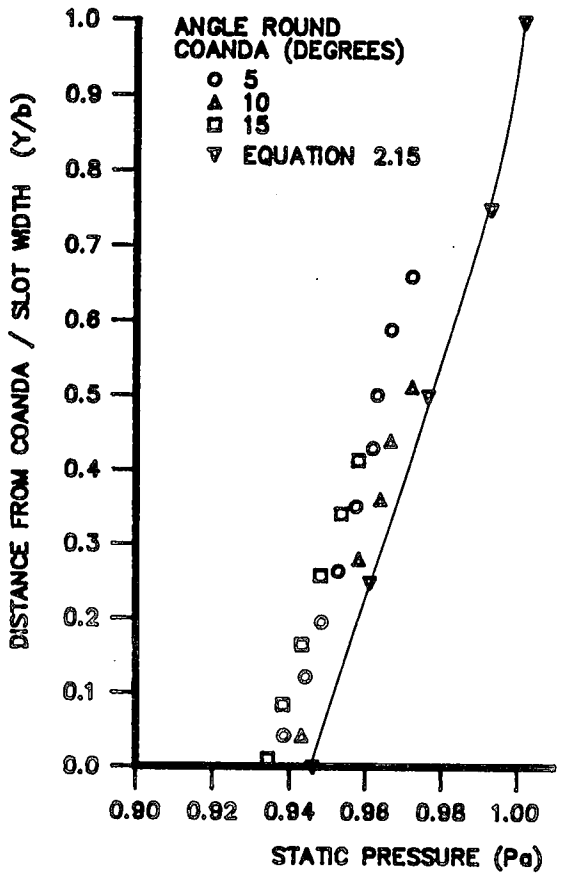

FIG 8.24 : 2 MM JET , Pa/Po = 0.653

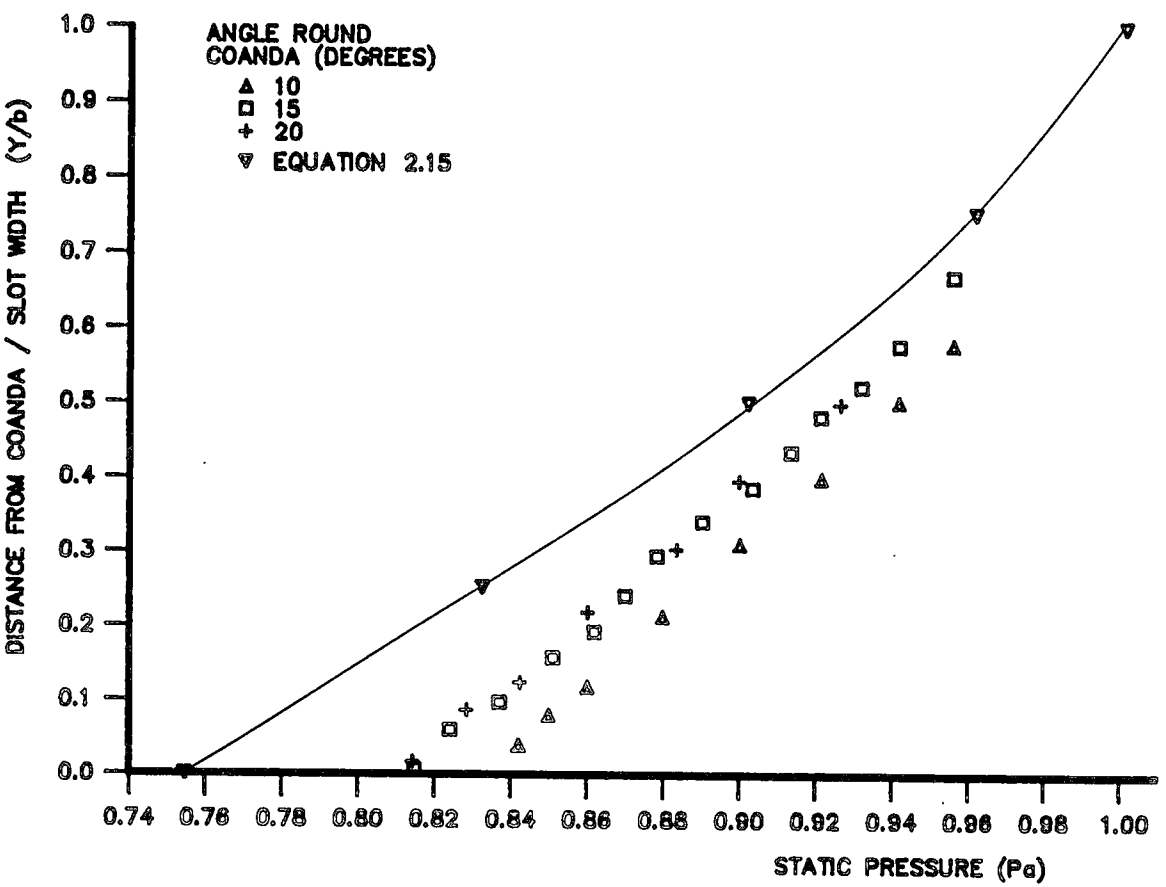

FIG 8.24B : 8 MM JET , Pa/Po = 0.644

FIG 8.24 : PRESSURE DISTRIBUTIONS THROUGH 2 MM AND 8 MM JETS

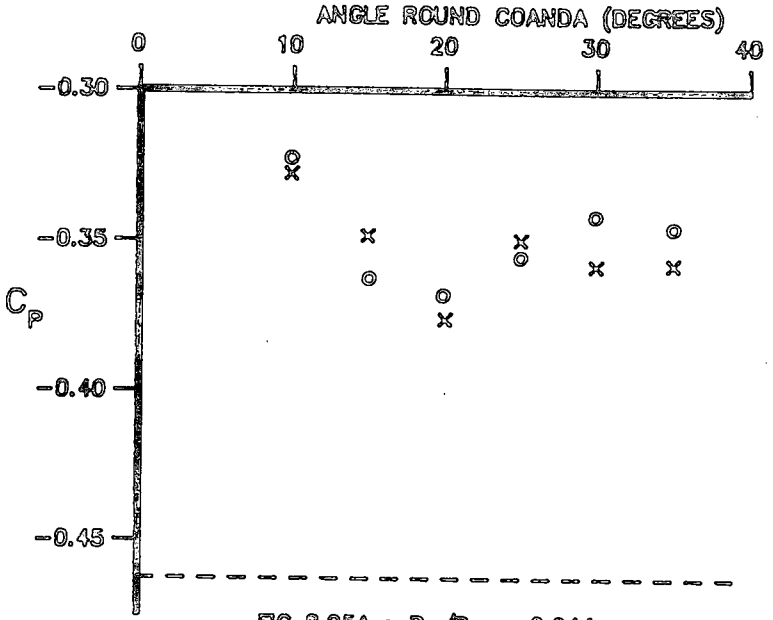

FIG 8.25A : Pa/Po = 0.644

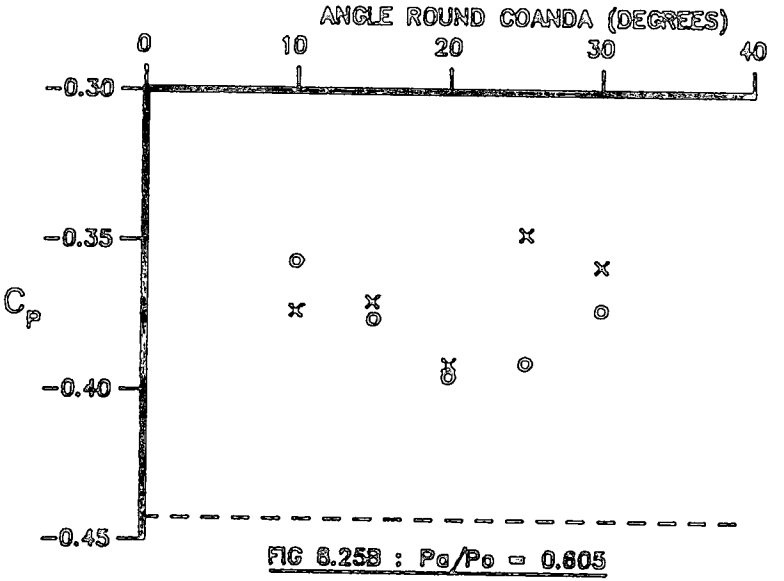

FIG 8.25B : Pa/Po = 0.605

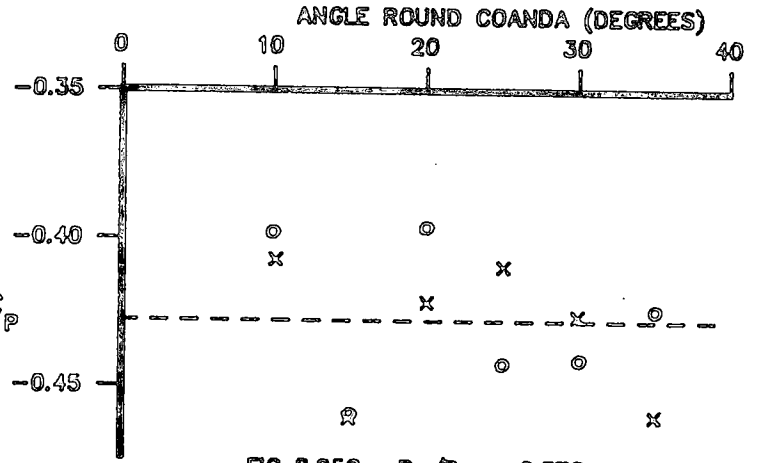

FIG 8.25C : Pa/Po = 0.570

KEY

- × STATIC PRESSURE TAPPING
- ◎ INTERFEROMETRY
- – – EQUATION 2.14

FIG 8.25 : SURFACE PRESSURES FROM AN 8 MM SLOT

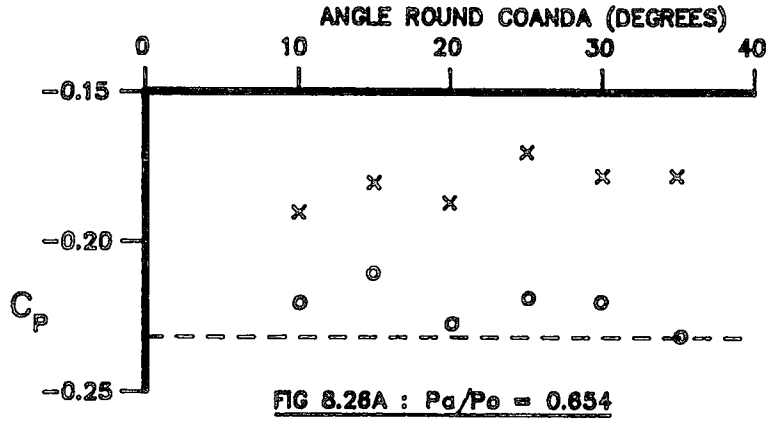

FIG 8.26A : Pa/Po = 0.654

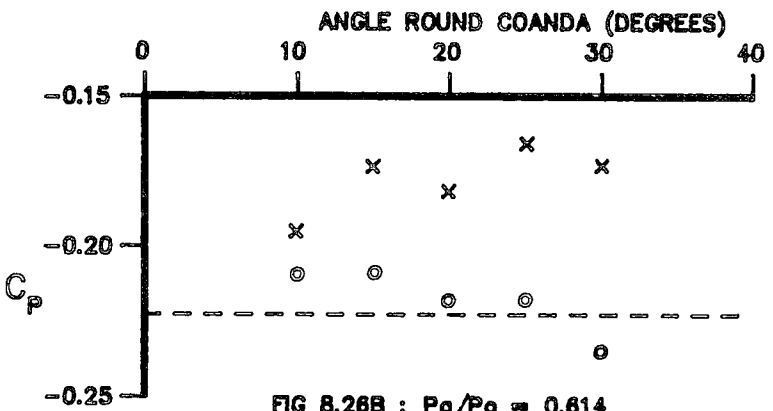

FIG 8.26B : Pa/Po = 0.614

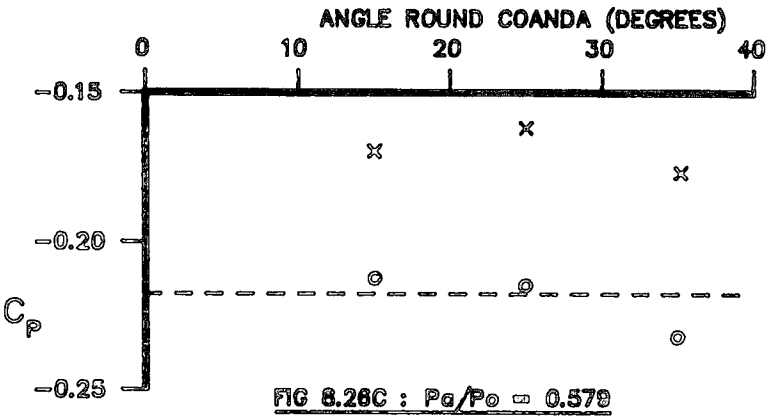

FIG 8.26C : Pa/Po = 0.579

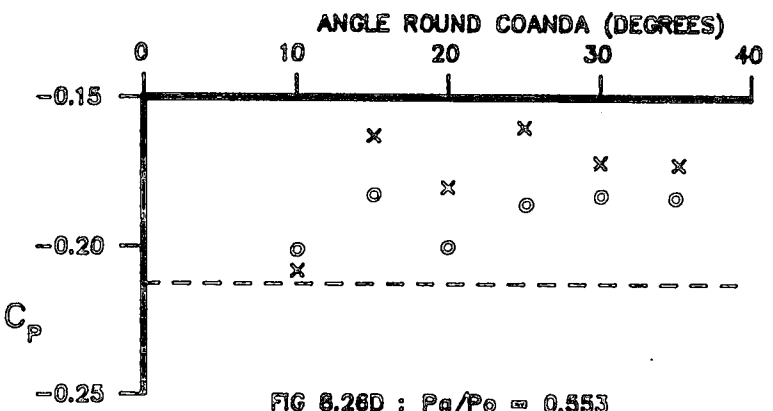

FIG 8.26D : Pa/Po = 0.553

KEY
× STATIC PRESSURE TAPPING
⊙ INTERFEROMETRY
– – EQUATION 2.14

FIG 8.26 : SURFACE PRESSURES FROM A 4 MM SLOT

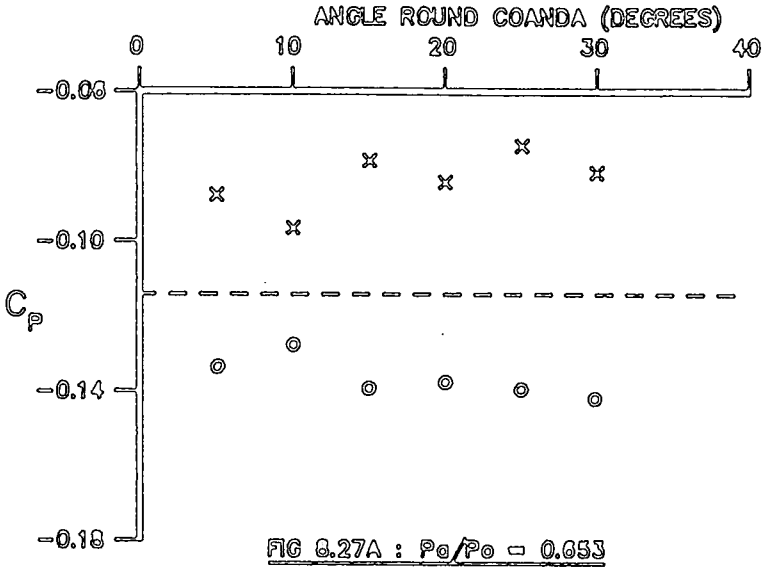

FIG 8.27A : Pa/Po = 0.653

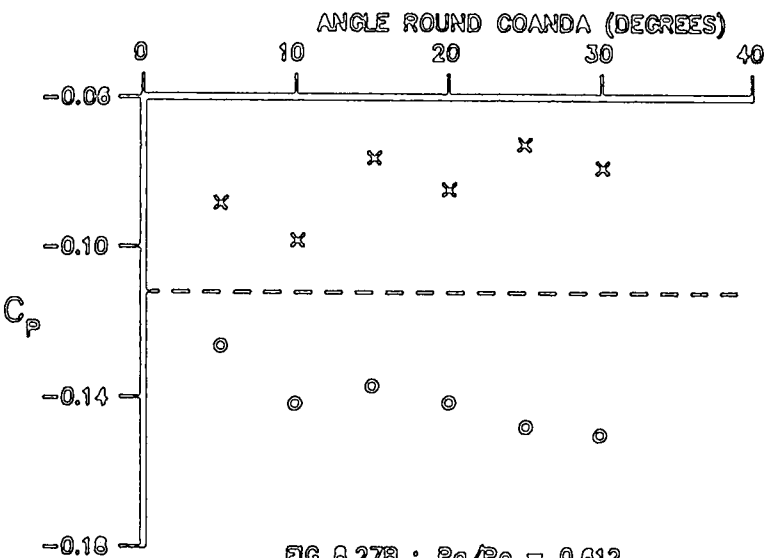

FIG 8.27B : Pa/Po = 0.612

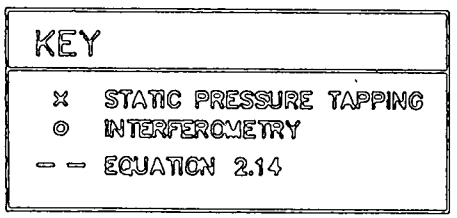

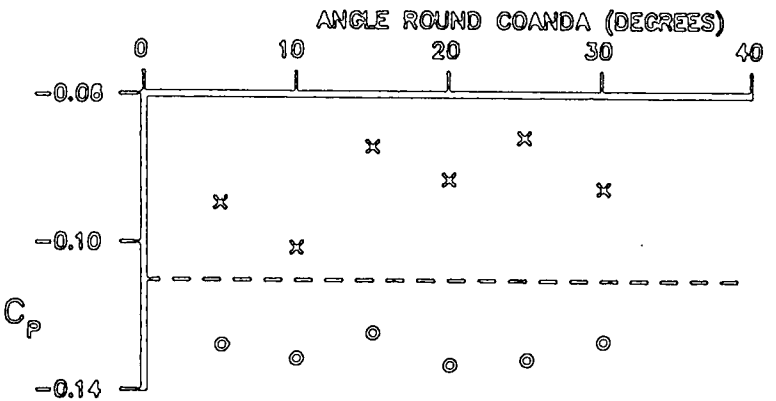

FIG 8.27C : Pa/Po = 0.580

FIG 8.27 : SURFACE PRESSURES FROM A 2 MM SLOT

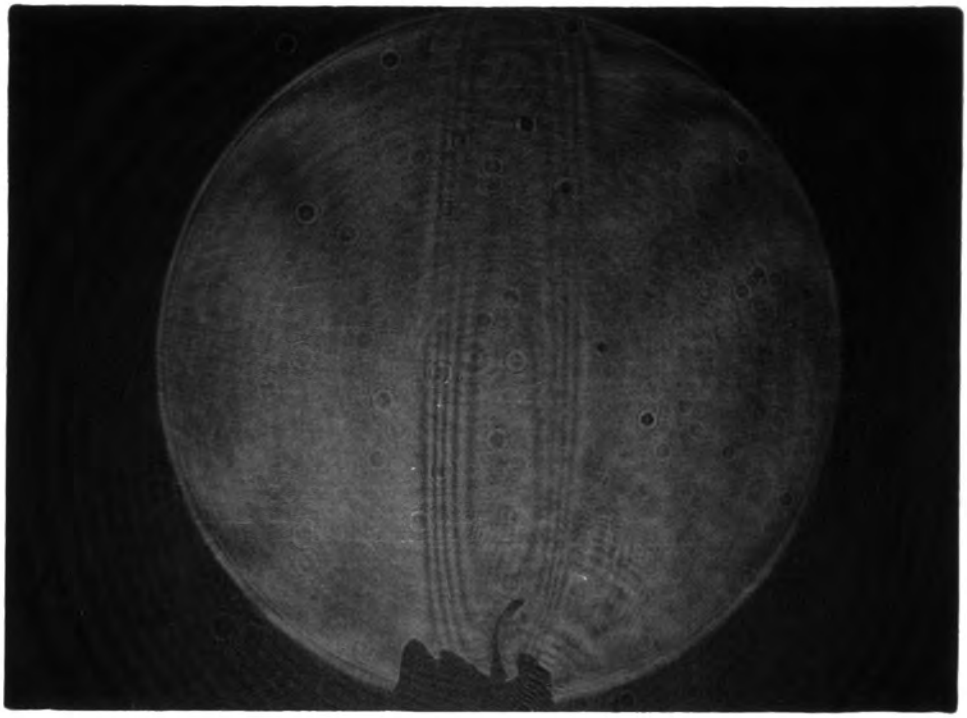

PLATE 1a: Infinite Fringe

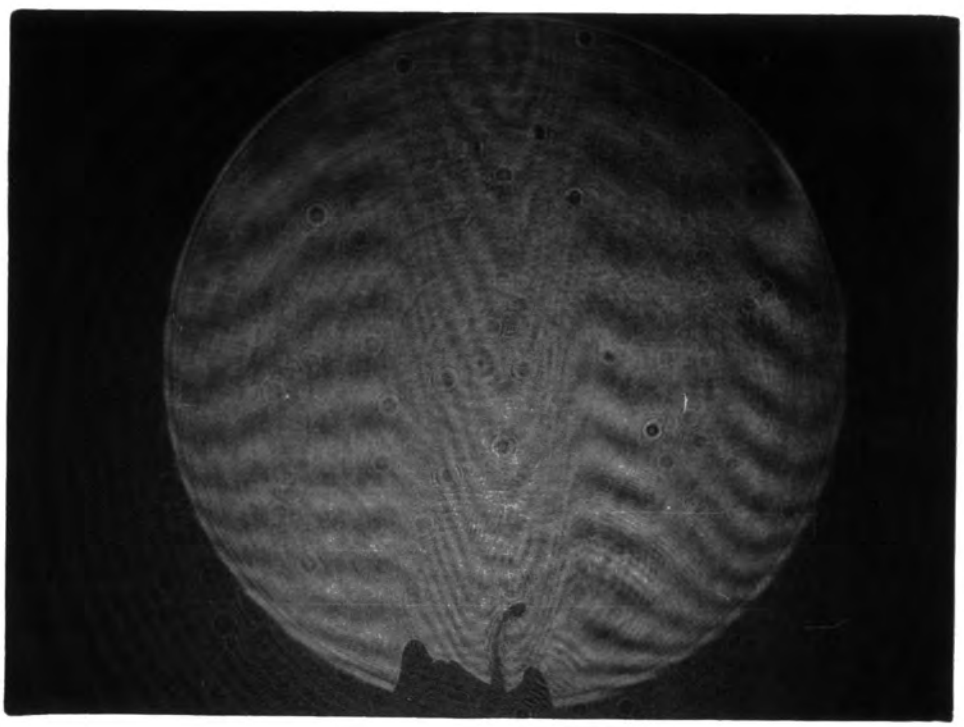

PLATE 1b: Finite Fringe

PLATE 1: DEMONSTRATION OF INTERFEROMETRY

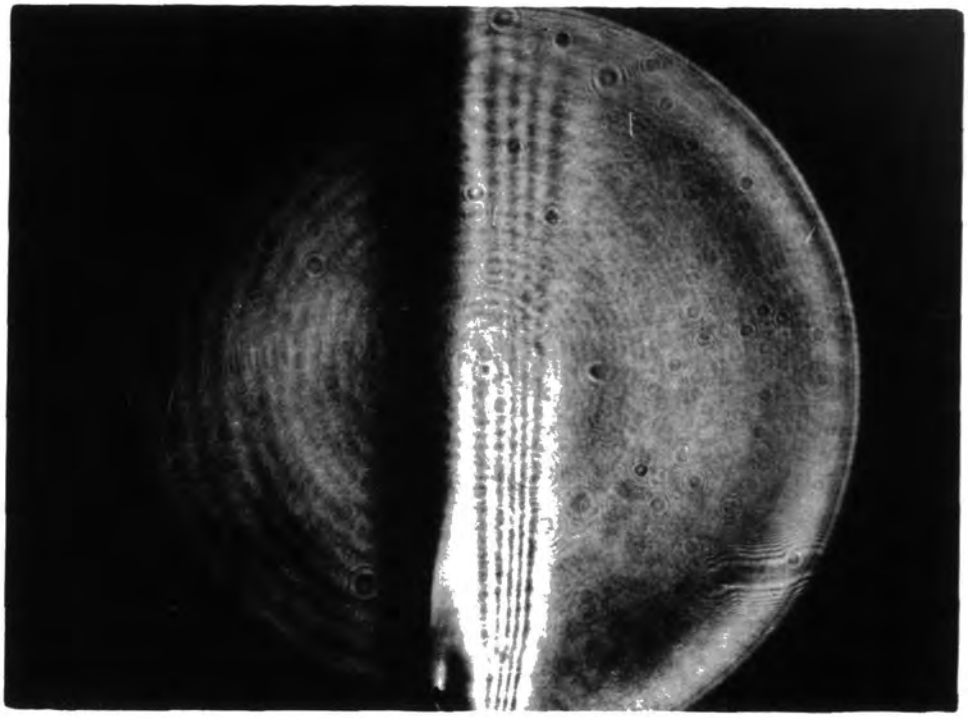

PLATE 2: Schlieren using razor blade cut-off

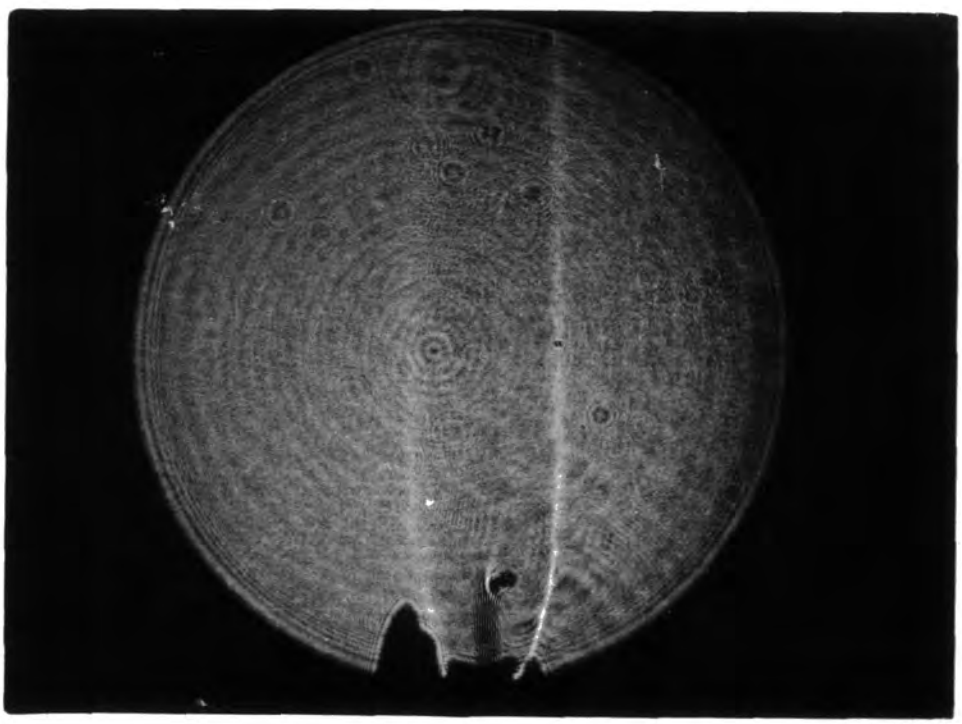

PLATE 3: Shadowgraph with laser source

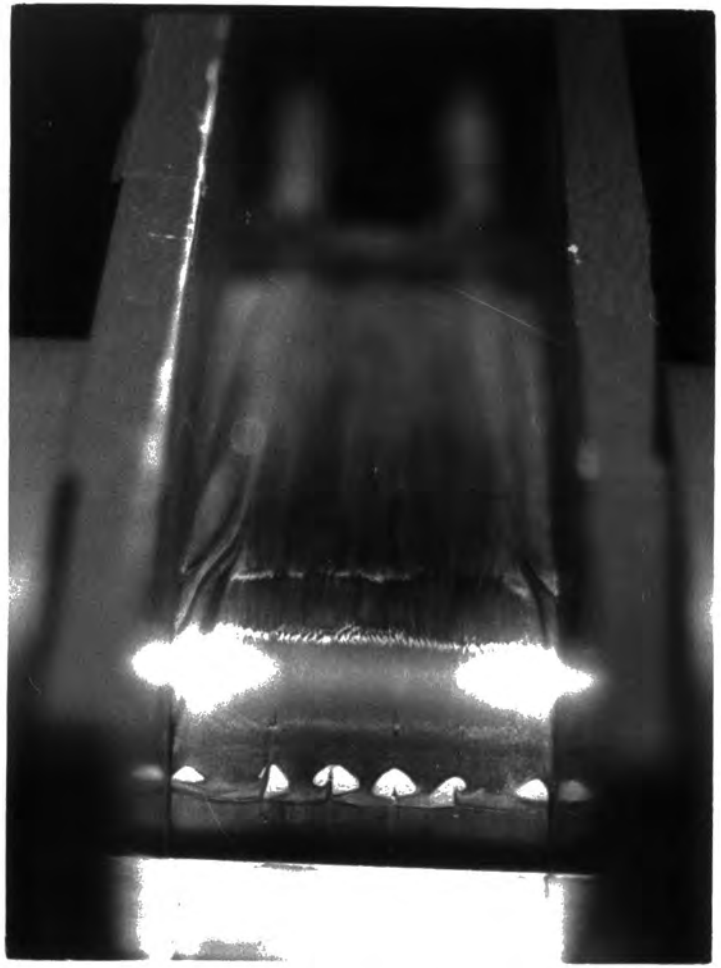

PLATE 4: Coanda Flow Visualization
Slot = 4 mm

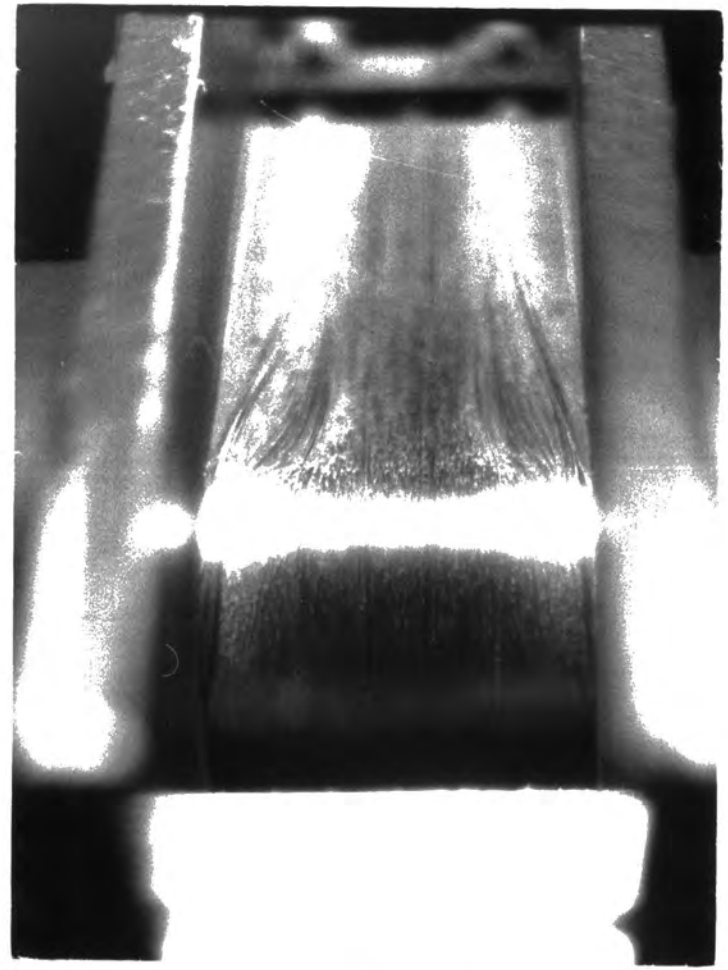

PLATE 5: Coanda Flow Visualization
Slot = 8 mm

PLATE 6: Corner Flow Visualization
Slot = 4 mm

PLATE 7: Side Wall Flow Visualization
Slot = 4 mm

PLATE 8: Shadowgraph, Pa/Po = 0.370
Slot = 4 mm

PLATE 9: Shadowgraph, Pa/Po = 0.323
Slot = 4 mm

PLATE 10: Shadowgraph, Pa/Po = 0.267
Slot = 4 mm

PLATE 11: Shadowgraph, Pa/Po = 0.241
Slot = 4 mm

PLATE 12: Shadowgraph, Pa/Po = 0.397
Slot = 8 mm

PLATE 13: Shadowgraph, Pa/Po = 0.167
Slot = 2 mm

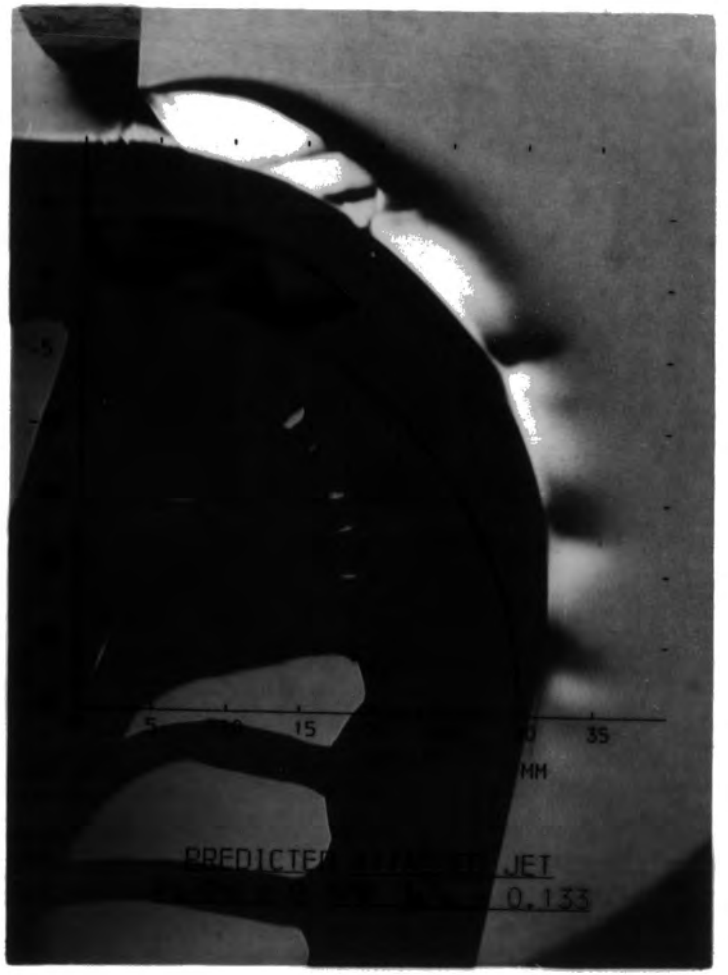

PLATE 14a: Vertical Density Gradients

PLATE 14b: Horizontal Density Gradient

PLATE 14: SCHLIEREN, Pa/Po = 0.370, SLOT = 4 mm

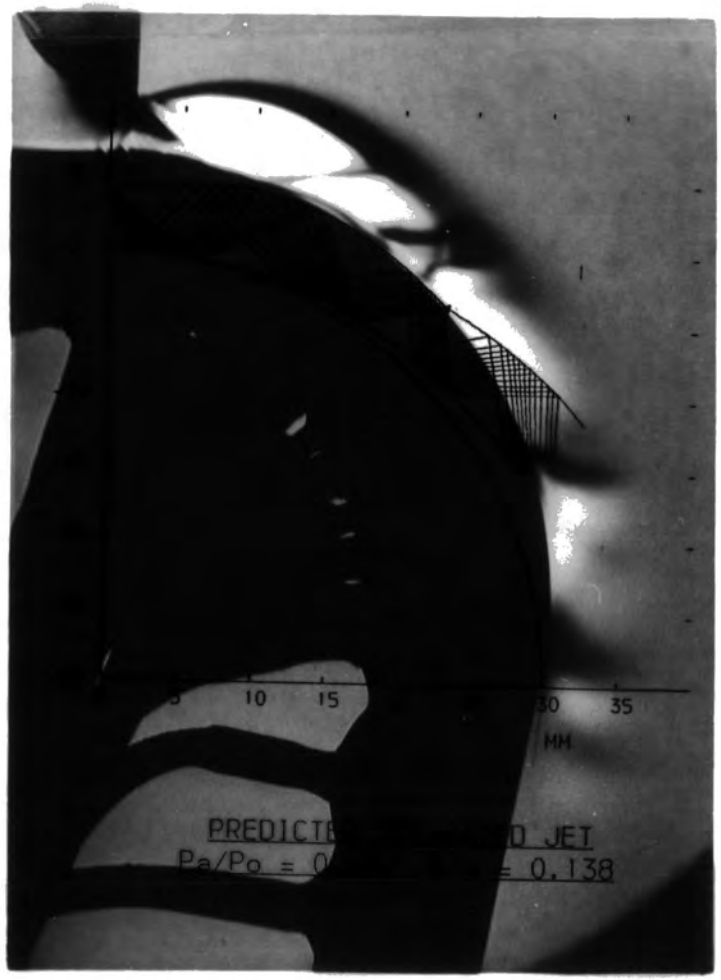

PLATE 15a: Vertical Density Gradients

PLATE 15b: Horizontal Density Gradients

PLATE 15: SCHLIEREN, Pa/Po = 0.323, SLOT = 4 mm

PLATE 16a: Vertical Density Gradients

PLATE 16b: Horizontal Density Gradients

PLATE 16: SCHLIEREN WITH REVERSED KNIFE-EDGE, Pa/Po = 0.323, SLOT = 4 mm

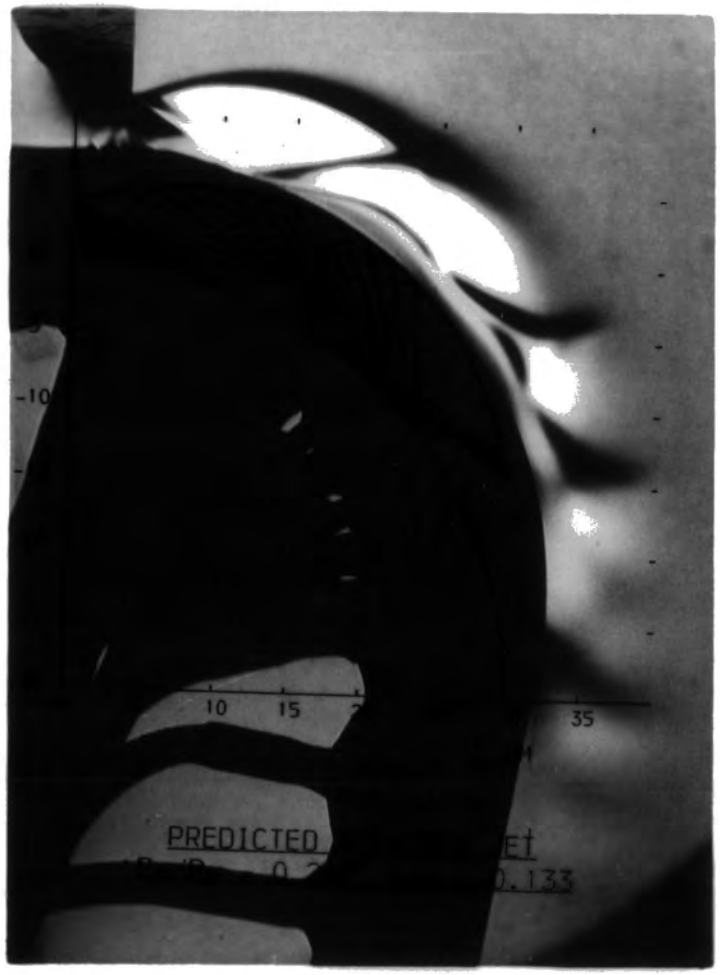

PLATE 17a: Vertical Density Gradients

PLATE 17b: Horizontal Density Gradients

PLATE 17: SCHLIEREN, Pa/Po = 0.267, SLOT = 4 mm

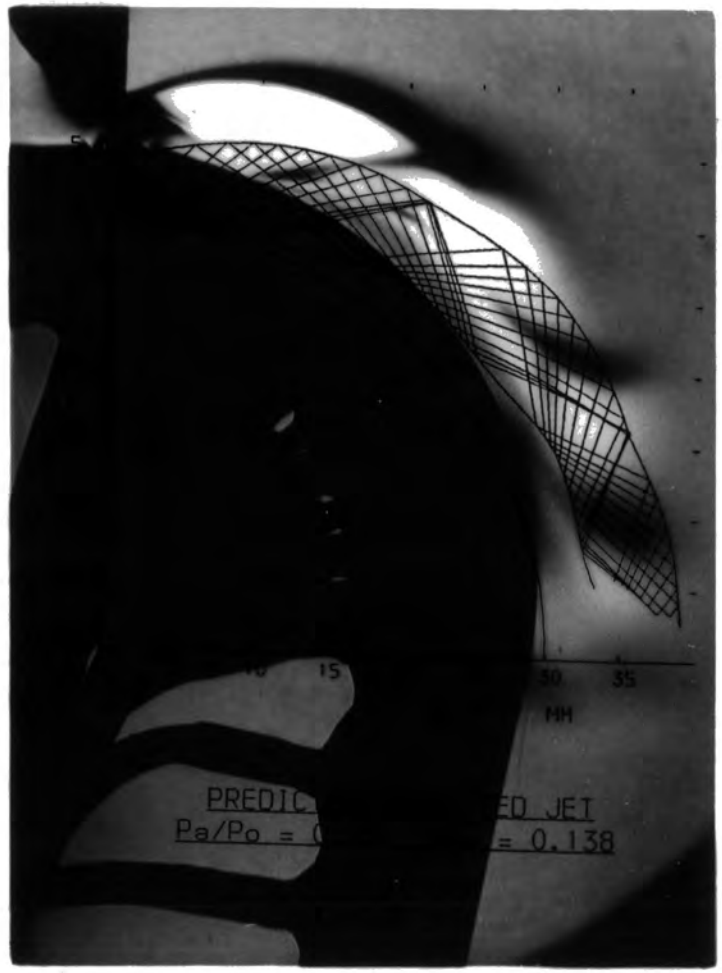

PLATE 18a: Vertical Density Gradients

PLATE 18b: Horizontal Density Gradients

PLATE 18: SCHLIEREN, Pa/Po = 0.241, SLOT = 4 mm

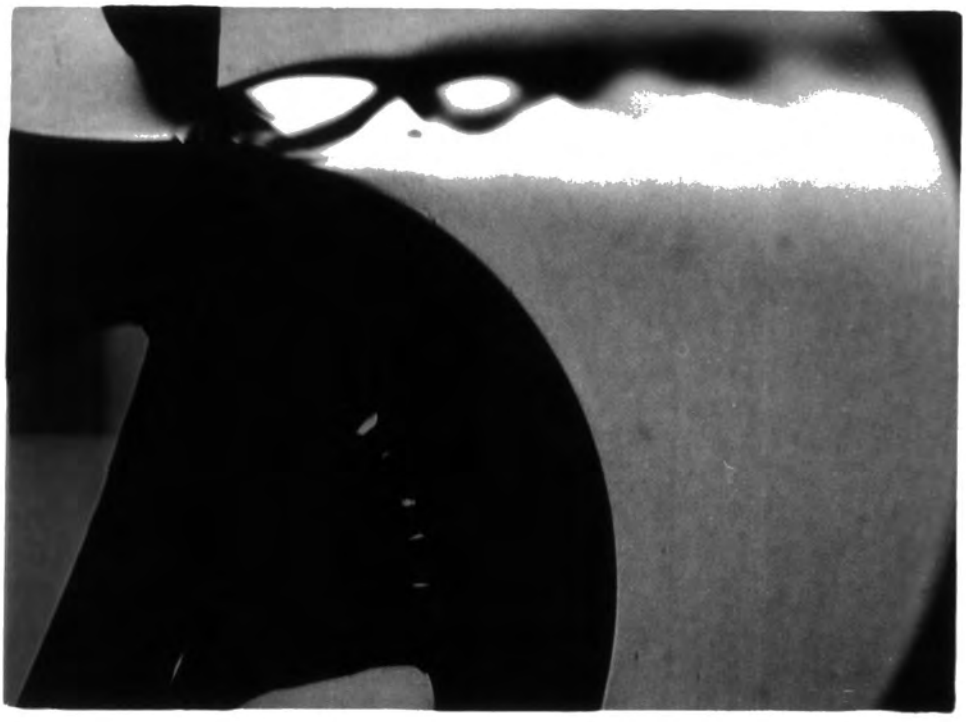

PLATE 19a: Vertical Density Gradients

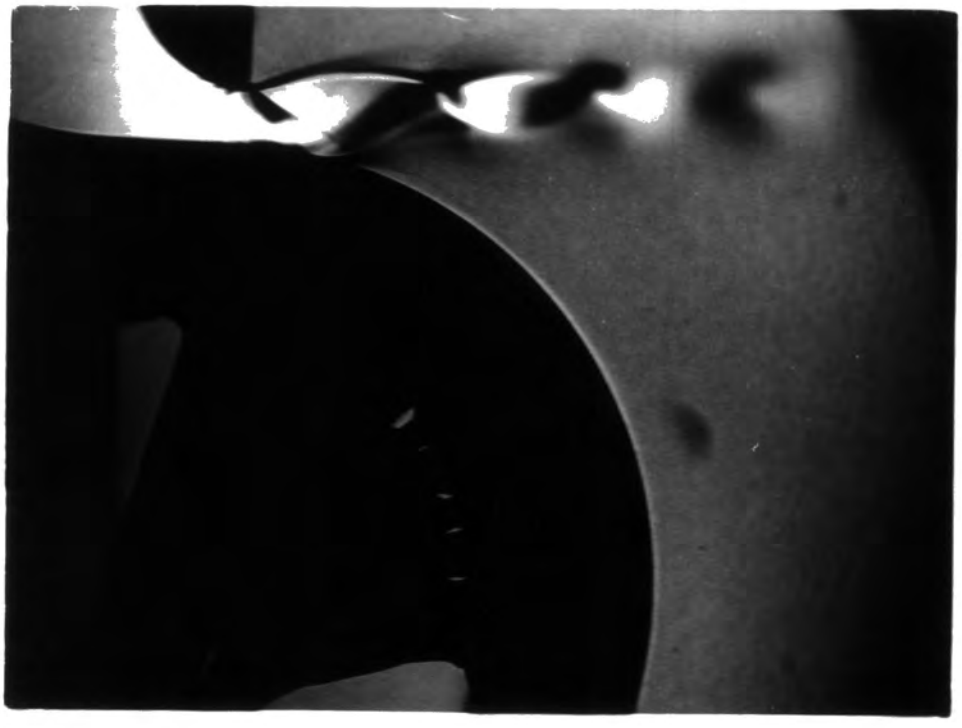

PLATE 19b: Horizontal Density Gradient

PLATE 19: SCHLIEREN, BREAKAWAY, SLOT = 4 mm

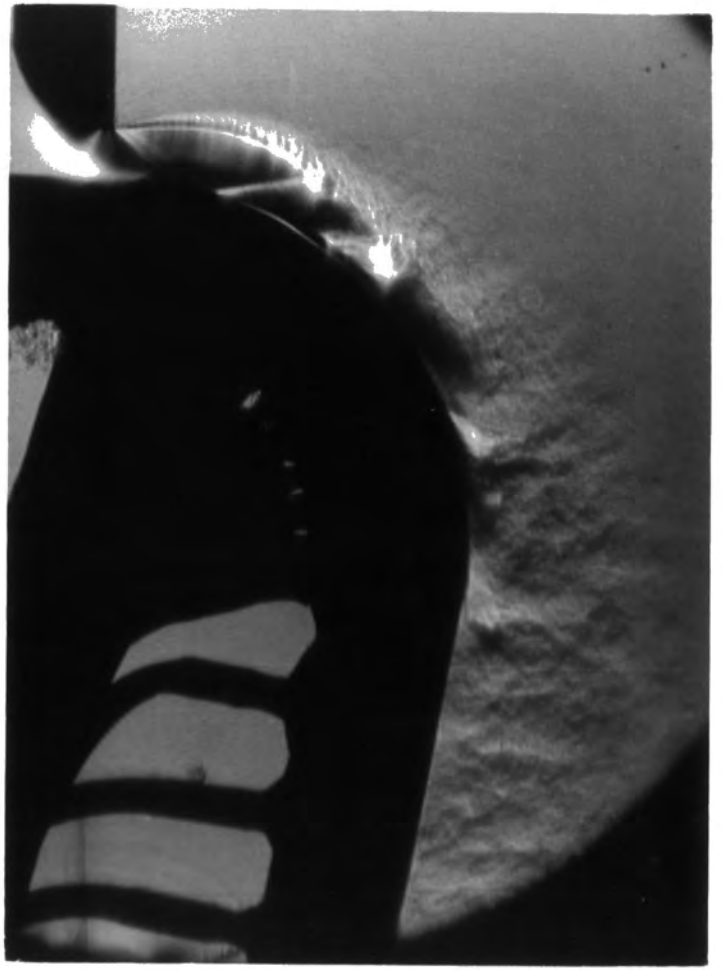

PLATE 20a: Vertical Density Gradients

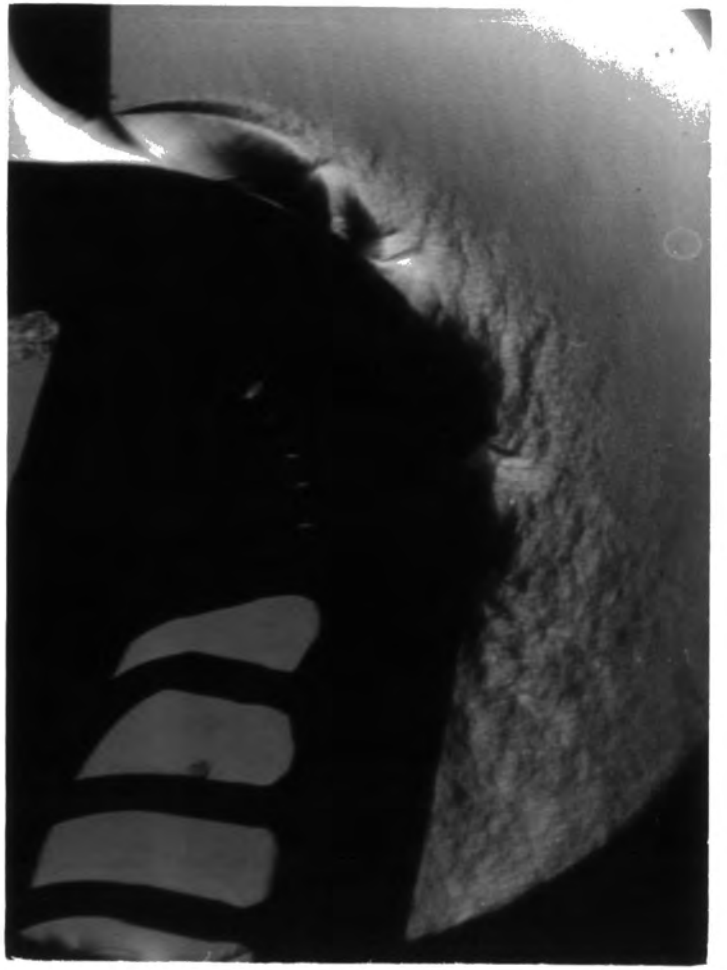

PLATE 20b: Horizontal Density Gradients

PLATE 20: SPARK SCHLIEREN, Pa/Po = 0.323, SLOT = 4 mm

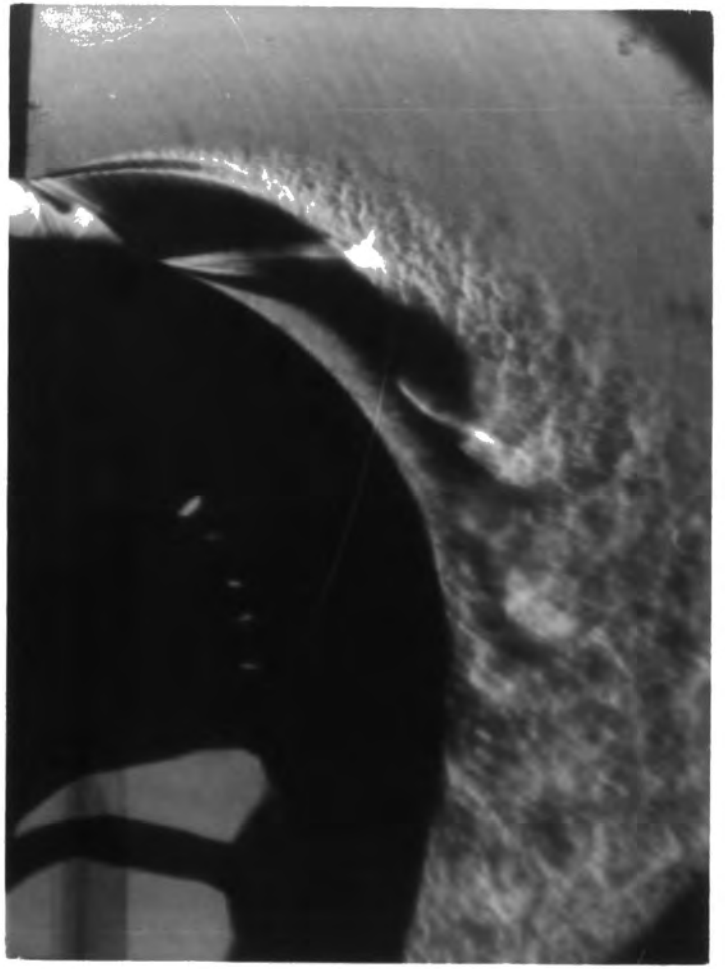

PLATE 21a: Vertical Density Gradients

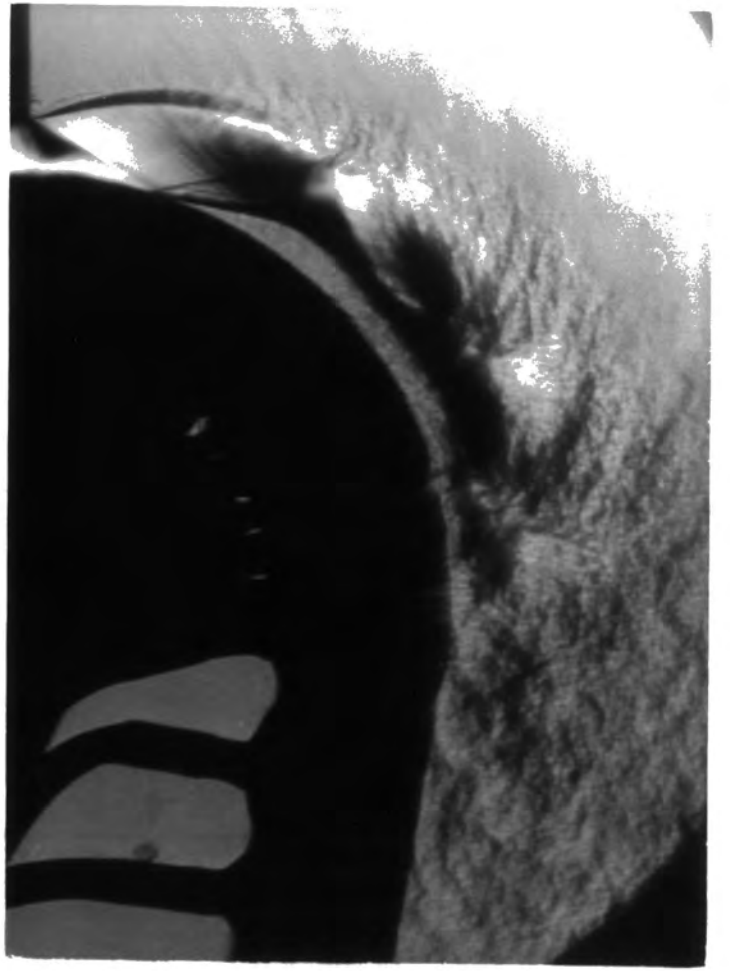

PLATE 21b: Horizontal Density Gradients

PLATE 21: SPARK SCHLIEREN, Pa/Po = 0.244, SLOT = 4 mm

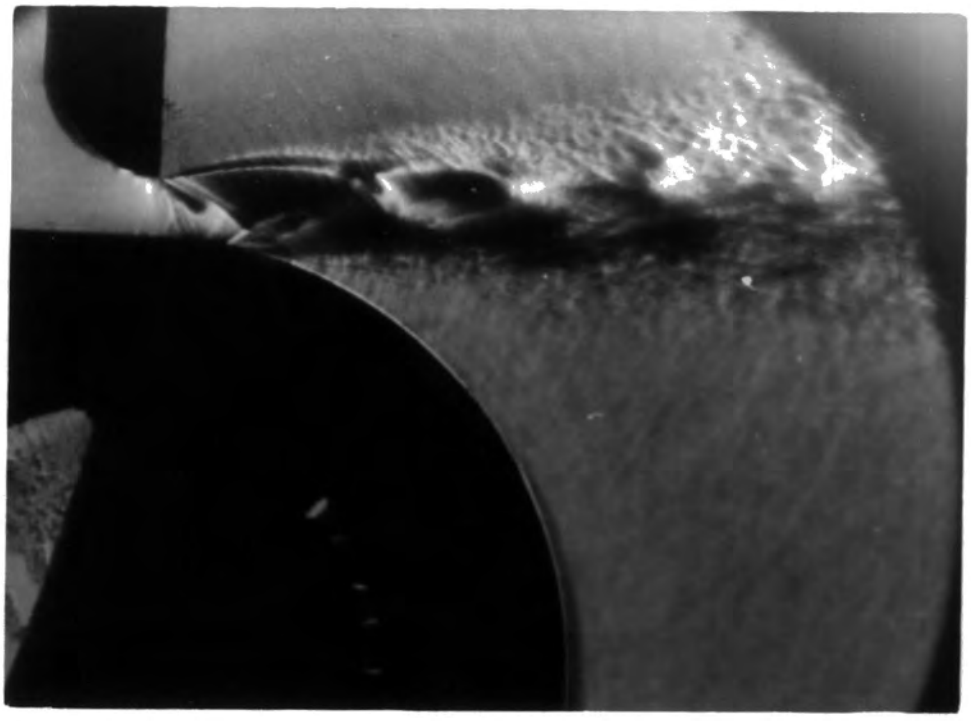

PLATE 22a: Vertical Density Gradients

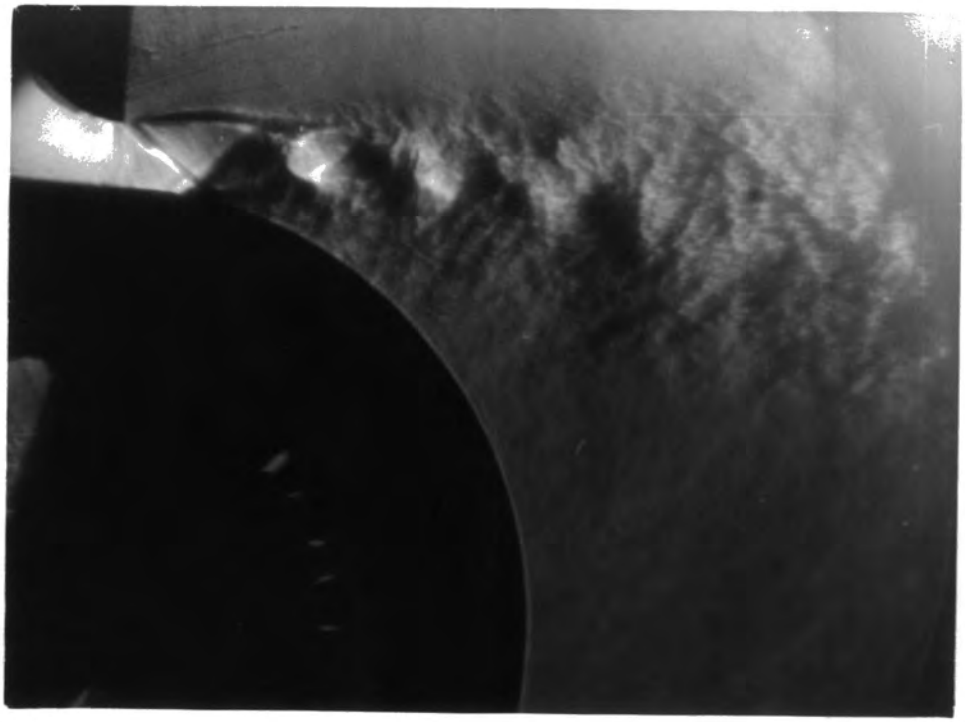

PLATE 22b: Horizontal Density Gradients

PLATE 22: SPARK SCHLIEREN, BREAKAWAY, SLOT = 4 mm

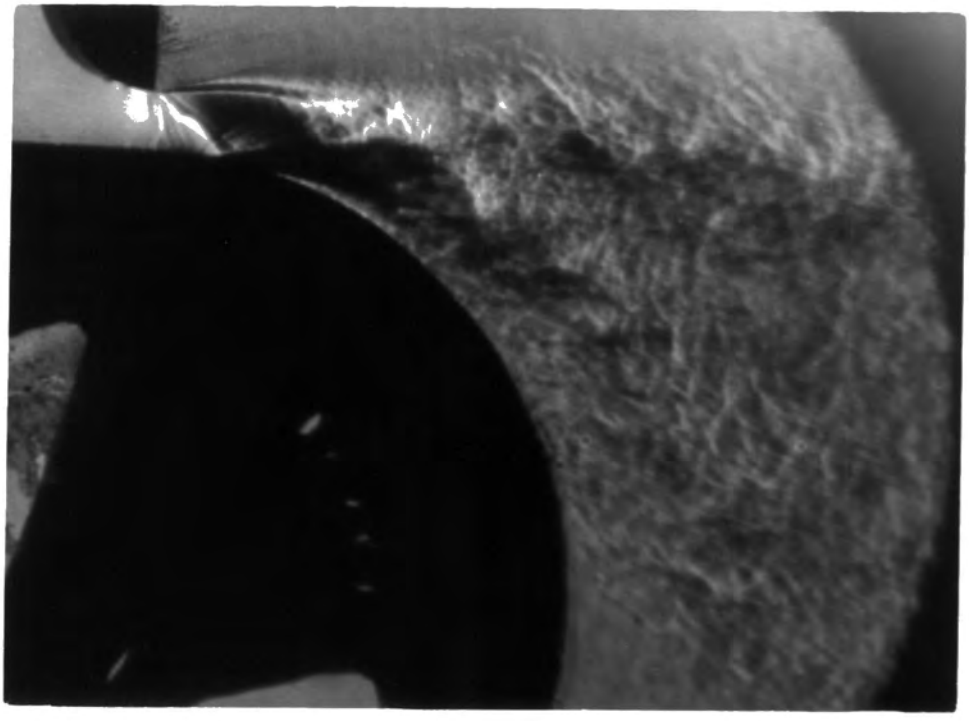

PLATE 23a: Vertical Density Gradients

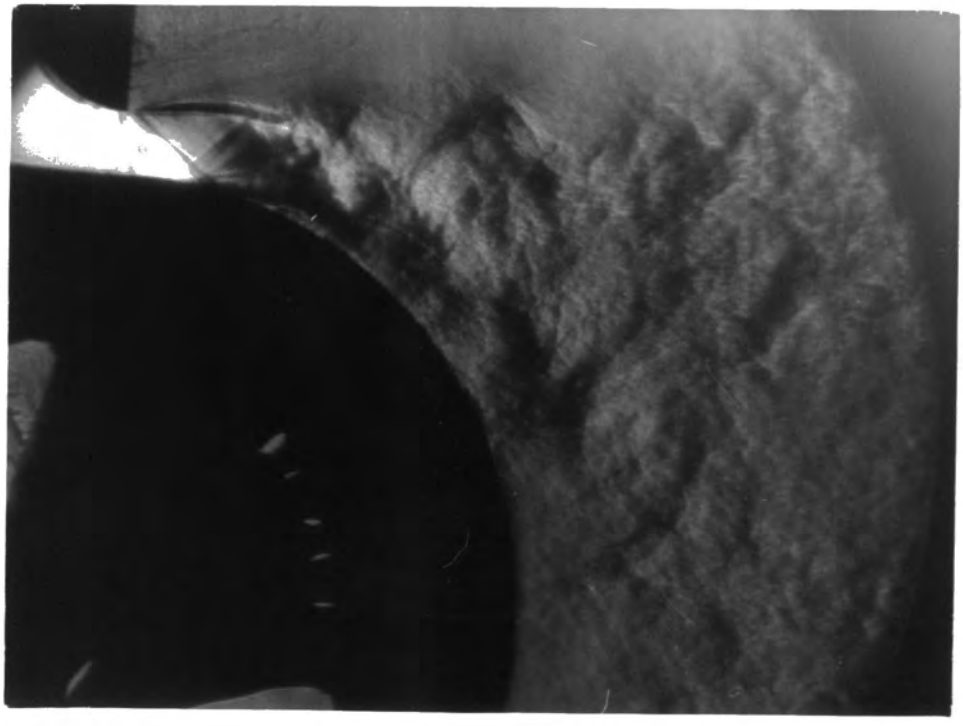

PLATE 23b: Horizontal Density Gradients

PLATE 23: SPARK SCHLIEREN, REATTACHMENT, SLOT = 4 mm

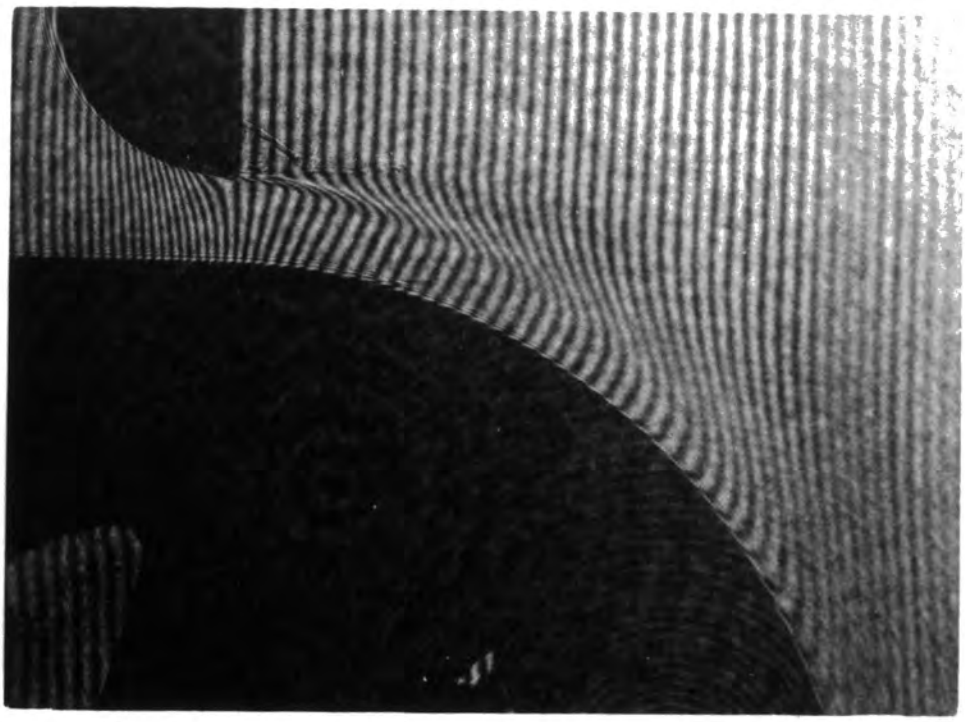

PLATE 24: Interferometry, Pa/Po = 0.654, Slot = 4 mm

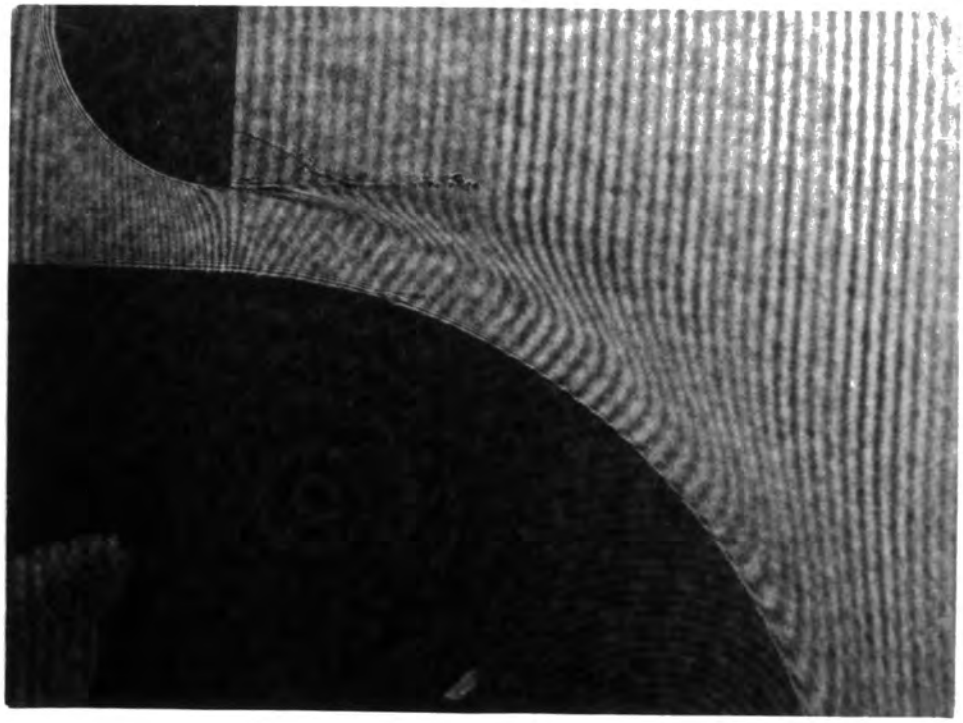

PLATE 25: Interferometry, Pa/Po = 0.579, Slot = 4 mm

THE DEVELOPMENT AND BREAKAWAY OF A COMPRESSIBLE AIR JET WITH STREAMLINE CURVATURE AND ITS APPLICATION TO THE COANDA FLARE

by

ANDREW ROBERT GILCHRIST B.Sc. (Dunelm)

Department of Engineering
University of Durham

A thesis submitted for the degree of Doctor of Philosophy
of the University of Durham

NOVEMBER 1985

Dedicated to my parents

ABSTRACT

This study concerns an underexpanded jet, issuing from a convergent slot into quiescent air, as it is deflected by a convex surface of constant radius. Emphasis is placed on the mechanism of breakaway, a phenomenon whereby the jet leaves the surface tangentially.

An optical system based on the standard Z-type Schlieren configuration and capable of interferometric, Schlieren and shadowgraph techniques has been designed. The techniques are interchanged simply, a laser source being employed for interferometry and a Xenon spark source for Schlieren and shadowgraph. Vibrations limit the interferometry and improvements are discussed. Shadowgraph and both spark and continuous Schlieren techniques gave good results.

Total pressure traverses and surface oil flow visualization show that the influence of secondary flows on breakaway is small. Measurements of the coefficient of discharge show an increase both as the stagnation pressure is increased and as the slot width is reduced. The existence of a separation bubble has been established from surface static pressure measurements and shadowgraph and Schlieren photographs. Surface oil flow visualization shows a region of reversed flow within the bubble. The bubble grows as the stagnation pressure is increased and eventually causes breakaway.

A potential flow calculation method using the method of characteristics has been developed. Calculation of a fully attached jet is inaccurate because the separation bubble is ignored. A calculation using the measured surface static pressures accurately predicts the main features of the first shock cell. Reattachment occurs further downstream of the jet and its breakaway should involve a coupling of the solutions of the outer shear layer, potential core and separated boundary layer, the latter including reversed flow.

ACKNOWLEDGEMENTS

I would like to express my gratitude to the people and organisations that have contributed to the work presented in this thesis. In particular to my supervisor Dr. David Gregory-Smith, not only for setting up the project, but also for his guidance throughout the study and the preparation of this thesis. To the Science and Engineering Research Council and British Petroleum Research Centre at Sunbury-on-Thames for their financial support. To Dr. John Boden and Dave Chesters of the B.P. Research Centre and Dave Etheridge and Garry Oskam of Kaldair Ltd. for their help and advice. To Bill, Terry, Ray, Mike, Frank and Brian for their technical help. To Chris for her efficient speedy typing. To Joe, who at last proved more of a help than a hinderance when acting as a solid ultra-violet lamp holder during the flow visualization photography. And to Alastair, whose light-fingeredness on the flow control valve enabled photographs such as those in Plate 23 to be taken.

C O N T E N T S

LIST OF FIGURES

LIST OF PLATES

PRINCIPAL NOTATION

A	area of slot
a	Coanda radius, speed of sound (Section 3.1, Appendix A)
b	slot width
c	settling tube width, speed of light (Chapter 4)
c_D	discharge coefficient
c_p	surface static pressure coefficient
$c_{p'}$	surface static pressure coefficient with curvature, $= - c_p(a/b)$
d	height of light source image above knife edge
e	breadth of light source image
f	focal length
I	light intensity
K	Gladstone–Dale constant
k	coefficient of heat viscosity
M	Mach number
m	mass flow rate
n	refractive index
p	static pressure
p_0	stagnation pressure
Q	coefficient in finite difference equations
R	universal gas constant, coefficient in finite difference equations (Section 3.1, Appendix A)
r	radius of curvature
Re	slot Reynolds number $= [(p_0-p_a)ab/\rho\nu^2]^{1/2}$
S	physical path length
T	static temperature, coefficient in finite difference equations (Section 3.1, Appendix A)
T_0	stagnation temperature

t	time
u	x-component of velocity
u_τ	wall shear velocity = $\sqrt{\tau_w/\rho}$
V	total velocity = $\sqrt{u^2 + v^2}$
v	y-component of velocity
x	streamwise coordinate along or parallel to surface
y	coordinate perpendicular to x-direction
$y_{1/2}$	value of y where $u = u_{m/2}$
z	coordinate along optical beam

Greek Symbols

α	Mach angle
γ	ratio of specific heats
ϵ	angle of light ray to z-direction
θ	angle of streamline to x-direction
λ_+	gradient of positive characteristic
λ_-	gradient of negative characteristic
λ_s	gradient of streamline
μ	viscosity
ν	dynamic viscosity = μ/ρ
ρ	static density
ρ_o	stagnation density
τ	shear stress
τ_w	wall shear stress
ϕ	angle round Coanda from slot exit
ϕ_o	angle round Coanda from hypothetical slot of zero width
ϕ_{SEP}	separation angle round Coanda from hypothetical slot of zero width